ELECTRON PARAMAGNETIC RESONANCE STUDIES OF SPIN AND MOLECULAR
MOTION IN SURFACTANT AGGREGATES

Lauren E. Jarocha

A dissertation submitted to the faculty at the University of North Carolina at Chapel Hill in
partial fulfilment of the requirements for a degree of Doctor of Philosophy in the Department of
Chemistry.

Chapel Hill
2014

Approved by:

Malcolm D. E. Forbes

Andrew Moran

James Cahoon

Jillian Dempsey

Sergei Sheiko

ABSTRACT

Lauren E. Jarocha: Electron Paramagnetic Resonance Studies of Spin and Molecular Motion
in Surfactant Aggregates
(Under the direction of Malcolm D. E. Forbes)

Steady-state (SSEPR) and time-resolved electron paramagnetic resonance (TREPR) spectroscopy have been used to examine the dynamic motion and spin wavefunction evolution of stable nitroxide radicals or photochemically generated radical pairs in aqueous surfactant aggregates, respectively. Alteration of the surfactant molecular structure has a pronounced effect on the aggregation behavior and physical properties of surfactant aggregates. The surfactant systems discussed here are known to form micelles, vesicles, lamellar phases, surfactant networks, and gels. Both SSEPR and TREPR are sensitive to the nanometer scale confinement of radicals, making these experimental techniques usefully in monitoring phase changes in caused by experimental conditions, such as temperature, concentration, equilibration time, molecular structure, or surfactant mixing. Analysis of the line shape of the EPR spectra of radicals confined in these supramolecular structures is accomplished through spectral simulations and provides information on the physical properties of surfactant aggregates, including size, polarity, and viscosity.

ACKNOWLEDGEMENTS

TABLE OF CONTENTS

LIST OF TABLES

LIST OF FIGURES

LIST OF SCHEMES

LIST OF ABBREVIATIONS AND SYMBOLS

Chemical Symbols

AQ	9,10-anthraquinone sodium salt
AQDS	9,10-anthraquinone-2,6-disulfonate disodium salt
AQS	9,10-anthraquinone-2-sulfonate sodium salt
AQSH·	semi-anthraquinone radical of 9,10-anthraquinone-2-disulfonate sodium salt
BP	benzophenone
BPd10	deuterated benzophenone
Brij 35	polyoxyethylene (23) lauryl ether
Brij 97	polyethylene glycol (10) oleyl ether
Brij 700	polyoxyethylene glycol (100) octadecyl ether
C_nE_m	poly(oxyethylene) alkyl ether surfactant
-·CH-	secondary radical
-·CH$_2$	primary radical
CH$_2$	methylene group
CH$_3$CN	acetonitrile
CH$_3$-N$^+$	methyl-ammonium bond in the DTAC head group
·CH$_3$	methyl radical
Cl$^-$	chlorine ion
CTAB	cetyltrimethyl ammonium bromide
CTAC	cetyltrimethylammonium chloride

DTAC	dodecyltrimethylammonium chloride
DBNBS	3,5-dibromo-4-nitrosobenzene sulfonate
D_2O	deuterium oxide
DSA	doxyl stearic acid
DSE	doxyl stearic acid methyl esters
$DTA^+–DS^-$	dodecyltrimethylammonium-dodecyl sulfate ion pair salt
EO	ethylene oxide
$EO_nPO_mEO_n$	Pluronic triblock copolymer surfactant
F68	poly(ethylene glycol)-*block*-poly(propylene glycol)-*block*-poly(ethylene glycol), $EO_{76}PO_{29}EO_{76}$
H	hydrogen
H_α	alpha hydrogens
H_β	beta hydrogens
H_γ	gamma hydrogens
H_2O	water
H_2O_2	hydrogen peroxide
4-HTB	4-hydroxy-TEMPO-benzoate
KrF	krypton fluorine gas mixture for excimer laser operation at 248 nm
L61	poly(ethylene glycol)-*block*-poly(propylene glycol)-*block*-poly(ethylene glycol), $EO_2PO_{32}EO_2$
L64	poly(ethylene glycol)-*block*-poly(propylene glycol)-*block*-poly(ethylene glycol), $EO_{13}PO_{30}EO_{13}$
Na^+	sodium ion
P85	poly(ethylene glycol)-*block*-poly(propylene glycol)-*block*-poly(ethylene glycol), $EO_{26}P40_0EO_{26}$

PEO	poly(ethylene oxide)
PEO-PPO-PEO	Pluronic triblock copolymer surfactant
PO	propylene oxide
PPO	poly(propylene oxide)
PPO-PEO-PPO	reverse Pluronic triblock copolymer surfactant
SCS	sodium cetyl sulfate
SDS	Sodium dodecyl sulfate
S–O	sulfur oxygen bond in the SDS head group
TEMPO	2,2,6,6-tetramethylpiperidine 1-oxyl
Triton X-100	polyethylene glycol (10) p-(1,1,3,3-tetramethylbutyl)-phenyl ether
Triton X-405	polyethylene glycol (40) p-(1,1,3,3-tetramethylbutyl)-phenyl ether
XeCl	xenon chloride gas mixture for excimer laser operation at 308 nm
17R4	poly(propylene glycol)-*block*-poly(ethylene glycol)-*block*-poly(propylene glycol), $PO_{14}EO_{24}PO_{14}$

Greek symbols

α	spin wavefunction representing electron spin state $m_s = \frac{1}{2}$
α	degree of counterion binding
α_D	Euler angle relating the magnetic frame of a nitroxide to the rotational frame of reference
β	spin wavefunction representing electron spin state $m_s = -1/2$
β_D	Euler angle relating the magnetic frame of a nitroxide to the rotational frame of reference
β_e	Bohr magneton

β_{int}	interaction parameter in the regular solution theory
γ_1	activity coefficient for surfactants 1 in a binary mixture
γ_2	activity coefficient for surfactant 2 in a binary mixture
γ_D	Euler angle relating the magnetic frame of a nitroxide to the rotational frame of reference
ε_0	vacuum permittivity
ϵ_μ	eigenvalues of the eigenfunctions of the SCRP, μ is the index for the state
ε_r	dielectric constant of the medium
η	viscosity
η	3/2 of the TM polarization
κ	Debye screening length
λ	exponential decay constant for the exchange interaction as a function of r
Λ_s	reactivity of the singlet state of the SCRP
μ	index for identifying members of a radical pair
μ_{el}	free energy per charge
μ_{ex}	excess free energy per aggregated molecule
μs	microsecond
ν	frequency
π	pi
ρ	density of states
σ	boundary condition for the micelle in the microreactor model
τ_{agg}	rotational correlation time for the rotational motion of a surfactant aggregate structure
τ_c	rotational correlation time

$\tau_{contact}$	time the radical pair spends in the contact state
τ_{doxyl}	rotational correlation time of the doxyl stearic acid spin probe
τ_{free}	time the radical pair spends in the free state
τ_R	rotational correlation time of a triplet sensitizer in a micelle
τ_{sp}	response time of the EPR spectrometer
$\tau_{\parallel}$	rotational correlation time parallel to the main axis of a molecule with axial symmetry
$\tau_{\perp}$	rotational correlation time perpendicular to the main axis of a molecule with axial symmetry
χ	nuclear spin configuration
χ_{SDS}	mole fraction of SDS
ψ	director tilt angle
Ψ	set of angles relating the director frame to the laboratory frame in the MOMD model
ψ_μ	eigenfunction of the Hamiltonian of an SCRP, μ is the index for the state
ω_0	operating frequency of the EPR spectrometer
ω_1	amplitude of the microwave field in frequency units
ω_μ	Larmor procession frequency of radical, μ is the index for the radical
Ω_D	set of Euler angles rotating the axes of the magnetic tensor into the rotational diffusion tensor

Roman Symbols

a	area per surfactant head groups
A_0	hyperfine coupling constant
a_1, a_2	activities for surfactant 1 or surfactant 2 in a binary mixture

A_N	isotropic hyperfine coupling constant of a nitroxide
A_{XX}, A_{YY}, A_{ZZ}	components of the hyperfine tensor along the canonical axes of molecular symmetry
Å	angstrom
$A+$	splitting between the low field and center field line in a nitroxide SSEPR spectrum
B_0	applied static magnetic field
B_1	magnetic component of the applied microwave radiation
C	concentration
C_{agg}	concentration of surfactant in aggregates
C_s	concentration of added salt
C_{total}	total concentration of all surfactants in a binary mixture
C_1^{free}	concentration of monomer surfactant in solution for surfactant 1 in a binary mixture
C_2^{free}	concentration of monomer surfactant in solution for surfactant 2 in a binary mixture
°C	degrees centigrade
cal	calories
CPP	critical packing parameters
CMC_1	CMC of surfactant 1 in a binary mixture of surfactants
CMC_2	CMC of surfactant 2 in a binary mixture of surfactants
CMC_{mix}	the CMC of a binary mixture of surfactants
CW	continuous wave irradiation
D	mutual diffusion coefficient of the radical pair
D	doublet state

D_{ZFS}	zero field splitting parameter
E	energy of a state
E_1	electric field component of the applied microwave radiation
ΔE	energy difference between spin states
e_{el}	charge of an electro
ESP	Electron Spin Polarization
Eq.	equation
E_{ZFS}	zero field splitting parameter
f(t)	window function for the microreactor model
g	g-factor
G	Gauss
g_e	g-factor of a free electron
G_E	excess free energy of mixing
GHz	gigahertz
h	Planck's constant
H	mean curvature at a surface of charge
$\mathcal{H}$	Hamiltonian operator
$\Delta H_{(+1)}$	peak to peak width of the $m_I = +1$ transition of a nitroxide
h_0	zero order expansion term in the expression for μ_{el}
h_1	first order expansion term for the expression of μ_{el}
H_E	excess free enthalpy of mixing
$\mathcal{H}_\mu$	spin Hamiltonian for individual members of a RP, where μ indexes the radical identity
Hz	s^{-1}

I	total nuclear spin quantum number
$I_{(+1)}$	arbitrary intensity of the $m_I = +1$ transition of a nitroxide
$I_{(-1)}$	arbitrary intensity of the $m_I = +1$ transition of a nitroxide
I_T, I_S	intensity of the T or S type components of the APS
$\hat{I}_z$	spin operator for the nuclear spin angular momentum along the z axis
j	dimensionless curvature of surfactant aggregate surface
J	exchange interaction
J_0	the value of the exchange interaction at the contact distance between two radicals
J_{eff}	effective exchange interaction in the CFN model
k	Boltzmann constant
K	Kelvin
k_{esc}	rate of radical escape from the micelle
k_g	rate constant for generation of the SCRP
k_μ	decay rate of radical, μ is the index for the radical identity
k_{rel}	rate constant for the relaxation of the electron spin state populations of an excited triplet state
L	radius of the region inside the micelle accessible to radical a in the microreactor model
$\hat{\mathcal{L}}$	Liouville operator
l_B	Bjerrum length
L_m	radius of the micelle in the microreactor model
L_t	length of the surfactant tail
m	meter
M	molar

$^3M*$	triplet excited state of a molecule
mL	milliliters
mg	milligram
MHz	megahertz
m_I	nuclear magnetic spin quantum number
min	minute
mm	millimeter
mM	millimolar
mol	mole
m_s	spin quantum number of an electron
mT	millitesla
M(t)	transverse magnetization of the RP
mW	milliwatts
M_w	molecular weight
N	anisotropy of molecular diffusion, $N=R_\parallel \backslash R_\perp$
N_A	Avogadro's number
N_{agg}	aggregation number
nm	nanometer
ns	nanosecond
p	population
r_μ	van der Waals radius of radical, where μ is the index for the radical
R	distance of closest approach of the radicals
R	gas constant

$\overline{R}$	isotropic rotational diffusion tensor
R_μ	Bloch relaxation matrix for free radical, where μ is the index for the radical
R_h	hydrodynamic radius
RST	regular solution theory
$R_\parallel$	rotational diffusion tensor element parallel to the molecular axis of symmetry
$R_\perp$	rotational diffusion tensor element perpendicular to the molecular axis of symmetry
s	seconds
s	dimensionless reduced surface charge density
S	total spin quantum number
S_0	singlet ground state
S_1	first singlet excited state
S_E	excess entropy of mixing for surfactants
S_{eff}	order parameter
ST_0	mixing of the S and T_0 states
ST_-	mixing of the S and T_- states
$\hat{S}_z$	spin operator for the electron spin angular momentum along the z axis
T	temperature
T	triplet state
T_1	spin lattice relaxation
T_2	longitudinal relaxation of the radical
T_X, T_Y, and T_Z	the triplet states of a molecule in the molecular frame

T_+, T_0, and T_-	the triplet states of a molecule in the laboratory frame using a high field basis set
q	local magnetic field difference, frequency of ST_0 mixing between members of the RP
Q	quartet state
Q-band	35 GHz operating microwave frequency for an EPR spectrometer
V_m	volume of the micelle
V_t	volume of the surfactant tail
wt. %	weight percent
x	mole fraction of surfactant 1 in solution
X, Y, Z	canonical axes of the molecule
X-band	9.5 GHz microwave frequency
x_D, y_D, z_D	axes for the director frame in the MOMD model
x_L, y_L, z_L	axes for the laboratory reference frame
x_M, y_M, z_M	axes for the magnetic tensor of a molecule
x_R, y_R, z_R	axes for the rotational diffusion tensor of a molecule
Z	frequency of forced radical reencounters

Abbreviations

A	absorption
APS	antiphase splitting
CAC	critical aggregation concentration
CFN	Closs, Forbes, Norris model for the spin-correlated radical pair
CIDNP	chemically induced dynamic nuclear polarization

CMC	critical micelle concentration
CMT	critical micelle temperature
cryo-TEM	cryogenic transmission electron microscopic
DC	direct current
DLS	dynamic light scattering
DVT	digital variable temperature controller
E	emission
EPR	electron paramagnetic resonance
ESEEM	electron spin echo envelope modulation
ESPT	electron spin polarization transfer
FDA	Federal Food and Drug Administration
FT-EPR	Fourier transform electron paramagnetic resonance
GaAs fet	gallium arsenide field effect transistor
HFC	isotropic hyperfine coupling
ID	inner diameter
ISC	intersystem crossing
MFE	magnetic field effect
MO	molecular orbital
MOMD	microscopic order macroscopic disorder
NMR	nuclear magnetic resonance
RP	radical pair
RPM	Radical Pair Mechanism
RTPM	Radical Triplet Pair Mechanism

SANS	small angle neutron scattering
SAXS	small angle x-ray scattering
SCRP	spin-correlated radical pair
SCRPM	spin-correlated radical pair mechanism
SLE	stochastic Liouville equation
S/N	signal to noise ratio
SOC	spin orbit coupling
SSEPR	steady-state electron paramagnetic resonance
TE	transverse electric
TM	triplet mechanism
TREPR	time-resolved electron paramagnetic resonance
UV	ultraviolet
UV-vis	ultraviolet/visible spectrometry
ZFS	zero field splitting

CHAPTER 1: Introduction to Electron Paramagnetic Resonance Spectroscopy

1.1 General Introduction

Molecular motion and diffusion are of fundamental importance for many chemical reactions; restricted motion can alter reactions rates or result in different chemical products. Nanoscale confinement of small organic molecules can be achieved using a wide range of supramolecular structures, including host-guest complexes,[1] nanocrystalline materials,[2] and self-aggregating surfactant systems like micelles and vesicles.[3] Surfactants aggregates have been particularly promising and heavily employed to study the effects of restricted diffusion on chemical reactions and molecular interactions because of the diversity of surfactant functions and physical properties of the resulting aggregates. Surfactants can act as detergents, wetting agents, emulsifies, foaming agents, or dispersants. The function of a surfactant is explicitly tied to the structure of both the hydrophobic and hydrophilic portions of the molecule. The shape and size of supramolecular surfactant aggregates can vary greatly, from disordered micelles to single lamellar layers or multi-lamellar vesicles. This diversity has led to their use in a wide variety of industrial, biological, and chemical applications, including household cleaning formulations,[4] petroleum clean up,[5] gel electrophoresis,[6] protein unfolding[7] or solubilization,[8] "nanoreactors" for control of chemical reactions or charge separation, [3c, 9] templates for nanostructured materials,[10] drug solubilization,[11] and targeted drug delivery systems.[12]

Experimentally, electron paramagnetic resonance (EPR) techniques are particularly sensitive to the molecular motions of radicals and radical pairs. Because of this sensitivity, supramolecular confinement of the radicals manifests itself in characteristic ways in their EPR

spectrum. Radicals created in supramolecular systems such as micelles show anomalies in both their magnetic resonance spectra and in the observation of magnetic field effects on their transient optical absorption spectra.[13] The links between magnetic resonance spectroscopy, photochemistry and supramolecular chemistry have provided a rich breeding ground for inter-disciplinary research and for the discovery of many interesting fundamental properties of both free radicals and surfactant-based supramolecular aggregates, including micelles,[14] reverse micelles,[15] and vesicles.[16]

Both steady-state and time-resolved electron paramagnetic resonance (EPR) techniques have been used extensively to explore the physical properties of surfactant aggregates and the effects of micellar confinement on the dynamic motion of radicals. Steady-state electron paramagnetic resonance (SSEPR) spectroscopy has been used to provide valuable information on microviscocity in micelles,[17] ordering of small organic radicals in lamellar phases,[18] phase transitions induced by pH[19] or temperature,[20] and hydration of the micelle interior.[17b, 21] Additional information on radical structure,[22] reaction dynamics, [3c, 9, 23] kinetics, [24] and the effects of confinement and intermolecular diffusion in radical reactions[25] can be obtained from time-resolved electron paramagnetic resonance (TREPR) spectroscopy, which combines the EPR technique with laser flash photolysis in order to observe radicals on the sub-microsecond timescale.

This dissertation describes the utilization of direct-detection SSEPR and TREPR in the study of radicals in supramolecular, surfactant-based structures. The goals of the present chapter is to provide a description of the SSEPR and TREPR experiment and to briefly outline the origin and appearance of TREPR spectra from several known mechanisms of CIDEP.[26] Later chapters will explore the details and nuances of experimental observations and the control of radical

dynamics in a wide range of surfactant systems that vary by chemical structure, charge, aggregate structure, and response to environmental stimuli.

1.2 Experimental Overview

1.2.2 Electron Paramagnetic Resonance (EPR)

Since its discovery in 1945 by Zavoisky,[27] EPR has been used as the primary technique for identifying and characterizing radical structures. As a magnetic resonance technique, EPR is directly analogous to nuclear magnetic resonance (NMR) of protons, but the spectral transitions observed in the EPR experiment are between electron spin states.[28] The electron has a total spin quantum number of S = 1/2, with two possible spin states that are referred to as α (m_s = 1/2) or β (m_s = -1/2). Typically, the energies of the α and β states of an unpaired electron are degenerate. When there is a strong applied magnetic field, this degeneracy is lifted. The splitting between the two states is referred to as the electron Zeeman interaction and the energy difference between the two is:

$$\Delta E = g\beta_e B_0 \tag{1}$$

where g is the g-factor of the electron and can be considered analogous to chemical shift in NMR experiments, β_e is the Bohr magneton, and B_0 is the static magnetic field.

In order to observe transitions between these two energy levels, the sample is exposed to continuous wave (CW) microwave irradiation. In the absence of any additional interactions, the resonance condition to observe an EPR transition for the unpaired electron occurs when the energy of the applied microwave radiation matches the splitting due to the Zeeman interaction.

$$h\nu = g\beta_e B_0 \tag{2}$$

Because the frequency of the microwave irradiation is constant (9.5GHz at X-band), the magnetic
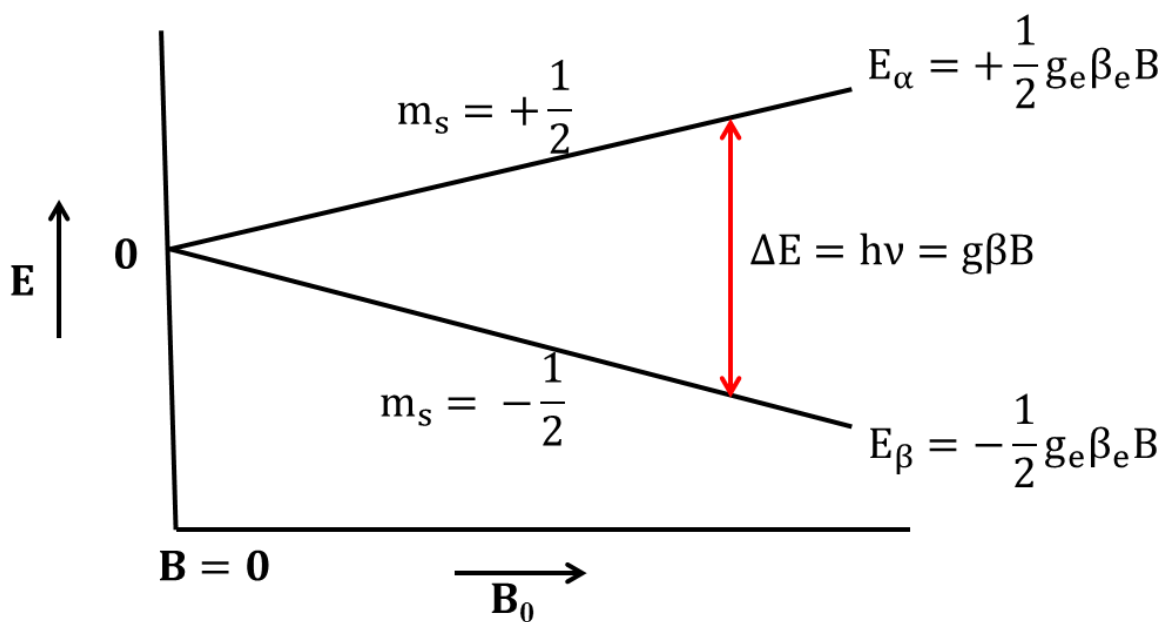
Figure 1.1: An energy level diagram showing the separation of the m_s = +1/2 and m_s = -1/2 spin states of a free electron as a function of the strength of the applied static magnetic field, B_0, due to the Zeeman interaction. An allowed EPR transition is observed when the difference in the energy between the two spin states matches the energy of the CW microwave radiation from the EPR bridge.

field strength is swept, and an EPR transition will be observed when the strength of the applied field causes this resonance condition to be met (Figure 1.1).

Additional splitting of EPR transitions are observed due to interactions between the electron's magnetic moment and the magnetic moment of neighboring nuclei. This additional splitting is referred to as an isotropic hyperfine interaction. The magnitude of the splitting is described with a hyperfine coupling constant (A_0). In the case of a neighboring hydrogen nucleus, each electron energy level is split into two − corresponding to the interaction of the unpaired electron with either $m_I = 1/2$ or $m_I = -1/2$ nucleus. In the case of a neighboring nitrogen nucleus, the nuclear spin, I, is equal to 1, and the energy levels of the electron are split into three ($m_I = +1$, 0, or -1). The selection rules for the EPR experiment dictate that $\Delta m_S = \pm 1$, $\Delta m_I = 0$. The allowed transitions for these hyperfine interactions are shown in Figure 1.2.

The simplest form of the spin Hamiltonian under consideration for the SSEPR experiments described here can then be written as:[28]

$$\widehat{\mathcal{H}} = g\beta_e B\hat{S}_z + \sum_i A_{0i}\hat{S}_z\hat{I}_{zi}$$

(3)

where $\hat{S}_z$ and $\hat{I}_z$ are the spin operators for the electron and nuclear spin angular momentum along the z axis of the magnetic field. The magnitude of the hyperfine interaction, A_0, and the spin of neighboring nuclei both vary. The summation in the second term allows for the inclusion of hyperfine interactions from multiple neighboring magnetic nuclei. From this basic Hamiltonian, structural information about neighboring nuclei that is analogous to the NMR experiment can be obtained. This spin Hamiltonian can also be modified for systems that have more than one unpaired electron, and additional interactions, including dipole-dipole interactions and Heisenberg spin exchange can be included as necessary.
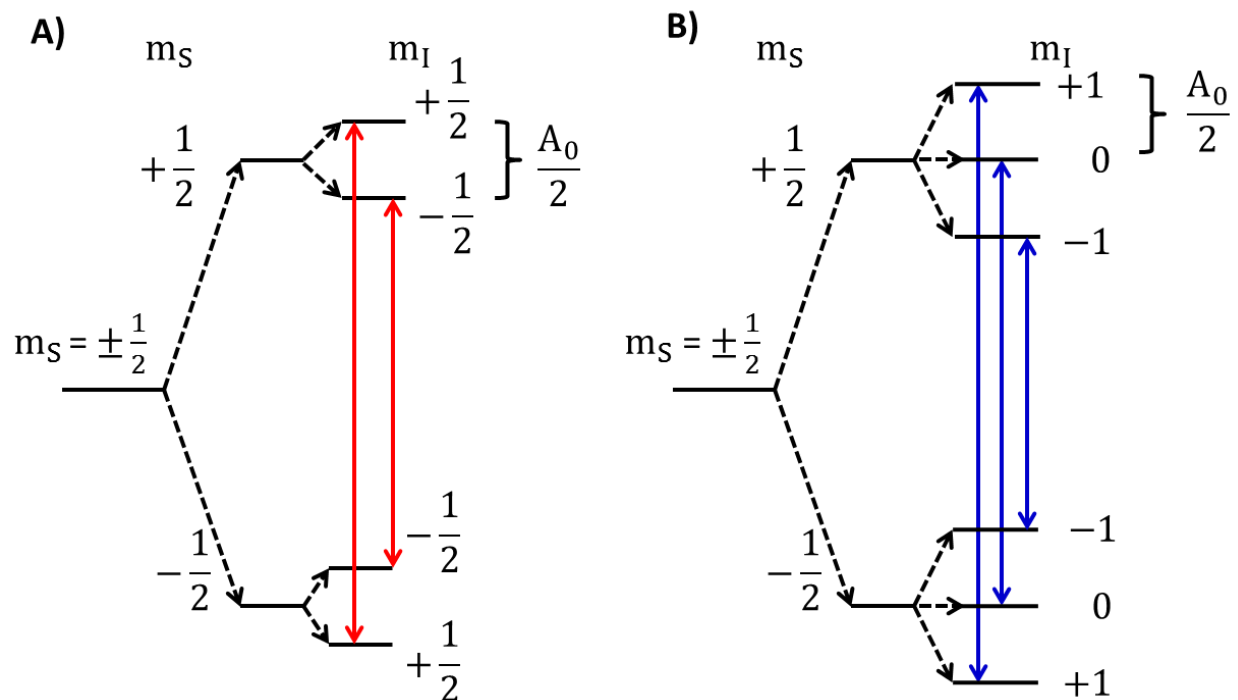
Figure 1.2: An energy level diagram showing the effect of a single hyperfine interaction, with a hyperfine coupling constant of A_0, with a hydrogen nucleus ($m_I = \pm 1/2$; A) or a nitrogen nucleus ($m_I = 0, \pm 1$; B) on the splitting of the energy levels and the observed transitions in the EPR experiment. Allowed transitions must obey the selection rules for the experiment, with $\Delta m_s = \pm 1$ and $\Delta m_I = 0$. This results in two observable EPR transitions in the case of a hydrogen nucleus (A) or three observable transitions in the case of a nitrogen nucleus (B).

It is important to note that the equations above treat both g and A_0 as constants. This treatment is only applicable in radicals experiencing very fast rotational motion such that they behave as if the molecule were magnetically isotropic. In most molecules, the g-factor is anisotropic and its value depends on the orientation of the radical with respect to the magnetic field. Both the g-factor and the hyperfine interaction may be accurately represented by 3rd rank tensors. For the radical to behave as if it is isotropic, the rate of rotation must be greater that the differences between the largest and smallest components of thee tensors. When the rate of rotation of the molecules is slow, the anisotropy of the g-factor and hyperfine interaction will affect the line shape of the EPR spectrum and must be accounted for using these tensors.

The EPR experiment is conducted by exposing a sample containing a paramagnetic species to continuous wave (CW) microwave irradiation. The sample is placed inside a microwave resonator that is designed in accordance with solutions to Maxwell's equations for the operating frequency of the spectrometer.[29] The conventional operating frequency, ω_0, for the EPR experiment is 9.5 GHz (X-band). The microwave irradiation propagates from a source in a microwave bridge, down a piece of waveguide, and into the resonator cavity. The use of a resonant cavity allows the microwaves to make multiple passes through the sample, increasing the probability for absorption. The resonator is placed in between the poles of an electromagnet, which provides the external magnetic field, B_0, typically in the range from 0-6 kG for an X-band spectrometer. To collect the EPR spectrum, the external magnetic field is swept through each EPR transition at a constant microwave frequency.[30] The instrument detects the reflected microwave power from the resonator cavity at each point in the magnetic field sweep and compares it to a reference sample diverted directly from the microwave source. After a sample is placed in an EPR cavity, the cavity is "tuned" before the EPR spectrum is collected. This involves three steps: 1)

changing the microwave source frequency to minimize reflected microwave power at the detector, 2) changing the coupling of the microwaves into the cavity from the waveguide, and 3) matching the phase of the microwaves from the working arm (cavity) and reference arms. The difference signal between the microwaves reaching the detector from the working arm and the reference arm is converted to a DC voltage. When the resonance condition (Eq. 2) is met, changes in the absorption of microwaves by the sample are detected as changes in the measured DC voltage and this makes up the EPR signal.

Although the fundamental principles are the same, differences in experimental design make the SSEPR and TREPR experiments sensitive to different timescales and different types of dynamic motion.[29] SSEPR is employed to study longer lived radical species, with lifetimes greater than 40 μs. It is also particularly sensitive to rotational motion of radicals – which can be affected by the local environment of the radical species, including temperature, viscosity, or polarity. On the other hand TREPR experiments involve photochemically generating radicals in situ, and these radicals are often short lived. At X-band, TREPR experiments are used to detect radical species between 50 ns to 10 μs after their creation. The TREPR spectrum is also very sensitive to changes in the radical spin states caused by translational diffusion. The source of these differences and important principles in their application to surfactant aggregates are discussed in greater detail below.

1.2.2 Steady-State Electron Paramagnetic Resonance (SSEPR)

A schematic representation of the standard, commercial X-band SSEPR is shown in Figure 1.3. All spectra presented here were recorded on a JEOL FA-100 spectrometer operating at X-band (9.5 GHz). The SSEPR experiment has a high sensitivity (as few as 10^{11} spins per sample)
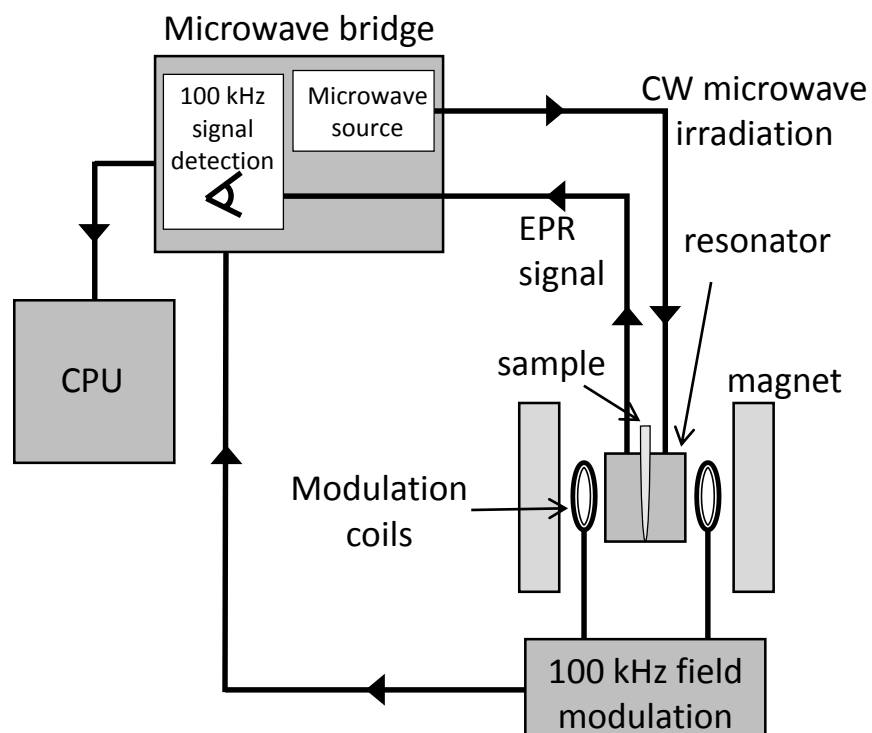
Figure 1.3: A block diagram illustrating the major components of the SSEPR experiment.

but a relatively slow instrument response time that limits its use to the detection of long-lived radical species or systems in which constant generation of short lived radicals allows for the build-up of a detectable "steady-state" concentration.[31] In order to obtain high sensitivity, SSEPR employs phase sensitive detection (Figure 1.4).[29] The external magnetic field is modulated as it is swept, usually at a frequency of 100 kHz. A narrow-band amplifier only passes signal with the same frequency as the modulation frequency of the EPR. Field modulation dramatically increases the signal to noise (S/N) ratio, but it also gives the resulting spectra a first derivative line shape. The amplitude of the field modulation must be kept smaller than the line widths of the EPR signals to avoid line shape distortions, but this limits the time response of the spectrometer, at best, to the inverse of the modulation frequency. Practically, for good S/N, three or four cycles of modulation are necessary within the line width of the EPR transition, which means that the SSEPR experiment is capable of detecting only those radical species that have lifetimes of 40 μs or more.[29] Most organic radicals have lifetimes in solution on the order of 10–100 μs, making their detection by SSEPR at room temperature problematic.

Another important feature of the SSEPR experiment relevant to the study of surfactant aggregates is the microwave resonator. Resonators for EPR spectroscopy fall into several categories depending on sample geometry, size, and dielectric properties,[32] but in general the sample geometry should match the cavity. The JEOL FA-100 uses a cylindrical TE011 resonator cavity, and the recommended sample geometry is a 4-5 mm quartz EPR tube. The resonator functions to provide a greater cross-section and, therefore, a greater probability of interaction between the sample and the CW microwave radiation. The sample is specifically situated inside the resonator cavity at the maximum of the magnetic component (B_1) of the microwave radiation and the minimum of the electric field component (E_1). This is important to ensure two conditions
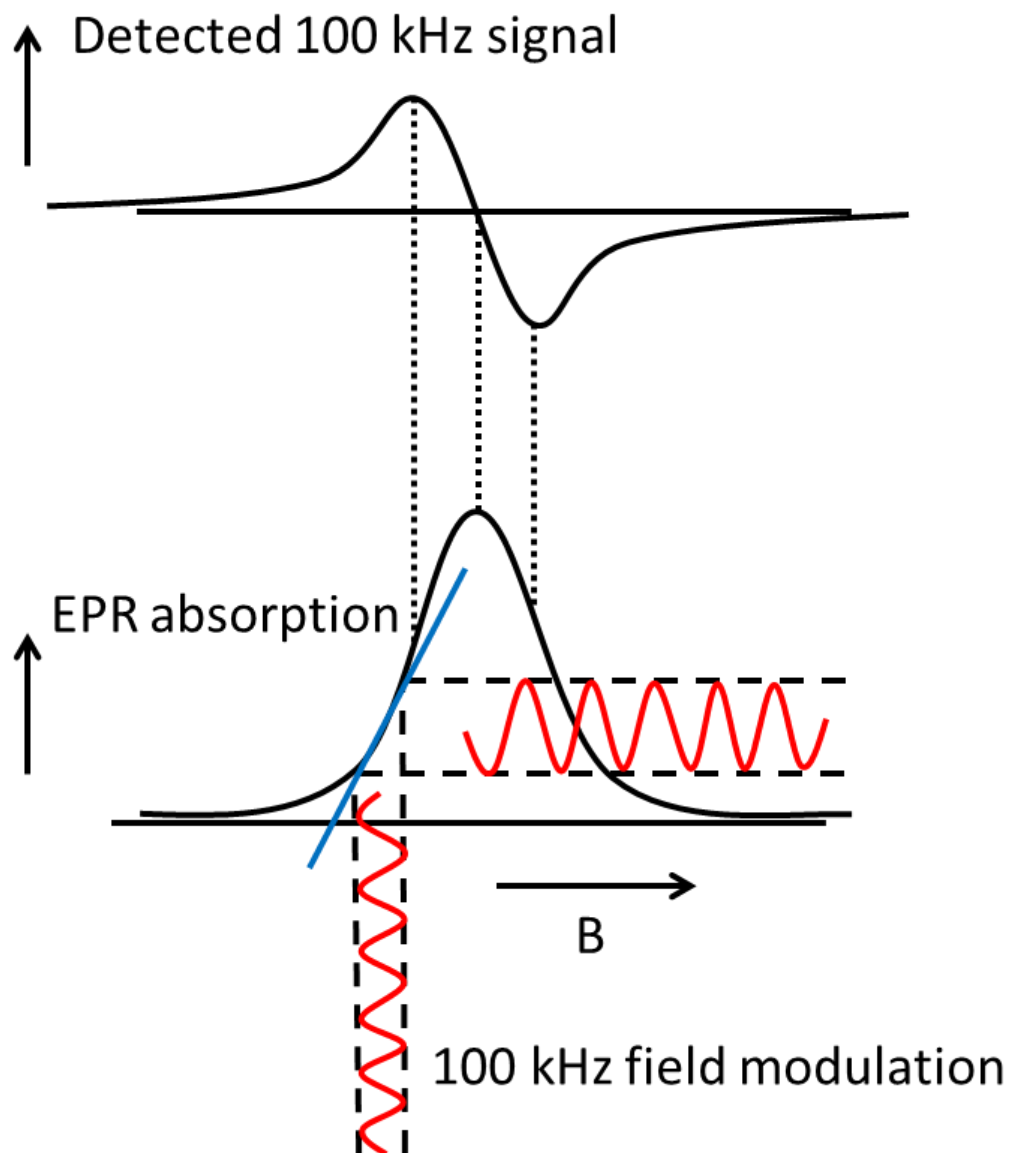
Figure 1.4: The SSEPR experiment employs a 100 kHz field modulation to improve the sensitivity of the experiment. The detection circuitry passes only those signal that match this frequency modulation. As a result, the SSEPR signal is actually detected as the change in absorption as a function of the change in the magnetic field, and the SSEPR signal appears as a first derivative of the EPR transition.

are met: 1) the sample has a strong interaction with B_1 in order to effect magnetic resonance transitions, and 2) samples with high dielectric constants, such as aqueous solutions, can be tuned. The latter is a particularly important point in the study of surfactant solutions, which are often aqueous. In general, any sample with a dielectric constant higher than 4 at X-band requires the use of a smaller sample volume in order to reduce any strong, unwanted interaction between the E field and the sample. Even with good positioning in the center of the EPR cavity, an aqueous solution in a 4 mm EPR tube will still interact too strongly with the E field of the microwave radiation, causing the resonator cavity to detune. For all SSEPR measurements described here, quartz capillaries with an ID of 0.5 mm instead of the standard 4-5 mm quartz EPR tube in order to reduce this unwanted interaction.

To study radical motion in surfactant aggregates by SSEPR, a stable radical referred to as a spin probe is often added to a surfactant solution. Information about the spin probe's g-factor, isotropic hyperfine coupling constant, and rotational dynamic motion are extracted from the line shape of the SSEPR spectrum.[33] Changes in the spectrum of the spin probe as a function of its environment, including conditions like solvent, temperature, and solubilization in a surfactant aggregate, are monitored to extract information on the properties of the environment. The line shape of the SSEPR spectrum is, in fact, very sensitive to changes in the rotational correlation time, τ_c, of the spin probe. Figure 1.5 demonstrates the significant changes that occur to the spectra of a nitroxide molecule over several different ranges of dynamic motion. In frozen or highly viscous solutions, the magnetic properties of the radical, including anisotropy in the g-factor or hyperfine coupling, can be extracted directly from the position of spectral transitions.[28] In the slow motion regime, magnetic parameters are convoluted with dynamic, anisotropic motion to create a complicated line shape. In the fast motion regime, the τ_c of the radical is so fast that any anisotropy
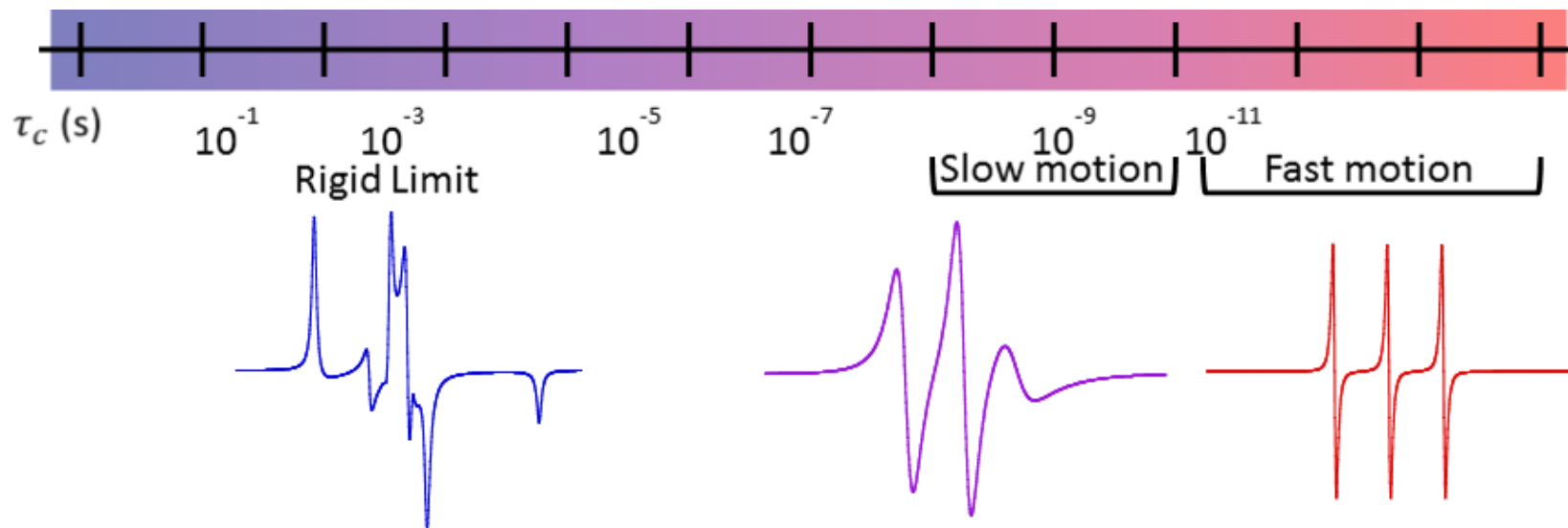
Figure 1.5: The relationship between SSEPR line shape and rotational correlation time (τ_c) in SSEPR spin probe measurement. The anisotropic spin probe doxyl-5-stearic acid is simulated under different conditions of motion: in the rigid limit (left) of a frozen glass matrix, in the slow motion limit where the dynamic motion and magnetic tensor information is convoluted in the line shape of the spectrum (middle), and in the fast motion limit where the anisotropies of the g-factor and hyperfine tensor are averaged out (right).

in the magnetic parameters or diffusion is averaged out and appears isotropic.[28]

1.2.2 Time-Resolved Electron Paramagnetic Resonance (TREPR)

The TREPR experiment is also called "direct detection EPR" or time-resolved (CW) EPR to distinguish it from pulsed and SSEPR methods. The apparatus and methodology couples laser flash photolysis to EPR, which was first developed by Trifunac and coworkers,[34] and has been widely used.[35] A schematic representation of the TREPR experiment, with all the necessary components, is shown in Figure 1.6. In addition to an operational EPR spectrometer, the TREPR experiment requires the following instrumentation: a pulsed laser to initiate radical reactions along with any required optics to guide the beam into the resonator, a microwave resonator designed for optical transmission,[36] a boxcar signal average or transient digitizer for trapping the EPR signal on the sub-μs time scale, a fast photodiode for observation of the laser pulse, an oscilloscope to monitor the timing of the experiment, and a pulse delay generator to control the timing of the laser pulses and fast signal detection.

Radicals are photochemically generated by a laser flash inside the EPR cavity[29, 37] and are detected by the voltage difference between two boxcar gates. The timing sequence for the generation of the radicals and the TREPR signal is depicted in Figure 1.7. The timing sequence is triggered and controlled by the pulse generator, and the sampling gates from the boxcar are positioned such that one is in front of the laser flash and one is after the laser flash. Subtraction of the two gate voltages gives only the light-induced TREPR signal. The gate width is typically between 100-300 ns, and the position of the gate after the laser flash can be varied from 100ns-10μs in order to investigate any time dependent behavior of the EPR signal, which can be of great interest and provide useful information on the time dependent spin wavefunction evolution of
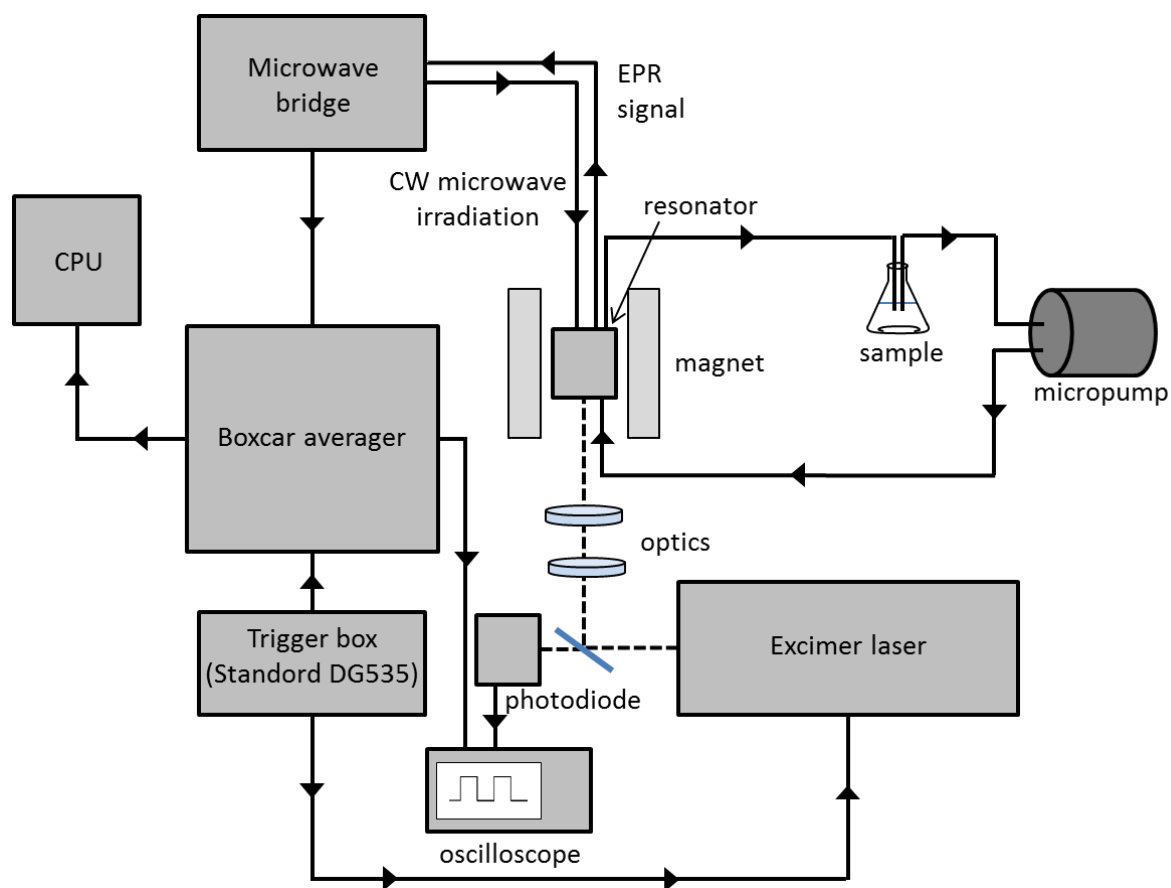
Figure 1.6: A block diagram illustrating the major components of the TREPR experiment
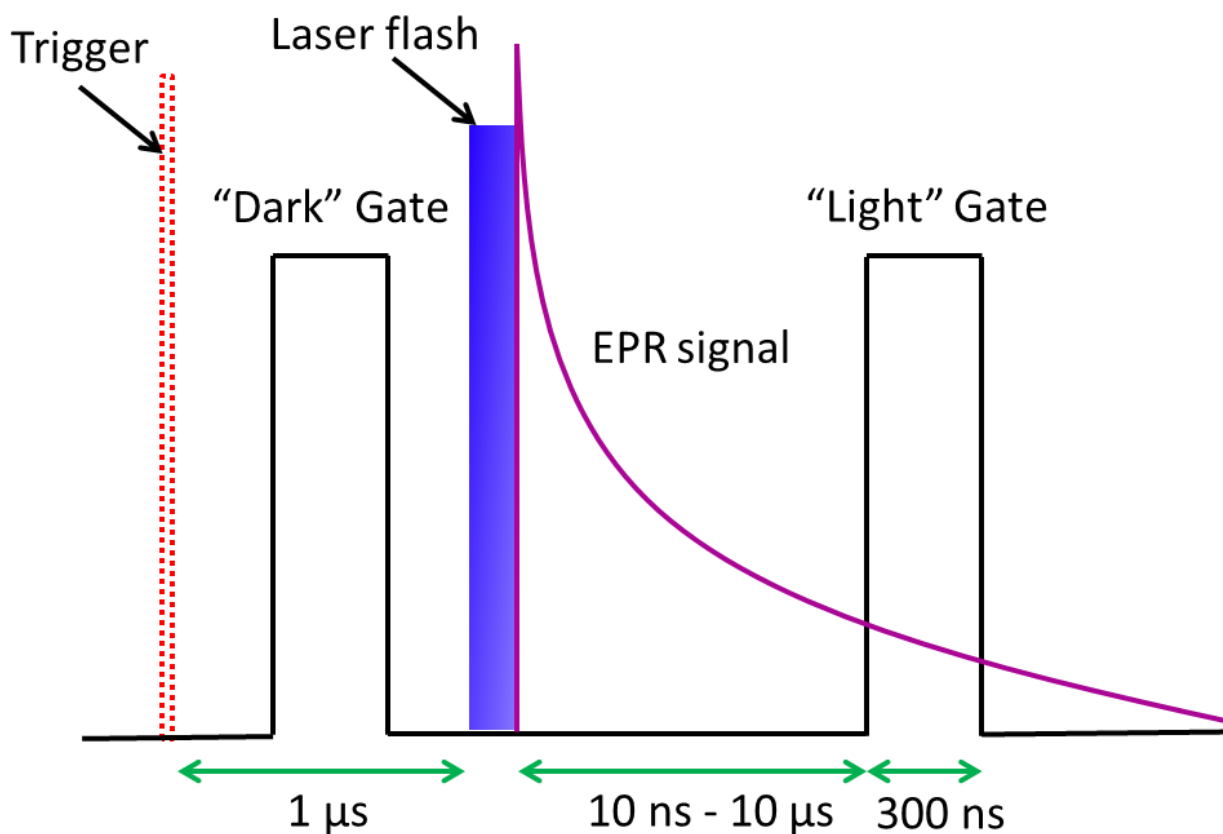
Figure 1.7: The timing sequence for the collection of TREPR spectra. A trigger supplied by a digital delay box triggers a boxcar integrator and the laser flash. The signal at the instrument detector samples the signal after the opening of a "dark" gate position before the laser flash and a "light" gate positioned after the laser flash. The boxcar integrator takes the difference between the voltage under the light and dark gates to give only the light induced TREPR signal. The time dependence of the TREPR signal can be obtained by changing the position of the light gate in time relative to the timing of the laser flash.

paramagnetic systems. Because the spin wavefunction evolution of radicals and radical pairs can be drastically altered by restrictions in translational diffusion, collection of TREPR spectra as a function of delay time has proven important in understanding systems involving confined radical pairs, including radicals in micelles or on surfaces and flexible biradicals in free solution.[38]

The TREPR instrument used for the experiments described here is a modified JEOL spectrometer. The timing sequence is triggered by a Stanford digital delay box outputting TTL pulses, which triggers both the boxcar average and the laser. A Lambda Physik LPX-100 excimer laser operating at 308 nm (XeCl) or Compex excimer laser operating at 248 nm (KrF) can be used at a repetition rate of 60 Hz for laser excitation. The high repetition rate can lead to substantial heating, sample degradation, and the buildup of secondary photoproducts.[39] To avoid these problems, samples are flowed through a quartz flat cell positioned at the center of the rectangular Varian TE_{103} microwave cavity using a micropump and Teflon tubing. The geometry of the quartz cell is chosen to match the geometry of the cavity, but it also maximizes the sample volume exposed to the laser pulse and simultaneously minimizes the total sample volume in the cavity so that the instrument can tune samples containing high dielectric solvents.

In addition to the differences from SSEPR mentioned above, the microwave bridge for the TREPR spectrometer has been altered to give it a faster time response, which is necessary for the detection of short lived radical species.[40] In TREPR, the 100 kHz field modulation is bypassed and the instrument uses a wide bandwidth amplifier with a range of 100 MHz to 0.1 Hz. The EPR signal from the spectrometer's microwave bridge preamplifier circuit is sampled directly after the photochemical generation of the radical if interest. The primary advantage to this direct detection is a vast improvement in the time response of the instrument, which is about 50 ns at X-band and 10 ns at Q-band (35 GHz). This also means that the line shape of the TREPR spectrum differs

substantially from the SSEPR experiment; in the TREPR spectra, transitions below the baseline are in emission (E), while those above the baseline are in enhanced absorption (A). This is different than conventional SSEPR spectra, which, as noted in Figure 1.4, are displayed as first derivative curves representing the change in detected intensity with the change in the external magnetic field.

The shorter time response of the instrument and the observation of chemically induced dynamic electron polarization (CIDEP) make the TREPR experiment sensitive to different radical motions than SSEPR.[29] CIDEP phenomena are observed on the same time scale of typical free radical electron spin relaxation (0.1 to 10 μs) and can result in substantial, non-Boltzmann spin populations of select energy levels of the radicals. Such overpopulations can also improve the signal intensity. These gains in signal intensity are typically large enough to make up for any loss in S/N that was a consequence of performing a direct detection experiment and bypassing the field modulation of SSEPR.

It's important to note that CIDEP polarization can be observed in the TREPR spectra because of quantum coherences as well as selective population of spin states leading to non-Boltzmann distributions. Observations of both single and double quantum coherences have been reported in pulsed, FT-EPR experiments.[41] As a general rule, CIDEP caused by coherences are not observed in the X-band TREPR experiment because they are short lived. Hyperfine interactions will rapidly average out the coherence. An instrument dead time of less than 10 ns is generally considered necessary to observe coherent oscillations in a direct detection experiment.[41a] Given that the detection limit of our apparatus is greater than 100ns, the CIDEP observed in the TREPR of radicals in surfactant aggregates reported here is most likely caused by non-Boltzmann spin state populations and not coherences between states.

CIDEP processes provide insight into the mechanism of the reaction that generated the radicals, their motional dynamics (both intra– and intermolecular), and other characteristics regarding the photochemical precursors, such as their spin multiplicity. The nature of these polarization processes, and the four mechanisms responsible for generating them, are discussed in greater detail below. In regard to TREPR studies of supramolecular systems, it is important to note that several polarization mechanisms are sensitive to the translational diffusion of radicals. Because supramolecular structures can alter translational diffusion, the TREPR experiment can be sensitive to supramolecular confinement. Like SSEPR, information about this motion can be extracted from the TREPR line shape. By photochemical generating radical species in surfactant aggregates and analyzing the resulting CIDEP polarization, it is possible to obtain additional information about molecular diffusion in these structures that is not available from SSEPR.

1.3 Chemically Induced Electron Spin Polarization (CIDEP) Mechanisms

Allowed transitions in spectroscopy are most often observed as absorptive lines due to the existence of a Boltzmann distribution that results in greater population in lower energy levels over higher energy states. CIDEP phenomena are the product of non-equilibrium spin populations, and can result in both enhanced absorption (greater absorptive signal intensity than predicted by the Boltzmann factors) and emission. What makes the non–Boltzmann populations observed in TREPR experiments so unusual is that, in some cases, electron or nuclear spin dependent chemical reactions are responsible for the polarization process. The observation and description of the nuclear spin polarization phenomenon (CIDNP) in NMR spectroscopy came first.[42] The general idea put forward for CIDNP was that that the nuclear spin state energy level differences, which are much smaller than kT at room temperature, could cause different chemical reaction rates. Since

these early descriptions, four primary CIDEP phenomena were discovered and explained. The earliest experimental observations[43] were of unusual phases of EPR and NMR transitions in thermal, photolytic, and radiolytic reactions involving free radical intermediates. This lead to a theoretical description of some of the results that is now known as the Radical Pair Mechanism (RPM).[42e, 44] With time, three additional polarization mechanisms have been added to explain other anomalous experimental results: the Triplet Mechanism (TM), the Radical Triplet Pair Mechanism (RTPM), and the Spin-Correlated Racial Pair Mechanism (SCRPM). In the following sections, an outline the basic phenomenon three of the four known CIDEP mechanisms that are relevant to the investigation of radical pair dynamics in surfactant aggregates are presented and explained in further detail.

1.3.1 The Triplet Mechanism (TM)

The triplet mechanism (TM) is often considered the simplest CIDEP mechanism.[45] A general theory for the TM was developed in detail by Wong et al.,[46] Pedersen and Freed,[47] and Atkins and Evans.[48] A qualitative picture of the mechanism is presented in Figure 1.8. Due to dipolar interactions, the three energy levels of the molecular triplet excited state are not degenerate. The labels T_X, T_Y and T_Z represent the triplet state energy levels in the molecular coordinate system. A molecule is excited into its first excited singlet state, S_1, and intersystem crosses (ISC) to the triplet state, T. Differences in the spin orbit coupling between the singlet and triplet sublevels leads to spin selectivity in populating the excited molecular triplet. The excess population of one molecular triplet state over the others is represented in Figure 1.8 by a thicker line, and this excess population persists in the laboratory frame where the molecule feels the effects of an external magnetic field. The excited triplet state can then react to form radicals, and the net polarization of
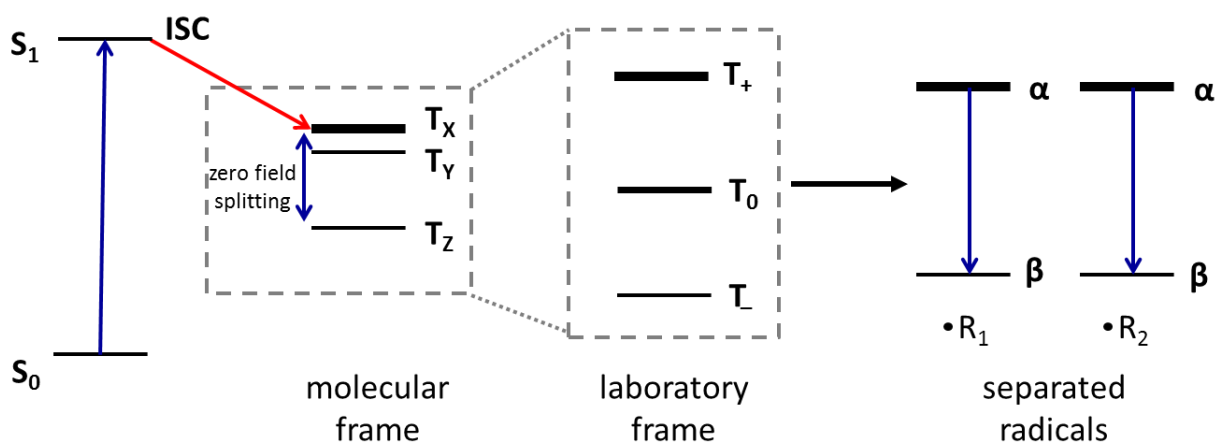
Figure 1.8: The TM of CIDEP. Photoexcitation of an organic molecule from the ground state (S_0) to the first excited singlet state (S_1) is followed by intersystem crossing by spin-orbit coupling to the first excited triplet state. The ISC is a spin selective process that overpopulates one triplet sublevel of the molecule over the others in the molecular frame. This overpopulation persists in the high-field basis set of the laboratory frame. The spin-polarized triplet undergoes a chemical reaction to create free radicals that are then observed in the TREPR experiment. In the case shown here, overpopulation of the α spin state of the radicals leads to the observation of net emissive TM polarization.

the electron spins in the triplet state precursor can ultimately be observed in the free radicals. It is the polarization of the free radical spin states, and not the molecular triplet state, that is observed in the TREPR experiment. Experimentally, all of the observed transitions in the TREPR spectrum are polarized equally and either positively (enhanced absorption, A) or negatively (emission, E) by the TM. The physical origin of TM polarization is described in greater detail below.

The electron spin triplet states of the most organic molecules have two electrons (spins) located on different molecular orbitals (MO) because of the Pauli principle. The triplet state is expected to be three-fold degenerate at zero magnetic field; however, the crystal field, spin-orbit coupling, electron spin-spin dipolar interaction remove this degeneracy. The difference in energy between the molecular triplet states is determined by the dipolar spin-spin interaction ("zero field splitting" or ZFS). The dipole-dipole interaction is particularly sensitive to molecular geometry, and anisotropic distributions of spins in the molecule are described using the ZFS parameters D_{ZFS} and E_{ZFS}. D_{ZFS} is the difference in energy between the $m_S = 0$ and the average of the $m_S = \pm 1$ states, and E_{ZFS} is the difference between the $m_S = 1$ and $m_S = -1$ states.[49] The spin Hamiltonian for the ZFS caused by the spin-spin dipolar interaction between two electrons is written as follows:

$$\hat{H}_{ZFS} = -\hat{\boldsymbol{S}} \cdot \widetilde{D} \cdot \hat{\boldsymbol{S}} \tag{3}$$

Where $\hat{\mathbf{S}}$ is the total spin $\hat{\mathbf{S}} = \hat{\mathbf{S}}_1 + \hat{\mathbf{S}}_2$ and $\widetilde{D}$ is a traceless interaction tensor with the principal values D_{XX}, D_{YY}, and D_{ZZ}. The coordinate axes X, Y, and Z represent the canonical axes to which the tensor is $\widetilde{D}$ is diagonal (the so–called "canonical" axes):

$$\hat{H}_D = D_{XX} \cdot \hat{S}_X^2 + D_{YY} \cdot \hat{S}_Y^2 + D_{ZZ} \cdot \hat{S}_Z^2 = D_{ZFS}\left(\hat{S}_Z^2 - \frac{1}{3}\hat{\boldsymbol{S}}^2\right) + E_{ZFS}\left(\hat{S}_X^2 - \hat{S}_Y^2\right) \tag{4}$$

with

$$D_{ZFS} = \frac{1}{2}(D_{XX} + D_{YY}) - D_{zz} \tag{5}$$

$$E_{ZFS} = -\frac{1}{2}(D_{XX} - D_{YY}) \tag{6}$$

here the dimensionality of the parameters D and E is energy, typically MHz, and the electron spin operators are considered to be dimensionless.

When the Z-axis is defined as the axis of quantization, the eigenfunctions of this spin-Hamiltonian are:

$$|T_X\rangle = \frac{1}{\sqrt{2}}(-|\alpha\alpha\rangle + |\beta\beta\rangle) \tag{7}$$

$$|T_Y\rangle = \frac{i}{\sqrt{2}}(|\alpha\alpha\rangle + |\beta\beta\rangle) \tag{8}$$

$$|T_Z\rangle = \frac{1}{\sqrt{2}}(|\alpha\beta\rangle + |\beta\alpha\rangle) \tag{9}$$

This basis set is referred to as the molecular frame. Just after the intersystem crossing the initial density matrix of the triplet state is:

$$\hat{\rho}(t=0) = p_x|T_X\rangle\langle T_X| + p_y|T_Y\rangle\langle T_Y| + p_z|T_Z\rangle\langle T_Z| \tag{10}$$

The matrix does not contain any off-diagonal elements, which means the process populating each triplet state is independent of all the others, and the initial populations after ISC can possess strong deviations from the Boltzmann distribution. In the presence of an external magnetic field $\mathbf{B}_0$, the spin Hamiltonian of the triplet state can be written as:

$$\hat{H} = \beta_e \mathbf{B}_0 \cdot \tilde{g} \cdot \hat{\mathbf{S}} + D_{ZFS}\left(\hat{S}_Z^2 - \frac{1}{3}\hat{\mathbf{S}}^2\right) + E_{ZFS}(\hat{S}_X^2 - \hat{S}_Y^2) \tag{11}$$

Where the Z axis is that directed along the applied magnetic field. The "high-field" basis set is used to describe the triplet energy levels in the presence of an applied magnetic field, and the basis functions in Eqs, 7-9 become:

$$|T_+\rangle = |1,1,\rangle = |\alpha'\alpha'\rangle \tag{12}$$

$$|T_0\rangle = |1,0\rangle = \frac{1}{\sqrt{2}}(|\alpha'\beta'\rangle + |\beta'\alpha'\rangle) \tag{13}$$

$$|T_-\rangle = |1,-1\rangle = |\beta'\beta'\rangle \tag{14}$$

where $|\alpha'\rangle$ and $|\beta'\rangle$ are the ordinary ½ spin wave functions, quantized along **B₀**.

The relationship between the molecular frame and the laboratory frame basis sets is as follows:

$$T_+ = \frac{1}{\sqrt{2}}(T'_X - T'_Y) \tag{15}$$

$$T_0 = T'_Z \tag{16}$$

$$T_- = -\frac{1}{\sqrt{2}}(T'_X + iT'_Y) \tag{17}$$

where T'_X, T'_Y, and T'_Z are the molecular frame basis set in Eqs 7-9 when the $|\alpha'\rangle$ and $|\beta'\rangle$ spin wave functions are used instead of $|\alpha\rangle$ and $|\beta\rangle$. The transformation between the two basis sets and the independent populations of the triplet sub-levels suggested in Eq. 10 help to explain the appearance of the TM in free radicals. For a triplet with its Z–axis directed along the applied magnetic field, the populations for the laboratory frame can be expressed in terms of the laboratory and molecular basis functions:

$$p_{T_+T_+} = |\langle T_X|T_+\rangle|^2 p_x + |\langle T_Y|T_+\rangle|^2 p_y + |\langle T_Z|T_+\rangle|^2 p_z \tag{18}$$

$$p_{T_0T_0} = |\langle T_X|T_0\rangle|^2 p_x + |\langle T_Y|T_0\rangle|^2 p_y + |\langle T_Z|T_0\rangle|^2 p_z \tag{19}$$

$$p_{T_-T_-} = |\langle T_X|T_-\rangle|^2 p_x + |\langle T_Y|T_-\rangle|^2 p_y + |\langle T_Z|T_-\rangle|^2 p_z \tag{20}$$

Because of the transformation between the basis sets, the mixing coefficients are all different. Therefore, if the initial populations p_x, p_y, p_z are different, the populations $p_{T_+T_+}$, $p_{T_0T_0}$, and $p_{T_-T_-}$ will also be different. The initial spin selectivity of populating the triplet state during ISC is carried

all the way through the process and is still conserved when the triplet molecule reacts, dissociates, or undergoes electron transfer to form radicals. Because of the relationship between the populations of the T_+, T_0, and T_- and the electron spin states in Eqs. 15-17, the ensuing free radicals can exhibit an overpopulation in either the α and β state. The sign of the radicals' net polarization (net E or net A) is dictated by which spin state of the free radicals is polarized and is determined by the sign of the sum $D_{ZFS} \cdot K + 3E_{ZFS} \cdot I$, where $K = (p_x + p_y - 2p_z)/2$ and $I = (p_x - p_y)/2$.[48]

1.3.2 The Radical Pair Mechanism (RPM)

The Radical Pair Mechanism (RPM) was the first theoretical explanation for both CIDEP and CIDNP phenomena.[42e, 44] The generation of RPM polarization depends fundamentally on the interplay between diffusion and spin state mixing in a radical pair (RP).[50] Figure 1.9 provides a physical picture of the origin of this polarization: the energy levels of the T_0 triplet state and S singlet state of the mobile RP in free solution are shown as a function of inter-radical distance. The energy difference between the two states is proportional to the exchange interaction, J, which is a complex function of several quantum mechanical terms such as the exchange integral, the Coulomb integral, and the orbital overlap integral. The exact form of J depends on which methodology is used for its derivation, but is often expressed as:[51]

$$J(r) = J_0 e^{-(r-R)/\lambda}$$

(21)

where r is the distance between the radicals, R is the distance of closest approach and is typically the sum of the van der Waals radii, and λ is an exponential decay constant for the exchange interaction as a function of r.

The spin Hamiltonian for the isotropic exchange interaction is given by:
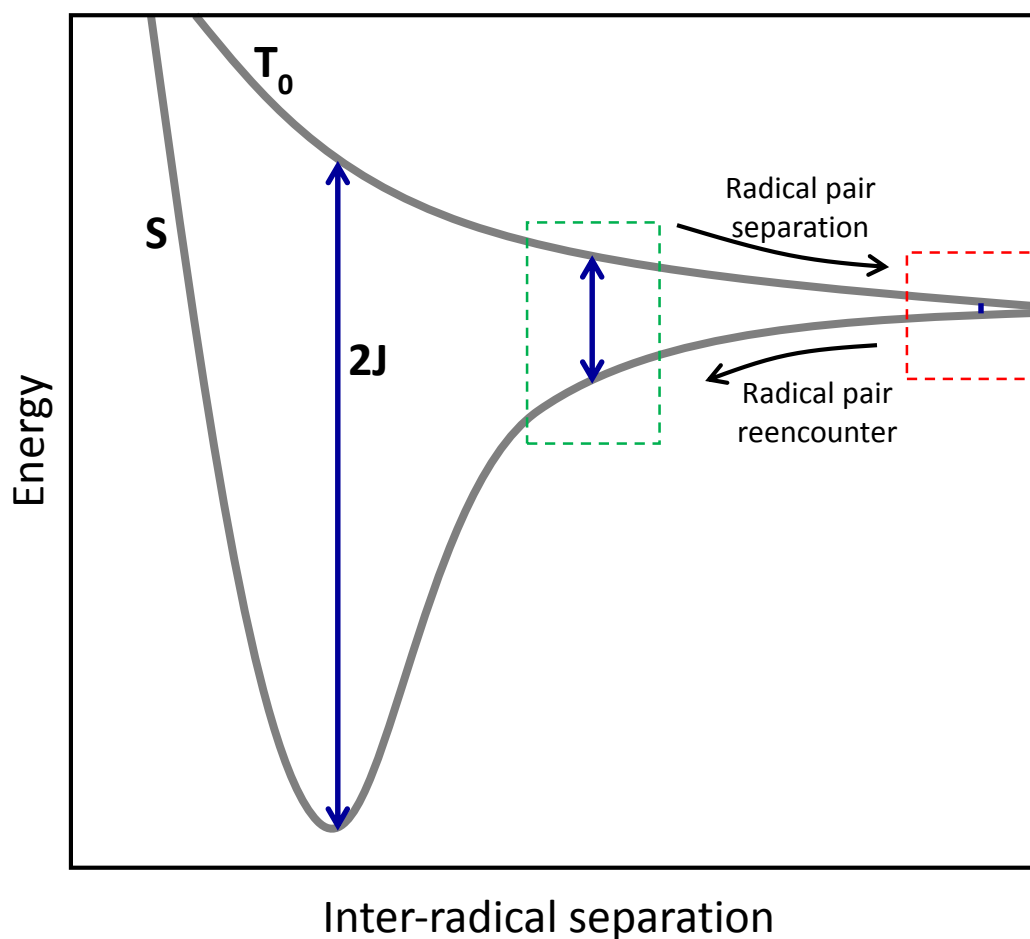
Figure 1.9: The energy levels of the radical pair triplet state (T_0) and singlet state (S) as a function of inter-radical separation. Motion to the right on the energy level diagram represents radical pair separation and increasing inter-radical distance, while motion to the left represents decreasing inter-radical distance ultimately leading to reencounter of the radical pair. The difference in energy between the T_0 and S states, shown by blue arrows, is equal to twice the exchange interaction, *J*. At close inter-radical distances where spin exchange is strong (left), no spin state mixing occurs. At long inter-radical distances (right, in red), spin exchange is weak and local magnetic field differences can affect the Larmor processional frequency of the separated radicals. As the members of the radical pair diffuse back together, they enter a region where 2*J* becomes stronger (green, middle) and the radical pair must choose the singlet or triplet energy manifold. This process of diffusion and reencounter is the origin of RPM polarization.

$$(\hat{H}_{exch})_{iso} = J_0 \hat{S}_1 \cdot \hat{S}_2 \qquad (22)$$

For short inter-radical distances, J is large compared to all other parameters in the full spin

Hamiltonian, and there is no mixing of the S and T_0 spin states. When there is greater separation

between the RP, the magnitude of J is negligibly small or zero, and the effect of local magnetic

fields, like hyperfine couplings and g-factors, can cause the magnetic moments of the two unpaired

electrons to fall out of phase. Since the S and T_0 spin wave functions are essentially related through

the phase of their Larmor precessional frequencies, the dephasing of these vectors may eventually

interconvert S and T_0.

A triplet-born radical pair will begin to diffuse apart within a few nanoseconds of its

creation, and as a consequence, the magnitude of J decreases and S-T_0 mixing occurs. If the

radicals continue to diffuse away from each other, there is essentially no effect on the spin

populations; however, if they re–encounter each other several nanoseconds later, $2J$ once again

becomes large and the RP must, by physical necessity, choose to be in either the singlet (S) or the

triplet (T_0) state. This motion of the RP along the reaction coordinate in Figure 1.9, with the

accompanying spin wave function evolution in the region where $2J$ is small or zero, alters the

relative populations of the S and T_0 state after the radicals reencounter each other and is the origin

of the electron spin polarization.[50] One final important point is that this spin polarization cannot

be observed in free solution until the radicals have diffused completely away from each other after

their reencounter.

The sign of the polarization of each line in the TREPR spectrum will depend on the effect

of local nuclear spin orientations on the Larmor precession frequency of the unpaired electron, and

the magnitude of the polarization will be a function of the rate of S-T_0 inter–conversion and one

or two reencounters of the RP. If the two radicals have different g-factors but little or no electron

nuclear hyperfine couplings, the RPM appears with one radical in emission and the other in absorption. If the g-factor difference is small and there are large hyperfine splitting, the low field lines will be appear with one phase and the high field lines will exhibit the opposite phase. Whether the spectrum appears with a low field E/high field A or a low field A/high field E pattern depends on the sign of J and the spin multiplicity of the excited state precursor.[52] For the triplet-born radical pairs generated in surfactant aggregates, the sign of J is negative and the RPM polarization appears in an E/A pattern.

The spectral shape resulting from the RPM is examined more closely in Figure 1.10, which shows the resulting population differences between the $|\alpha\beta\rangle$ and $|\beta\alpha\rangle$ states of a separated RP that has experienced S–T$_0$ mixing. There are large differences in the spin state populations for these spectral lines; however, the two transitions are degenerate. The degeneracy of the two transitions is a direct consequence of the fact that the RP has separated completely so that $J = 0$ at the time of detection. Most of the population difference cancels, and the remaining small overpopulation of either the α or β electronic spin state manifests itself in the TREPR spectrum as either an E or A polarized line, respectively.

One more important feature of RPM polarized TREPR spectra is that the intensity ratios of the transitions do not follow the normal binomial coefficient pattern expected from the n+1 rule.[30] The intensity of RPM polarization for any given line depends on the local magnetic field difference, q (Eq. 23), between the members of each radical pair, as defined by their line positions in the spectrum (Eq 24).

$$q = \frac{1}{2}(\omega_a - \omega_b) \tag{23}$$

$$\omega_\mu = g_\mu \mu_B B_0 + \sum_k A_k^\mu m_{z,k} - \omega \tag{24}$$
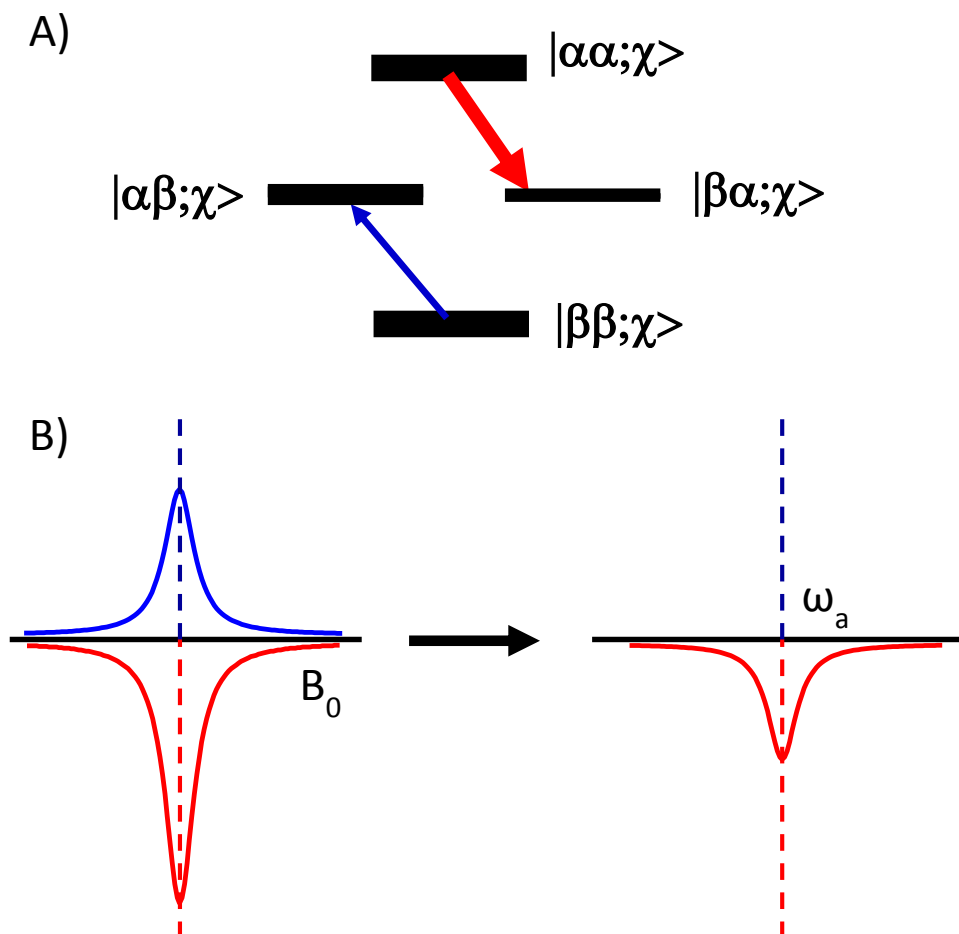
Figure 1.10: The spectral shape of the RPM. A) An energy level diagram of the radical pair after separation (right, Figure 1.8). After diffusion and reencounter, ST_0RPM creates a population difference between the $|\alpha\beta\rangle$ and $|\beta\alpha\rangle$ configurations of the RP. The arrows represent the allowed EPR transitions of radical **a** of the RP, which will have a different intensity due to the difference in population. Because the creation of this population difference is dependent on local magnetic fields, the generation of RPM polarization is dependent on the nuclear spin configuration, χ. The two transitions are degenerate in energy (B), so that the observed EPR signal is what remains after cancellation of the two oppositely polarized transitions.

Here ω is the microwave frequency. The first term in Eq. 24 accounts for the effect to of the g-factor and the second term accounts for the effect of all the applicable hyperfine interactions on the frequency at which the radical is observed. For transitions at the perimeter of the TREPR spectrum, the value of q is large, but the binomial coefficients are small. For the lines near the center of the spectrum, the binomial coefficients are large, but the q values are small. As a result, the RPM intensity generally scales with $q^{1/2}$, as long as the product of the radical lifetime and q is << 1. The RPM intensities then follow a "sine wave" pattern from low to high field.

1.3.3. The Spin-Correlated Radical Pair Mechanism (SCRPM)

The dynamics, spin physics, and reactivity of RPs in confined spaces or otherwise experiencing restricted diffusion can be drastically different from the properties of identical radicals in free solution. Confinement of radicals undergoing spin wave function mixing and diffusion controlled reencounters, as described above for the RPM, has a profound effect on the appearance of their TREPR spectra.[1c, 53] Confinement on the nanometer scale is easily accomplished with self-assembled surfactant-based structures such as micelles [14, 53a, 54] and vesicles,[55] or with more rigid molecular architectures such as cyclodextrins[1c] and organic nanocrystals.[56] Flexible biradicals[53b] also experience restricted diffusion with results similar to the supramolecular confinement mentioned above. The fundamental result of this confinement, whether it is supramolecular or structural, is to restrict the diffusion of the RP. This ultimately, leads to the observation of spin-correlation that contributes additional spectral complexity to the experimental spectra of a RP.[57]

The term spin-correlated radical pair (SCRP) is used to emphasize the entangled nature of the quantum electron spin system of confined radical pairs created in a geminate state.[58] This

entanglement plays a crucial role in the physical characterization of the system, particularly when analyzing the TREPR spectra of SCRPs confined to micelles or other surfactant aggregates. Mathematically, entanglement means that it is impossible to represent the spin density operator of a particular SCRP as the direct product of the spin density operators of the individual radicals that comprise the SCRP. This also means that the populations of the electron-nuclear-spin states of the SCRP can deviate substantially from the populations that are expected after a random encounter of the two radicals in free solution. This directly implies the existence of a persistent phase relationship between the two electron spins in a SCRP.

The physical picture of the diffusion of the members of the RP after their generation and the effect that this diffusion has on the strength of the exchange interaction is similar to the diffusion responsible for RPM polarization (Figure 1.9). As a matter of fact, if inter-radical spin-spin interactions could be neglected, the resulting electron spin polarization of a SCRP observed by TREPR would differ very little from the RPM polarization pattern because the components of the relevant TREPR transitions are doubly degenerate and their intensities cancel each other out (Figure 1.9). Inter-radical interactions, including exchange or dipolar interactions, can remove this degeneracy. The result is the observation of much stronger electron spin polarization with a different spectral pattern. The spin-spin exchange interaction causes a shift in the resonant frequency of each transition, so that each individual spectroscopic line in the TREPR spectrum is then split by this interaction into two lines of opposite phase (Figure 1.11). This spectral pattern is known as the "Anti-Phase Splitting," (APS) of the SCRP.[53i]

The spectroscopy of SCRP's is complex and rich in information about structure, dynamics, and the nature of the RP confinement. For RP systems confined to surfactant aggregates, the relative size of supramolecular aggregate can have a strong effect on the line shape of the TREPR
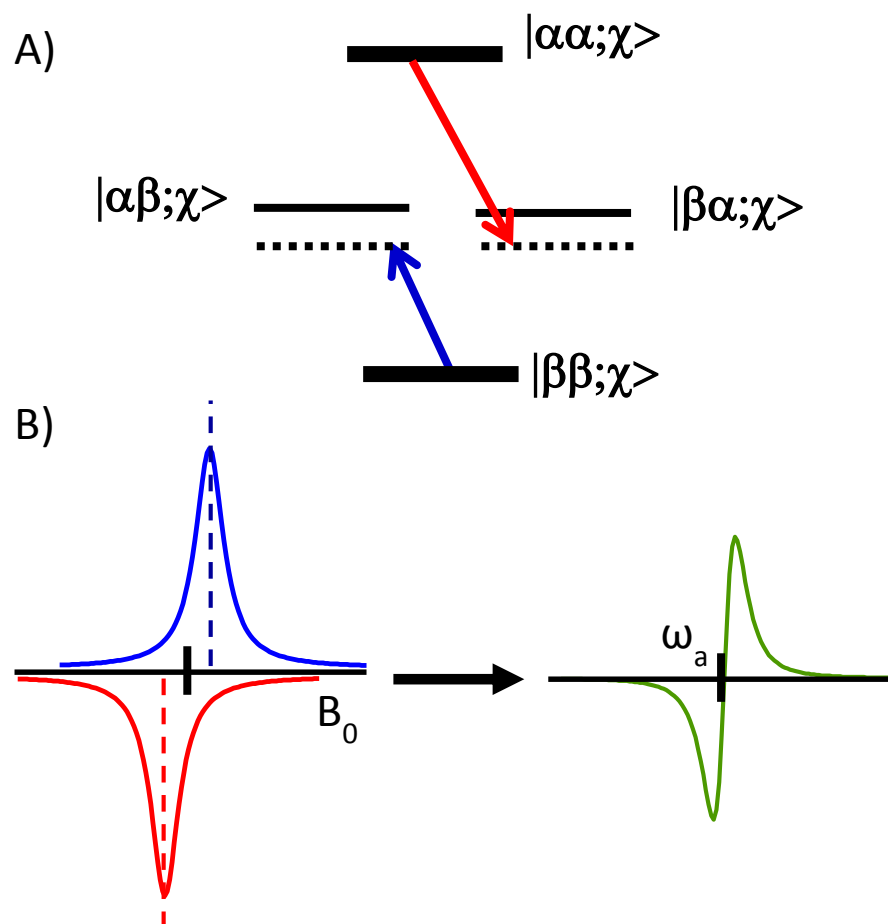
Figure 1.11: The spectral shape of the SCRPM. A) An energy level diagram of the SCRP after the RP has separated (Figure 1.8, right). The spin exchange interaction, J, shifts the energy of the RP $|\alpha\beta\rangle$ and $|\beta\alpha\rangle$ configurations (dotted lines) relative to their energies in the absence of J (solid lines). This lifts the degeneracy of the two allowed EPR transitions of radical a and appears in the TREPR spectrum as a shift in the resonant frequency of the absorptive and emissive components of the transition (B). The resulting TREPR signal appears as an E/A doublet that appears like a first derivative line shape and has been termed the APS of the SCRP.

spectrum. An accurate simulation of the line shapes leads to a much deeper understanding of the connection between the spin states, coherences, populations, confinement and freedom of molecular motion. A more detailed description of the information available from the SCRP line shape and simulations of these complex spectra is provided in the next chapter.

REFERENCES

1.   (a) Takamori, D.; Aoki, T.; Yashiro, H.; Murai, H., Time-resolved ESR study on the photochemistry of naphthoquinones included in cyclodextrins. *J. Phys. Chem. A* **2001,** *105* (25), 6001-6007; (b) Pemberton, B. C.; Singh, R. K.; Johnson, A. C.; Jockusch, S.; Da Silva, J. P.; Ugrinov, A.; Turro, N. J.; Srivastava, D. K.; Sivaguru, J., Supramolecular photocatalysis: insights into cucurbit 8 uril catalyzed photodimerization of 6-methylcoumarin. *Chem. Commun.* **2011,** *47* (22), 6323-6325; (c) Krumkacheva, O. A.; Gorelik, V. R.; Bagryanskaya, E. G.; Lebedeva, N. V.; Forbes, M. D. E., Supramolecular Photochemistry in beta-Cyclodextrin Hosts: A TREPR, NMR, and CIDNP Investigation. *Langmuir* **2010,** *26* (11), 8971-8980.

2.   Lebedeva, N. V.; Tarasov, V. F.; Resendiz, M. J. E.; Garcia-Garibay, M. A.; White, R. C.; Forbes, M. D. E., The Missing Link Between Molecular Triplets and Spin-Polarized Free Radicals: Room Temperature Triplet States of Nanocrystalline Radical Pairs. *J. Am. Chem. Soc.* **2010,** *132* (1), 82-84.

3.   (a) Khomane, R. B.; Kulkarni, B. D., Nanoreactors for nanostructured materials. *Int. J. Chem. React. Eng.* **2008,** *6*; (b) Prado-Gotor, R.; Jimenez, R.; Perez-Tejeda, P.; Lopez-Cornejo, P.; Lopez-Lopez, M.; Sanchez, A.; Muriel-Delgado, F.; Sanchez, F., Electron transfer reactions in micellar systems. *Prog. React. Kinet. Mech.* **2000,** *25* (4), 371-407; (c) Manju, T.; Manoj, N.; Gejo, J. L.; Braun, A. M.; Oliveros, E., Micellar control of the photooxidation pathways of 10-methyl phenothiazine: electron versus energy transfer mechanisms. *Photochem. Photobiol. Sci.* **2014,** *13* (2), 281-292; (d) Shtykov, S. N., Chemical analysis in nanoreactors: Main concepts and applications. *J. Anal. Chem.* **2002,** *57* (10), 859-868.

4.   (a) Effendy, I.; Maibach, H. I., Surfactants and experimental irritant contact dermatitis. *Contact dermatitis* **1995,** *33* (4), 217-25; (b) Deo, N.; Somasundaran, P.; Subramanyan, K.; Ananthapadmanabhan, K. P., Electron paramagnetic resonance study of the structure of lipid bilayers in the presence of sodium dodecyl sulfate. *J. Colloid Interface Sci.* **2002,** *256* (1), 100-105.

5.   Ouyang, Y.; Mansell, R. S.; Rhue, R. D., Emulsion-mediated transport of nonaqueous-phase liquid in porous media: A review∗. *Critical Reviews in Environmental Science and Technology* **1995,** *25* (3), 269-290.

6.   (a) Sawada, H.; Kashiwamata, S., Sodium dodecyl sulfate disk gel electrophoresis patterns of bovine lung surfactant *Biochim. Biophys. Acta* **1977,** *490* (1), 44-50; (b) Konig, S.; Schmidt, O.; Rose, K.; Thanos, S.; Besselmann, M.; Zeller, M., Sodium dodecyl sulfate versus acid-labile surfactant gel electrophoresis: Comparative proteomic studies on rat retina and mouse brain. *Electrophoresis* **2003,** *24* (4), 751-756.

7.   Hayashi, T.; Itagaki, H.; Fukuda, T.; Tamura, U.; Sato, Y.; Suzuki, Y., Hemoglobin denaturation caused by surfactants *Biological & Pharmaceutical Bulletin* **1995,** *18* (4), 540-543.

8.   Igarashi, T.; Shoji, Y.; Katayama, K., Anomalous Solubilization Behavior of Dimyristoylphosphatidylcholine Liposomes Induced by Sodium Dodecyl Sulfate Micelles. *Anal. Sci.* **2012,** *28* (4), 345-350.

9.   McCaffrey, V. P.; Forbes, M. D. E., Energy transfer studied using spin polarized free radicals. Effect of substrate structure and a comparison between micellar confinement and free solution. *Tetrahedron* **2000,** *56* (36), 6991-6997.

10.   (a) Srivastava, S.; Sharma, S. K.; Sharma, R. K., Synthesis of gold nanorods using concentrated aerosol OT in hexane and its application as catalyst for the reduction of eosin. *Colloids and Surfaces A: Physicochemical and Engineering Aspects* **2011,** *373* (1–3), 61-65; (b) Tanev, P. T.; Pinnavaia, T. J., Biomimetic assembly of porous lamellar silica molecular sieves with a vesicular particle architecture. *Supramol. Sci.* **1998,** *5* (3-4), 399-404.

11.   Nagarajan, R., Solubilization by amphiphilar aggregates. *Curr. Opin. Colloid Interface Sci.* **1997,** *2* (3), 282-293.

12.   (a) Mahmoudzadeh, M.; Fassihi, A.; Emami, J.; Davies, N. M.; Dorkoosh, F., Physicochemical, pharmaceutical and biological approaches toward designing optimized and efficient hydrophobically modified

chitosan-based polymeric micelles as a nanocarrier system for targeted delivery of anticancer drugs. *Journal of Drug Targeting* **2013,** *21* (8), 693-709; (b) Sun, H. L.; Meng, F. H.; Cheng, R.; Deng, C.; Zhong, Z. Y., Reduction-sensitive degradable micellar nanoparticles as smart and intuitive delivery systems for cancer chemotherapy. *Expert Opinion on Drug Delivery* **2013,** *10* (8), 1109-1122; (c) Yin, Q.; Shen, J. N.; Zhang, Z. W.; Yu, H. J.; Li, Y. P., Reversal of multidrug resistance by stimuli-responsive drug delivery systems for therapy of tumor. *Advanced Drug Delivery Reviews* **2013,** *65* (13-14), 1699-1715.

13.   (a) Trifunac, A. D.; Nelson, D. J., Chemically induced dynamic electron polarization. Pulse radiolysis of aqueous solutions of micelles. *Chem. Phys. Lett.* **1977,** *46* (2), 346-348; (b) Sakaguchi, Y.; Hayashi, H.; Murai, H.; I'Haya, Y. J., CIDEP study of the photochemical reactions of carbonyl compounds showing the external magnetic field effect in a micelle. *Chem. Phys. Lett.* **1984,** *110* (3), 275-279; (c) Murai, H.; Sakaguchi, Y.; Hayashi, H.; Ihaya, Y. J., An anomalous phase effect in the individual hyperfine lines of the CIDEP spectra observed in the photochemical reactions of benzophenone in micelles. *The Journal of Physical Chemistry* **1986,** *90* (1), 113-118; (d) Closs, G. L.; Forbes, M. D. E.; Norris, J. R., Spin-polarized electron paramagnetic resonance spectra of radical pairs in micelles: observation of electron spin-spin interactions. *The Journal of Physical Chemistry* **1987,** *91* (13), 3592-3599; (e) Buckley, C. D.; Hunter, D. A.; Hore, P. J.; McLauchlan, K. A., Electron spin resonance of spin-correlated radical pairs. *Chem. Phys. Lett.* **1987,** *135* (3), 307-312.

14.   Forbes, M. D. E.; Schulz, G. R.; Avdievich, N. I., Unusual Dynamics of Micellized Radical Pairs Generated from Photochemically Active Amphiphiles. *J. Am. Chem. Soc.* **1996,** *118* (43), 10652-10653.

15.   White, R. C.; Gorelik, V.; Bagryanskaya, E. G.; Forbes, M. D. E., Photoredox Chemistry of AOT: Electron Transfer and Hydrogen Abstraction in Microemulsions Involving the Surfactant. *Langmuir* **2007,** *23* (8), 4183-4191.

16.   (a) Bratt, P. J.; Kevan, L., Electron spin resonance line shape analysis of x-doxylstearic acid spin probes in dioctadecyldimethylammonium chloride vesicles. *J. Phys. Chem.* **1992,** *96* (16), 6849-6852; (b) Bratt, P. J.; Kevan, L., Electron spin resonance line shape analysis of x-doxylstearic acid spin probes in dihexadecyl phosphate vesicles and effects of cholesterol addition *J. Phys. Chem.* **1993,** *97* (28), 7371-7374.

17.   (a) Lebedeva, N.; Ranganathan, R.; Bales, B. L., Location of spectroscopic probes in self-aggregating assemblies. II. The location of pyrene and other probes in sodium dodecyl sulfate micelles. *J. Phys. Chem. B* **2007,** *111* (21), 5781-5793; (b) Bales, B. L.; Zana, R., Characterization of micelles of quaternary ammonium surfactants, as reaction media I: Dodeclytrimethylammonium bromide and chloride. *J. Phys. Chem. B* **2002,** *106* (8), 1926-1939; (c) Lebedeva, N. V.; Shahine, A.; Bales, B. L., Aggregation number-based degrees of counterion dissociation in sodium n-alkyl sulfate micelles. *J. Phys. Chem. B* **2005,** *109* (42), 19806-19816.

18.   (a) Smith, A. K.; Freed, J. H., Dynamics and ordering of lipid spin-labels along the coexistence curve of two membrane phases: An ESR study. *Chem. Phys. Lipids* **2012,** *165* (3), 348-361; (b) Ge, M. T.; Freed, J. H., An electron spin resonance study of interactions between gramacidin-A' and phosphatidylcholine bilayers *Biophys. J.* **1993,** *65* (5), 2106-2123; (c) Mangels, M. L.; Cardon, T. B.; Harper, A. C.; Howard, K. P.; Lorigan, G. A., Spectroscopic characterization of spin-labeled magnetically oriented phospholipid bilayers by EPR spectroscopy. *J. Am. Chem. Soc.* **2000,** *122* (29), 7052-7058.

19.   (a) Dejanovic, B.; Mirosavljevic, K.; Noethig-Laslo, V.; Pecar, S.; Sentjurc, M.; Walde, P., An ESR characterization of micelles and vesicles formed in aqueous decanoic acid/sodium decanoate systems using different spin labels. *Chem. Phys. Lipids* **2008,** *156* (1-2), 17-25; (b) Dejanovic, B.; Noethig-Laslo, V.; Sentjurc, M.; Walde, P., On the surface properties of oleate micelles and oleic acid/oleate vesicles studied by spin labeling. *Chem. Phys. Lipids* **2011,** *164* (1), 83-88.

20.   (a) Caldararu, H., Structural aspects in self-assembled systems of polyoxyethylene surfactants, as studied by the spin probe technique. *Spectroc. Acta Pt. A-Molec. Biomolec. Spectr.* **1998,** *54* (14), 2309-2336; (b) Benatti, C. R.; Feitosa, E.; Fernandez, R. M.; Lamy-Freund, M. T., Structural and thermal characterization of dioctadecyldimethylammonium bromide dispersions by spin labels. *Chem. Phys. Lipids* **2001,** *111* (2), 93-104; (c) Bastrop, M.; Meister, A.; Metz, H.; Drescher, S.; Dobner, B.; Mader, K.; Blume, A., The Motional Dynamics in Bolaamphiphilic Nanofibers and Micellar Aggregates: An ESR Spin Probe Study. *J. Phys. Chem. B* **2009,** *113* (2), 574-582.

21.   (a) Vasilescu, M.; Caragheorgheopol, A.; Caldararu, H.; Bandula, R.; Lemmetyinen, H.; Joela, H., Micropolarity and order in the reverse micelles of L62 and L64 pluronic copolymers, as studied by molecular probe techniques. *J. Phys. Chem. B* **1998,** *102* (40), 7740-7751; (b) Griffiths, P. C.; Cheung, A. Y. F.; Farley, C.; Paul, A.; Heenan, R. K.; King, S. M.; Pettersson, E.; Stilbs, P.; Ranganathan, R., Small-angle neutron scattering, electron paramagnetic resonance, electrophoretic NMR, and time-resolved fluorescence quenching studies of sodium dodecyl sulfate and tetra(ethylene oxide) dodecyl ether mixed surfactant micelles. *J. Phys. Chem. B* **2004,** *108* (4), 1351-1356; (c) Griffiths, P. C.; Paul, A.; Heenan, R. K.; Penfold, J.; Ranganathan, R.; Bales, B. L., Role of counterion concentration in determining micelle aggregation: Evaluation of the combination of constraints from small-angle neutron scattering, electron paramagnetic resonance, and time-resolved fluorescence quenching. *J. Phys. Chem. B* **2004,** *108* (12), 3810-3816; (d) Alves, M.; Bales, B. L.; Peric, M., Effect of lysophosphatidylcholine on the surface hydration of phospholipid vesicles. *Biochimica Et Biophysica Acta, Biomembranes* **2008,** *1778* (2), 414-422.

22.   Chaney, E. E.; Forbes, M. D. E., Dynamics of spin-correlated radical pairs in non-ionic surfactant solutions. *J. Phys. Chem. B* **2003,** *107* (18), 4464-4469.

23.   Kumbhakar, M.; Goel, T.; Mukherjee, T.; Pal, H., Role of micellar size and hydration on solvation dynamics: A temperature dependent study in Triton-X-100 and Brij-35 micelles. *J. Phys. Chem. B* **2004,** *108* (50), 19246-19254.

24.   Badjic, J. D.; Kostic, K. M., Reactivity of organic compounds inside micelles embedded in sol-gel glass. Kinetics of isomerization of azobenzene inside CTAB and SDS micelles embedded in silica matrix. *J. Phys. Chem. B* **2001,** *105* (31), 7482-7489.

25.   (a) Tarasov, V. F.; Forbes, M. D. E., Time resolved electron spin resonance of spin-correlated micelle confined radical pairs: Shape of the anti-phase structure. *Spectrochimica Acta Part A: Molecular and Biomolecular Spectroscopy* **2000,** *56* (2), 245-263; (b) Tarasov, V. F.; White, R. C.; Forbes, M. D. E., Photo-oxidation of diglycine in confined media: Relaxation of longitudinal magnetization in spin-correlated radical pairs. *Spectrochimica Acta Part A: Molecular and Biomolecular Spectroscopy* **2006,** *63* (4), 776-783; (c) Forbes, M. D. E.; Schulz, G. R., Low-Temperature Disappearance of Spin Correlation in Flexible 1,n-Biradicals (n = 22, 24, 26). *J. Am. Chem. Soc.* **1994,** *116* (22), 10174-10177.

26.   (a) K. M. Salikhov, Y. N. M., R. Z. Sagdeev, A. L. Buchachenko, Spin Polarization and Magnetic Effects in Radical Reactions. In *Studies in Physical and Theoretical Chemistry*, Steiner, U., Ed. Elsevier: 1984; Vol. 22, pp 1168B-1169; (b) Harbron, E. J.; Forbes, M. D. E., Chemically-Induced Nuclear and Electron Polarization (CIDNP and CIDEP). In *Encyclopedia of Chemical Physics and Physical Chemistry*, Institute of Physics Publishing: 2001; pp 1389-1417; (c) Muus, L. T.; Atkins, P. W., *Chemically Induced Magnetic Polarization: Proceedings from the NATO Advanced Study Institute, Sogesta/Urbino, Italy*. D. Reidel Publishing Co. : 1977; Vol. 34.

27.   Zavoisky, E. K., *J. Phys.* **1945,** *9*, 211-216.

28.   Weil, J. A.; Bolton, J. R., *Electron Paramagnetic Resonance:Elementary Theory and Practical Applications*. Wiley: Hoboken, NJ, 2006.

29.   Forbes, M. D. E.; Jarocha, L. E.; Sim, S.; Tarasov, V. F., Time-Resolved Electron Paramagnetic Resonance Spectroscopy: History, Technique, and Application to Supramolecular and Macromolecular Chemistry. In *Advances in Physical Organic Chemistry, Vol 47*, Williams, I. H.; Williams, N. H., Eds. 2013; Vol. 47, pp 1-83.

30.   Weil, J. A.; Bolton, J. R., *Electron Paramagnetic Resonance: Elementary Theory and Practical Applications*. 2nd ed.; John Wiley & Sons, Inc.: Hoboken, NJ, 2007.

31.   Piette, L. H., In *Sixth International Symposium on Free Radicals*, Cambridge University Press: 1963.

32.   Poole, C. P., *Electron Spin Resonance: A comprehensive Tratise on Experimental Techniques*. Courier Dover Publications: 1996.

33.   (a) Freed, J. H., ESR studies of spin probes in anisotropic media *ACS Symp. Ser.* **1976,** (34), 1-15; (b) Ernandes, J. R.; Schreier, S.; Chaimovich, H., Spin label studies of micellar and pre-micellar aggregates *Chem. Phys. Lipids* **1976,** *16* (1), 19-30; (c) Schreier, S.; Polnaszek, C. F.; Smith, I. C. P., Spin labels in membranes-problems in practice *Biochim. Biophys. Acta* **1978,** *515* (4), 375-436; (d) Earle, K. A.; Budil, D. E.; Freed, J. H., 250-GHz EPR of

nitroxides in the slow-motional regime - models of rotational diffusion. *J. Phys. Chem.* **1993**, *97* (50), 13289-13297; (e) Cassol, R.; Ferrarini, A.; Nordio, P. L., Dynamics of nitroxide probes linked to flexible chains *J. Phys. Chem.* **1993**, *97* (12), 2933-2940; (f) Budil, D. E.; Lee, S.; Saxena, S.; Freed, J. H., Nonlinear-least-squares analysis of slow-motion EPR spectra in one and two dimensions using a modified Levenberg-Marquardt algorithm. *J. Magn. Reson., Ser A* **1996**, *120* (2), 155-189.

34.   Trifunac, A. D., The Study of Fast Processes and Transient Species by Electron Pulse Radiolysis. In *Proceedings of the ASI (NATO)*, Baxendale, J. H.; Busi, F., Eds. Capri, Italy, 1982.

35.   (a) Fukuju, T.; Yashiro, H.; Maeda, K.; Murai, H.; Azumi, T., Singlet-Born SCRP Observed in the Photolysis of Tetraphenylhydrazine in an SDS Micelle: Time Dependence of the Population of the Spin States. *The Journal of Physical Chemistry A* **1997**, *101* (42), 7783-7786; (b) Yamauchi, S.; Ueda, T.; Satoh, M.; Akiyama, K.; Tero-Kubota, S.; Ikegami, Y.; Iwaizumi, M., A time-resolved electron paramagnetic resonance study on the photoinduced electron transfer reactions from metalloporphyrins to quinones. *Journal of Photochemistry and Photobiology A: Chemistry* **1992**, *65* (1–2), 177-182; (c) Moribe, S.; Ikoma, T.; Akiyama, K.; Tero-Kubota, S., Time-resolved EPR study on photoreduction of sodium anthraquinone-2-sulfate in liposomes. *Chem. Phys. Lett.* **2008**, *457* (1-3), 66-68; (d) Ohara, K.; Terazima, M.; Hirota, N., CIDEP Studies in Low-Frequency Microwave Regions. Magnetic Field Dependence of the Triplet Mechanism. *The Journal of Physical Chemistry* **1995**, *99* (51), 17814-17821; (e) McLauchlan, K. A., In *Advanced EPR: Applications in Biology and Biochemistry*, Hoff, A. J., Ed. 1989; (f) Regev, A.; Galili, T.; Levanon, H., The photoexcited triplet state as a probe of dynamics and phase memory in a multiphase liquid crystal - time resolved electron paramagnetic resonance spectroscopy *J. Chem. Phys.* **1991**, *95* (11), 7907-7916; (g) Kroll, G.; Plüschau, M.; Dinse, K. P.; van Willigen, H., Fourier transform–electron paramagnetic resonance spectroscopy of correlated radical pairs. *The Journal of Chemical Physics* **1990**, *93* (12), 8709-8716.

36.   Forbes, M. D. E., A fast 35-GHz time-resolved EPR apparatus. *Rev. Sci. Instrum.* **1993**, *64* (2), 397-402.

37.   Forbes, M. D. E., Time-resolved (CW) electron paramagnetic resonance spectroscopy: An overview of the technique and its use in organic photochemistry. *Photochem. Photobiol.* **1997**, *65* (1), 73-81.

38.   (a) Tarasov, V. F.; Yashiro, H.; Maeda, K.; Azumi, T.; Shkrob, I. A., Time-resolved ESR in a spin-correlated radical pair with large hyperfine coupling constant at 31P. Micellar size effects and the role of flip-flop transitions. *Chem. Phys.* **1998**, *226* (3), 253-269; (b) Forbes, M. D. E.; Myers, T. L.; Dukes, K. E.; Maynard, H. D., Biradicals and spin-correlated radical pairs anchored to SiO2 surfaces: probing diffusion at the solid/solution interface. *J. Am. Chem. Soc.* **1992**, *114* (1), 353-354; (c) Closs, G.; Forbes, M. E., EPR Study of Polymethylene Biradicals. In *Kinetics and Spectroscopy of Carbenes and Biradicals*, Platz, M., Ed. Springer US: 1990; pp 51-75.

39.   Forbes Malcolm, D. E., Time-Resolved EPR Spectroscopy in the Q-Band Microwave Region. 2. Magnetic Field Effects on CIDEP in Radicals, Biradicals, and Spin-Correlated Radical Pairs*. In *Z. Phys. Chem.*, 1993; Vol. 182, p 63.

40.   Forbes, M. D. E.; Peterson, J.; Breivogel, C. S., Simple modification of Varian E-line microwave bridges for fast time resolved EPR spectroscopy *Rev. Sci. Instrum.* **1991**, *62* (11), 2662-2665.

41.   (a) Laukenmann, K.; Weber, S.; Kothe, G.; Oesterle, C.; Angerhofer, A.; Wasielewski, M. R.; Svec, W. A.; Norris, J. R., Quantum Beats of the Radical Pair State in Photosynthetic Models Observed by Transient Electron Paramagnetic Resonance. *The Journal of Physical Chemistry* **1995**, *99* (12), 4324-4329; (b) Bussandri, A.; van Willigen, H., Observation of radical pair zero quantum coherence effects in the FT-EPR spectra of SO3- and e(aq)(-) generated by photoionization of sulfite ions. *Chem. Phys. Lett.* **2001**, *344* (1-2), 49-54; (c) Saxena, S.; Freed, J. H., Double quantum two-dimensional Fourier transform electron spin resonance: Distance measurements. *Chem. Phys. Lett.* **1996**, *251* (1-2), 102-110.

42.   (a) Closs, G. L., A mechanism explaining nuclear spin polarizations in radical combination reactions *J. Am. Chem. Soc.* **1969**, *91* (16), 4552-&; (b) Closs, G. L.; Trifunac, A. D., Chemically induced nuclear spin polarization as a tool for determination of spin multiplicites of radical pair precursors. *J. Am. Chem. Soc.* **1969**, *91* (16), 4554-&; (c) Closs, G. L.; Trifunac, A. D., Chemically induced nuclear spin polarization as a tool for determination of spin multiplicities of radical pair precursors *J. Am. Chem. Soc.* **1969**, *91* (16), 4554-&; (d) Kaptein, R.; Oosterhoff, J. L., Chemically induced dynamic nuclear polarization II - (Relation with anomalous ESR spectra). *Chem. Phys. Lett.* **1969**,

4 (4), 195-197; (e) Kaptein, R.; Oosterhoff, L. J., Chemically induced dynamic nuclear polarization III (anomalous multiplets of radical coupling and disproportionation products). *Chem. Phys. Lett.* **1969,** *4* (4), 214-216.

43.   (a) Bargon, J.; Fischer, H.; Johnsen, U., Nuclear magnetic resonance emission lines during fast radical reactions. I. Recording methods and examples. *Z. Naturforsch.* **1967,** *22*, 1551-1555; (b) Ward, H. R.; Lawler, R. G., Nuclear magnetic resonance emission and enhanced absorption in rapid organometallic reactions. *J. Am. Chem. Soc.* **1967,** *89* (21), 5518-5519; (c) Fessenden, R. W.; Schuler, R. H., Electron Spin Resonance Studies of Transient Alkyl Radicals. *The Journal of Chemical Physics* **1963,** *39* (9), 2147-2195.

44.   (a) Closs, G. L., Mechanism explaining nuclear spin polarizations in radical combination reactions. *J. Am. Chem. Soc.* **1969,** *91* (16), 4552-4554; (b) Closs, G. L.; Trifunac, A. D., Chemically induced nuclear spin polarization as a tool for determination of spin multiplicities of radical-pair precursors. *J. Am. Chem. Soc.* **1969,** *91* (16), 4554-4555; (c) Closs, G. L.; Trifunac, A. D., Theory of chemically induced nuclear spin polarization. III. Effect of isotropic g shifts in the components of radical pairs with one hyperfine interaction. *J. Am. Chem. Soc.* **1970,** *92* (7), 2183-2184; (d) Kaptein, R.; Oosterhoff, J. L., Chemically induced dynamic nuclear polarization II: (Relation with anomalous ESR spectra). *Chem. Phys. Lett.* **1969,** *4* (4), 195-197.

45.   Atkins, P. W.; McLauchlan, K. A., In *Chemically Induced Magnetic Polarization*, A.R., L.; Closs, G. L., Eds. Wiley: London, 1978; pp 41-93.

46.   Wong, S. K.; Hutchinson, D. A.; Wan, J. K. S., Chemically induced dynamic electron polarization. II. A general theory for radicals produced by photochemical reactions of excited triplet carbonyl compounds. *The Journal of Chemical Physics* **1973,** *58* (3), 985-989.

47.   Pedersen, J. B.; Freed, J. H., Theory of chemically induced dynamic electron polarization. III. Initial triplet polarizations. *The Journal of Chemical Physics* **1975,** *62* (5), 1706-1711.

48.   Atkins, P. W.; Evans, G. T., Electron spin polarization in a rotating triplet. *Mol. Phys.* **1974,** *27* (6), 1633-1644.

49.   El-Sayed, M. A., Multiple resonance techniques in the study of the magnetic, radiative, and non-radiative properties of the triplet state. *Pure Appl. Chem.* **1970,** *24* (3), 475-494.

50.   Adrian, F. J., Role of Diffusion-Controlled Reaction in Chemically Induced Nuclear-Spin Polarization II. General Theory and Comparison with Experiment. *The Journal of Chemical Physics* **1971,** *54* (9), 3912-3917.

51.   Goldberg, A. H.; Dougherty, D. A., Effects of through-bond and through-space interactions on singlet-triplet energy gaps in localized biradicals. *J. Am. Chem. Soc.* **1983,** *105* (2), 284-290.

52.   Kaptein, R., Simple rules for chemically induced dynamic nuclear polarization. *Journal of the Chemical Society D: Chemical Communications* **1971,** (14), 732-733.

53.   (a) Caregnato, P.; Jarocha, L. E.; Esinhart, H. S.; Lebedeva, N. V.; Tarasov, V. F.; Forbes, M. D. E., Electrostatic Control of Spin Exchange Between Mobile Spin-Correlated Radical Pairs Created in Micellar Solutions. *Langmuir* **2011,** *27* (9), 5304-5309; (b) Closs, G. L.; Forbes, M. D. E.; Piotrowiak, P., Spin and reaction dynamics in flexible polymethylene biradicals as studied by EPR, NMR, and optical spectroscopy and magnetic field effects - measurements and mechanisms of scalar electron spin coupling *J. Am. Chem. Soc.* **1992,** *114* (9), 3285-3294; (c) Turro, N. J., Photochemistry of organic molecules in microscopic reactors *Pure Appl. Chem.* **1986,** *58* (9), 1219-1228; (d) Ricks, A. B.; Solomon, G. C.; Colvin, M. T.; Scott, A. M.; Chen, K.; Ratner, M. A.; Wasielewski, M. R., Controlling Electron Transfer in Donor-Bridge-Acceptor Molecules Using Cross-Conjugated Bridges. *J. Am. Chem. Soc.* **2010,** *132* (43), 15427-15434; (e) Garcia-Garibay, M. A.; Zhang, Z. Y.; Turro, N. J., Diffusion and percolation of radical pairs in zeolite media - a product analysis study *J. Am. Chem. Soc.* **1991,** *113* (16), 6212-6218; (f) Veerman, M.; Resendiz, M. J. E.; Garcia-Garibay, M. A., Large-scale photochemical reactions of nanocrystalline suspensions: A promising green chemistry method. *Org. Lett.* **2006,** *8* (12), 2615-2617; (g) Ramamurthy, V.; Eaton, D. F.; Caspar, J. V., Photochemical and photophysical studies of organic molecules included within zeolites *Accounts Chem. Res.* **1992,** *25* (7), 299-307; (h) Tarasov, V. F.; Chemerisov, S. D.; Trifunac, A. D., H-atom electron-spin polarization in irradiated water and ice confined in the nanopores of Vycor glass. *J. Phys. Chem. B* **2003,** *107* (6), 1293-1301; (i) Shushin, A. I., Diffusion theory of CIDEP spectra of spin-correlated radical pairs *Chem. Phys. Lett.* **1991,** *177* (3),

338-344; (j) White, R. C.; Tarasov, V. F.; Forbes, M. D. E., Photooxidation of diglycine in confined media. Application of the microreactor model for spin-correlated radical pairs in reverse micelles and water-in-oil microemulsions. *Langmuir* **2005,** *21* (7), 2721-2727.

54. Closs, G. L.; Forbes, M. D. E.; Norris, J. R., Spin-polarized electron paramagnetic resonance spectra of radical pairs in micelles - observation of electron spin-spin interactions *J. Phys. Chem.* **1987,** *91* (13), 3592-3599.

55. Jarocha, L. E.; Tarasov, V. F.; Forbes, M. D. E., *Langmuir* **2014, in preparation**.

56. Lebedeva, N. V.; Tarasov, V. F.; Resendiz, M. J. E.; Garcia-Garibay, M. A.; White, R. C.; Forbes, M. D. E., The Missing Link Between Molecular Triplets and Spin-Polarized Free Radicals: Room Temperature Triplet States of Nanocrystalline Radical Pairs. *J. Am. Chem. Soc.* **2010,** *132* (1), 82-+.

57. (a) Tarasov, V. F.; Forbes, M. D. E., Time resolved electron spin resonance of spin-correlated micelle confined radical pairs - Shape of the anti-phase structure. *Spectroc. Acta Pt. A-Molec. Biomolec. Spectr.* **2000,** *56* (2), 245-263; (b) Tarasov, V. F.; White, R. C.; Forbes, M. D. E., Photo-oxidation of diglycine in confined media relaxation of longitudinal magnetization in spin-correlated radical pairs. *Spectroc. Acta Pt. A-Molec. Biomolec. Spectr.* **2006,** *63* (4), 776-783.

58. Buckley, C. D.; Hunter, D. A.; Hore, P. J.; McLauchlan, K. A., Electron spin resonance of spin-correlated radical pairs *Chem. Phys. Lett.* **1987,** *135* (3), 307-312.

CHAPTER 2: The Asymmetry of the Anti-Phase Structure (APS) of Spin-Correlated Radical Pairs (SCRP)

2.1 Introduction

The structure, spin dynamics, and reactivity of RPs in confined environments have been the subject of intense research activity in the field of spin chemistry for several decades. [1] Confinement of RPs can have a significant effect on the TREPR spectra because the CIDEP mechanism that are responsible for the TREPR signal have their origin in the spin wavefunction evolution of radicals undergoing diffusive motion. Micellar environments have a long history of being employed as nanoreactors and nanocontainers for chemical reactions, including radical chemistry. [2] The radius of a micelle typically ranges in size between 1-10 nm. As a result of this small size, the micellar environment can significantly restrict the diffusion of chemical species, which can affect radical reaction rates, products, and yields.

In addition to the effects on chemical reactions mentioned above, micellar confinement can also lead to the formation of a spin-correlated radical pair (SCRP). Early TREPR studies of RPs that were photochemically generated in micellar solutions were accompanied by the observation of unusual splittings of the EPR transitions,[3] and the SCRP mechanism of CIDEP was developed to adequately explain them.[4] This additional splitting is now commonly referred to as the anti-phase structure (APS) of the SCRP.[5] Observation of the APS line shape that results from SCRPM polarization is commonplace in TREPR and has been observed in experimental spectra of SCRPs created by photodissociation[6] and photoreduction[7] in micellar solutions, in biradicals,[8] and in charge separated states of photosynthetic reaction centers and model systems.[9] The earlier models
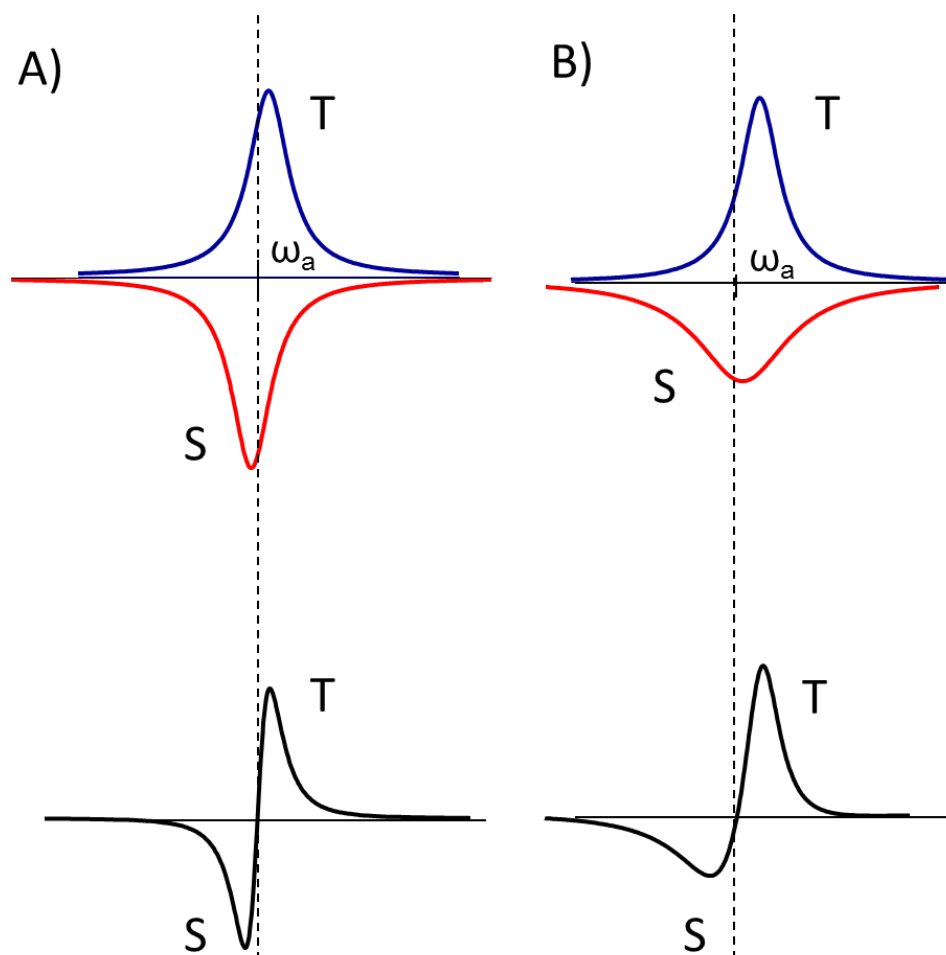
Figure 2.1. The shape of the APS. Previous theoretical descriptions for the origin of the APS predict a symmetric line shape (A) where the absorptive and emissive component are equal and opposite in phase, and shifted away from the center frequency of the transition (ω_a) in equal but opposite directions. In many experimental observations of micellized radical pairs, the APS appears asymmetric (B), with different line widths and unexpected spectral shifts to the emissive and absorptive components

for the SCRPM correctly explained the origin of the splitting, which arises from the exchange interaction J, but did not account for the role of diffusion and the nature of the confinement accurately.

One particularly striking feature of the TREPR spectra of SCRPs that has not been fully explained is the asymmetry of the APS observed in experimental data. As shown in Figure 2.1, most theoretical models predict that J will split each EPR transition into two transitions that are opposite in phase, but equally polarized.[4] In practice, however, the transitions often appear asymmetric, as if there were a different intensity and line width to the polarization of the individual E and A components of the APS.[10] This is particularly true for experimental observations of SCRPs in surfactant aggregates such as micelles. Accurate simulations that reproduce this asymmetry have recently been achieved for micellar systems[11] using the microreactor model developed by Tarasov et al.,[12] and the physical origin of this asymmetry is still being examined.[13]

This chapter presents a detailed examination of the asymmetric appearance of the APS in micellar solutions of sodium dodecyl sulfate (SDS) with benzophenone (BP). This behavior is assessed qualitatively using the microreactor model,[12a, 14] which specifically account for the effects of restricted molecular diffusion of RPs in the micellar environment. A brief overview of the problem of APS asymmetry is presented, along with temperature dependent TREPR spectra of an SCRP confined by a SDS micelle.[11] Simulations of the TREPR spectra require a detailed understanding of the micelle structure, hyperfine and spin exchange parameters, escape processes, and spin relaxation rates. The SDS micelle presents an ideal model system for exploring the asymmetry problem because it has been thoroughly studied by both TREPR and several other characterization techniques, which have independently measured the necessary simulation

parameters. Discussion of the theoretical model and the simulation parameters, as well as simulation results that accurately reproduce the asymmetry observed in the experimental spectra, are also presented, and the physical origin of this asymmetry will be discussed briefly.[13]

2.2 Background

2.2.1 Micellar Surfactant Aggregates

Before any discussion of the unusual features of the CIDEP of micellized radical pairs, it is important to have a well-developed understanding of the aggregation behavior of surfactants and the salient features of the supramolecular micellar structure, which can influence the observed polarization. Fundamentally, surfactants are amphiphilic molecules which, when dissolved in an aqueous solution, lower surface tension. The term surfactant is specifically derived from this behavior and is a shortened form of "surface active agent." Under certain solution conditions, including concentration, pH, dissolution of additives, or temperature, the amphiphilic surfactant molecules can self-assemble into a wide range of supramolecular structures. The most prevalent and, perhaps, the most simplistic is a micelle.

The model of a micelle as an oil droplet protected from the aqueous environment by an ionic shell was proposed as early as the 1930's by Hartley.[15] A more realistic structure of micellar aggregates as highly disordered hydrophobic supramolecular structures in solution was worked out in the early 1980's.[16,17] The non-radial position of the surfactant tails and the general "disordered" nature of the micelle structure, was advocated as the correct model of a micelle by both Zana[17] and Menger[18] to explain experimental results like the preferential insertion of oxygen at the C-11 position of SDS and CTAB micelles after photolysis[18-19], incorporation of structural probes in the micelle tail,[20] kinetic measurements for the oxidation of olefins incorporated into

SDS micelles[18] and deuterium labeled SANS studies of the SDS micelle.[17] In present thermodynamic descriptions of micelle formation and structure, the micelle is treated as a separate pseudophase existing in a bulk aqueous phase.[21] This micellar pseudophase is more hydrophobic and presents a real, though permeable and ill-defined, barrier in solution.[22]

There are a few important physical parameters for the micelle that are relevant to the diffusion of RPs in the micelle environment and the subsequent observation of their TREPR spectra. Surfactant aggregation into micelle structures only occurs above a concentration called the critical micelle concentration (CMC).[23] Below this concentration, surfactants will exist as free monomers in solution. Generally, the concentration of monomer in solution is considered to equal the CMC, while any additional surfactant added above this concentration associates into a micelle structure. For the SDS surfactant discussed in this chapter, the value of the CMC = 8.2 mM.[24]

An important physical parameter of the micelle that determines other properties, like size and viscosity, is the number of surfactant monomers that associate to form the aggregate structure. This is called the aggregation number, N_{agg}.[25] The aggregation number differs for every surfactant, but for most spherical micelle structures ranges between approximately 50-100 monomer units. The size of a spherical micelle is related to N_{agg} and the general length of the surfactant molecule, since most spherical micelle structures cannot have a radius that greatly exceeds the length of the fully extended conformation of the surfactant molecule.[23] For the SDS molecule under standard conditions at 25°C, the value of N_{agg} has been found to be 62 molecules[26] and the radius of the spherical micelle structure is approximately 1.8 ±0.2 nm.[27] It's important to note that the value of N_{agg} and the size of micelle structures are highly variable, even for the same surfactant monomer, because these values intimately depend on other solution conditions, including dissolved salt concentrations and temperature. [25b, 27a, 27b, 28] Changes in micelle size or shape can dramatically

alter diffusion of small organic molecules, including radicals, inside the micellar environment. Thus, any theoretical model that seeks to explain the diffusive motion of these molecules, or observations that rely on this diffusion, must account for these structural features of the surfactant aggregate.

2.2.2 The Micellized Radical Pair

In order to observe the TREPR of micellized RPs, a chemical system that allows for the photochemical generation of RPs must be incorporated into the surfactant solution. A wide variety of different systems have been previously studied, but the work discussed in this chapter will focus on one of the most well studied RP systems in the micellar environment: the SDS alkyl radical – BP ketyl radical pair. [3a, 29] The photochemistry used to create the radicals of interest is outlined in Scheme 2.1. The benzophenone molecule is commonly referred to as a triplet sensitizer, because photochemical excitation of this molecule is followed by efficient intersystem crossing to the triplet excited state. This triplet state can then be used to perform radical chemistry. Hydrogen atom abstraction from the alkyl tail of the surfactant leads to the photoreduction of the BP excited triplet state (^{3}BP*) to the ketyl radical $Ph_2\dot{C}OH$ and an SDS-based alkyl radical, whose specific structure depends on the site of the abstraction reaction. The general structure is $CH_3(CH_2)_n\dot{C}H(CH_2)_{10-n}OSO_3^-$ (n=0-9). For the purpose of this discussion, the surfactant-based radical will be designated as radical **a** and the BP ketyl radical as radical **b**. Of the four possible alkyl radicals, only two are observed experimentally.[30] Radical **a1** and radical **a4** are not observed because they are destabilized by the neighboring anion or are less stable than the other radical products based on hyperconjugation, respectively. All the other possible secondary radicals except one (n=0, radical **a2**) give rise to an over lapping TREPR signal, which will be referred to as radical

Scheme 2.1

n=0-9
m=10-n

n=0-9
m=10-n

hv

=

SDS

a1

a3 (n=1-9)
radical a

a2 (n=0)

a4

46
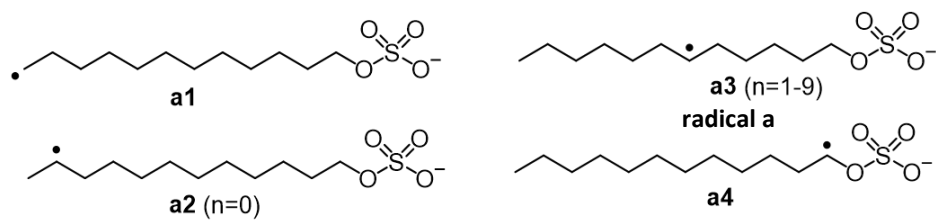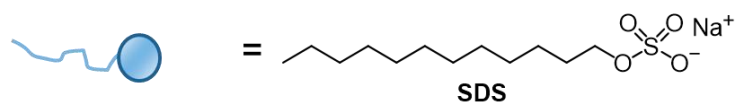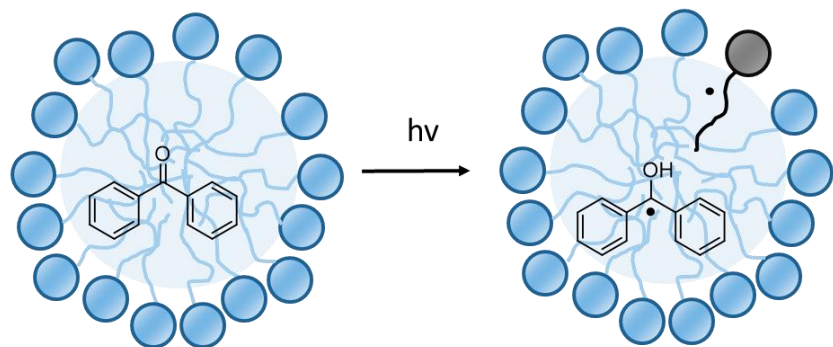
a in the remainder of the text, and are observed in the expected statistical ratio relative to the radical generated at n=0,[31] which will be referred to as radical **a2**.

The TREPR transitions for the radical **a** are designated by the configuration of the H_β and H_α nuclear spins, where $m_s(H_\beta)$ = 2,1,0,-1,-2 is the total sum of the nuclear magnetic quantum number of the four equivalent H_β nuclei and $m_s = \alpha$ or β is the m_s of the H_α nucleus. The stick plot in Figure 2.2 shows the location of each transition with these assignments in the TREPR spectra. An experimental spectra of the escaped SDS radical is shown at the bottom of the figure for comparison, and additional EPR transitions observed for radical **a2** are marked with an asterisk for clarity. The hyperfine coupling constants for each radical and other important spectroscopic parameters are discussed in greater detail in section 2.3.2 in the context of our spectral simulations using the microreactor model.

Given the identity and structure of the photochemically generated radical pair under discussion here, it is important to consider some of the more salient features of the TREPR of micellized RPs. The fundamental features of the TREPR spectra are inherently dictated by the structure and physical properties not only of the RP, but also of the supramolecular surfactant aggregate. These, in turn, are dictated by the molecular structure of the surfactant and the solution conditions. Changes in surfactant structure or solution conditions can lead to changes in aggregate size, shape, or viscosity – all of which can affect RP diffusion in the micellar environment.

The fundamental differences in the TREPR spectra find their source in differences in the CIDEP of the RP. Several CIDEP phenomena arise specifically because of the effects of diffusion on spin-wavefunction evolution of the radicals, radical pairs, and paramagnetic species. Of the four known CIDEP mechanism, three contribute regularly to the TREPR spectra of micellized RPs: the TM, RPM, and SCRPM.[1] All three of these are sensitive to some form of diffusive motion.
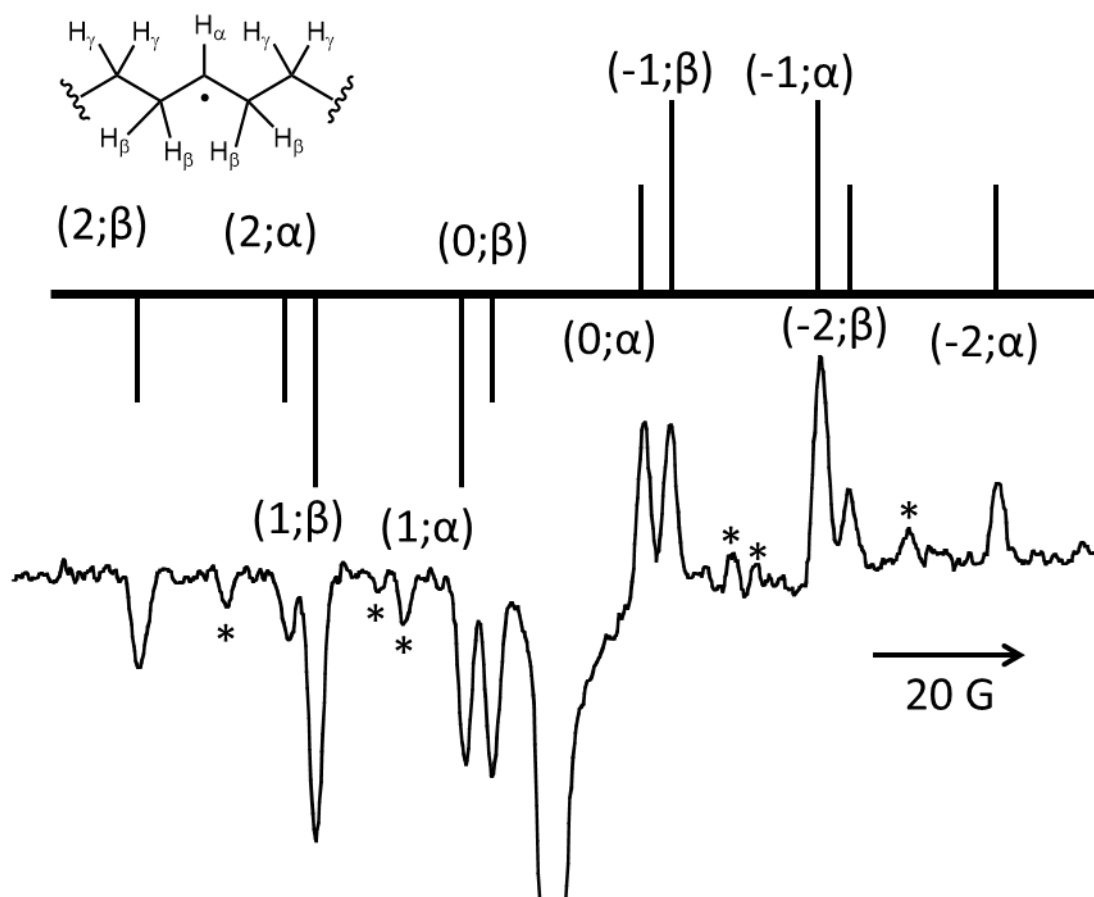
Figure 2.2 Stick figure plot of the TREPR transitions expected for the primary alkyl radical product from the photochemical reduction of the alkyl chain of a surfactant by a triplet sensitizer (top). A TREPR spectrum of the escape radicals of SDS is shown at the bottom for comparison, with transitions from radical **a2** that are visible in the spectrum marked with an asterisk. The center line in the experimental spectrum arises from the sensitizer radical and has been cut off to allow for better visualization of the surfactant alkyl radicals.

The TM is particularly sensitive to viscosity. Fast rotational diffusion of the excited triplet state can relax population differences between the triplet sublevels in the molecular frame, which makes TM contributions more pronounced in systems where the triplet is located in an environment with a high viscosity. RPM and SCRPM polarization are both the product of spin wavefunction evolution of the radical spin states during the mutual diffusion of the RP. In both cases, the RP must make several diffusive reencounters for significant spin polarization to be generated. The fundamental differences between these two CIDEP mechanism is also related to this translational diffusion; in order for SCRPM polarization to be observed, there must be some physical restriction on the diffusion of the RP that keeps the radicals in close enough proximity that spin correlation between the two radicals is maintained. The TREPR spectrum of a micellized RP is often a superposition of one or more of these polarization mechanisms. Any changes to the surfactant solution that impact the diffusion of the RP in or around the surfactant aggregate manifests themselves as changes in the CIDEP and may be observed by TREPR.

Futhermore, because diffusion is a time sensitive process, the observation of CIDEP is inherently time dependent. The diffusion of the RP in a micelle is most commonly described in terms of the supercage model, which naturally lends itself to understanding the time evolution of the SCRP spectra.[32] In the supercage model, immediately after its creation the members of the RP are unaware of their confinement because the physical barrier of the micelle surface is very far relative to the distance between the members of the RP. Immediately after their creation, the radicals diffuse around the micelle interior as if they are in unrestricted space. Prior to "feeling" the effects of their supramolecular confinement, the members of the RP can still make diffusive reencounters, and at very early time delays, the TREPR spectra of micellized RPs can appear very similar to the predictions of RPM polarization. When one of the radicals diffuses far enough that

it encounters the interface between the micelle core and the aqueous bulk, the diffusion of the radical is disrupted. At this point, the radical may either exit the micelle or diffuse back in toward the micellar core. Provided that the radical does not escape the micelle, its continued diffusion inside the micelle will ultimately approach a homogenous distribution where the members have sampled all the available space of the micelle interior. This process is commonly referred to as the "filling out" of the micelle (Figure 2.3) and typically takes several nanoseconds. After this point, the members of the RP reencounter each other with a frequency defined as the frequency of forced encounters, Z, to differentiate it from the frequency of encounters the RP would make if diffusion were not restricted by the micellar boundary. Because the micellar boundary is not a rigid or even well-defined barrier, one or more members of the RP may ultimately diffuse out of the micelle. A radical generated in another location may also diffuse into the micelle, creating what is known as a "random" RP, meaning that the members of the RP were not generated from the same photochemical event.

Through the observation of time dependent CIDEP phenomena, the time resolution provided by the TREPR experiment provides a valuable tool for evaluating the spin dynamics of diffusive RPs. In particular, the observation of spin correlation in heterogeneous solutions containing a micellar phase is sensitive to the time at which the RP is observed. At shorter delay times, the members of the RP will not have diffused as far apart and spin correlation is more likely to be observed. At longer delay times where the RP has had time to diffuse over a greater distance, the initial spin correlation may be lost. We refer RPs where spin correlation is observed as spin-correlated radical pairs (SCRP), while the later are referred to as "escape" radicals. SCRPs are identified by their hallmark APS, while escape radicals typically exhibit some combination of TM and RPM polarization.
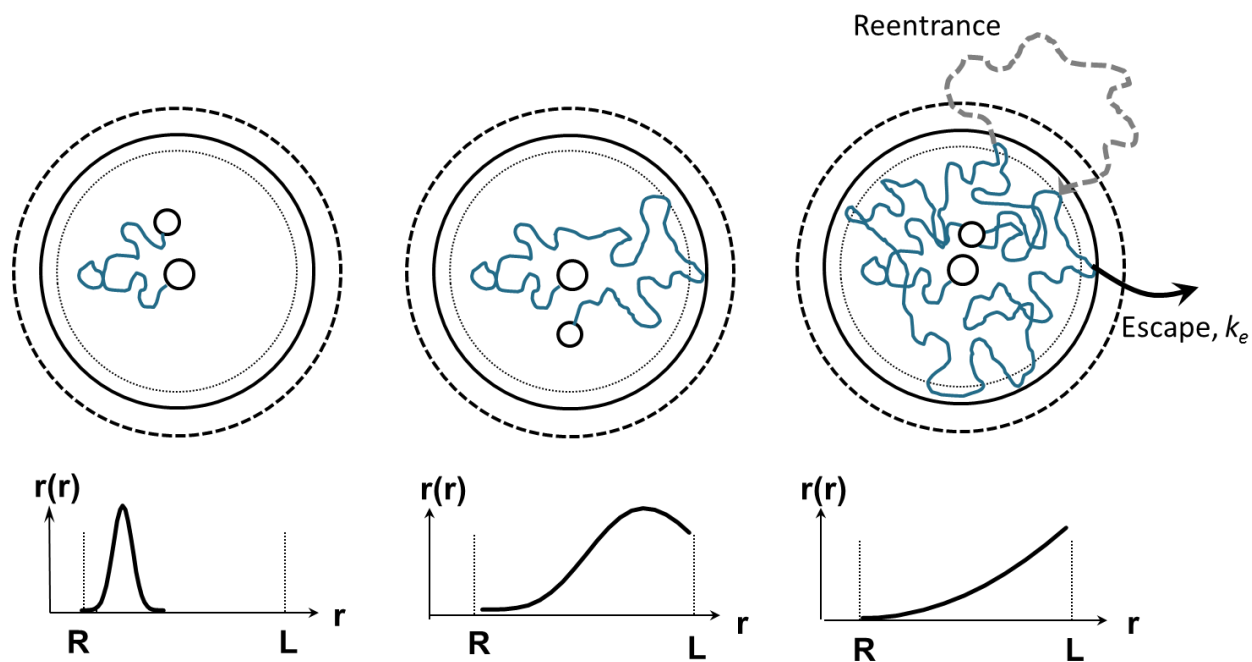
Figure 2.3: The filling out of the micelle in the "supercage" model for radical pair diffusion. At early times after the RP is generated (left), the RP can be described by cage effect diffusion inside a supercage, and the RP has not felt the effects of the confinement because it has not encountered the micelle boundary. At intermediate times (middle), the RP has encountered the boundary and begins to make diffusive reencounters. At longer times on the order of tens of nanoseconds, the micelle is filled out, the RP has made several diffusive reencounters, and SCRPM polarization is observed in the TREPR spectrum.

It is important to note that there are several physical processes that can contribute to the observation of escape radicals. Generally, the RPM polarization pattern may be expected in situations where the RP has separated to such an extent that inter-radical spin interactions are vanishingly small. Mutual diffusion of the RP can occur inside the micelle such that the members of the RP separate to a distance where the exchange interaction is negligible. This is still the geminate RP confined to the original micelle, and the RP can make a forced diffusive re-encounter later. For such RPs, the EPR spectrum is not simply a superposition of the "contact" RP state where inter-radical spin interactions are strong and the "separated" RP where they are effectively negligible because there is spectral exchange between these two-sites. This fact is critical to the appearance and symmetry of the APS. Since the RP has not truly escaped its confinement, this situation is excluded in any subsequent discussion about "escaped" radicals.

A true escape radical signal is generated when one or both members of the RP physically leave the original micelle. Given the hydrophobic nature of both members of the RP in the SDS-BP case, it is unlikely that either radical truly escapes into the aqueous bulk in a literal sense. The temporary fusion of two micelles and subsequent division of the original micelle is quantitatively identical to RP escape to the aqueous bulk if the members of the RP end up in different micelle structures since the members of the RP are no longer confined to the original supramolecular structure in which they were generated. Although possible, the probability that the geminate RP will reencounter after such a separation is incredibly small. There is a large distance between the radicals and a long interval of time between any possible reencounters. The polarization pattern in the TREPR spectra of these escaped radicals appears as ST_0RPM polarization.

Another possible origin of escaped radical signals is a chemical process related to the decay of the radical pairs. Such decay processes are modeled with first order kinetics that have rate

constants of k_a and k_b, to describe the decay of radical **a** or **b**, respectively. Of course, the decay of radical **a** with a rate constant k_a, results in the formation of a free radical **b** with a rate determined by the rate constant k_a. Chemical decay of one of the members of the RP leads to a truly irreversible form of separation of the RP. In addition to describing chemical processes that physically destroy a member of the RP, the kinetic model can also be used to describe other forms of irreversible separation of the RP. A great example of this will be discussed in greater detail in Chapter 3, where strong electrostatic effects cause the irreversible, physical separation of the geminate RP but neither radical decays.

2.2.3 History and Theoretical Explanations of the APS

The initial observation of the APS spectral pattern was reported by Trifunac and Nelson in 1977,[33] although the explanation of the observed line shape was incorrect. Additional observations of the APS in micellar aqueous solutions followed in systems in which the surfactant participated in the photochemistry[3a] or merely served as a non-participatory compartment in which the RP was generated.[34] The theoretical models for the creation of APS in micellar systems was published almost simultaneously by Buckley, *et al.*[4b] and Closs, Forbes and Norris[29a] (referred to in the text as the CFN model) in 1987. Both models suggest that the members of the RP must be interacting through a spin-spin interaction (either the electron spin exchange interaction or dipolar interactions) at the moment of observation. Because the TREPR spectra were obtained at room temperature in solution, the dipolar interaction is assumed to average to zero and the isotropic electron spin exchange interaction must ultimately be responsible for the appearance of the APS. Because of their fundamental simplicity, both models are still widely used in simulations of the TREPR spectra of SCRPs

In both the CFN[4a] and Buckley et al.[4b] models, the Hamiltonian governing the SCRP is

given by:

$$\hat{\mathcal{H}} = \omega_a \hat{S}_{za} + \omega_b \hat{S}_{zb} - J(1/2 + 2\hat{\mathbf{S}}_a \hat{\mathbf{S}}_b) \tag{1}$$

where J given is a generic expression for the exchange interaction that differs between the two

models, and

$$\omega_\mu = g_\mu \beta B_0 + \sum_{\{\chi\}_\mu} A_k^\mu m_k^\mu, \ \mu = a, b \tag{2}$$

are the resonance frequencies of the non-interacting radical **a** and **b**, $\{X\}_\mu$ is the spin configuration

of the magnetic nuclei, and A_k^μ and m_k^μ are the hyperfine coupling constant and nuclear magnetic

quantum numbers for each respective radical. The matrix representation of this Hamiltonian is

given by:

$$\hat{\mathcal{H}}(r) = \begin{bmatrix} \omega - J & 0 & 0 & 0 \\ 0 & J & q & 0 \\ 0 & q & -J & 0 \\ 0 & 0 & 0 & -\omega - J \end{bmatrix} \tag{3}$$

where $\omega = \frac{1}{2}(\omega_a + \omega_b)$ and the frequency of ST$_0$ mixing is $q = \frac{1}{2}(\omega_a - \omega_b)$.[4b, 10]

When initially generated, the members of the RP are in close contact and the exchange

interaction is strong, but when the RP diffuses apart and the exchange interaction is comparable to

or less than the hyperfine interaction, mixing between the $|S\rangle$ and $|T_0\rangle$ states can occur. This mixing

shows up as a phase relationship in the eigenfunctions of the Hamiltonian. These eigenstates are

given by:

$$\psi_1 = |T_+; \chi\rangle \tag{4}$$

$$\psi_2 = cos\theta |T_0; \chi\rangle + sin\theta |S; \chi\rangle \tag{5}$$

$$\psi_3 = -sin\theta |T_0; \chi\rangle + cos\theta |S; \chi\rangle \tag{6}$$

$$\psi_4 = |T_1; \chi\rangle \tag{7}$$

where θ is dependent on J and the hyperfine interaction.[4a] Since ST_0 mixing only occurs in states that have the same nuclear wave function, the value of θ can be related to both q and J by $tan\theta = -J/q$. The eigenvalues of the Hamiltonian are: [4b, 10]

$$\epsilon_1 = -J + \omega \tag{8}$$

$$\epsilon_2 = \Omega \tag{9}$$

$$\epsilon_3 = -\Omega \tag{10}$$

$$\epsilon_4 = -J - \omega \tag{11}$$

Since the new mixed states described by ψ_2 and ψ_3 contain both S and T_0 character, transitions can occur between these states and the T_+ and T_- states. Figure 2.4 shows an energy level diagram for the separated and mixed RP states. We can then separate the allowed spectral transitions in Figure 2.4 into S and T type transitions based on whether they correlated with the triplet states of the RP in the separated condition or the singlet state. Table 2.1 shows the energy of each transition, its spectral shift from the expected resonance frequency due to the exchange interaction, and an assignment of the singlet or triplet character of each transition.

The fundamental difference between the two models comes from how they treat the exchange interaction, J. The CFN model employs a time independent effective exchange interaction, J_{eff}, that can be understood as the average Heisenberg exchange interaction over the entire volume of the micelle.[29a] One problem with using J_{eff} when trying to build a physical understanding of RP dynamics in surfactant aggregate systems is that the value of J_{eff} in the same chemical system under the same conditions can vary dramatically when obtained from different experiments. In the model proposed by Buckley *et al.*,[4b] the distance dependence of the exchange interaction is accounted for with a quasi-static approach. The TREPR spectra is computed as a sum over all the TREPR spectra corresponding to all the possible distances between the members of
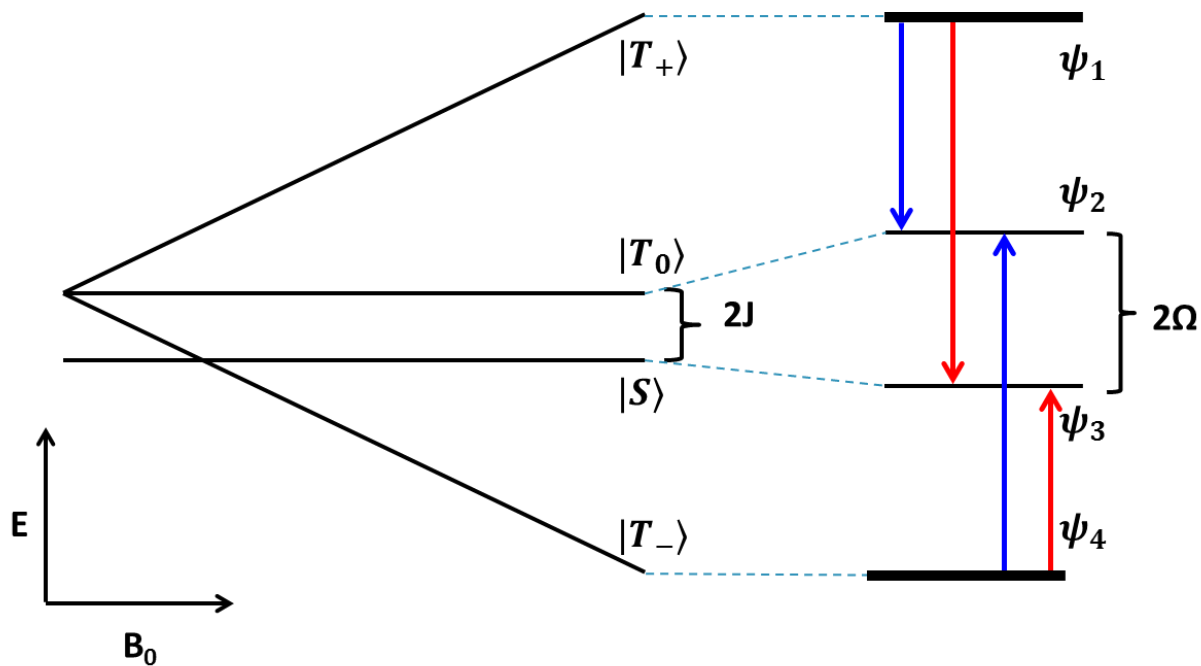
Figure 2.4 Energy level diagram for a radical pair in a magnetic field and an exchange interaction, *J*, in the CFN and quasi-static models. The left side shows the field dependence of the singlet and triplet radical pair states in the high field basis set. The right side shows the states after spin state mixing. The possible transitions between the mixed spin states are colored according to whether or not they a triplet character (blue) or singlet character (red) components of the APS.

Table 2.1: Assignment of the energies, spectral shifts, and transition type for the APS components in the CFN and quasi-static models

Transition	Spectral Shift	Type of Transition
$\psi_4 \rightarrow \psi_3 = \omega + J - \epsilon$	$\Delta\omega = -q - J + \epsilon$	S_b
$\psi_1 \rightarrow \psi_2 = \omega - J - \epsilon$	$\Delta\omega = -q + J + \epsilon$	T_b
$\psi_4 \rightarrow \psi_2 = \omega + J + \epsilon$	$\Delta\omega = q - J - \epsilon$	T_a
$\psi_1 \rightarrow \psi_3 = \omega - J + \epsilon$	$\Delta\omega = q + J - \epsilon$	S_a

the RP at the moment of observation. Ultimately, this model may not be an appropriate choice at the short delay times at which the radicals are observed (often shorter than the T_2 of the radicals) and because it leads to an overestimation of the role of the contact RP. Conventionally, the concept of an effective exchange interaction from the CFN model is often employed in conjunction with the model in Buckley *et al.*, in which the populations of the spin levels are also described in terms of sudden perturbations. However, both an average exchange interaction and the quasi-static approach neglect important dynamic behavior of the RP related to its diffusion. As a result, both models predict symmetric APS line shapes. [35] More sophisticated theories for the origin of the APS that specifically include the diffusive behavior of the RP have been proposed, but these models still do not accurately account for the asymmetry of the APS.

Numerical solutions of the stochastic Liouville equation (SLE) using what is known as the microreactor model[36] for the micellized SCRP can produce accurate numerical solutions.[14, 37] The microreactor model has been extensively analyzed, but the theoretical analysis of the model itself does not predict the asymmetry of the APS.[32, 38] However, the spectral features of micellized RPs, including the asymmetry of the APS, can be accurately reproduced with this model. [10, 11] A comparison of the TREPR of SDS and BP at a wide range of delay times and temperatures was

undertaken to develop an understanding of the conditions under which strong asymmetry of the APS may be observed. Simulations of these spectra using the microreactor model allows us to determine which simulation parameters are most crucial in influencing the spectral line shape and may provide some insight into the relationship between the RP confinement and the appearance of the APS.

Successful numerical simulations do not provide much insight into the origin of the asymmetry itself because of the sheer number factors and parameters involved in the SLE calculations. Some suggestions for the physical origin of the phenomena include a difference in the line widths of the A and E components of the APS,[14, 37] which is supported by theoretical analysis of the TREPR spectra using the two-site model for the spin exchange interaction,[10] or equilibration of the populations of particular electron spin states,[39] leading to stochastic modulation of the exchange interaction. [10, 29b] The end of this chapter will detail recent work on the spectral decomposition of the TREPR of micellar RPs using a two-site model that, despite its simplicity, provides greater physical insight into the origin of the APS.

2.2.4 The Microreactor Model for the Micellized Radical Pair

The microreactor model was specifically developed to simulate the TREPR spectra of micellized radical pairs. [12] The model is based upon numerical integration of the master stochastic Liouville equation for both spin-correlated and free radicals and employs a supercage model in order to specifically account for the diffusion of the radicals inside a confined environment. There are a few important features that the microreactor model was designed to address. First, the decay of spin correlation due to escape of radicals from the micellar environment and the spin relaxation of the radicals caused by magnetic interactions occur on a similar timescale. The microreactor

model explicitly accounts for these processes. Second, the APS signals from SCRPs are often superimposed on signal from free radicals that are spin polarized by the RPM or TM, which can complicated the quantitative analysis of the line shape and must also be accounted for in the model. Finally, diffusive motion of the RP in the micellar environment is relatively slow, and it is necessary to account for both slow diffusion rate and the confinement of the RP in order to accurately reproduce the spectral features.

In a strong magnetic field, $\mathbf{B_0}$, the spin-Hamiltonian of the SCRP in the rotating frame is:

$$\mathcal{H}(r) = \mathcal{H}_a + \mathcal{H}_b - J(r)\left(2S_aS_b + \frac{1}{2}\right) \tag{12}$$

where $J(r)$ is the distance dependent exchange potential given by:

$$J(r) = J_0 e^{-(r-R)/\lambda} \tag{13}$$

with r as the distance between the radicals, R as the closest distance of approach, and $\mathcal{H}_\mu$ as the spin Hamiltonians of the individual radicals (μ=a,b).

$$\mathcal{H}_\mu = \omega_\mu S_{\mu z} + \omega_1 S_{\mu x} \tag{14}$$

$$\omega_\mu = g_\mu \mu_B B_0 + \sum_k A_k^\mu m_{z,k}^\mu - \omega \tag{15}$$

where ω_μ is the frequency of the transition, ω is the microwave frequency, and $\omega_1 \sim 2\mu_B B_1$ is amplitude of the microwave field in frequency units. In addition, g_μ are the g factors of the radicals, μ_B is the electron Bohr magneton, and A_k^μ and $m_{z,k}^\mu$ are the hyperfine constant and spin projection of individual neighboring nuclei.

The micelle is modelled as a homogenous spherical drop with a radius L_m. One of the radicals (radical **a**) is permanently fixed at the center of the micelle and the other (radical **b**) diffuses throughout the remaining volume of the micelle and may escape into the bulk water. This approximation is not an accurate physical picture, but is necessary to simplify the computational

demands of the model. To account for the more realistic situation in which both radicals diffuse inside the micelle, the model employs the mutual diffusion coefficient D, and the diffusion coefficient of radical **b** is assumed to be the sum of the diffusion coefficients of both radicals. The density operator for the SCRP:

(16)

$$\rho(t) = \rho_{out}(t) + \int dr \, 4\pi \, r^2 \rho_{in}(r, t)$$

accounts for contributions both from RPs confined to the same micelle (ρ_{in}) and from RPs that have escaped such that the members of the RP are now located in two different micelles (ρ_{out}). The corresponding SLEs for the "in" and "out" states are:

$$\frac{d}{dt}\rho_{in}(r) = \left(\frac{d}{dt}\rho_{in}(r)\right)_{gen} + \frac{d}{dr^2}\frac{D}{r}(r\rho_{in}) - \hat{L}(r)\rho_{in}(r) \tag{17}$$

$$\frac{d}{dt}\rho_{out} = 4\pi L^2 D \frac{d}{dr}\rho_{out}|_{r=L} - \hat{L}_{out}\rho_{out} \tag{18}$$

where the first term in equation 17 accounts for the rate of SCRP generation, $L = L_m$ - r_b is the radius of the region inside the micelle that is accessible to the radical **a**, r_b is the van der Waals radius of radical **b**, and $\hat{L}$ is the Liouville operator. The Liouville operator is given by:

$$\hat{L}(r)\rho = -i[\rho H(r) - H(r)\rho] + \{R_a \otimes 1_b + 1_a \otimes R_b\}\rho + (k_a + k_b) \tag{19}$$

$$\hat{L}_{out} = \hat{L}(r \rightarrow \infty) \tag{20}$$

The Liouville operator accounts for both the spin Hamiltonian for the SCRP and for the relaxation and chemical decay processes of the radicals. Radicals may decay due to non-spin-selective reactions:

$$\frac{d}{dt}\rho_a = k_a \boldsymbol{Tr}_b\rho - \hat{L}_a\rho_a \tag{21}$$

$$\frac{d}{dt}\rho_b = k_b \boldsymbol{Tr}_a\rho - \hat{L}_b\rho_b \tag{22}$$

60

where k_a and k_b are first order rate constants for the radical decay. R_μ is the Bloch relaxation matrix for a free radical:

$$\left(j|R_\mu\rho_\mu|k\right) = \frac{\delta_{jk}}{T_{1\mu}\left\{(j|\rho_\mu|j) - \frac{1}{2Tr\rho_\mu}\right\}} + \frac{1 - \delta_{jk}}{T_{2\mu}\left(j|\rho_\mu|k\right)} \tag{23}$$

where j and k are α_μ or β_μ, and $T_{1\mu}$ and $T_{2\mu}$ are the relaxation times, which are assumed to be independent of the nuclear spin configuration of the radicals. The Bloch relaxation matrix is the same for radical pairs in either the "in" or "out" states and for individual radicals, because these radicals are expected to be located in the micellar phase at all times.

The expressions for the SLE is complemented with two boundary conditions:

$$\frac{d}{dr}\rho_{in} = \frac{\Lambda_s}{R}Q_s\rho_{in} \; at \; r = R \tag{24}$$

$$\frac{d}{dr}\rho_{in} = -\frac{\sigma}{L}\rho_{in} \; at \; r = L \tag{25}$$

$$Q_s\rho = \frac{1}{2\{|S\rangle\langle S|\rho + \rho|S\rangle\langle S\rangle} \tag{26}$$

where σ is the boundary factor, and Λ_s characterizes the reactivity of the singlet SCRP. For the triplet born RP:

$$\rho_{in}(r; t = 0) = \frac{\delta(r - R)}{4\pi rR}\rho^0; \; \rho_{out} = 0 \tag{27}$$

$$\rho^0 = 1/3\{(1 + \eta)|T_+\rangle\langle T_+| + |T_0\rangle\langle T_0| + (1 - \eta)|T_1\rangle\langle T_1|\} \tag{28}$$

where η is equal to 3/2 of the TM polarization.

Transverse magnetization $M(t)$ is proportional to $<S_y(t)>$, the y-component of the net electron spin ($S = S_a + S_b$) in the rotating frame[12a, 14]:

$$M(t) \propto \sum_{\omega\mu} Tr\left[(S_{ay} + S_{by})\rho(t)\right] \tag{29}$$

Solving the SLE in the time domain is beyond our computational facilities. Instead, we employ a windowing method to obtain numerical solutions to the SLE. The experimental signal is proportional to:

$$\langle M \rangle = \int dt f(t) \int dt' M(t - t')(\tau_{sp})^{-1} e^{-t'/\tau_{sp}} \tag{30}$$

where τ_{sp} is the response time of the EPR spectrometer and $f(t)$ is the window function (for example, the boxcar gate). The window function is chosen such that $<M>$ can be found without calculating $\rho(t)$. The function $f_1(t) = (t/\tau^2)exp(-t/\tau)$ is chosen because it has a maximum at $t = \tau$ and zero at $t = 0$. Using this windowing function, the expression for the expectation value of the transverse magnetization becomes:

$$\langle M \rangle = d\{(1 + \frac{\tau_{sp}}{\tau})^{-1} M_\tau\}/d\tau \tag{31}$$

where $<M>$ is proportional to M_τ, the Laplace image of $M(t)$.

The signal may be obtained by numerical differentiation of M_τ. The Laplace image ρ_τ of the density matric $\rho(t)$ can be then found without integration of the SLE in the time domain. By applying the Laplace transform to both sides of Eq. 17:

$$\tilde{\rho}_{in,\tau}(r) = 4\pi R r D \int dt \rho_{in}(r,t) e^{-t/\tau} \tag{32}$$

$$\int dr \, 4\pi r^2, \rho_{in,\tau} = 1/(RD) \int dr \, r \, \tilde{\rho}_{in}(r) \tag{33}$$

$$\rho_{out,\tau} = \tau\sigma/R[1 + \tau L_{out}]^{-1} \tilde{\rho}_{in}(L) \tag{34}$$

$$-\rho^0 \delta(r - R) = \frac{d^2 \tilde{\rho}_{in}}{dr^2} - \frac{\tilde{\rho}_{in}(r)}{\tau} - D^{-1} L(r) \tilde{\rho}_{in}(r) \tag{35}$$

$$at \, r = R, \frac{d\tilde{\rho}_{in}}{dr} = (k_s \tau_s Q_s + 1)/R \tilde{\rho}_{in} \tag{36}$$

$$at \, r = L, \frac{d\rho_{in}}{dr} = \frac{1 - \sigma}{L \rho_{in}} \tag{37}$$

where $\tau_r = \Delta R/D$. These equations were integrated numerically following Pedersen and Freed[40] in order to fit the experimental spectra.

2.3 Results and Discussion.

2.3.1 Time and Temperature Dependence of the APS

Because diffusion and escape of RPs from the micelle are time dependent processes, the time dependence of TREPR spectra can be very informative. Figure 2.5 shows the time-dependence of the X-band (9.5 GHz) TREPR spectra collected after an 25 ns excimer laser flash (308 nm) used to excite BP in a 0.1 M aqueous solution of SDS at a temperature of 32°C. The central line in the spectrum, which is broad and emissive at shorter delay times, comes from the BP ketyl radical. This net emission is due to the TM. The remaining radicals appearing on the high and low field side of the center transition are due to the alkyl radicals of SDS. At intermediate times, these radicals display a first-derivative like APS structure, which is converted into a low field emissive, high field absorptive RPM polarization pattern at the longest delay time (2.5 μs). The low field E, high field A pattern that is indicative of a negative J, and the conversion of SCRPM polarization to an RPM polarization pattern is due to the time-dependent escape and decay processes of the geminate RP. The general trend of this time dependence holds for all temperatures at which the SDS and BP radical pair system was studied, and the complete time dependence from 0.15 to2.5 μs for the SDS-BP RP at temperatures of 16°C, 32°C, 43°C, and 66°C can be found in Tarasov et al. [35] It is important to note that there is a time interval when the shape of the APS and the appearance of the TREPR spectra do not depend on the time of observation. Although this time interval changes (from 0.5-1 μs at 16°C to 0.3-0.8μs at 66°C), this particular feature suggests that there is a time period during which escaped radicals make a negligible contribution to the observed
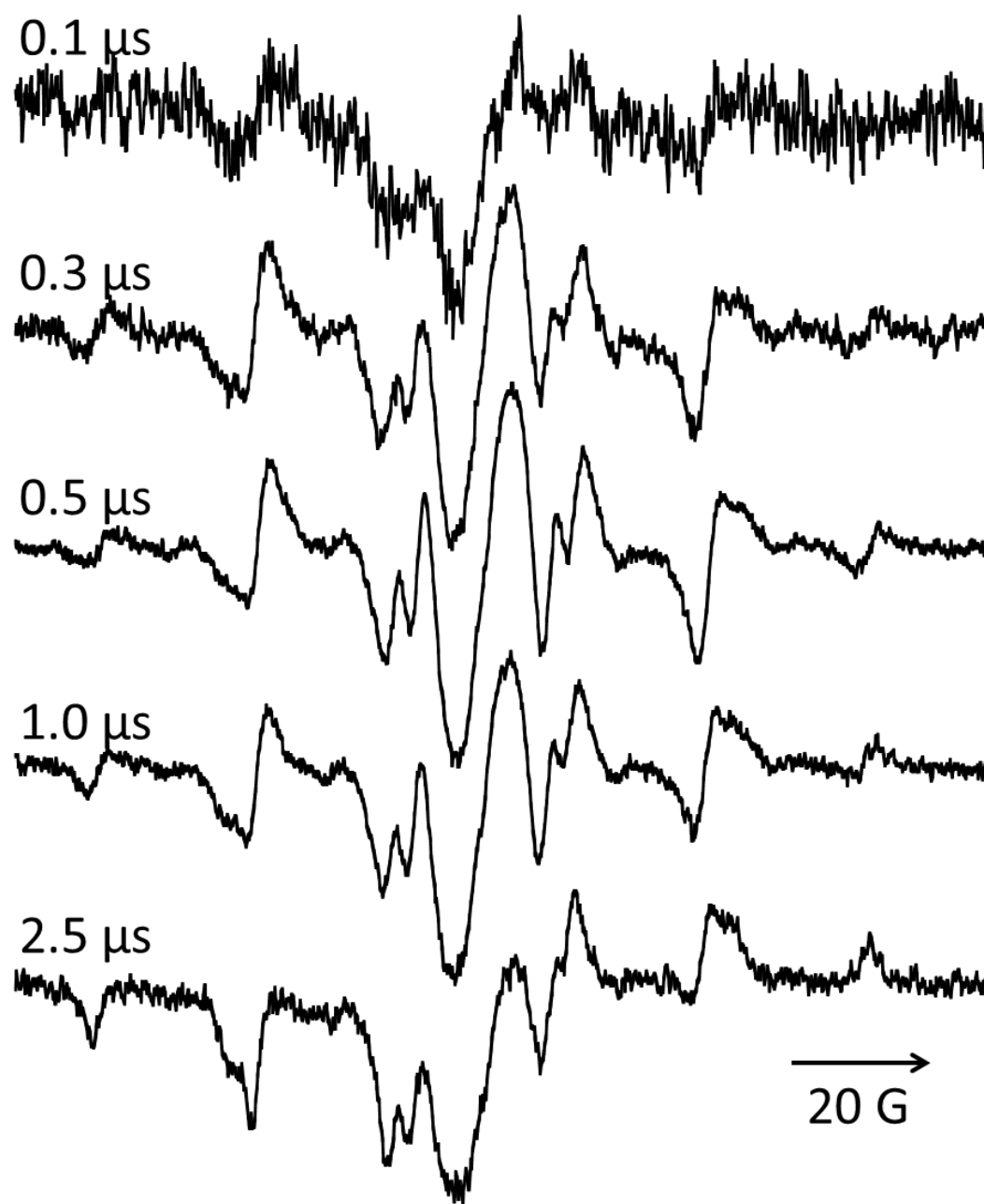
Figure 2.5 The time dependent behavior of the TREPR spectra of the SDS-BP radical pair, collected at a temperature of 32 °C with time delays of 0.10μs, 0.3 μs, 0.5 μs, 1.0 μs, and 2.5 μs. Excitation was at 308 nm with a 60 Hz repetition rate, boxcar gate width of 100 ns, and scan time of 2 min.

TREPR line shape, and therefore, the line shape of the escape radicals is not obscuring any features of the APS. In addition, this long time interval allows the windowing method to be applied to the simulations. This is ideal, because the windowing method emulates the experimental sampling method of the boxcar integrator, which makes it particularly suited for the calculation of the TREPR spectra collected in this fashion.

Figure 2.6 shows a comparison of the TREPR spectra collected at a delay time of 0.5 µs for four different temperatures: 16°C, 32°C, 43°C, and 66°C. All spectra show a strong contribution of SCRPM polarization leading to the observation of the APS line shape, but no appreciable contribution from the escape radicals to the TREPR spectra. The width of the APS component and the value of the APS splitting, as measured by the distance between the APS extrema, increase continuously with increasing temperature. At 16°C (Fig 2.4A), the APS appears nearly symmetrical; however, at higher temperatures the APS line shape has a pronounced asymmetry. This is most noticeable in the broadening and asymmetry of the 1β and -1α lines of the alkyl radicals (see Fig 2.2 for the assignments). In addition, the outer lines, 2β and -2α become weaker to the point that they are practically invisible at 66°C. The inner most transitions, 1α, 0β, 0α, and -1β are strongly superimposed and cannot be analyzed directly. One very interesting feature of the spectra is that, while the transitions from the alkyl radical broaden with increasing temperature, the unresolved signal from the BP ketyl radical actually becomes narrower with increasing temperature (Figure 2.7).

Figure 2.8 shows the TREPR spectra of the SDS and BP radicals at the same temperatures as Figure 2.6, but at a time delay of 0.15 µs (0.1 µs for 32°C). At this short delay time, the lower temperature spectra (Figure 2.8, 16°C and 32°C) consist almost exclusively of a single, broad and emissive transition. This net emission disappears from the time dependence of the 16°C or 32°C
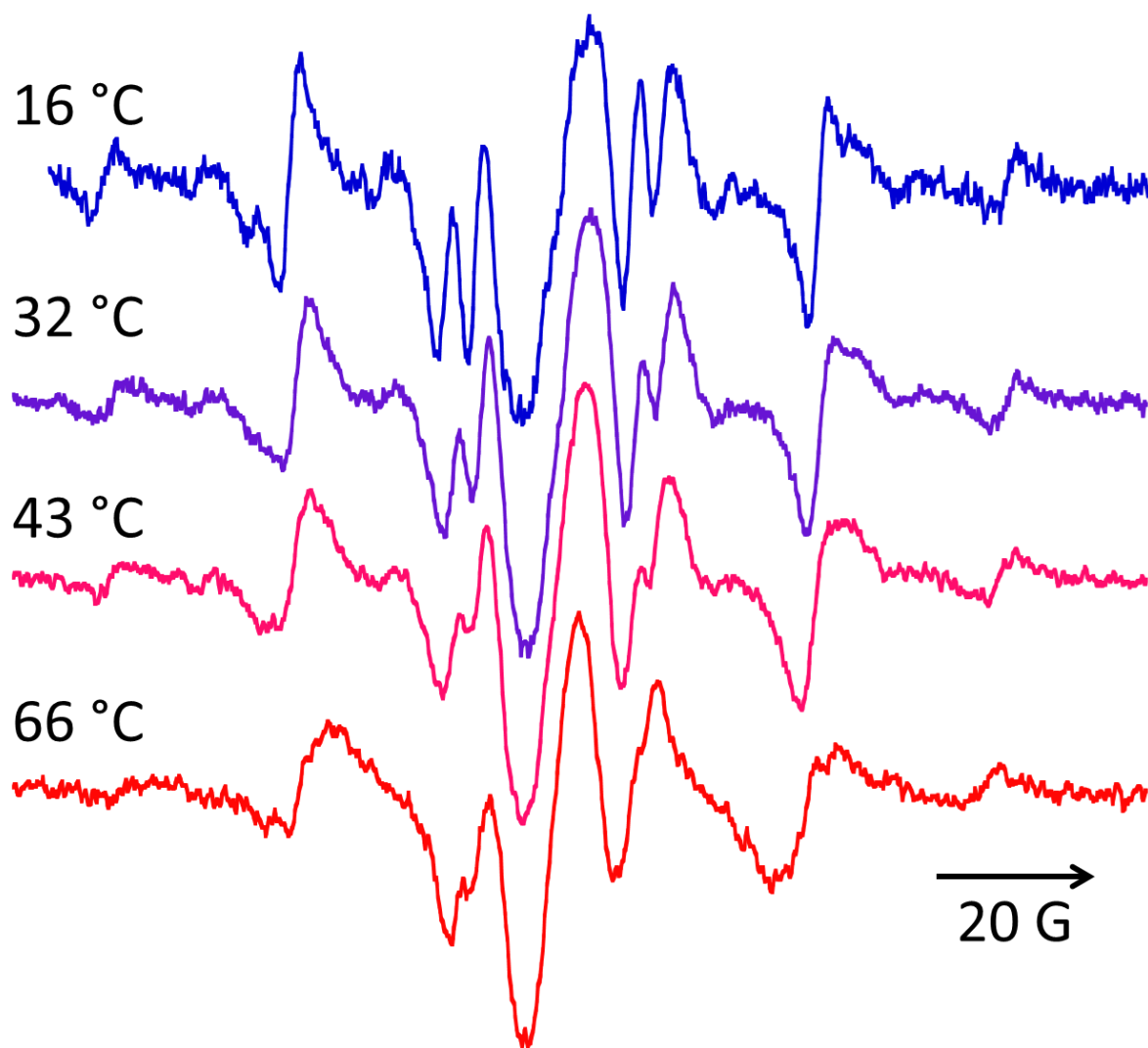
Figure 2.6 The temperature dependence of the TREPR spectra of the SDS-BP radical pair in solutions of 0.1 M SDS and 2 mM BP, collected at temperatures of 16°C, 32°C, 43°C, and 66°C. Delay time is 500ns, following 308 nm excimer excitation at a 60 Hz repetition rate.
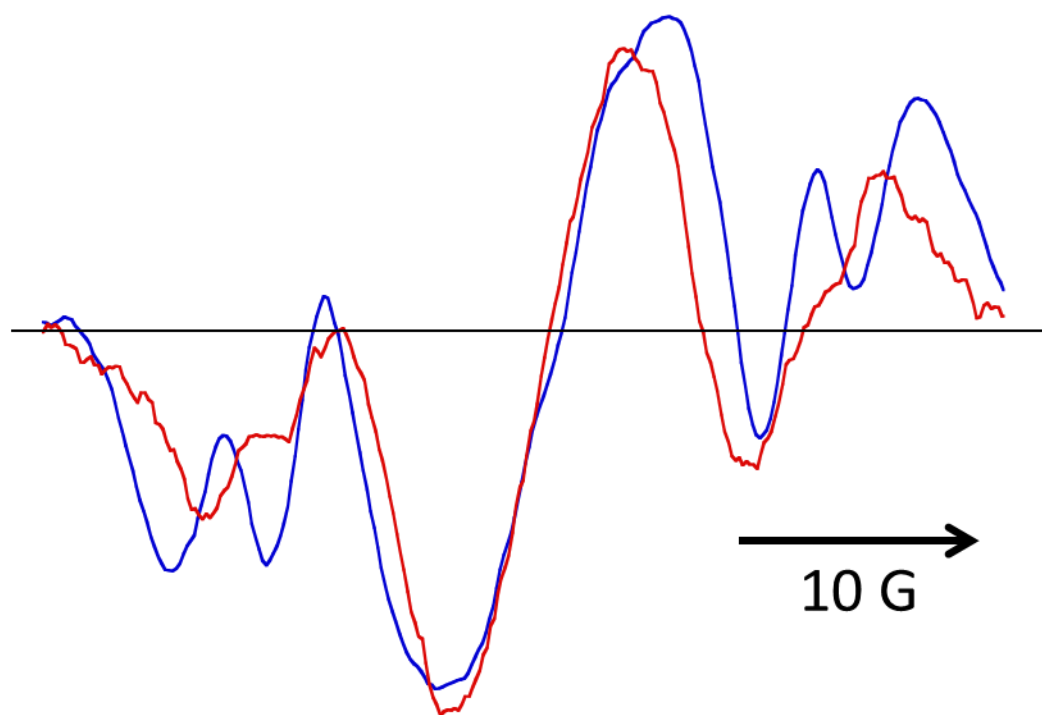
Figure 2.7 A comparison of the central portion of the TREPR spectra in solutions of 0.1 M SDS and 2 mM BP that is due to the BP ketyl radical at 21°C (blue line) and 65°C (red line) collected at a delay time of 500ns. The resonant frequency of the EPR cavity depends on temperature, so the spectra have been shifted slightly to align the center of the BP ketyl radical signal. The black line represents the baseline.

TREPR spectra relatively quickly (between 300-500 ns). This strong net emission does not appear in spectra that are collected at higher temperatures. The overall net emissive character of the low temperature spectra at 0.15 µs can potentially arise from the two different and distinct polarization mechanisms, the TM or an additional CIDEP mechanism known as Radical Triplet Pair Mechanism (RTPM). In order to establish which mechanism is responsible for the TREPR signal, the concentration dependence of the emission as a function of BP concentration was examined. The spectra presented in Figure 2.8 are normalized, but it is important to note that the overall intensity of the signal increases greatly with increasing temperature. This is most likely due to the improved solubility of BP in the micelles at higher temperatures. The strength of the net emissive character of the short delay time, low temperature spectra in Figure 2.8 increases with increasing concentration of BP, but does not decrease at lower concentrations. RTPM polarization is highly concentration dependent. If the RTPM was the source of emission then the net emissive character of the TREPR spectra should decrease and ultimately disappear as the concentration of BP is reduced. Because the net emissive component of the spectrum does not decrease with decreasing BP concentration, the emissive polarization in Figure 2.8 is consistent with TM polarization and not RTPM.

One additional feature of the spectra in Fig 2.8 that deserves mention is the line width. The transitions observable in the spectra acquired at a 0.15 µs delay exhibit about 2 Gauss of additional homogenous broadening that was unexpected and unobserved in spectra collected at longer delay times. This is relatively small compared to the separation of the transitions due to the hyperfine splitting, so the features of the alkyl radical transitions are not obscured. The width of the spectral lines at 66°C (Figure 2.8, red) is also narrower than the width at lower temperatures. The additional homogenous broadening in these spectra can be explained by the kinetics of the RP

16 °C

32 °C

43 °C

66 °C

20 G
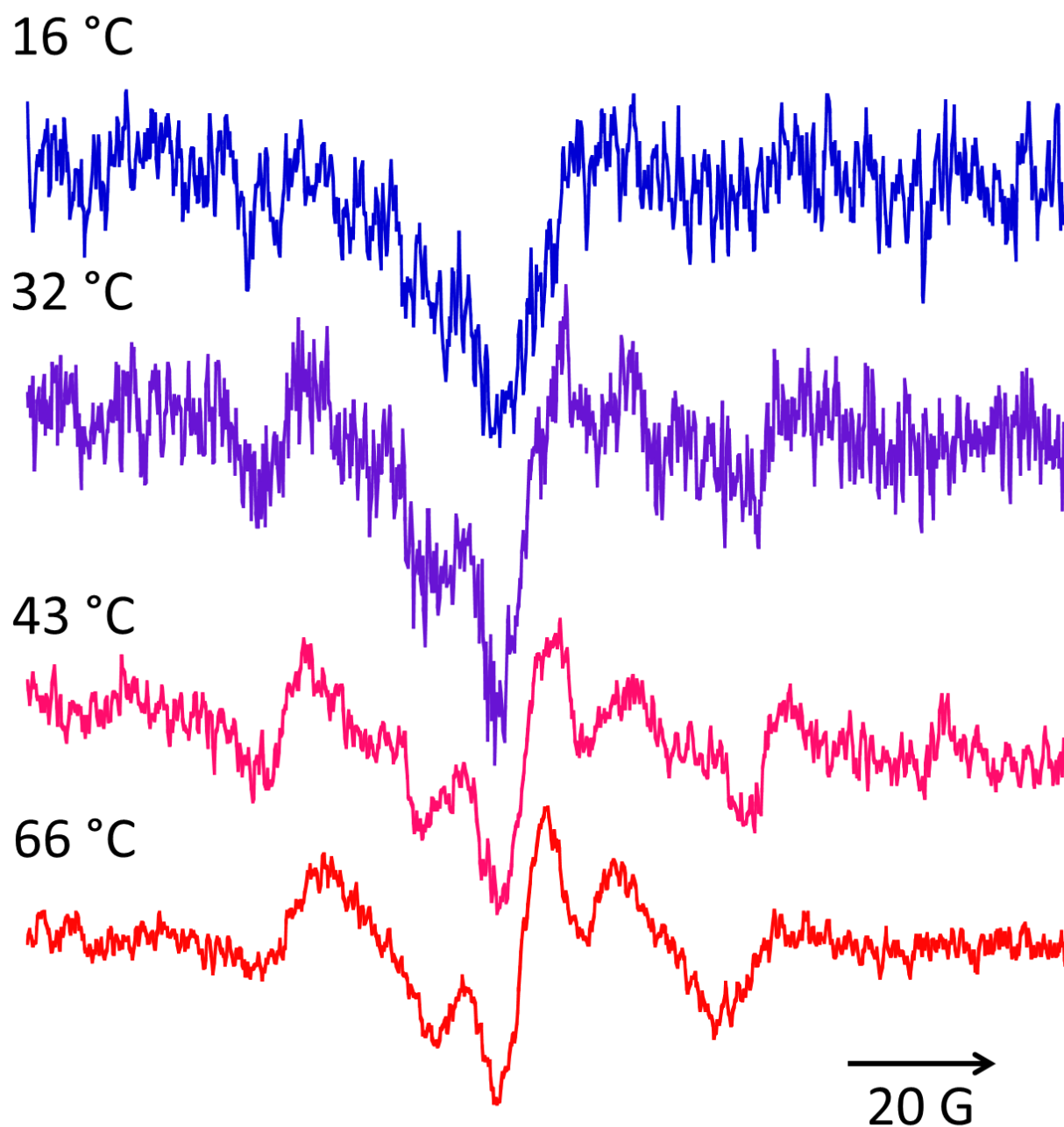
Figure 2.8 The temperature dependence of the TREPR spectra of the SDS-BP radical pair in solutions of 0.1 M SDS and 2 mM BP, collected at temperatures of 16°C, 32°C, 43°C, and 66°C. Delay time is 150 ns, following 308 nm excimer excitation at a 60 Hz repetition rate.

generation. The photoreduction of BP in micelles is a relatively slow reaction.[29d] As a result, at 0.15 μs and low temperature, the radicals are observed during their creation, which is the source of the additional broadening. The line width decreases at higher temperatures because the photoreduction reaction becomes faster, and. the radicals are created well before the sampling gate of the boxcar opens.

Spectra acquired at a long delay time, (1.0 μs for 66°C, 2.5 μs at all other temperatures) are shown in Figure 2.9. Escape radicals dominate the TREPR spectra, and the primary contribution to the observed polarization comes from the RPM. The term escape radical refers only to the fact that the members of the radical pair are no longer making diffusive reencounters with their original partner (the exact same radical partner with which they were generated) and does not imply that the radicals are no longer located in a micelle. Contrary to the observations of the line width of the APS component in Figure 2.7 for the BP ketyl radical, the line width of the resonances from the escaped alkyl radicals decreases with increasing temperature. This is illustrated quite clearly be a comparison of the 2β, 2α, and 1β transitions, which are marked with an asterisk. For the low field 2β and corresponding high field -2α transitions the line width decreases by a factor of 1.5 when the temperature increases from 14 to 55°C. Because of the hydrophobic nature of the alkyl radical and a total concentration of surfactant, which is well above the CMC of SDS (8.2 mM),[24] the escaped alkyl radicals must still be located inside a micelle – although perhaps not the micelle in which the radical was originally generated. Therefore, the decrease in the line width of the escaped radical signal with increasing temperature indicates an increase in the diffusive mobility of the radical in the micellar phase. This hypothesis is supported by quantitative measurements of the rotational correlation time of micellized nitroxide spin probes measured in SDS at different temperatures,[35] which demonstrate a reduction in the rotational correlation time

(which may also be thought of as an increase in the rate of rotational diffusion) by a factor of 4 as the temperature is increased from 20° C to 70° C.

A decrease in the internal viscosity of the micelle alone is not sufficient to explain the changes in line width and the increasing asymmetry of the APS. The size of the SDS micelle also decreases with increasing temperature.[27b, 41] The temperature effects observed in the TREPR spectra, including the line broadening and asymmetry of the APS components of the alkyl radical, the narrowing of the TREPR signal from the BP ketyl radical, and the narrowing of the line width of the escaped alkyl radicals, must be a consequence of both the decrease in internal viscosity and the decrease in the size of the micelle with decreasing temperature. The contradictory nature of these observations – that is to say – the observation of both line broadening and narrowing of different radicals in the same spectra – must be accounted for accurately by any computational model that seeks to address these systems in a quantitative fashion

2.3.2 Simulations of the TREPR Spectra

The necessary micellar, magnetic, and kinetic parameters for simulation of the TREPR spectra of the SDS-BP radical pair have, to a large degree, been obtained from other experiments. The vast amount of information available regarding the photochemical and photophysical properties of the precursors to the RP, the structures of the radicals, and the properties of the SDS micelles across a wide range of temperatures provide the opportunity to make direct comparisons between the simulation results and previously measured values as a way of evaluating the validity of the simulation method.
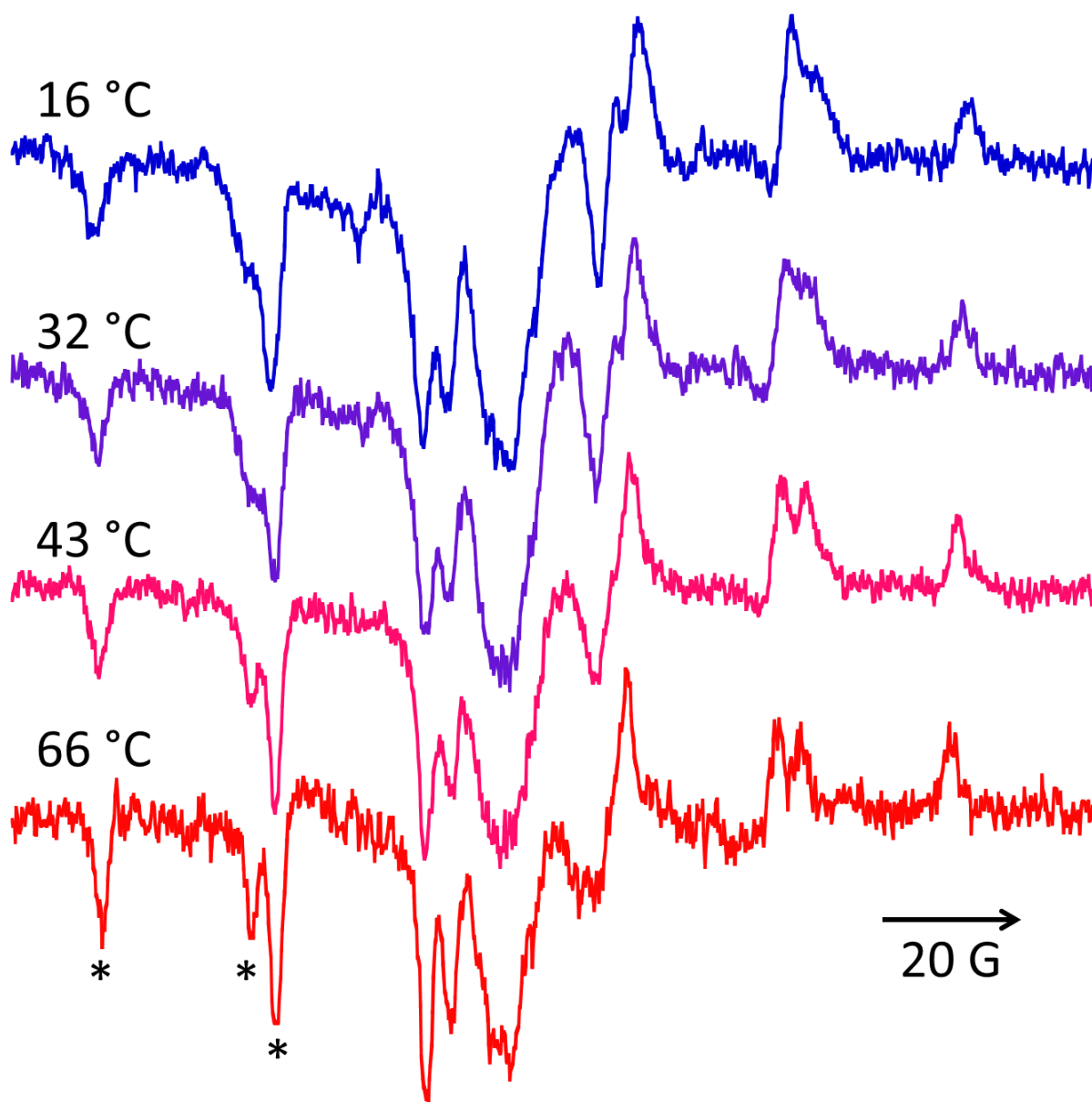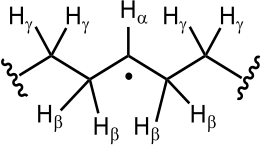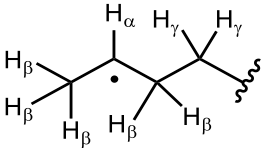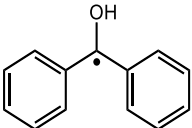
Figure 2.9 The temperature dependence of the TREPR spectra of the SDS-BP radical pair in solutions of 0.1 M SDS and 2 mM BP, collected at temperatures of 16°C, 32°C, 43°C, and 66°C. Delay time is 2.5 μs for all spectra except the one at 66°C, where the delay time is 1.0 μs, and were collected following 308 nm excimer excitation at a 60 Hz repetition rate. The transitions marked with an asterisk on the bottom spectra are marked to illustrate the sharpening of the alkyl radical signal as the temperature increases from 16°C to 66°C.

2.3.2a Spectroscopic Parameters

Our simulations take into account nine hyperfine couplings for radical **a** (H_α, four H_β, and four H_γ). The value of the hyperfine coupling constants used in these simulations and the structure of the relevant radicals are shown in Table 2.2. The coupling constant $A[H_\alpha]$ and $A[H_\beta]$ are very close to those previously published for this radical at room temperature. [27b, 31] The coupling constant for $A[H_\gamma]$ is small, and can only be estimated from the simulation. Its small size means that it is unresolved and only influences the observable line widths of the TREPR signal. As was shown in Scheme 2.1, there are four possible radicals that can be formed on the SDS alkyl chain that may contribute to the TREPR signal. It is worth noting that these hyperfine parameters are correct for radical **a** at positions n = 2-8 on the alkyl chain (Scheme 2.2, **a3**). Radical **a** at n=1 has one additional H_γ proton, but the small magnitude of this hyperfine coupling constant means that inclusion of this additional coupling does not improve the quality of the simulation. The value of the A[CHO] hyperfine in radical **a** at position n = 9 is very different than that measured for SDS radicals located at other positions on the alkyl chain because at n = 9, the radical is much closer in proximity to the head group. However, including this hyperfine for the n = 9 position also does not improve the quality of the simulation. The hyperfine coupling constant is known to vary with temperature, so the H_β hyperfine coupling constant of radical **a** was varied to fit the experimental spectra. For radical **a2**, where n = 0 (scheme 2.1, **a2**), eight protons are taken into account (H_α, five H_β, and two H_γ).[42] Because this radical is so weak in the TREPR spectra, the hyperfine values could not be measured directly from the spectra and were not allowed to vary in order to fit the experimental spectra.

Eleven hyperfine interactions were considered for the BP ketyl radical (four H_{ortho}, four H_{meta}, two H_{para} and one OH). The hyperfine constants used for the simulation were obtained from

Table 2.2 Structure and hyperfine coupling constants for the SDS and BP radicals

Radical Structure	Parent molecule	Hyperfine parameters[43]
radical a	SDS	$a(H_\alpha) = 20.6$ G $a(H_\beta) = 24.9$ G $a(H_\gamma) = 0.7$ G
radical a2	SDS	$a(H_\alpha) = 20.4$G $a(H_\beta) = 24.4$G $a(H_\gamma) = 24.4$G
radical b	BP	$a(4H_o) = 3.16$ G $a(2H_p) = 1.22$ G $a(2H_m) = 3.58$ G $a(OH) = 3.25$ G

the EPR spectrum of BP in 1-propanol. [42] Using a different set of hyperfine coupling constants from BP in other solvents has no noticeable effect on the quality of the simulation results. The spectral fit was found to be insensitive to variation in the BP hyperfine coupling constants, so these temperature effects on these hyperfine values are neglected.

Because there is a strong influence of spin-spin relaxation on the APS shape, it is important to know the T_2 of the alkyl radicals. The value of T_{2a}, where the letter subscript denotes the member of the RP, was determined from the most intense 1β transition of the escaped radical and increases from 0.08 μs at 16 °C to 0.12 μs at 66 °C. These values differ considerably from the literature values for T_{2a},[29a] but previous reports of this value neglected the H_γ hyperfine coupling constants, which contribute to the line width of the transitions even though they are not resolved.

There is no data available for T_{1a}, but the rate of the longitudinal relaxation has been estimated by extrapolating from laser flash photolysis experiments. The rate constant for the decay of the SCRP at room temperature in a magnetic field of 3400 G is approximately 5.5×10^5 s^{-1}, and the escape rate constant of the radicals is known to be $k_{esc} = 2.0 \times 10^5$ s^{-1}.[29c, 29d] The resulting rate of singlet-triplet interconversion at this magnetic field should be about 3.5×10^{-5} s^{-1}. The decay of the SCRP is controlled by paramagnetic relaxation,[44] so this rate includes both spin-lattice relaxation and the relaxation of populations due to interradical interactions. The rate of singlet-triplet interconversion puts a lower limit on the longitudinal relaxation time of the alkyl radicals; it cannot be shorter than 3 µs. If spin relaxation due to interradical interactions is negligible, the upper limit for the longitudinal relaxation is 6.5 µs when the rotational correlation time, τ_c, is approximately 0.4 ns.[35] The simulations presented here use a value of $T_{1a} = 4$ µs, but there is no noticeable effect on the shape of the spectral lines when it is varied in the range from 3-6.5 µs.

A value of $J_0 = -(1-2) \times 10^{10}$ rad·s^{-1} has been reported for pairs of arylalkyl/arylacyl radicals when a value of $\lambda = 0.5$ Å is assumed.[14, 37, 45] In the situation where the exchange interaction is strong $|J_0| \lambda R/D \gg 1$ and the motion of the radicals is slow $|q| L^3/3RD > 1$,[10, 14, 37] the shape of the APS depends weakly on J_0. Conversely, very strong exchange $|2J_0| > B_0$ in a long lived radical pair will give rise to ST$_-$ polarization. The shape of the APS suggests that the value of J_0 cannot be weak, but previous work on the benzoyl/sec-phenyl RP showed no contribution from the ST$_-$ mechanism of spin polarization.[14a] This puts limits on the value of J_0; it cannot exceed 3×10^{10} rad s^{-1} or substantial ST$_-$ polarization would be observed, but it must satisfy the condition $|J_0| \lambda R/D > 1$ or the difference between the resonance frequencies of the APS components would exceed their line widths and the APS shape would not appear like a first derivative.[10, 14, 37]

2.3.2b Micelle Parameters

The coefficient of mutual diffusion, D, and the size of the available volume for diffusion in the microreactor are related to one another through two key theoretical parameters. The first term is the frequency of forced radical encounters:

$$Z = \frac{4\pi RD}{V_m} = \frac{3RD}{L^3 - R^3} \tag{38}$$

This term is referred to as the frequency of forced reencounters to differentiate from the frequency of encounters experienced by radicals when they are in close proximity and to emphasize that these reencounters are a consequence of confinement of the RP on the nanometer scale. The second parameter is the efficiency of Heisenberg exchange, $|J_0|\lambda R/D$. Most analytical solutions that describe the SCRP are applicable to either very strong or relatively weak exchange, but cannot account for the intermediate. Ideally, spectral simulations that aim to accurately reproduce the features of the APS of SCRPs should be able to account for a full range of the parameter $|J_0|\lambda R/D$.

The radius of the micelle is roughly proportional to the cube root of the aggregation number, N_{agg}, which is the number of monomer surfactant units incorporated into a single micellar aggregate. N_{agg} is known to decrease for SDS micelles as a function of temperature, from N_{agg}=68 at 25 °C to N_{agg}=48 at 60°C as measured by small angle neutron scattering (SANS)[41] or from N_{agg} = 75 at 20 °C to N_{agg} = 49 at 51.4°C as measured by the quenching of pyrene excimers in SDS micelles.[27b] This would correspond to a decrease in the radius of available volume for diffusion of the radical pair, L, from roughly 16.8 Å to 14.8 Å over the temperature range presented here. From previous work, the SDS micelle can be characterized by values of $L = 15.4$ Å and $D = 0.72$ x 10^{-6} cm^2 s^{-1} for the benzoyl/*sec*-phenethyl SCRP[10] and $L = 16$ Å and $D = 0.44$ x 10^{-6} cm^2 s^{-1} for the 2,4,6 –trimethylbenzoyl/diphenyl-phosphine SCRP. [14]

2.3.2c Kinetic Parameters

The rate constant for photoreduction of $^3BP^*$ in hexane is 4.11 x 10^5 M^{-1} s^{-1}.[46] Therefore, we assume a rate constant for the generation of the SCRP at 25 °C of k_g = 3.2 x 10^6 s^{-1} with an approximate quantum yield of unity for the photoreduction, because this results in a good agreement with the lifetime of $^3BP^*$ in SDS at room temperature.[29c, 29d] The activation energy for the photooxidation of cyclohexane by $^3BP^*$ is also reported as 7.6 kcal mol^{-1}. [46] This was used to estimate the temperature effect of k_g, the rate constant for the generation of the RP, and results in a 6 fold increase as the temperature increases from 16 °C to 66 °C.

The rate of relaxation of the electron spin state populations of the non-equilibrated $^3BP^*$ is given by: [47]

$$k_{rel} = T_1^{-1} = \frac{2}{15} D_{ZFS}^2 \left[\frac{\tau_R^{-1}}{\omega_0^2 + \tau_R^{-2}} + \frac{4\tau_R^{-1}}{4\omega_0^2 + \tau_R^{-2}} \right]$$

(39)

where D = 5.4 x 10^9 s^{-1} and τ_R is the rotational correlation time for BP.[48] The value of τ_R can be approximated from the rotational correlation time, τ_c, measured by SSEPR of a nitroxide spin probe of similar molecular value.[35] The activation energy for the rotational diffusion of the nitroxide is equal to 2.7 kcal mol^{-1}, which gives us an estimate of k_{rel} = 2.2 x 10^8 s^{-1} at 16 °C and k_{rel} = 6.8 x 10^8 s^{-1} at 66 °C.

The decay rate of the SCRP at 28 °C and zero applied magnetic field is 2.8 x 10^6 s^{-1}.[29c, 29d] As long as the frequency of forced radical encounters, Z, is lower than the frequency of ST_0 mixing, the recombination rate at zero applied magnetic field should be equal to $[\Lambda_S/(1 + \Lambda_S)]Z/4$. Assuming that there is a small activation energy for recombination and a value of Z approximately equal to 1.4 x 10^7 s^{-1}, then a value of $\Lambda_S/(1 + \Lambda_S)$ = 0.8 can be reasonably used throughout the calculations.

The escape rate, $k_{esc} = 2 \times 10^5$ s^{-1}, of the SCRP at room temperature does not depend on the chemical structure of the aromatic ketone used as a triplet sensitizer and, therefore, seems to depend primarily on the escape rate of the alkyl radicals.[29c, 29d] The exit rate of an SDS monomer from the micelle is reported as 1.65×10^5 s^{-1}.[49] The temperature dependence of k_{esc} can be estimated from thermodynamic data and should increase by a factor of five over the temperature range of the TREPR experiment reported here.

2.3.2d Results

The fits of the experimental spectra obtained by simulation using the microreactor model and numerical solutions to the SLE are shown in Figure 2.10 for all four temperatures at a delay time of 0.5 µs. The numerical values obtained for the important simulation parameters are reported in Table 2.3. The asymmetry of the APS can be understood from a comparison of the two key theoretical parameters mentioned above, the efficiency of Heisenberg spin exchange, $|J_0|\lambda R/D$ and the relative speed of radical motion, $|q|/Z$. In relation to the magnetic parameters of interest, the data in Table 2.3 support the assertion that the Heisenberg spin exchange in this system is quite strong at room temperatures ($|J_0|\lambda^2 R/D > 1$) and cannot be considered weak ($|J_0|\lambda R/D > 1$) at any temperature. In particular, in the region above 50 °C, the fact that the exchange interaction is close to a value of 1 and cannot be considered either weak or strong means that none of the existing analytical solutions are applicable to the RP; they are applicable only in cases of truly weak or truly strong exchange. It is also important to note that the motion of the RP is slow $|q|/Z > 1$ for all nuclear spin configurations at low temperature, but at higher temperatures the motion of the RP is fast for only the $q(0,\alpha)$ and $q(0,\beta)$ configurations. This motion is of

fundamental importance to the appearance of the APS asymmetry, which is discussed in greater detail below.

In relation to micellar parameters, the best fit for the spectral simulations returns a value of L = 16.8-17.2 Å at 16 °C and L = 14.8 Å at 66 °C. These values are in good agreement with the values expected (L = 16.8Å - 14.8Å) due to the change in aggregation number and size of the SDS micelle as a function of temperature.[27b, 41] Accounting for the temperature dependence of L over this range and treating D as an adjustable parameter allows us to estimate the effect of temperature on the diffusion coefficient, D, which varies from D = 2 x 10^{-7} cm^2 s^{-1} at 16 °C and D = 8 x 10^{-7} cm^2 s^{-1} at 66 °C. The activation energy for translational diffusion can then be estimated to be 6.0 kcal mol^{-1}. Using this value, D can be estimated for the temperatures of 32 °C and 46 °C where there is no external experimental information to confirm of the value of L. The values of D reported in Table 2.3 are somewhat lower than previously reported values;[10, 14] however, this is expected for the SDS-BP radical pair since the alkyl radical is likely fixed in the micellar phase. Any further decrease in D or increase of L causes a strong contribution of ST_0 RPM polarization to the spectral shape of the APS that is not observed experimentally

In terms of kinetic parameters, the simulation of the low and high temperature spectra at 500 ns returns a value of k_{rel} = 2.0 x 10^8 s^{-1} at 16 °C and k_{rel} = (6-8) x 10^8 s^{-1}at 66 °C, which is in good agreement with the value obtained from Eq. 39 of k_{rel} = 2.2 x 10^8 s^{-1} and k_{rel} = 6.8 x 10^8 s^{-1}, respectively. Eq. 39 was then used to calculate the values of k_{rel} for the intermediate temperatures. Given a value for the kinetic parameter of k_{rel}, it is possible to calculate the value of the initial polarization, $\rho_{T_+T_+} - \rho_{T_-T_-} = 2\eta/3 = 0.2$. The escape rate, k_{esc}, can be obtained from the simulation results through the value of D and L, since $k_{esc} = \sigma D/L^2$. The simulations results are indicative of a four-fold increase in D and a decrease of L^2 by 1.35 between 16 °C and 66 °C,
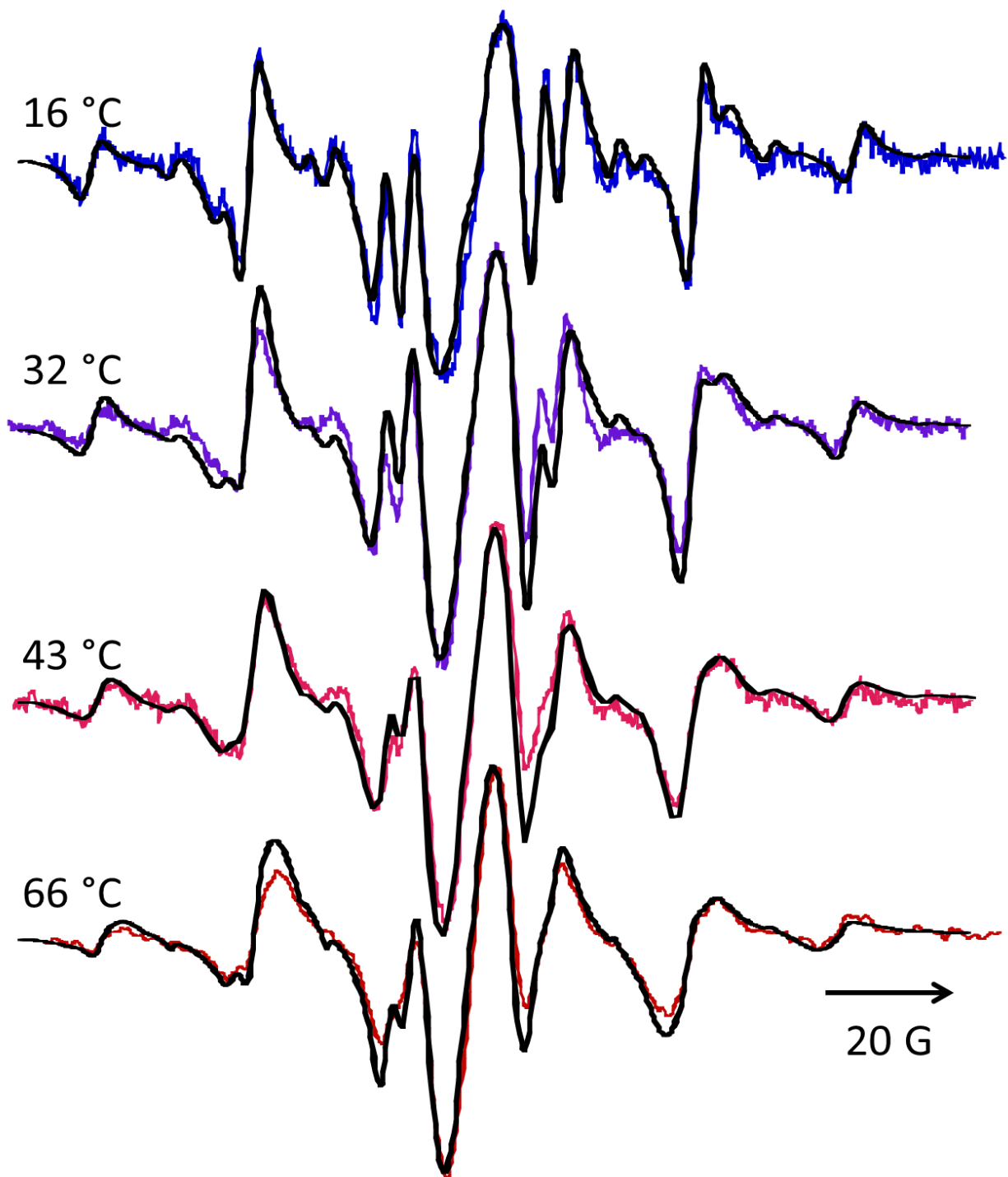
Figure 2.10 Best fits (black) obtained from numerical solutions of the SLE using the microreactor model for radical pair diffusion in a micelle for the temperature dependent TREPR spectra of the SDS-BP radical pair in solutions of 0.1 M SDS and 2 mM BP, collected at temperatures of 16°C (blue), 32°C (purple), 43°C (pink), and 66°C (red). Delay time is 500ns, following 308 nm excimer excitation at a 60 Hz repetition rate. Center field is approximately 3380 G, with a microwave frequency of 9.45 GHz, sweep width of 150 G, boxcar gate width of 100ns, and sweep time of 2 minutes. The parameters obtained from the fits can be found in Table 2.3.

Table 2.3 Parameters from the simulation of the TREPR spectra of the SDS/BP radical pair in micelle solutions of different temperatures

Temp (±0.5°C)	L (Å)	$D \times 10^{-7}$ (cm^2 s^{-1})	$A[H_\beta]$ (G)	T_{2a} (μs)	$k_{rel} \times 10^8$ (s^{-1})	$k_g \times 10^{-6}$ (s^{-1})	$Z \times 10^7$ (s^{-1})	$J_0\lambda R/D$ ($J_0\lambda^2/D$)	$q(0,\alpha)$ /Z
16	17.2	2.0	24.9	0.080	2.0	2.2	0.74	36 (3)	3.1
32	16.3	3.5	24.6	0.095	3.3	4.5	1.5	21 (1.8)	1.5
43	15.6	5.3	24.4	0.107	4.8	4.8	2.7	14 (1.2)	0.84
66	14.6	8.0	24.2	0.120	6.8	13	4.8	9.0 (0.8)	0.47

which would result in a five-fold increase in the value of k_{esc}. This is in perfect agreement with the predicted increase based on thermodynamic estimates.

It is suggested that both the strong increase in the rate of photoreduction and the increase in the rate of relaxation of populations of the non-equilibrated ^{3}BP* states are responsible for the fast evolution of the broad emissive central line observed at short delay times and low temperatures (Figure 2.8, top) into a more conventional first-derivative like APS pattern (Figure 2.6, top). The TREPR spectra of the RP at 16 °C and 66 °C and 0.15 μs were simulated using the kinetic parameters estimated above to test the solutions of the microreactor model under conditions where this strong emission is observed. The parameters for the spectral fits are identical to those used in Figure 2.10 and in Table 2.3, but the t-window function was shifted to 60 ns for these calculations in order to avoid the accumulation of signal contributions from longer delay times. The general simulation approach gives very reasonable agreement between the experimental spectra and the simulation results (Figure 2.11). The simulation results (Table 2.3) support the hypothesis that these two changes to the kinetic parameters, k_{rel} and k_g, play a strong role in the appearance of the APS at early delay times.

2.3.3 Spectral Decomposition

Although simulations performed with the microreactor model have proven to be incredibly
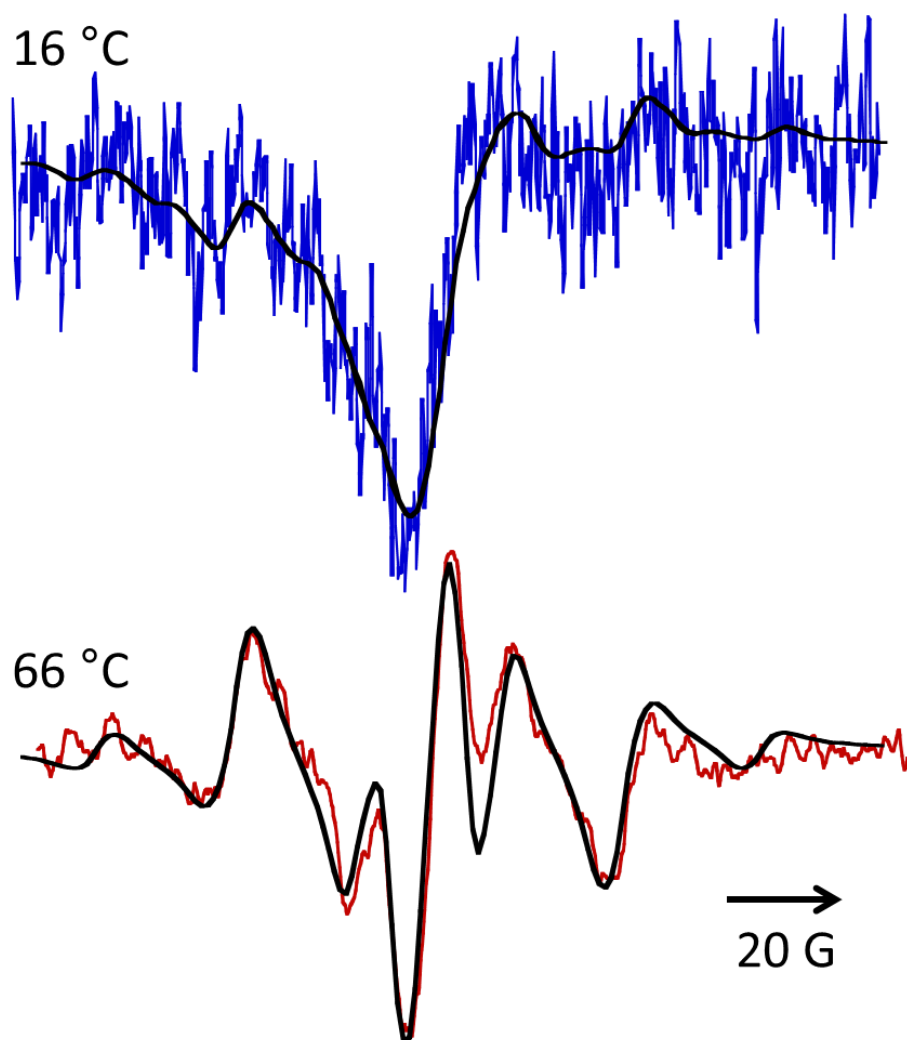
Figure 2.11 Best fits (black) obtained from numerical solutions of the SLE using the microreactor model for radical pair diffusion in a micelle for the temperature dependent TREPR spectra of the SDS-BP radical pair in solutions of 0.1 M SDS and 2 mM BP, collected at temperatures of 16°C (blue) and 66°C (red). Delay time is 150 ns, following 308 nm excimer excitation at a 60 Hz repetition rate. Center field is approximately 3380 G, with a microwave frequency of 9.45 GHz, sweep width of 150 G, boxcar gate width of 100ns, and sweep time of 2 minutes. The parameters obtained from the fits can be found in Table 2.3.

successful, they do not provide a physical intuition about the origin of the asymmetry of the APS and the time dependence of the TREPR spectra. The two-site model can be used as an approximation for the more exact numerical solutions of the microreactor model in order to obtain more exact, qualitative computational analysis of the APS asymmetry. It has also already been used extensively to describe the kinetics of the decay of RPs due to spin selective chemical reactions and previous descriptions of the shape of the APS.[10] Although previous models for the SCRP that were static or based on fixed distances could not reproduce the asymmetry of the APS, the two-site model, based on the concept of site exchange due to both radical motion and Heisenberg spin exchange, is able to provide insight into the asymmetry of the APS as a function of temperature.[10]

The two-site model for the exchange interaction is also intimately related to the supercage model for RP diffusion in the micelle environment.[32a] During the diffusion of the RP, we can identify two regions where the RP exists, one where both radicals are close to the center of the micelle so the exchange interaction is strong and one where a member of the RP is closer to the interface of the micelle and the aqueous phase so that the exchange interaction is essentially negligible.[10, 13] Mathematically, we can differentiate between these two regions separated by a distance r^* such that $|J(r^*)| = |q|$ and $r^* = R + \lambda \ln |J_0/q|$. Both regions are inside the micelle interior. The SCRP is referred to as a contact SCRP when $R < r < r^*$ and a separate SCRP when $L > r > r^*$. The region in which $|J(r)| \approx |q|$ is approximately equal to λ. The diffusion process is then reduced to a discrete two-site model where the time the RP spends in the contact and separate states are characterized by the values of $\tau_{contact}$ and τ_{free}, respectively, where the subscript "free" for the separated state refers to the fact that, in this state, the members of the RP can be treated as free radicals.

The time the RP spends in the contact and separate states can be estimated from the probability of finding the radical at distance r from the center of the micelle, which is $\sim r^2$. The time that the RP spends in the separated state $(r > r^*)$ where exchange is negligible is defined as:

$$\frac{1}{\tau_{free}} = Z\frac{L^3 - R^3}{L^3 - r^{*3}} = \frac{3RD}{L^3 - r^{*3}} \approx Z \tag{40}$$

and the time spent in the contact state $(r < r^*)$ is given by:

$$\frac{1}{\tau_{contact}} = Z\frac{L^3 - R^3}{r^{*3} - R^3} = \frac{3RD}{r^{*3} - R^3} \tag{41}$$

If the micelle is relatively large so the $R \ll L$, this expression can be simplified to $\tau_{contact} = R\lambda/D$. The average exchange interaction in the contact state can very reasonably be approximated as J_0.

As with the CFN and quasi-static models, the components of the APS line shape can be broken into individual transitions of either singlet (S) or triplet (T) character. The resonance frequencies of the individual monoradicals are still denoted by ω_a and ω_b, respectively, and along with their respective nuclear spin configurations, χ_a and χ_b are used to define the frequency of ST_0 mixing, $q = \frac{1}{2}(\omega_a - \omega_b)$ in the noninteracting RP. In the high field approximation, the eigenstates of the contact SCRP are given by the high field basis set with an isotropic exchange interaction: $|T_+; \chi\rangle$, $|T_0; \chi\rangle$, $|T_-; \chi\rangle$, and $|S; \chi\rangle$. The eigenstates for the separated state are described by the multiplicative spin functions $|\alpha\alpha; \chi\rangle$, $|\alpha\beta; \chi\rangle$, $|\beta\alpha; \chi\rangle$, and $|\beta\beta; \chi\rangle$. For values of $q > 0$ and a negative exchange interaction, the $|T_0; \chi\rangle$ and $|S; \chi\rangle$ eignetstates of the contact SCRP correlate to the $|\alpha\beta; \chi\rangle$ and $|\beta\alpha; \chi\rangle$ eignestates of the separate SCRP. T-type transitions occur between electron spin states involving the $|\alpha\beta; \chi\rangle$ state because these correspond with the triplet states of the SCRP in the high field basis set, while S type transitions involve the $|\beta\alpha; \chi\rangle$ state, which correlate to transitions between spin states of singlet and triplet multiplicity in the high-field basis set.

Furthermore, the S- and T- type transitions can be divided into "a" and "b type transitions depending on whether the electron spin involved in the resonance is located on radical **a** or radical **b**. These assignments are identical to those described in Table 2.1.

Figure 2.12 and Fig 2.13 show the spectral decomposition of the results using the two-site model in order to provide insight into the processes responsible for the spectral features of the TREPR of the SCRP for two different values of the mixing term, q. Fig 2.12 shows the spectral decomposition of the line shape of the SCRP for a temperature of 16 °C for $q = 30.15$ G and $q = 5.1$ G. These values represent the maximum and minimum values of $|q|$ in the SDS-BP radical pair. The uppermost spectra belong to a triplet born SCRP in which all three triplet states were equally populated, which is analogous to the experimental TREPR spectra shown above if additional polarization mechanism, escape processes, and relaxation processes are neglected.

It is clear from the top of Fig 2.12 that the shape of the APS is symmetric for both values of q. The observed intensity of the T-type component, I_T, of the APS exceeds the intensity of its associated S-type component, I_S. In addition, the S-type components are broader than the T-type components. The ratio I_T/I_S is greater with smaller values of q. For both $q = 30.15$ and $q = 5.1$, the TREPR signal of the APS is zero at the resonant frequencies of radical **a** and radical **b**. At these frequencies, the intensity of the emissive and absorptive components of the APS are equal to one another and completely cancel out. It is important to note that the experimental spectrum at 16 °C (Figure 2.6, blue) do not show the strong asymmetry of the APS and do not appear to correlate to the line shapes in the top of Figure 2.12. The T_2^{-1} caused by spin exchange for the components of the APS can be estimated as approximately $Z/2 = 3.7 \times 10^6$ s^{-1}. The spin-spin relaxation leading to broadening of the transitions of the RP is $T_{2a}^{-1} = 1.3 \times 10^7$ s^{-1}. As a result, in the experimental spectra, the broadening of the components of the APS due to Heisenberg spin exchange are small
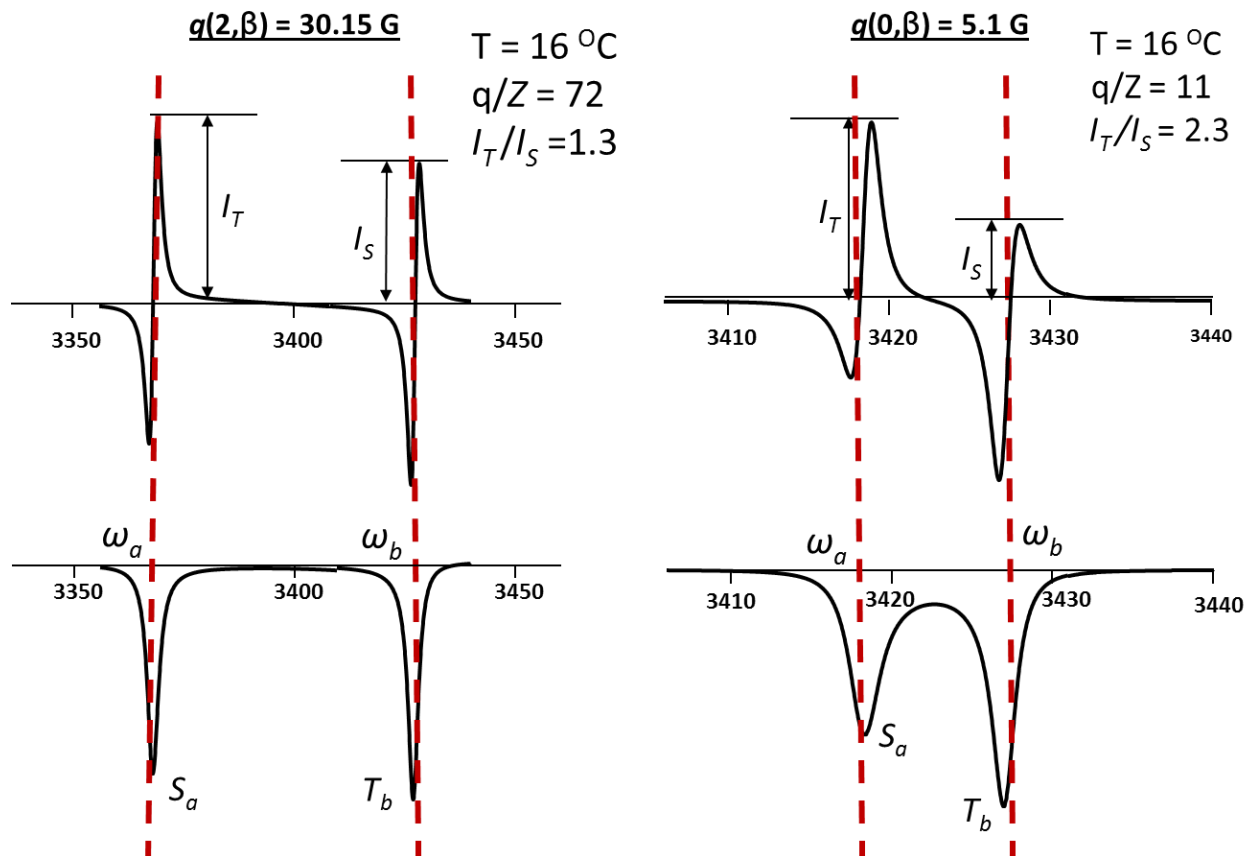
Figure 2.12 The spectral decomposition of the APS line shape for the SDS-BP radical pair at 16°C and two different values of q. The configuration of the nuclear spin states for each value of q are specified at the top, and correspond to the assignment of the transitions in Figure 2.2. The model calculations (top) are for a triplet born SCRP with equal population of all three triplet sublevels. The bottom spectra are a spectra decomposition showing only the contributions to the APS originating from the T_+ state. Model parameters for the spectral decomposition were taken from solutions to the SLE presented in Table 2.3. The dotted lines represent the resonant frequencies of the free surfactant radical (ω_a) and BP ketyl (ω_b) radicals.

compared to the broadening due to the spin-spin relaxation processes in the RP, which causes the spectral shape to appear more symmetric than predicted by the spectral decomposition.

The bottom of Figure 2.12 shows only the contribution to the APS line shape in the upper spectra that originate from the pure $|T_+; \chi\rangle$ state. Because of the linear properties of the SLE, this form of spectral decomposition is not simply a mathematical construct.[13] The whole TREPR spectra can be constructed as a linear superposition of transitions from each of the four spin states, so the components of the APS shown in the bottom of Figure 2.12 are physically meaningful. In this representation, it is much easier to observe the spectral shifts of the individual T-type and S-type components of the APS. At 16 °C, the T_b line is shifted 0.75 G toward the center of the spectrum for $q = 30.15$ G and 4.4 G for $q = 5.1$. The S-type transition for $q = 30.15$ G does not measurably shift in frequency, but for $q = 5.1$ G it shifts toward the center of the spectrum by 1.3 G. The differences in the magnitude of the shift for different values of q are the result of the different nuclear spin configurations influencing ST_0 mixing for each transition.

The top of Figure 2.13 shows the spectral decomposition of the components of the APS for the SCRP at a temperature of 66 °C. Similar to the shape of the APS observed at 16 °C, the shape of the APS is symmetric for both values of q, the intensity of the T-type components is greater than the S-type, and the S-type is still broader than the T-type. In the experimental spectra (Figure 2.6, red), the asymmetry of the APS is clearly observed and matches the line shape predicted by the two-site model. At this temperature, the Heisenberg spin exchange contributes much more strongly to the width of the transitions (2.4×10^7 s^{-1}) than the spin-spin relaxation (8.3×10^6 s^{-1}), which leads the asymmetry of the APS to be much more pronounced at higher temperatures than lower temperatures for the SDS-BP radical pair.

Similar to the shifts observed for the components of the APS at 16 °C, shifts in the
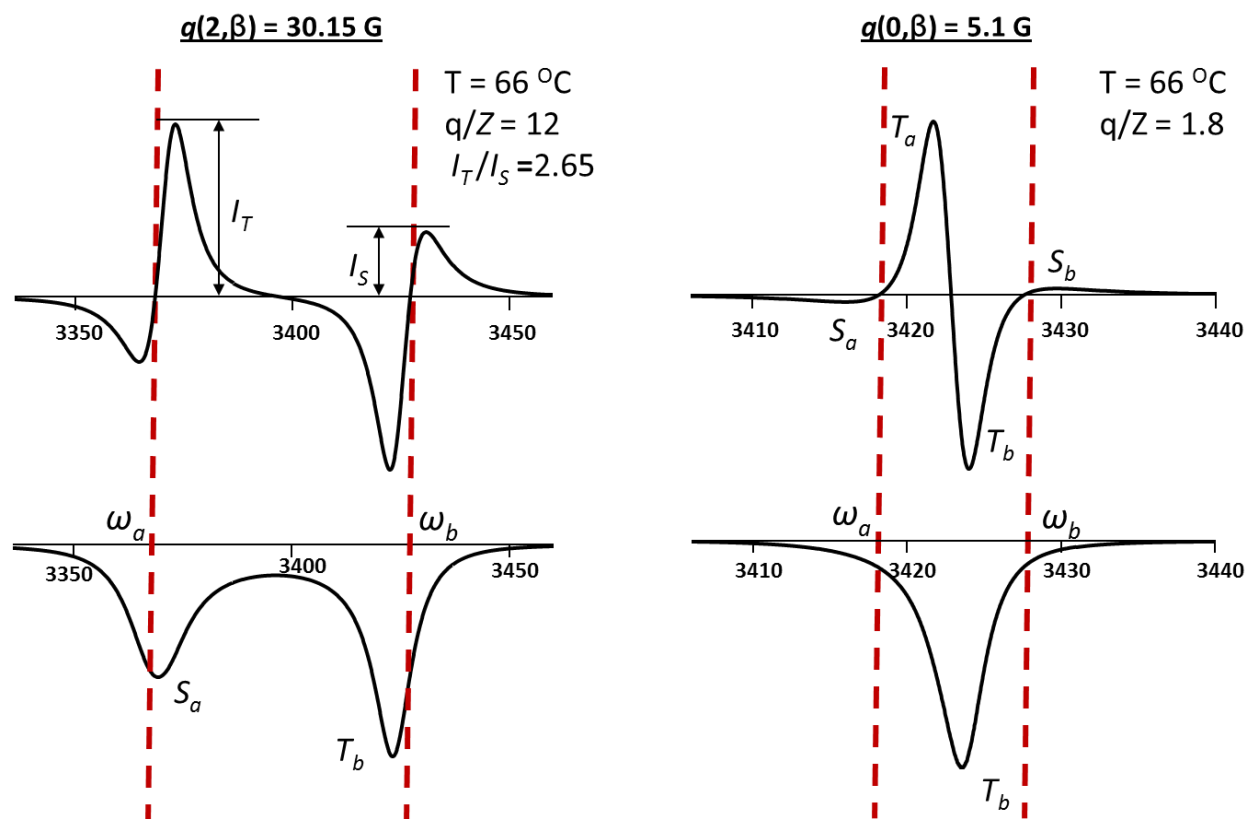
Figure 2.13 The spectral decomposition of the APS line shape for the SDS-BP radical pair at 66 °C and two different values of q. The configuration of the nuclear spin states for each value of q are specified at the top, and correspond to the assignment of the transitions in Figure 2.2. The model calculations (top) are for a triplet born SCRP with equal population of all three triplet sublevels. The bottom spectra are a spectra decomposition showing only the contributions to the APS originating from the T_+ state. Model parameters for the spectral decomposition were taken from solutions to the SLE presented in Table 2.3. The dotted lines represent the resonant frequencies of the free surfactant radical (ω_a) and BP ketyl (ω_b) radicals.

frequency of the APS components are clearly observed in the spectral decomposition for the radical pair at 66 °C (Figure 2.13, bottom). In fact, the frequency shifts of the S- and T-type transitions are much more pronounced at higher temperature, and a shift of the S-type transition toward the center of the spectrum can be observed even for $q = 30.15$. However, the most notable feature of the spectral decomposition in Figure 2.13 is that, for the smallest mixing value of $q = 5.1$, the components of the APS for radicals **a** and **b** converge and appear as one single transition. This occurs because the spectral shifts of the T-type transitions are close to the value of $|q|$. The overlap of the T_a and T_b components creates and "inverted APS" that appears to have an E/A instead of an A/E polarization pattern and is centered at the midpoint between the resonance frequencies of the free radicals. In fact, this spectral pattern is not true APS, since it is a superposition of two T-type transitions rather than one T-type and one S-type transition. Previous models for the SCRP predict that the S-type transitions should be observed at low and high field and shifted far away from the position of the T-type transitions. In actuality, the S-type transitions are weak due to broadening and appear near the midpoint frequency as the "wings" of the inverted APS signal.

The overall width of the spectral components is greater at higher temperatures (Figure 2.13, 66 °C) than those at lower temperature (Fig 2.12, 16 °C). This broadening is due to an increase in the rate of exchange interaction induced spin relaxation with increasing temperature. The product of the efficiency of the spin exchange, which is inversely proportional to D, and the frequency of enforced reencounters, which is proportional to D, is independent of changes to the diffusion coefficient. Therefore, this increase in exchange-induced relaxation cannot be due to changes in the diffusion coefficient. Instead, the decrease in the value of L with increasing temperature is responsible for this additional broadening by increasing the fraction of time that the radicals spend in regions where the exchange interaction can be felt. This increases the overall efficiency of the

spin exchange process, which is observed through this additional broadening of the EPR transitions.

For all values of the mixing parameter, the S-type components of the APS are broader than their corresponding T-type components. Also, under most conditions, the frequency of the individual components of the APS originating from the $|T_+\rangle$ state are observed to shift toward the midpoint of the resonant frequencies of the free radicals. The extensive details and a mathematical description of the predictions of the two-site model for the spectral shifts and line widths of the components of the APS are given elsewhere, but in general, these effects may be attributed TO differences in the rate of site exchange between contact and free, and S-type and T-type states. As a result, the analysis of the spectral decomposition of the APS in terms of the two-site model is able to reproduces all of the observed features of the experimental spectra of SCRPs, including the frequency shifts of the components of the APS, broadening of the individual components of the APS as a function of both the type of transition and the value of q, and the overall temperature dependence of the observation of APS.

2.4 Conclusions and Future Directions

Figure 2.10 and 2.11 show that, despite essential simplifications, numerical solutions of the SLE using the microreactor model are capable of reproducing the key features of the experimental spectra over a wide range of temperatures.[11] These features include 1) increased broadening of the APS components with an increase in temperature, 2) strong asymmetry in the APS line shape, 3) narrowing of the ketyl radical signal with increased temperature, and 4) narrowing of the line widths of the escaped alkyl radicals with increased temperature. As discussed above, the parameters that were varied to achieve the best fit (Table 2.3) are in reasonable

agreement with data available from other experimental techniques. These successful simulation results demonstrate that the asymmetry of the APS cannot be explained without taking into account the diffusion of the radicals in the micellar phase, with the most important parameters being the efficiency of Heisenberg exchange per each encounter and the rate of forced radical reencounters as a function of the mixing term q. The temperature dependence of the micelle properties and its effect on the inter-radical diffusion of the RP are responsible for the substantial variation observed in the shape of the APS, and the microreactor model is presently the only model that is able to directly and precisely account for the observed temperature dependence in the TREPR of micellized SCRPs. Furthermore, spectral decomposition of the APS components using the two-site model reveals that the interplay between different line widths and the spectral shifts of the triplet and singlet components of the APS is the main cause of the asymmetric APS line shape.[13] These simulations represent the most sophisticated quantitative treatment of the micellized RP to date, and a significant step forward in understanding the physical origin of the APS line shape. Given how well this model performs in terms of matching independent, experimental measurements to the parameters varied in the spectral fitting, future work will seek to apply this model to additional micelle systems, including those presented in subsequent chapters

2.5 Experimental

SDS was obtained from Aldrich and purified by repeated recrystallization from 80:20 ethanol:ether. Benzophenone was obtained from Aldrich with the highest grade available and used as received. Samples were prepared in MilliQ water at a concentration of 0.1 M SDS and a benzophenone concentration of approximately 2 mM. Excitation of the BP was accomplished with a 308 nm LPX 100i excimer laser (Lambda Physik) at a repetition rate of 60 Hz. Samples were

flowed through a quartz flat cell with a path length of 0.6 mm centered in a rectangular TE_{103} optical cavity, and temperature was controlled by flowing the samples through a copper coil wrapped in heating tape, with temperature controlled and monitored by a thermocouple positioned just before and just after the flat cell. TREPR spectra were collected with a sweep width of 150G, a scan time of 2 minutes, and a boxcar gate width of 100 ns at a microwave frequency of approximately 9.45 GHz and power of 5 mW. TREPR transitions below the baseline represent emission while transitions above the baseline represent absorption.

REFERENCES

1.	Forbes, M. D. E.; Jarocha, L. E.; Sim, S.; Tarasov, V. F., Time-Resolved Electron Paramagnetic Resonance Spectroscopy: History, Technique, and Application to Supramolecular and Macromolecular Chemistry. In *Advances in Physical Organic Chemistry, Vol 47*, Williams, I. H.; Williams, N. H., Eds. 2013; Vol. 47, pp 1-83.

2.	(a) Manju, T.; Manoj, N.; Gejo, J. L.; Braun, A. M.; Oliveros, E., Micellar control of the photooxidation pathways of 10-methyl phenothiazine: electron versus energy transfer mechanisms. *Photochem. Photobiol. Sci.* **2014,** *13* (2), 281-292; (b) McCaffrey, V. P.; Forbes, M. D. E., Energy transfer studied using spin polarized free radicals. Effect of substrate structure and a comparison between micellar confinement and free solution. *Tetrahedron* **2000,** *56* (36), 6991-6997; (c) Srivastava, S.; Sharma, S. K.; Sharma, R. K., Synthesis of gold nanorods using concentrated aerosol OT in hexane and its application as catalyst for the reduction of eosin. *Colloids and Surfaces A: Physicochemical and Engineering Aspects* **2011,** *373* (1–3), 61-65; (d) Tanev, P. T.; Pinnavaia, T. J., Biomimetic assembly of porous lamellar silica molecular sieves with a vesicular particle architecture. *Supramol. Sci.* **1998,** *5* (3-4), 399-404.

3.	(a) Sakaguchi, Y.; Hayashi, H.; Murai, H.; Ihaya, Y. J., CIDEP study of the photochemical reactions of carbonyl compounds showing the external magnetic field effect in a micelle. *Chem. Phys. Lett.* **1984,** *110* (3), 275-279; (b) Sakaguchi, Y.; Hayashi, H.; Murai, H.; Ihaya, Y. J.; Mochida, K., CIDEP study of the formation of a cyclohexadienyl type radical in the hydrogen abstraction reactions of triplet xanthone *Chem. Phys. Lett.* **1985,** *120* (4-5), 401-405; (c) Murai, H.; Sakaguchi, Y.; Hayashi, H.; Ihaya, Y. J., An anomalous phase effect in the individual hyperfine lines of the CIDEP spectra observed in the photochemical reactions of benzophenone in micelles *J. Phys. Chem.* **1986,** *90* (1), 113-118.

4.	(a) Closs, G. L.; Forbes, M. D. E.; Norris, J. R., Spin-polarized electron paramagnetic resonance spectra of radical pairs in micelles - observation of electron spin-spin interactions *J. Phys. Chem.* **1987,** *91* (13), 3592-3599; (b) Buckley, C. D.; Hunter, D. A.; Hore, P. J.; McLauchlan, K. A., Electron spin resonance of spin-correlated radical pairs *Chem. Phys. Lett.* **1987,** *135* (3), 307-312.

5.	Shushin, A. I., Diffusion theory of CIDEP spectra of spin-correlated radical pairs *Chem. Phys. Lett.* **1991,** *177* (3), 338-344.

6.	Wu, C. H.; Jenks, W. S.; Koptyug, I. V.; Ghatlia, N. D.; Lipson, M.; Tarasov, V. F.; Turro, N. J., Time-resolved ESR examination of a simple supramolecular guest-host system - electron spin exchange interaction in micellized spin-correlated radical pairs *J. Am. Chem. Soc.* **1993,** *115* (21), 9583-9595.

7.	Akiyama, K.; Tero-Kubota, S., One- and two-dimensional EPR studies on the radical pair generated by the photoreduction of 9,10-anthraquinone-1,5-disulfonate in aerosol OT reverse micelles. *J. Phys. Chem. B* **2002,** *106* (9), 2398-2403.

8.	(a) Closs, G. L.; Forbes, M. D. E., EPR spectroscopy of electron spin polarized biradicals in liquid solutions - technique, spectral simulation, scope, and limitations *J. Phys. Chem.* **1991,** *95* (5), 1924-1933; (b) Forbes, M. D. E., Effect of p-system spacers on exchange couplings and end to end encounter rates in flexible biradicals *J. Phys. Chem.* **1993,** *97* (13), 3396-3400; (c) Forbes, M. D. E., Effect of localized unsaturation on the scalar exchange couplilng in flexible biradicals *J. Phys. Chem.* **1993,** *97* (13), 3390-3395; (d) Forbes, M. D. E.; Bhagat, K., Quantitative EPR measurement of long distance electronic interactions in 2 geometric isomers of an unsaturated biradical *J. Am. Chem. Soc.* **1993,** *115* (8), 3382-3383; (e) Closs, G. L.; Forbes, M. D. E.; Piotrowiak, P., Spin and reaction dynamics in flexible polymethylene biradicals as studied by EPR, NMR, and optical spectroscopy and magnetic field effects - measurements and mechanism of scalar electron spin-spin coupling *J. Am. Chem. Soc.* **1992,** *114* (9), 3285-3294; (f) Koptyug, I. V.; Ghatlia, N. D.; Turro, N. J.; Jenks, W. S., Determining the hyperfine splittings of biradical termini by combining biradical trapping and time resolved ESR techniques. *J. Phys. Chem.* **1993,** *97* (28), 7247-7252.

9.	(a) Angerhofer, A.; Bittl, R., Radicals and radical pairs in photosynthesis. *Photochem. Photobiol.* **1996,** *63* (1), 11-38; (b) Levanon, H.; Mobius, K., Advanced EPR spectroscopy on electron transfer processes in photosynthesis and biomimetic model systems. *Annu. Rev. Biophys. Biomol. Struct.* **1997,** *26*, 495-540.

10.   Tarasov, V. F.; Forbes, M. D. E., Time resolved electron spin resonance of spin-correlated micelle confined radical pairs - Shape of the anti-phase structure. *Spectroc. Acta Pt. A-Molec. Biomolec. Spectr.* **2000,** *56* (2), 245-263.

11.   Tarasov, V. F.; Jarocha, L. E.; Avdievich, N. I.; Forbes, M. D. E., TREPR spectra of micelle-confined spin-correlated radical pairs: I. Molecular motion and simulations. *Photochem. Photobiol. Sci.* **2014,** *13* (2), 439-453.

12.   (a) Shkrob, I. A.; Tarasov, V. F.; Bagryanskaya, E. G., Electron spin exchange in micellized radical pairs 1. C-13 low field chemically induced dynamic nuclear polarization (CIDNP) and C-13 radio frequency stimulated nuclear polarization (SNP)

Chem. Phys. **1991,** *153* (3), 427-441; (b) Tarasov, V. F.; Ghatlia, N. D.; Buchachenko, A. L.; Turro, N. J., Probing the exchange interaction through micelle size 1. Probability of recombination of triplet geminate radical pairs *J. Am. Chem. Soc.* **1992,** *114* (24), 9517-9526.

13.   Tarasov, V. F.; Jarocha, L. E.; Forbes, M. D. E., TREPR spectra of micelle-confined spin-correlated radical pairs: II. Spectral decomposition and asymmetric line shapes. *Photochem. Photobiol. Sci.* **2014,** *13* (2), 454-463.

14.   (a) Tarasov, V. F.; Yashiro, H.; Maeda, K.; Azumi, T.; Shkrob, I. A., Time-resolved ESR in a spin-correlated radical pair with large hyperfine coupling constant at P-31. Micellar size effects and the role of flip-flop transitions. *Chem. Phys.* **1998,** *226* (3), 253-269; (b) Tarasov, V. F.; Yashiro, H.; Maeda, K.; Azumi, T.; Shkrob, I. A., Spin-correlated radical pairs in micellar systems: Mechanism of CIDEP and the micelle size dependence. *Chem. Phys.* **1996,** *212* (2-3), 353-361.

15.   Hartley, G. S., *Aqueous solutions of paraffin-chain salts; a study in micelle formation*. Hermann & cie: Paris, 1936.

16.   Zana, R.; Yiv, S.; Strazielle, C.; Lianos, P., Effects of alcohol on the properties of micellar systems 1. critical micellization concentration, micelle molecular weight and ionization degree, and solubility of alcohols in micellar solutions *J. Colloid Interface Sci.* **1981,** *80* (1), 208-223.

17.   Zana, R., Micellization of amphiphiles: Selected aspects. *Colloid Surf. A-Physicochem. Eng. Asp.* **1997,** *123*, 27-35.

18.   Menger, F. M.; Doll, D. W., On the structure of micelles *J. Am. Chem. Soc.* **1984,** *106* (4), 1109-1113.

19.   Menger, F. M., Structure of micelles *Accounts Chem. Res.* **1979,** *12* (4), 111-114.

20.   Menger, F. M.; Jerkunica, J. M.; Johnston, J. C., Water concent of a micelle interior - Fjord vs Reef models. *J. Am. Chem. Soc.* **1978,** *100* (15), 4676-4678.

21.   Holland, P. M.; Rubingh, D. N., Mixed surfactant systems - an overview *ACS Symp. Ser.* **1992,** *501*, 2-30.

22.   Bruce, C. D.; Berkowitz, M. L.; Perera, L.; Forbes, M. D. E., Molecular dynamics simulation of sodium dodecyl sulfate micelle in water: Micellar structural characteristics and counterion distribution. *J. Phys. Chem. B* **2002,** *106* (15), 3788-3793.

23.   Langevin, D., Micelles and Microemulsions. *Annu. Rev. Phys. Chem.* **1992,** *43* (1), 341-369.

24.   Mandal, A. B.; Nair, B. U.; Ramaswamy, D., Determination of the critical micelle concentration of surfactants and the partition coefficient of an electrochemical probe by using cyclic voltammetry. *Langmuir* **1988,** *4* (3), 736-739.

25.   (a) Griffiths, P. C.; Paul, A.; Heenan, R. K.; Penfold, J.; Ranganathan, R.; Bales, B. L., Role of counterion concentration in determining micelle aggregation: Evaluation of the combination of constraints from small-angle neutron scattering, electron paramagnetic resonance, and time-resolved fluorescence quenching. *J. Phys. Chem. B* **2004,** *108* (12), 3810-3816; (b) Lebedeva, N. V.; Shahine, A.; Bales, B. L., Aggregation number-based degrees of counterion dissociation in sodium n-alkyl sulfate micelles. *J. Phys. Chem. B* **2005,** *109* (42), 19806-19816.

26.   Bales, B. L., A definition of the degree of ionization of a micelle based on its aggregation number. *J. Phys. Chem. B* **2001,** *105* (29), 6798-6804.

27.   (a) Prevost, S.; Gradzielski, M., SANS investigation of the microstructures in catanionic mixtures of SDS/DTAC and the effect of various added salts. *J. Colloid Interface Sci.* **2009,** *337* (2), 472-484; (b) Malliaris, A.; Lemoigne, J.; Sturm, J.; Zana, R., Temperature dependence of the micelle aggregation number and rate of intramicellar excimer formation in aqueous surfactant solutions *J. Phys. Chem.* **1985,** *89* (12), 2709-2713; (c) Bezzobotnov, V. Y.; Borbely, S.; Cser, L.; Farago, B.; Gladkih, I. A.; Ostanevich, Y. M.; Vass, S., Temperature and Concentration Dependence of Properties of Sodium Dodecyl Sulfate Micelles Determined from Small Angle Neutron Scattering Experiments. *The Journal of Physical Chemistry* **1988,** *92* (20), 5738-5743.

28.   Wang, Z. W.; Larson, R. G., Molecular Dynamics Simulations of Threadlike Cetyltrimethylammonium Chloride Micelles: Effects of Sodium Chloride and Sodium Salicylate Salts. *J. Phys. Chem. B* **2009,** *113* (42), 13697-13710.

29.   (a) Closs, G. L.; Forbes, M. D. E.; Norris, J. R., Spin polarized electron paramagnetic resonance spectra of radical pairs in micelles - observation of electron spin-spin interactions INTERACTIONS. *J. Phys. Chem.* **1987,** *91* (13), 3592-3599; (b) Breslow, R.; Kitabatake, S.; Rothbard, J., Photoreactions of charged benzophenone with ampiphiles in micelles and multicomponent aggregates as conformational probes *J. Am. Chem. Soc.* **1978,** *100* (26), 8156-8160; (c) Scaiano, J. C.; Abuin, E. B.; Stewart, L. C., Photochemistry of benzophenone in micelles - formation and decay of radical pairs. *J. Am. Chem. Soc.* **1982,** *104* (21), 5673-5679; (d) Scaiano, J. C.; Lougnot, D. J., Electrostatic and magnetic field effects on the behavior of radical pairs derived from ionic benzophenones *J. Phys. Chem.* **1984,** *88* (15), 3379-3382; (e) Turro, N. J.; Gratzel, M.; Braun, A. M., Photophysical and photochemical processes in micellar systems *Angewandte Chemie-International Edition in English* **1980,** *19* (9), 675-696.

30.   Caregnato, P.; Jarocha, L. E.; Esinhart, H. S.; Lebedeva, N. V.; Tarasov, V. F.; Forbes, M. D. E., Electrostatic Control of Spin Exchange Between Mobile Spin-Correlated Radical Pairs Created in Micellar Solutions. *Langmuir* **2011,** *27* (9), 5304-5309.

31.   Hewgill, F.; Proudfoot, G., An E.S.R study of the oxidation of sodium alkyl sulphates by hydroxyl radicals. *Aust. J. Chem.* **1977,** *30* (3), 695-697.

32.   (a) Shushin, A. I., Electron spin polarization in radical pair recombination in micelles - cage and supercage models. *J. Chem. Phys.* **1994,** *101* (10), 8747-8755; (b) Pedersen, J. B.; Jorgensen, J. S., High-field supercage model for radical pair reactions in micelles. *J. Phys. Chem. A* **1997,** *101* (4), 566-571.

33.   Trifunac, A. D.; Nelson, D. J., Chemically induced dynamic electron polarization - pulse radiolysis of aques solutions of micelles *Chem. Phys. Lett.* **1977,** *46* (2), 346-348.

34.   Sakaguchi, Y.; Hayashi, H.; Murai, H.; Ihaya, Y. J.; Mochida, K., CIDEP study of the formation of cyclohexadienyl type radical in the hydrogen abstraction reactions of triplet xanthone *Chem. Phys. Lett.* **1985,** *120* (4-5), 401-405.

35.   Tarasov, V.; Jarocha, L. E.; Avdievich, N. I.; Forbes, M. D. E., TREPR Spectra of Micelle-Confined Spin-correlated Radical Pairs I. Molecular Motion and Simulations. *Photochem. Photobiol. Sci.* **2013**.

36.   (a) Tarasov, V. F.; Ghatlia, N. D.; Buchachenko, A. L.; Turro, N. J., Probing the exchange interaction through micelle size. 1. probability of recombination of triplet geminate radical pairs *J. Am. Chem. Soc.* **1992,** *114* (24), 9517-9526; (b) Shkrob, I. A.; Tarasov, V. F.; Bagryanskaya, E. G., Electron spin exchange in micellized radical pairs. 1. ^{13}C low field chemically induced dynamic nuclear polarization (CIDNP) and ^{13}C radio frequency stimulated nuclear polarization (SNP) *Chem. Phys.* **1991,** *153* (3), 427-441.

37.   White, R. C.; Tarasov, V. F.; Forbes, M. D. E., Photooxidation of diglycine in confined media. Application of the microreactor model for spin-correlated radical pairs in reverse micelles and water-in-oil microemulsions. *Langmuir* **2005,** *21* (7), 2721-2727.

38.   (a) Shushin, A. I., The effect of spin relaxation on ESR spectra of spin-correlated radical pairs. *Chem. Phys. Lett.* **1997,** *275* (3-4), 137-144; (b) Pedersen, J. B.; Shushin, A. I.; Jorgensen, J. S., Magnetic field dependent yield of

geminate radical pair recombination in micelles - test of the Johnson-Merrifield approximation *Chem. Phys.* **1994,** *189* (3), 479-487; (c) Purtov, P. A.; Doktorov, A. B.; Popov, A. V., The green function method in the theory of nuclear and electron spin polarization 2. The first approximation and its applications in the CIDEP theory *Chem. Phys.* **1994,** *182* (2-3), 149-166; (d) Popov, A. V.; Purtov, P. A., Calculations of chemically induced nuclear polarization in molecular systems occupying a limited volume. *Chemical Physics Reports* **1997,** *16* (1), 27-43.

39.   Terazima, M.; Maeda, K.; Azumi, T.; Tanimoto, Y.; Okada, N.; Itoh, M., CIDEP studies on the intramolecular hydrogen abstraction reaction of polymethylene linked systems- population relaxation between the ST_0 mixed states *Chem. Phys. Lett.* **1989,** *164* (5), 562-566.

40.   Pedersen, J. B.; Freed, J. H., Theory of chemically induced dynamic electron polarization. II. *The Journal of Chemical Physics* **1973,** *59* (6), 2869-2885.

41.   Bezzobotnoy, V. Y.; Borbely, S.; Cser, L.; Farago, B.; Gladkih, I. A.; Ostanevich, Y. M.; Vass, S., Temperature and concentration dependence of properties of sodiumdodecyl sulfate micelles determined from small angle neutron scattering experiments *J. Phys. Chem.* **1988,** *92* (20), 5738-5743.

42.   In *Landolt-Bornstein-Organic Carbon Centered Radicals*, Springer: Berlin, 1977; Vol. 1, part b, p 127.

43.   Landolt-Bornstein, *Organic C Centered Radicals*. Springer: Berlin, 1977.

44.   Hayashi, H.; Nagakura, S., Theoretical study of relaxation mechanism in magnetic field effects on chemical reactions *Bull. Chem. Soc. Jpn.* **1984,** *57* (2), 322-328.

45.   Levin, P. P.; Shafirovich, V. Y.; Kuzmin, V. A., Magnetic isotope effects on the decay kinetics of micellized triplet ketyl phenoxyl radical pairs - role of hyperfine, exchange, and dipole-dipole interactions *J. Phys. Chem.* **1992,** *96* (24), 10044-10048.

46.   (a) Formosinho, S. J.; Arnaut, L. G., A Unified View of Ketone Photochemistry. In *Advances in Photochemistry*, John Wiley & Sons, Inc.: 2007; pp 67-117; (b) Okamoto, M.; Teranishi, H., Effect of pressure on the primary process of benzophenone photoreduction *J. Am. Chem. Soc.* **1986,** *108* (20), 6378-6380.

47.   Freed, J. H.; Pedersen, J. B., The Theory of Chemically Induced Dynamic Spin Polarization. In *Advances in Magnetic and Optical Resonance*, John S, W., Ed. Academic Press: 1976; Vol. Volume 8, pp 1-84.

48.   Hochstrasser, R. M.; Lin, T. S., Magnetic and electric field spectra of organic crystals - optical measurements of zero-field splittings *J. Chem. Phys.* **1968,** *49* (11), 4929-&.

49.   Aniansson, E. A. G.; Wall, S. N.; Almgren, M.; Hoffmann, H.; Kielmann, I.; Ulbricht, W.; Zana, R.; Lang, J.; Tondre, C., Theyr of kinetics of micellar equilibriu and quantitative interpretation of chemical relaxation studies of micellar solutions of ionic surfactants *J. Phys. Chem.* **1976,** *80* (9), 905-922.

CHAPTER 3: Electrostatic and Hydrophobic Effects in the TREPR of Ionic Surfactants

3.1 Introduction

Ionic surfactants are widely used in industrial and consumer applications, in chemical and materials research, and in biological and health based applications.[1] Surfactant solutions have been extensively studied in the scientific literature because of their wide usage and the fact that the behavior of a surfactants – in terms of phase, aggregation behavior, degree of hydration, size, and many other physical properties – depend significantly on their molecular structure. A chemical change as simple as a change in the surfactant counterion, for instance, can effect significant changes in the phase behavior of surfactants that are otherwise structurally identical.[2] In particular, the charge on the head group of ionic surfactants makes these surfactants particularly sensitive to environmental stimuli, such as dissolved ions in solution[3] or changes in pH.[4]

One of the most promising applications of surfactants is the solubilization of hydrophobic drug targets and the controlled release of small organic molecules from surfactant-based nanostructures for drug delivery applications.[5] Effective design of drug delivery systems that exhibit controlled release of solubilized molecules, whether by destruction of or diffusion out of the aggregate, requires a detailed understanding of concentration behavior, phase and aggregation characteristics, and environmental response of the surfactants employed.[5b, 6] An additional concern with the use of ionic surfactants for such applications is the effect of electrostatic charge on diffusion in the interior of the aggregates formed.[7] This may be particularly important in a biological environment, since natural phospholipids and solubilized proteins in cell membranes

are also ionic and could be subject to electrostatic interactions with ionic surfactants used in drug delivery applications. [4b,8]

SSEPR[9] and TREPR[7a, 10] have both been used extensively to study the diffusive behavior of small organic molecules in the vicinity of or solubilized in ionic micelles. In fact, the CFN model for the origin of the APS[11] was developed specifically to explain observation of a first-derivative like signal of a RP photochemically generated in an anionic SDS micelle in 1987 .[12] The APS observed in the TREPR of the SDS – BP radical pair in micellar solutions was discussed extensively in the previous chapter.[10c, 13] This chapter will explore the interplay between electrostatic effects arising from interactions with the head group and hydrophobic effects on a series of charged anthraquinones solubilized in anionic and cationic micellar environments.

3.2 Background

The term surfactant is derived from "surface active agent."[14] Surfactant molecules are amphiphiles that have both a polar (head group) and a non-polar (tail) component that spontaneously absorb at a free surface and lower the surface tension when dissolved in water. Although not a universal feature of surfactants, many will form aggregate structures known as micelles above a certain concentration, also known as the critical micelle concentration (CMC). The number of monomers incorporated into a micelle is referred to as the aggregation number, N_{agg}. Its value varies strongly with surfactant concentration, or with environmental conditions such as salt concentration[3a, 15] or temperature.[9b, 9c, 16] The shape of the micellar aggregate is dictated, fundamentally, by the ratio between the volume occupied by the head group and the tail.[14] The radius of a spherical micellar aggregate generally does not exceed the length of the surfactant tail. Disk like micelles,[17] cylindrical[18] and thread or worm like micelles[3b], and vesicles[19] or

bilayers[20] can also form. Because the shape of the micelle is fundamentally dictated by the effective volume of the polar and nonpolar portions of the amphiphile, the addition of salts or aromatic molecules has been shown to induce phase and shape changes in micelles by screening the electrostatic repulsion between charged head groups.[3b, 14] Strong variations in phase behavior have also been observed in surfactant systems that differ only in counterion identity. For example, the phase behavior of dodecyl trimethylammonium bromide (DTAB) and dodecyl trimethylammonium chloride (DTAC), which have an identical head group and tail structure, are so different in the aqueous phase that the two surfactants cannot be considered interchangeable in applications or scientific studies.[2] As discussed briefly in Chapter 2, micelle formation and physical characteristics like size, aggregation number, shape, and phase can also be dependent on solution conditions such as temperature or pH.[4, 21] Although they appear small, these changes were substantial enough to lead to significant differences in the asymmetry of the APS and the diffusive behavior of RPs in SDS micelles.[22]

The micellization of amphiphilic molecules has been of significant interest for decades because of their wide variety of uses, particularly in personal care products and detergents, industrial products and processes,[1] and more recently – medical applications and drug delivery systems.[5b-d, 23] When employed for drug delivery purpose, ionic surfactants are commonly mixed with amphiphilic block copolymers,[24] nonionic surfactants,[25] or natural phospholipids,[26] because such mixtures have been shown to have better stability than ionic micelles under biological conditions. Pure SDS micelles, for instance, are known to disperse into cell membranes or tissue and have been shown to be effective in the dissolution of phosphatidylcholine based liposomes.[27] While these properties may be desirable to facilitate the entry of a target molecule into a liposome or cellular environment for a therapeutic treatment, this process is fast and ionic micelles do not

last long in biological conditions. However, the simplicity of ionic micelles, the hydrophobic properties of micelle aggregates, and electrostatic effects due to head group charge of ionic surfactants have made anionic surfactants like SDS and cationic surfactants like cetyl trimethylammonium chloride (CTAC) or DTAC useful as model systems for understanding the influence of micellization on drug interactions, solubilization, and diffusion. Recent studies employing ionic surfactants for drug delivery applications have focused on understanding the effects of structure on the aggregation behavior and singlet oxygen production of hydrophobic photosensitizers in the micellar environment,[28] characterizing changes in aggregate phase, interaction enthalpies, and drug release kinetics in mixtures of ionic drug targets and surfactants[29] and utilizing electrostatic interactions of micelles with charged polymers or hydrophobic interactions with uncharged polymers to immobilize and later trigger the controlled release of micelles and vesicles.[5b, 30]

This chapter will focus on the TREPR of radical pairs which have been photochemically generated in solutions of three common ionic surfactants: anionic SDS, cationic DTAC, and cationic CTAC. SDS is one of the most commonly used surfactants in consumer, industrial, and research applications. DTAC shares the same alkyl tail as SDS, but the quaternary ammonium head group occupies a larger volume and is of opposite charge.[31] Quaternary ammonium salts have been explored for possible drug delivery applications, but primarily in mixed surfactant solutions due to the toxicity of these surfactants.[32] CTAC has been extensively studied in the literature because it exhibits strong changes in micelle structure as a function of solution conditions, particularly counterions concentration and identity.[3b, 33]

In addition to these three surfactants, the TREPR of one zwitterionic surfactant – Zwittergent 3-12 – is included for a qualitative comparison. This surfactant is interesting to

Table 3.1. Physical Properties of Ionic surfactants

Surfactant	CMC (mM)	N_{agg}	Size (nm)
SDS	8.2	62	1.8
DTAC	20.3	48	1.5
CTAC	1.6	100	2.5
Zwittergent 3-12	3.6	55	2.4

examine in relation to the anionic and cationic surfactants presented above because the head group consists of a quaternary ammonium group separated from a sulfonate group by only three carbons. The surfactant tail is a twelve carbon alkyl chain identical to the tail of SDS or DTAC. In terms of physical properties like size, however, Zwittergent 3-12 forms micellar aggregates of a similar size to CTAC.[34] Although they are not direct structural analogues, such zwitterionic surfactants bear important similarities to biologically relevant, zwitterionic phospholipids.

As discussed in the previous chapter, the SDS micellar system has been extensively characterized using a wide variety of experimental techniques, including both SSEPR and TREPR. The SSEPR of quaternary ammonium based surfactants has been explored in considerable detail by Bales and coworkers[9c] – who used these surfactants as model systems to explore changes in aggregation number and differences in dynamic rotational information of doxyl-stearic acid based spin probes in the micellar environment. The TREPR of the quaternary ammonium surfactants DTAC and CTAC have not previously been studied by TREPR, with the first qualitative description of the DTAC TREPR spectrum in relation to the SDS spectra published only recently.[7a] The SSEPR and TREPR of Zwittergent surfactants have not been extensively studied relative to the analogous ionic surfactants. For all the surfactants discussed here, the TREPR spectra is observed by photochemically generating a RP through a hydrogen atom abstraction reaction similar to the one discussed in Chapter 2. In this chapter, a series of anthraquinone based

Scheme 3.1

CTAC

DTAC

SDS

Zwittergent 3-12

AQ; $R_1 = R_2 = H$
AQS; $R_1 = H, R_2 = SO_3^-$
AQDS; $R_1 = R_2 = SO_3^-$
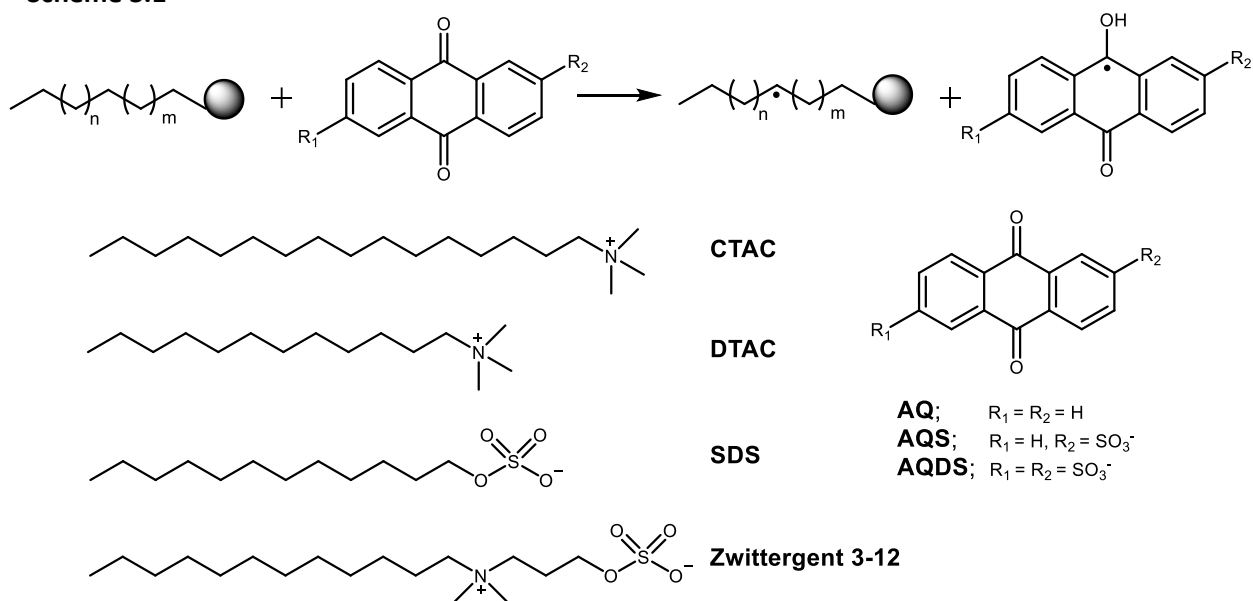
photosensitizers (Scheme 3.1) are employed in place of benzophenone. The anthraquinones vary in electrostatic charge, from the neutral 9,10-anthraquinone (AQ), the singly charged 9,10-anthraquinone-2-sulfonate sodium salt (AQS), and the doubly charged 9,10-anthraquinone-2,6-disulfonate disodium salt (AQDS). This variation allows us to examine the effect of electrostatic repulsion and attraction on the TREPR of RPs in ionic micelles. Although less well characterized than the BP sensitizer, anthraquinones have been used extensively to study reverse micelles,[35] micelles,[7a] and liposomes[36] by TREPR.

Valuable information about the diffusion of both neutral and charged small organic molecules in solutions of ionic surfactants can be obtained by simulating the TREPR spectra of these RPs. Such information is of particularly importance in applications that rely on the solubilization and diffusion of RPs in micelles, such as studies of magnetic field effects where micelles are used to enhance the MFE by altering radical recombination[37] or isotope separations and enrichment of photochemical products.[38] A systematic study of structurally related sensitizers, such as the one presented here, also provides valuable information about how hydrophobicity and charge affect the diffusive motion of small molecules in micellar solutions. Such information could be critical to making appropriate design choices in other applications, such as surfactant-based drug delivery systems where solubilization of hydrophobic drug targets and diffusion out of the aggregate structure are critical to performance.

3.3 Results and Discussion

3.3.1 Electrostatic effects in the TREPR of Ionic Micelles

Figure 3.1 shows the TREPR spectrum acquired after a 308 nm excimer laser flash in an aqueous solution of SDS, DTAC, or CTAC and the AQDS sensitizer. The central line in all three
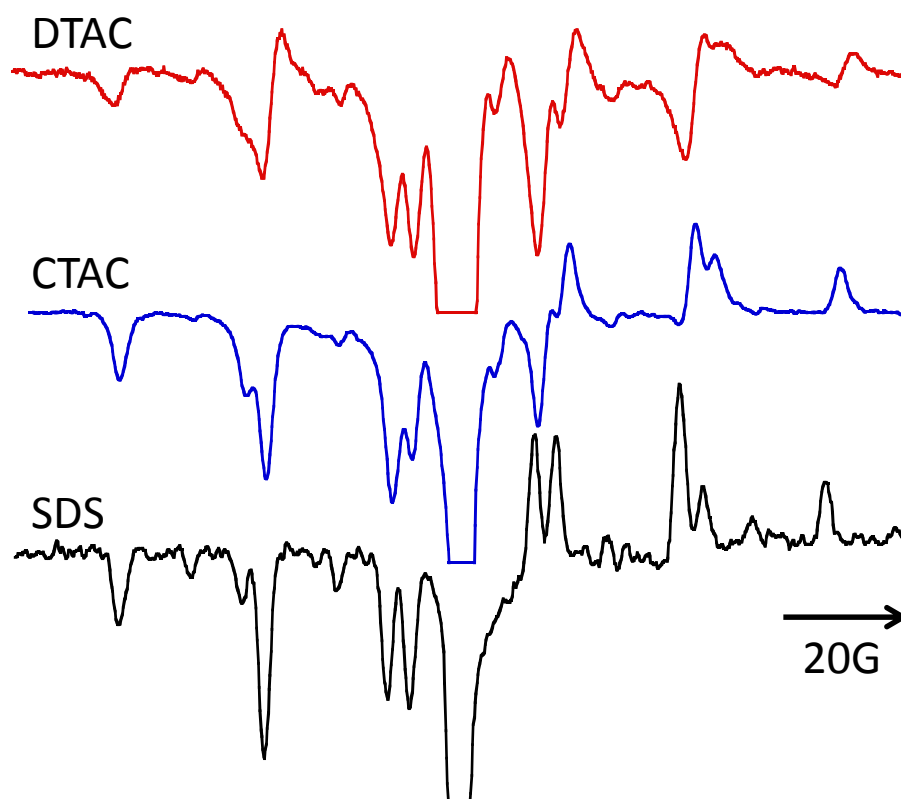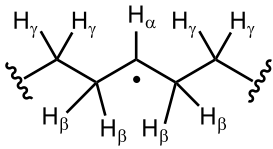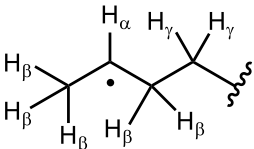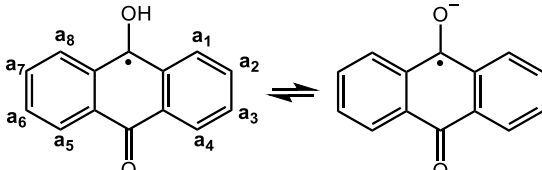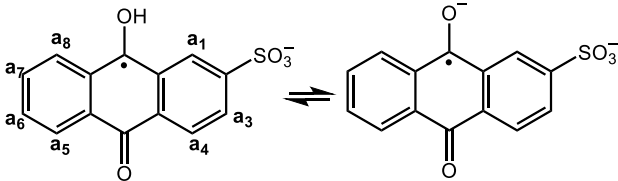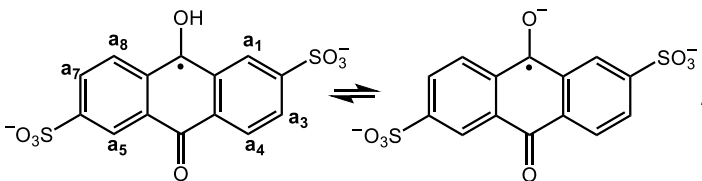
Figure 3.1: X-band TREPR spectra acquired 500 ns after a 308 nm laser flash in aqueous solutions of 50 mM DTAC (top), CTAC (middle), and SDS (bottom) with 1.1 mM AQDS. The central line in the spectrum is due to the AQDS radical and has been cut off to vertically expand the signal of the surfactant alkyl radicals.

Table 3.2 Hyperfine coupling constants for surfactant alkyl radicals and anthraquinone sensitizer radicals employed in simulations of the TREPR spectra using the microreactor model

Radical Structure	Parent molecule	Hyperfine parameters[39]
radical *a*	SDS DTAC CTAC	$a(H_\alpha) = 20.6$ G $a(H_\beta) = 24.9$ G $a(H_\gamma) = 0.7$ G
radical *a'*	SDS DTAC CTAC	$a(H_\alpha) = 20.4$ G $a(H_\beta) = 24.4$ G $a(H_\gamma) = 24.4$ G
radical *b*	AQ	$a(4H; 1,3,6,8) = .0591$ G $a(2H; 2,7) = 2.762$ G $a(2H; 4,5) = 2.406$ G $a(OH) = 0.531$ G pKa = 3.9 $a(4H; 1,4,5,8) = 0.98$ G $a(4H; 2,3,6,7) = 0.492$ G
radical *b*	AQS	pKa = 3.2 $a(H; 1) = 0.25$ G $a(H; 3) = 1.23$ G $a(H; 4) = 0.5$ G $a(H; 5) = 0.75$ G $a(H; 6) = 0.78$ G $a(H; 7) = 0.94$ G $a(H; 8) = 0.63$ G
radical *b*	AQDS	pKa = 3.2 $a(2H; 1,5) = 0.363$ G $a(2H; 3,7) = 1.242$ G $A(2H, 4,8) = 0.433$ G

spectra is due to the AQDS semianthraquinone radical, which deprotonates in solution to form the anthraquinone radical anion. The sensitizer radicals have very small hyperfine interactions (Table 3.2) that are unresolved under the conditions of the experiments discussed here and, therefore, observed as a single intense transition. In Figure 3.1, the signal from the AQDS radical is cut off to allow for better visualization of the features of the surfactant alkyl radicals. The remaining lines in the spectrum can be assigned to two possible secondary alkyl radicals, where the hydrogen atom abstraction takes place at either the penultimate carbon of the alkyl tail of the surfactant (radical **a2**), or any other position along the alkyl chain (radical **a**). Abstraction from the terminal CH_3 group of the alkyl tail or the CH_2 group adjacent to the head group are both energetically disfavored, and these radicals are not observed. The two possible alkyl radicals **a** and **a2** appear in a statistically expected ratio in the TREPR that corresponds directly with the difference in the number of sites available for hydrogen atom abstraction leading to these radicals. The details of the hyperfine interactions of each radical were discussed thoroughly in Chapter 2 for the SDS alkyl radicals created after hydrogen atom abstraction by $^3BP^*$. The fundamental structure of the alkyl radicals and the relevant hyperfine splitting along the alkyl chain are identical when either BP or anthraquinone (AQ) is employed as the triplet sensitizer.

The effects of electrostatic interactions on the appearance of the TREPR spectra in Figure 3.1 are evident from the appearance or absence of APS splitting. Strong electrostatic attraction between the anionic sensitizer and a cationic micelle can restrict the diffusion of the radicals after generation leading to the observation of a SCRP.[7a] This is evident from the strong contribution of APS to the DTAC-AQDS spectra (Figure 3.1, top), where each hyperfine transition in the EPR spectrum is split into an E/A doublet and appears to have a strongly symmetric, first derivative-like line shape.

Because of the charges on the AQDS sensitizer, it is expected to reside in the bulk water rather than in the hydrophobic interior of the micelle. In fact, AQDS is regularly employed as a triplet sensitizer in reverse micelles – where the sensitizer is confined to a water pool surrounded by surfactant molecules in a larger hydrophobic solvent – because of its high solubility in the aqueous phase.[35] Given the boundary that exists between the aqueous and micellar phase, a question that naturally arises is how an aqueous sensitizer manages to access the hydrophobic interior of the micelle to abstract hydrogen from the alkyl tails of the surfactant? In fact, the conceptual picture of the micelle as a purely hydrophobic droplet comprised of alkyl chains and shielded from the surrounding water by a hydrophilic layer created by the head groups is inaccurate. Zana[1] and Menger[40] both proposed more realistic models for the micelle in the 1980's, which have been confirmed extensively by experimental results and molecular dynamics simulations. There can also be a significant penetration of water molecules into the hydrophobic regions of the micelle,[33, 41] and there are a vast number of hydrogen atoms along the entire length of the alkyl chain of the surfactant that are accessible on the surface of the micellar aggregate at any given time.[9c, 41a, 42]

If the AQDS sensitizer exists outside of the micellar aggregate, the next question that arises from the observation of APS in the DTAC-AQDS spectra (Fig. 3.1, top) is why the APS observed at all. The SCRP mechanism of CIDEP is only operative when there is some confinement that restricts diffusion and leads to forced reencounters of the RP,[43] but in this system, the AQDS radical is in the aqueous phase exterior to the micelle while the alkyl radical exists inside a micelle structure.[7a] In fact, the strong electrostatic attraction between the opposite charges of the micelle surface and the sensitizer radical restricts the diffusion of the RP. The sensitizer radical is repeatedly drawn back toward the micelle surface, resulting in forced reencounters of the RP and
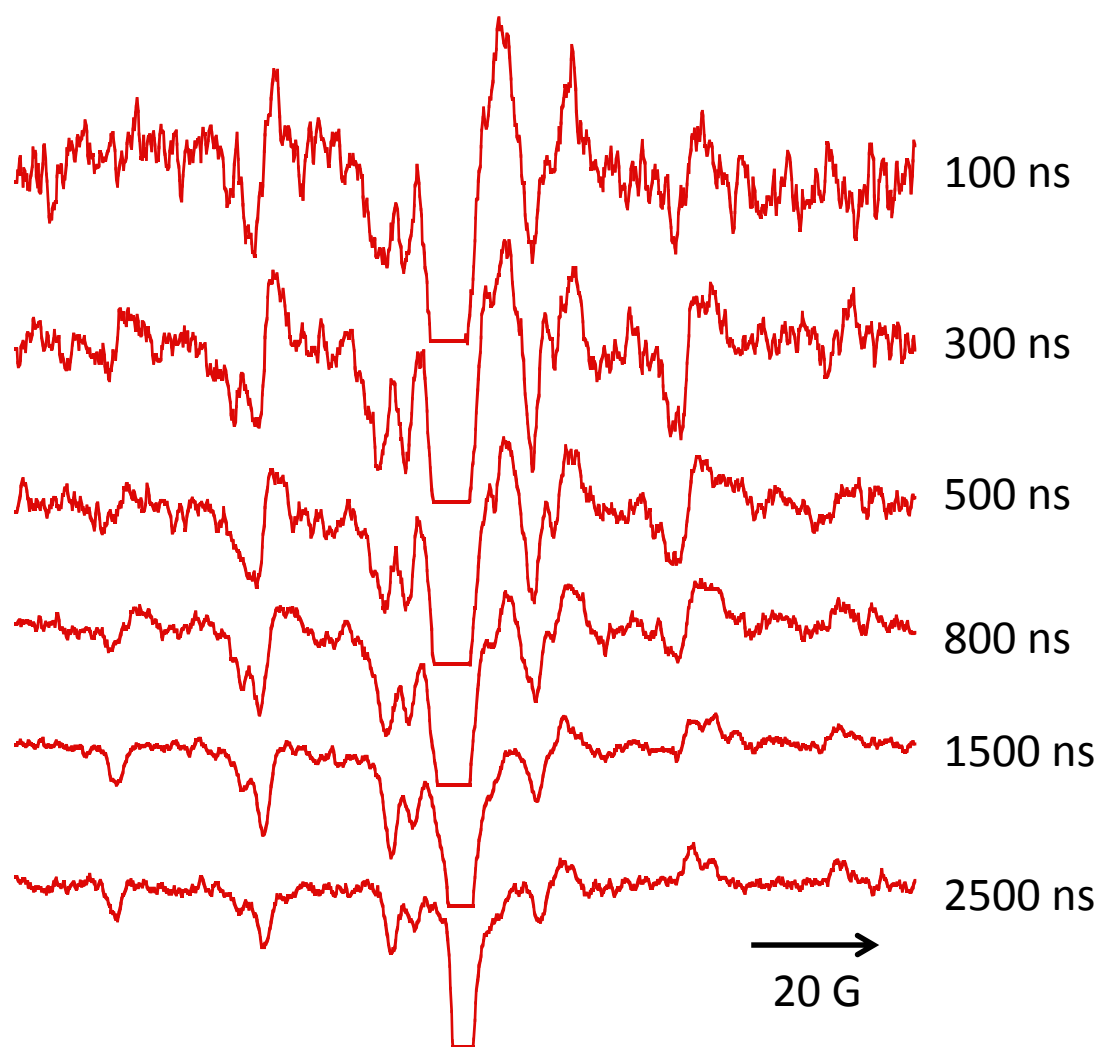
Figure 3.2: Time-dependence of the X-band TREPR spectra acquired from aqueous solutions of 50 mM DTAC and 1.1 mM AQDS after photolysis at 308 nm. The central line in the spectrum is due to the AQ radical and has been cut off to vertically expand the signal of the surfactant alkyl radicals.

the observation of spin-correlation. A time dependence of the DTAC-AQDS system is shown in Figure 3.2.. At later delay times (< 1 µs), escape radicals dominate the line shape of the TREPR spectrum and the observed polarization pattern is primarily the result of the RPM. The time dependence of the E/A splitting of the EPR transitions confirms that this polarization pattern arises from a SCRP.

An APS line shape is also observed in the TREPR spectrum of CTAC-AQDS (Figure 3.1, middle), although the shape of the APS is much more asymmetric than that of the DTAC-AQDS RP. Figure 3.3 shows the time dependence of the CTAC-AQDS system. The observation of APS in the TREPR persists for a similar amount of time to the DTAC-AQDS system in Figure 3.2, with escape radicals dominating the line shape of the spectra after approximately 1 µs in DTAC and by 0.8 µs in CTAC. CTAC and DTAC both have an identical head group structure. AQDS is also hydrophilic and expected to diffuse in the aqueous phase rather than the micelle interior, so its diffusive behavior is not likely to be changed much by the differences between the CTAC and DTAC tails. Similar diffusive behavior of AQDS in the aqueous phase of solutions of CTAC and DTAC is expected to lead to the observation of APS for both surfactants. However, the a comparison of the DTAC-AQDS and CTAC-AQDS spectra at times of 500ns (Figure 3.1) or shorter (Figure 3.3) reveals that there is a stronger low field E/high field A polarization pattern in the CTAC-AQDS spectra that is indicative of strong contributions to the spectra from escape radicals exhibiting RPM polarization. These differences can be explained by differences in the physical properties of the micelles themselves. Table 3.1 lists some important structural features of the SDS, DTAC, and CTAC micelles. In particularly, the size of the CTAC and DTAC micelles differ by almost 1 nm in diameter.[31, 34a, 34b] This gives a larger volume in which the alkyl radical is confined, resulting in a greater average distance between the two members of the RP in solutions
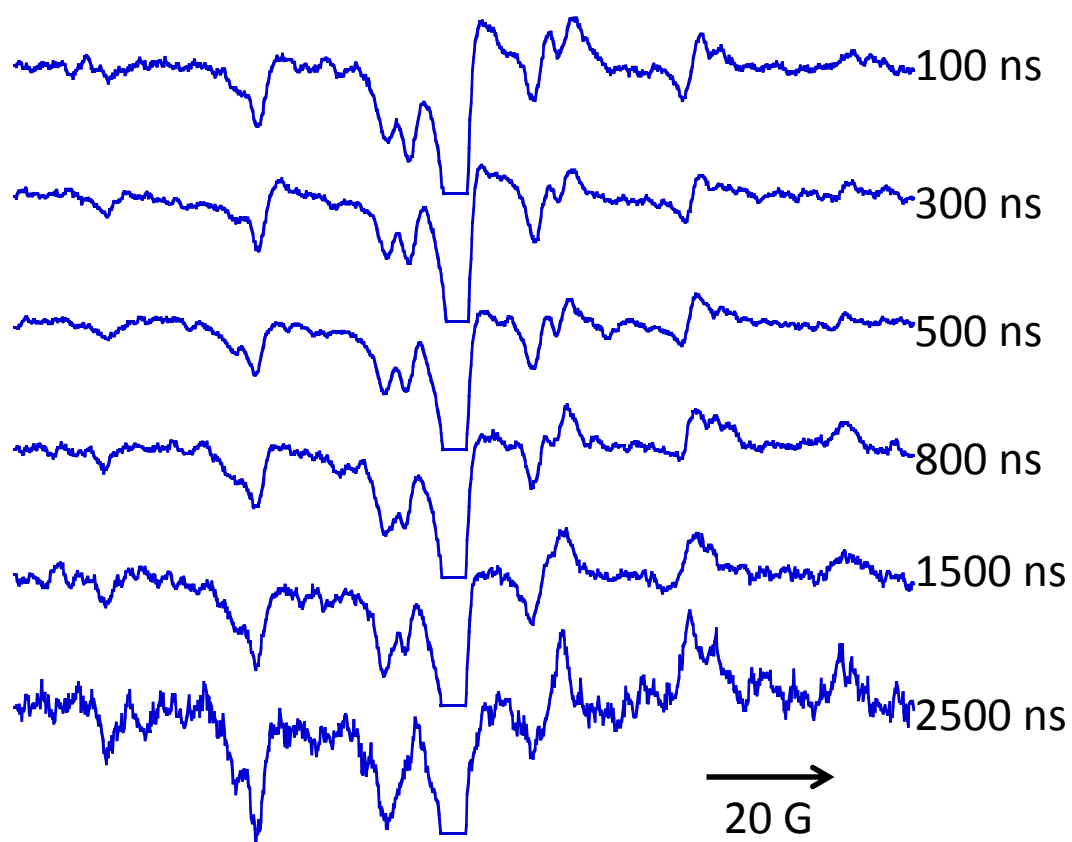
Figure 3.3: Time-dependence of the X-band TREPR spectra acquired from aqueous solutions of CTAC and 1.1 mM AQDS after photolysis at 308 nm. The central line in the spectrum is due to the AQ radical and has been cut off to vertically expand the signal of the surfactant alkyl radicals.

containing CTAC micelles. This larger available volume for diffusion likely leads to a reduced frequency of reencounters of the RP and a greater contribution of escaped radicals to the CTAC-AQDS spectra at earlier time delays.

The effect of electrostatic repulsion between the RP is exemplified by the TREPR spectra of SDS and AQDS (Figure 3.1, bottom). The TREPR spectrum consists of EPR transitions with a Lorentzian line shape and a low field emissive, high field absorptive pattern characteristic of the ST_0 RPM mechanism of CIDEP.[7a] Even at very short time delays, no contribution from the APS is observed. There is also a small contribution of net emissive TM polarization to the spectra, which is evident from the strongly emissive characteristics of the central signal from the AQDS radical and the slightly greater intensity of the high field $(-1;\beta)$ transition compared to the low field $(1;\alpha)$transition (see Figure 2.2 for the assignment of the transitions). In the SDS micelle, as soon as the RP is created, strong electrostatic repulsion between the surface of the micelle and the sensitizer radical limit the number of encounters and causes quick separation of the RP. This fast separation of the RP in SDS-AQDS micellar solutions is confirmed by spectral simulations using the microreactor model. A simulation of the SDS-AQDS spectra is shown in Figure 3.4. One unusual feature of the SDS-AQDS spectra is the relative intensities of the $(1;\beta)$ and $(1;\alpha)$ transitions. A comparison to Figure 2.2, which was a stick plot showing the expected intensities of the transitions of radical **a**, reveals that the $(1;\beta)$ and $(1;\alpha)$ transitions are predicted to be of equal intensity; however, in Figure 3.4 it is clear that the transitions in the experimental spectra do not match the predicted intensity ratio. This unusual intensity pattern can be reproduced if the simulation allows for separation of the radical pair on a very fast timescale, within 2.5 ns after its generation. All other parameters in the simulation are otherwise identical to the simulations of the SDS micelle presented in Chapter 2. This fast separation makes sense in relation to the strong
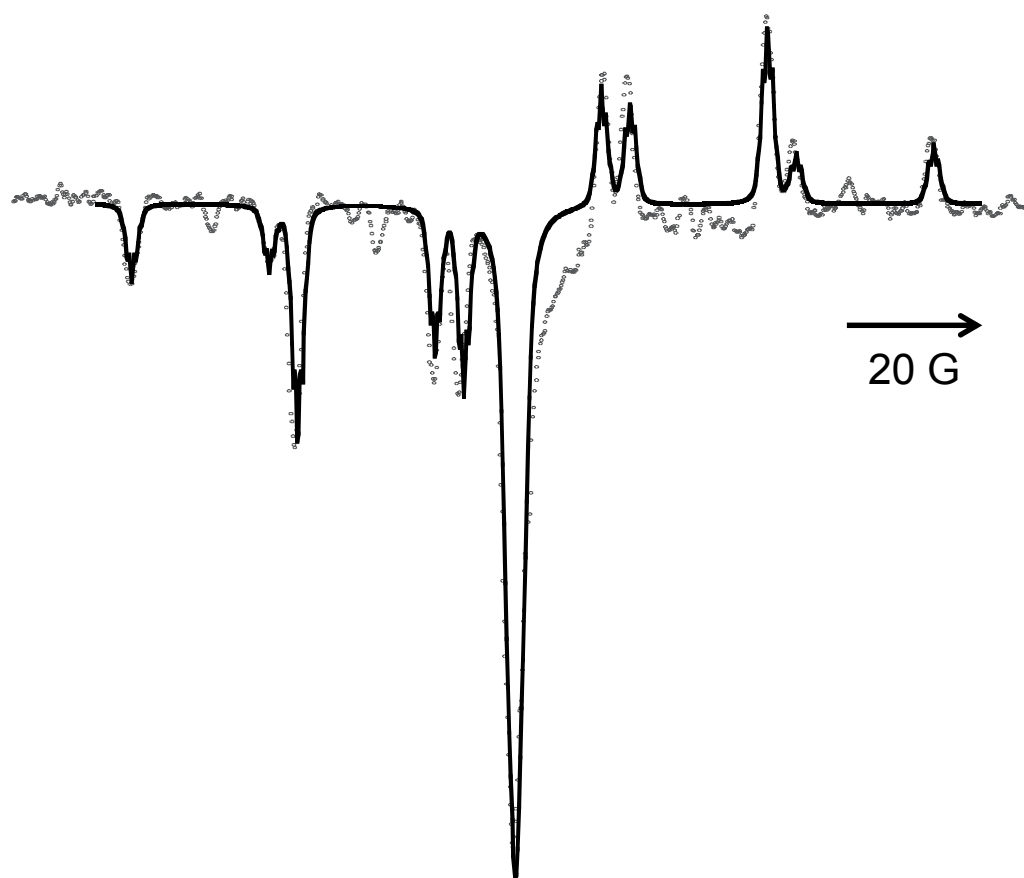
Figure 3.4. X-band TREPR spectra acquired after a 308 nm laser flash in aqueous solutions of SDS at a delay time of 500 ns (gray) using the AQDS sensitizer (1.1mM). The solid black line is the best fit simulation of the experimental data using the microreactor model.

electrostatic repulsion expected between the micelle surface and the anionic sensitizer radical.

3.3.2 Hydrophobic Effects in the TREPR of Ionic Micelles

AQ is a neutral analogue to the AQDS sensitizer. It has not been as commonly employed as the BP sensitizer discussed in Chapter 2 because of its much lower solubility, and therefore, there is less data on its photophysical properties available in the literature. The complete insolubility of AQ in room temperature water and its low solubility in surfactant solutions make it highly likely that the AQ molecule, once solubilized, exists almost exclusively in the micellar phase. The TREPR of AQ in SDS, DTAC, and CTAC collected at 500 ns delay are shown in Figure 3.5. There is a strong similarity between all three spectra, which have pronounced first derivative-like line shapes. The poor S/N ratio relative to the previous spectra is due to the substantially lower concentration of AQ that could be dissolved in the surfactant solutions. The S/N ratio on the DTAC spectrum is, in fact, too poor to allow for quantitative simulations, although it appears similar in line shape to the SDS-AQ spectra.

Comparison of the SDS-AQ and CTAC-AQ simulations accounts for some of the subtle differences between the two spectra (Figure 3.6). A simulation of the SDS-AQ spectrum (Figure 3.6, top) can be obtained with almost identical set of parameters as the simulations of SDS-BP presented in Chapter 2, but a greater contribution of TM polarization is observed in the AQ spectrum. This can be accounted for by simulation results that indicate a slightly faster relaxation rate for the populations of the triplet excited states of the anthraquinone ($k_{rel} = 1.28$ x 10^8 s^{-1} for AQ vs $k_{rel} = 2\text{-}3$ x 10^{-8} s^{-1} for BP around room temperature) and an escape rate for the RP from the micelle of 2.5 x 10^5 s^{-1}. The presence of a cationic versus and anionic head group seems to make very little qualitative difference to the spectra, with only minor differences in the line shape
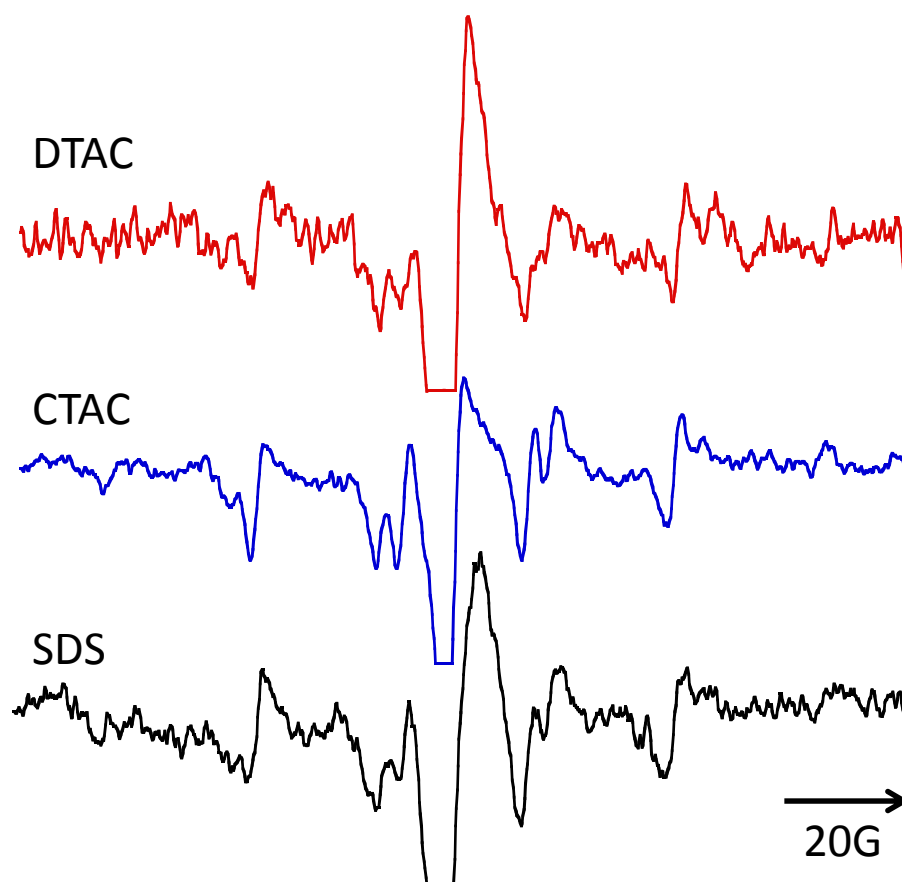
Figure 3.5. X-band TREPR spectra acquired 500 ns after a 308 nm laser flash in aqueous solutions of 50 mM DTAC (top), CTAC (middle), and SDS (bottom) with 1.1 mM AQ. The central line in the spectrum is due to the AQ radical and has been cut off to vertically expand the signal of the surfactant alkyl radicals.
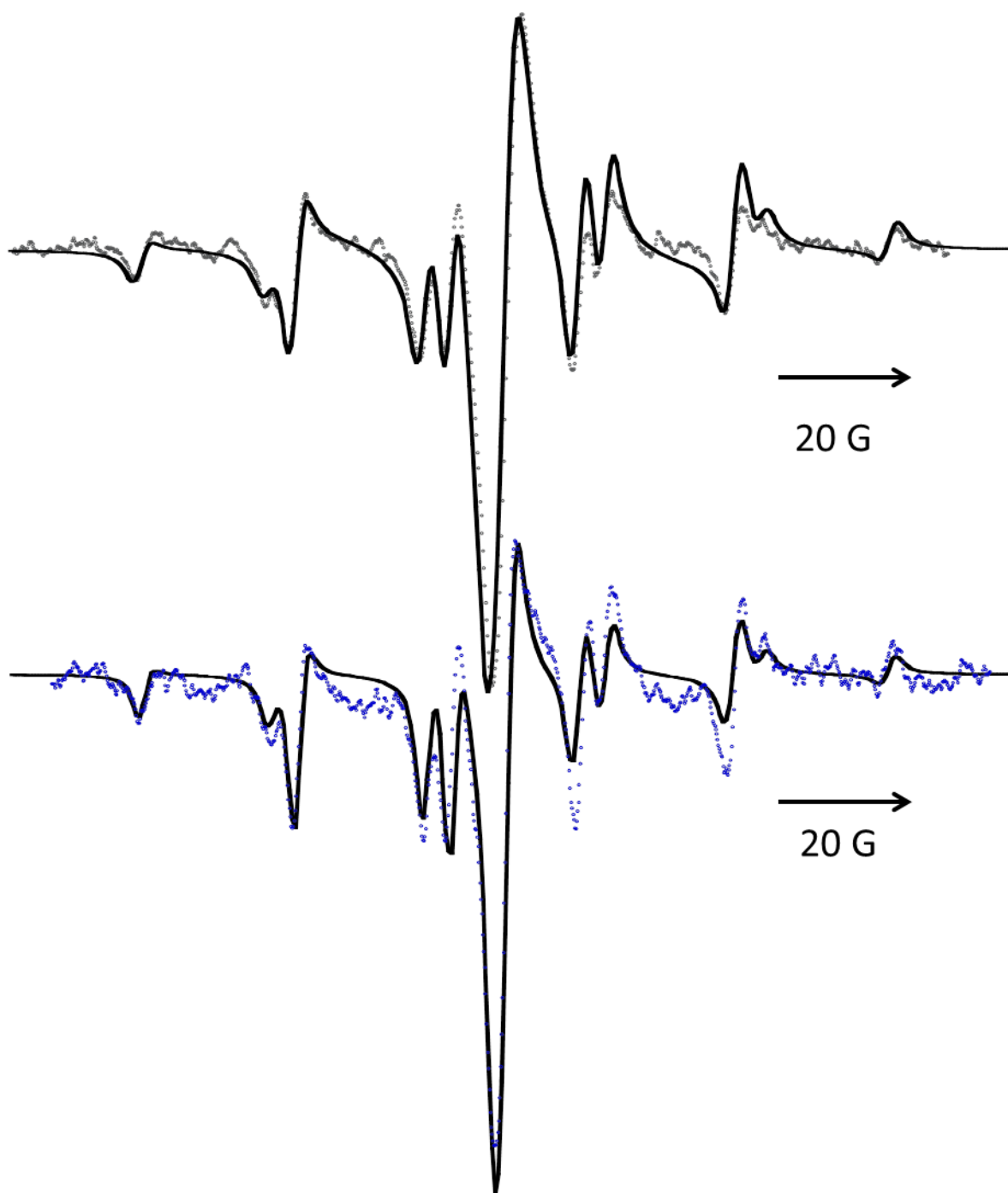
Figure 3.6. X-band TREPR spectra acquired after a 248 nm laser flash in aqueous solutions of SDS (grey) and CTAC (blue) at a delay time of 500 ns using the AQ sensitizer (1.1mM). The solid black line is the best fit simulation of the experimental data using the microreactor model.

observed most clearly in the signal from the AQ radical. The simulation results for AQ in CTAC micelles (Figure 3.6, bottom) return a lower limit on the value of $k_{rel} = 0$ s^{-1} and an escape rate of the RP from the micelle of 5.1 x 10^5 s^{-1}. These differences allow for greater accumulation of the semianthraquinone radical in the CTAC spectrum and are most likely related to differences in the micelle properties.

Based strictly on a comparison the AQDS and AQ sensitizers, introduction of an electrostatic charge on the sensitizer molecule may be expected to lead to Coulombic attraction or repulsion that will have profound effects on the diffusive behavior of the RP and the observed CIDEP in the TREPR spectra. However, the TREPR results of the singly charged, AQS sensitizer do not exhibit the same clear-cut electrostatic control of diffusion that is observed in for the AQDS sensitizer. The opposite charges of the AQS sensitizer and the DTAC micelles naturally lead to the prediction of strong APS in the TREPR spectra, which is indeed observed (Figure 3.7). Minor differences between line shape of the spectra of DTAC and CTAC with AQS mirror the differences observed between CTAC and DTAC with AQDS, including a more pronounced contribution of escape radicals in the CTAC spectrum and broader line widths for the DTAC alkyl radicals. These are likely due to differences in the micelle aggregation number and size. However, a relatively strong contribution of SCRP polarization is also observed in the SDS-AQS spectra. In fact, both the SDS-AQS and CTAC-AQS spectra can be fit with identical simulation parameters (Figure 3.8).

The observation of strong SCRP polarization in both anionic and cationic micellar systems requires some explanation. The AQS sensitizer is more hydrophilic than the AQ sensitizer, but is solubilized better in the presence of surfactants than in pure water. The strong similarity between the spectra further suggests that the hydrophobicity of the AQS sensitizer is largely responsible for
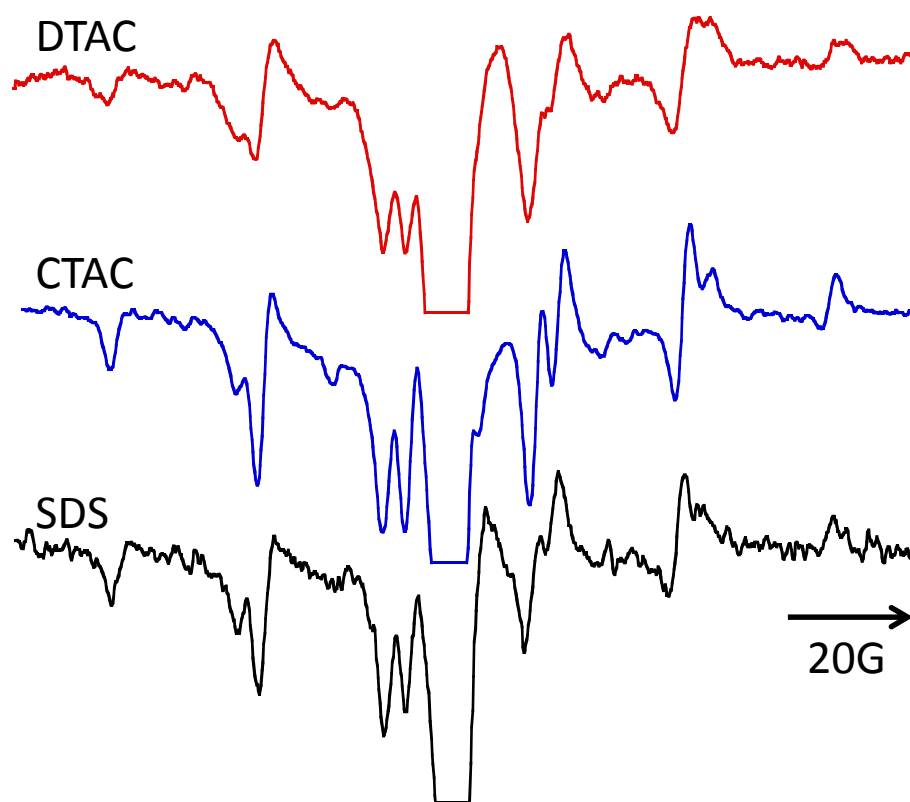
Figure 3.7. X-band TREPR spectra acquired 500 ns after a 308 nm laser flash in aqueous solutions of 50 mM DTAC (top), CTAC (middle), and SDS (bottom) with 1.1 mM AQS. The central line in the spectrum is due to the AQS radical and has been cut off to vertically expand the signal of the surfactant alkyl radicals.
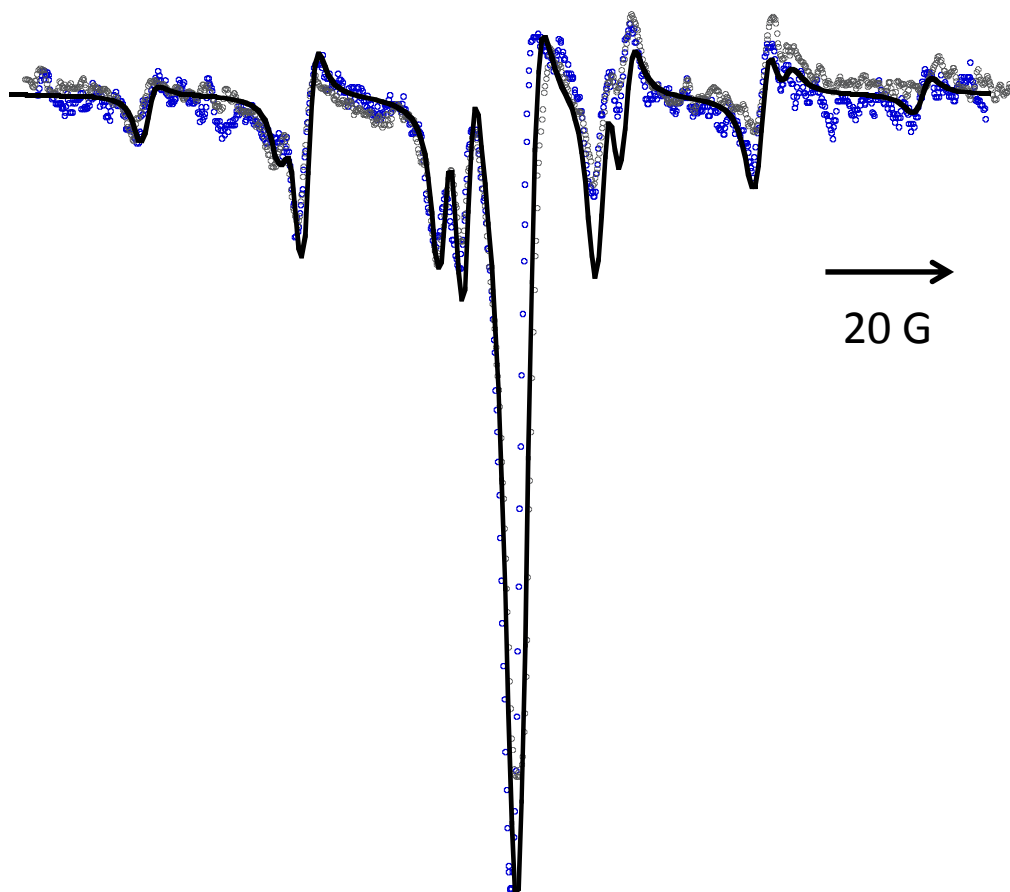
Figure 3.8. X-band TREPR spectra acquired after a 308 nm laser flash in aqueous solutions of SDS at a delay time of 500 ns (gray) or CTAC at a delay time of 300 ns (blue) using the AQS sensitizer (1.1mM). The solid black line is the best fit simulation of the experimental data using the microreactor model.

the observed CIDEP. Despite its charged, AQS must still strongly and preferentially associate with the hydrophobic interior of the micelle, and this hydrophobic interaction must be strong enough to overcome the effects of electrostatic repulsion between the SDS micelle surface and the AQS radical.

An explanation of the similarities between CTAC and SDS must then have its source in the physical properties of the interior of the micelle. A stable nitroxide spin probe, 2,2,4,4-tetramethyl-1,2,3,4-tetrahydro-γ-carboline-3-oxyl was incorporated into solutions of the three surfactants. This particular spin probe was chosen for a comparison because it has a similar molecular volume to the triplet sensitizers used in the TREPR experiment. The nitroxide group is marginally hydrophilic, but molecule on the whole is better solubilized in organic solvents or surfactant solutions. The rotational correlation time of the spin probe was measured by SSEPR and extracted from the line shape of the SSEPR spectra using a program by Freed et al.[44] The results of the spin probe study are reported in Table 3.3. It is clear that for this particular spin probe, which has a molar volume closes to that of the sensitizer, the rotational correlation times in SDS and CTAC are very close to one another ($\tau_c = 6.4 \times 10^{-10}$ s and $\tau_c = 6.2 \times 10^{-10}$ s), despite the difference in the length of the alkyl tail and the size of the micelles of the two surfactants. This implies that, for molecules of a similar structure, the rotational diffusion inside the SDS and CTAC micelles is essentially identical. A similarity in the diffusive behavior of AQS in SDS and CTAC micelles most likely accounts for the striking similarities between the TREPR spectra.

Spin probe studies of three other stable nitroxide molecules were conducted in the SDS, DTAC, and CTAC systems. In all cases, the rotational correlation times of these spin probes were more similar for SDS and DTAC micelles than for CTAC micelles. It is important to note, however, that the molecular volume and the mobility of the nitroxide radicals as a result of their

Table 3.3 SSEPR results for the rotational correlation times of four spin probes incorporated into micellar solutions of SDS, DTAC, and CTAC

Surfactant	Probe 1	Probe 2	Probe 3	Probe 4
SDS	6.4×10^{-10}s	2.1×10^{-10}s	5.9×10^{-10}s	3.7×10^{-10}s
DTAC	3.6×10^{-10}s	2.3×10^{-10}s	5.9×10^{-10}s	3.3×10^{-10}s
CTAC	6.2×10^{-10}s	3.3×10^{-10}s		6.6×10^{-10}s

Probe 1
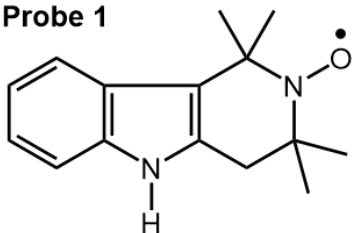
Probe 3
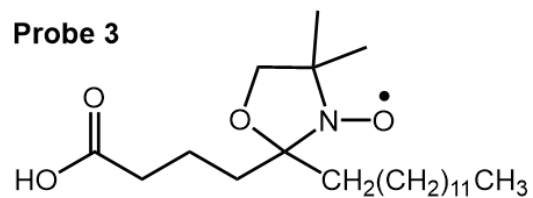
Probe 2
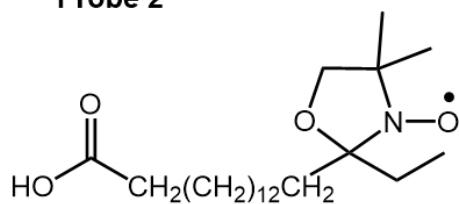
Probe 4
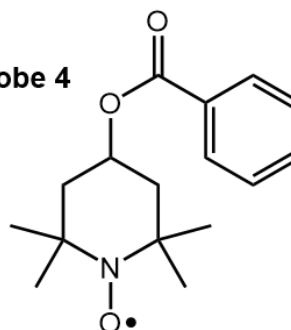
structure is substantially different from that of Probe 1. Probe 1 has a relatively ridged, three ring structure. Both of the doxyl-stearic acid probes (probe 2 and 3) are very commonly used to characterize micelle viscosity by SSEPR. The length of the stearic acid chain, and the attachment of the nitroxide at different positions along that alkyl chain, make these spin probes particularly sensitive to the motion of long alkyl chains in the micelle core. The ubiquitous use of these spin probes to characterize micelles is a result of the expectation that the motion of the stearic acid chain will be sensitive to or even mimic the motion of the alkyl chains of the surfactant tails when incorporated into a micelle. These structures, and the diffusive behavior of an alkyl chain in the micelle, are very different than the diffusive behavior of the much more rigid Probe 1. Probe 4 is also often used to explore the properties of micelle via SSEPR, but it is important to note that Probe 4 is relatively hydrophilic. It is often observed to partition between the aqueous phase and the micelle interior. This partitioning was also observed for this particular spin probe in the SDS, DTAC, and CTAC solutions. Spectral decomposition into a fast motion component, which represents the diffusional behavior of the spin probe in the bulk aqueous phase, and a slower motion "micellar" component that reflects the properties of the micellar phase, is necessary. Only the rotational correlation time obtained from the slow motion component is reported in Table 3.3 – but for obvious reasons, this superposition issue renders Probe 4 a less reliable measure of the rotational diffusion or solubilization behavior of AQS in these surfactant solutions.

3.3.3 TREPR of Zwitterionic Surfactants

Experiments were performed with one additional surfactant, Zwittergent 3-12, a zwitterionic analogue to SDS and DTAC that contains both a quaternary ammonium and sulfonate functionality in its head group. These presence of both functional groups present an opportunity

for both local electrostatic attraction and repulsion to occur at the surface of the micelle. The TREPR spectrum of the Zwittergent surfactant with AQDS at a 500ns delay is shown in Figure 3.9 (top) and exhibits a strong contribution from the APS. In fact, this spectrum is qualitatively identical to the spectrum of CTAC with the neutral AQ sensitizer taken at 300ns (Figure 3.6), and the fit of the CTAC spectrum is shown superimposed on the Zwittergent spectrum. The similarity between the Zwittergent-AQDS spectrum and the CTAC-AQ spectrum suggest that, despite the net neutral charge of the Zwittergent surfactant, electrostatic interactions between the polar shell of the Zwittergent 3-12 micelles and the anionic AQDS sensitizer are strong enough that the diffusion of the RP is substantially restricted and a SCRP is generated.

The features of the APS in the Zwittergent-AQDS spectrum and the shape of the central transitions for the AQDS radical suggest that there is very little relaxation between the triplet sublevels of the sensitizer and that the escape rate of the radical pair from the micelle is relatively fast when compared to other surfactant systems where APS is observed. This similar relaxation rate and fast escape make sense respectively, given the fact that CTAC[3b, 34a] and SDS[31, 41b] have very similar micellar radii (Table 3.1) and local interactions between the anionic sensitizer and surfactant head groups on the surface of the micelle can be both attractive and repulsive. It is important to note, however, that this comparison is between spectra collected at different delay times. The time dependence of the Zwittergent-AQDS system shows that there is still a small contribution of APS to the TREPR line shape can be observed out to delay times of 1.2 µs, as opposed to 800ns in the CTAC spectra (Figure 3.3). A comparable contribution of escape radicals to the Zwittergent 3-12 spectrum takes 200 ns longer to develop than the CTAC spectrum it resembles. This suggests that the rate of escape is not actually identical for RPs confined to these two micelles.

The TREPR spectra of Zwittergent 3-12 with AQS also shows a strong APS component at
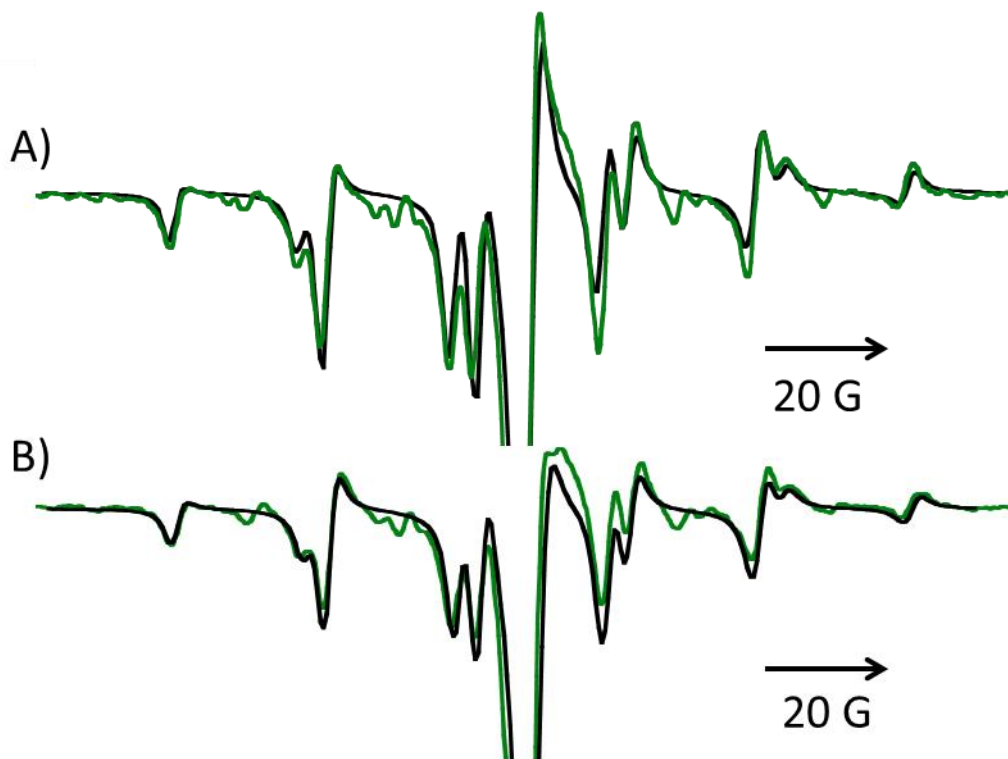
Figure 3.9. Zwittergent 3-12 with AQDS (A) or AQS (B) collected 500 ns after the 308 nm laser flash. For all intents and purposes, the characteristics of A are identical to the CTAC-AQ spectra, and the fit from the CTAC-AQ simulation is over laid (black) for comparison. Spectra B is shown with the simulation fit from the CTAC-AQS simulation (black).

a 500 ns delay time. In Figure 3.9 (bottom), the same simulation results that fit both the SDS-AQS and CTAC-AQS spectra is overlaid on the Zwittergent-AQS spectrum. The similarities between TREPR spectra collected of RPs in all three ionic micelles and the zwitterionic micelles is further evidence that the features of the observed CIDEP originate because the RP formed by the AQS sensitizer is confined to the micelle interior due to hydrophobic effects.

3.3.4 TREPR of Surfactant Monomers in Solution

It might be argued that for both hydrophilic sensitizer (AQDS and AQS), the observed photochemistry in the TREPR experiment takes place exclusively in solution between "free" sensitizer molecules and non-aggregated surfactant monomers. The maximum concentration of non-micellized surfactant molecules is generally accepted to be equal to the CMC, while any surfactant molecules above this threshold concentration are incorporated into surfactant aggregates. In some cases, such as SDS, the concentration of free monomer can be much lower than the CMC because they form transitory aggregates at concentrations below the CMC. This is known as the critical aggregate concentration (CAC) at which aggregates begin to form. The CAC of SDS has been measured by NMR as approximately 4 mM,[45] which is approximately half of the literature value for the CMC.[46] The concentration of surfactant in these experiments reported here was 50 mM, well above the CAC and CMC in all cases. This means that the majority of the alkyl radical signal observed by TREPR must be generated from micellized radicals.

To confirm that micellized radicals were the source of the alkyl radical signal, the TREPR spectra of SDS with AQDS were collected for total surfactant concentration of 10 mM, 4 mM, and 1 mM (Figure 3.10). These concentrations are just above the CMC, at the CAC, and well below both the CMC and CAC of the surfactant. Above the CMC, the signal from the alkyl radicals and

the AQDS radical are both clearly visible. At the CAC, the alkyl radical transitions are visible in the spectra, but weak. Below the CMC and CAC, only the signal from the AQDS radical is visible, and it exhibits net absorptive TM polarization.

A change in the polarization of the AQS radical signal from emissive in a hydrophobic lipid bilayer to absorptive in the aqueous phase has been reported previously by Moribe et al.[36] Collisions of ^{3}AQS and excess Cl$^-$ form an exciplex, ^{3}(AQS$^-$ Cl$^-$)*that leads to the quenching of the ^{3}AQS*. Exciplex formation involving heavy atoms have been known alter the population of the triplet excited state sublevels through spin orbit coupling in the exiplex. Exciplex formation between the ^{3}AQDS and counterions in solution well below the CMC of the surfactant would account for the observed change in polarization in Figure 3.10 (top). The observation of a change in polarization of the AQS radical from emissive when interacting with a hydrophobic structure to absorptive in free solution is further evidence that the AQDS and AQS must interact strongly with a hydrophobic micelle structure to generate the TREPR signal in Figures 3.1 and 3.7, since the contribution of the TM is net emissive in these spectra.

Because there is no contribution of APS to the SDS-AQDS spectra, it is important to confirm that the appearance of APS is due to the presence of micellar aggregates and not due to interactions between the monomer and sensitizer in free solution. The aggregation of surfactant molecules can be disrupted by the addition of organic solvents. A comparison of the spectra of SDS and DTAC with AQDS in a solution of 50:50 acetonitrile:water with the spectra of SDS-AQDS in aqueous solution reveals that any APS splitting disappears from the spectra when surfactant aggregation is disrupted. In Figure 3.11, only RPM polarization from escape radicals is observed for all surfactant solutions. There is little difference between the spectra in Figure 3.11 (B) where SDS forms micelles and (C) where micelle formation is disrupted, which suggests that

125
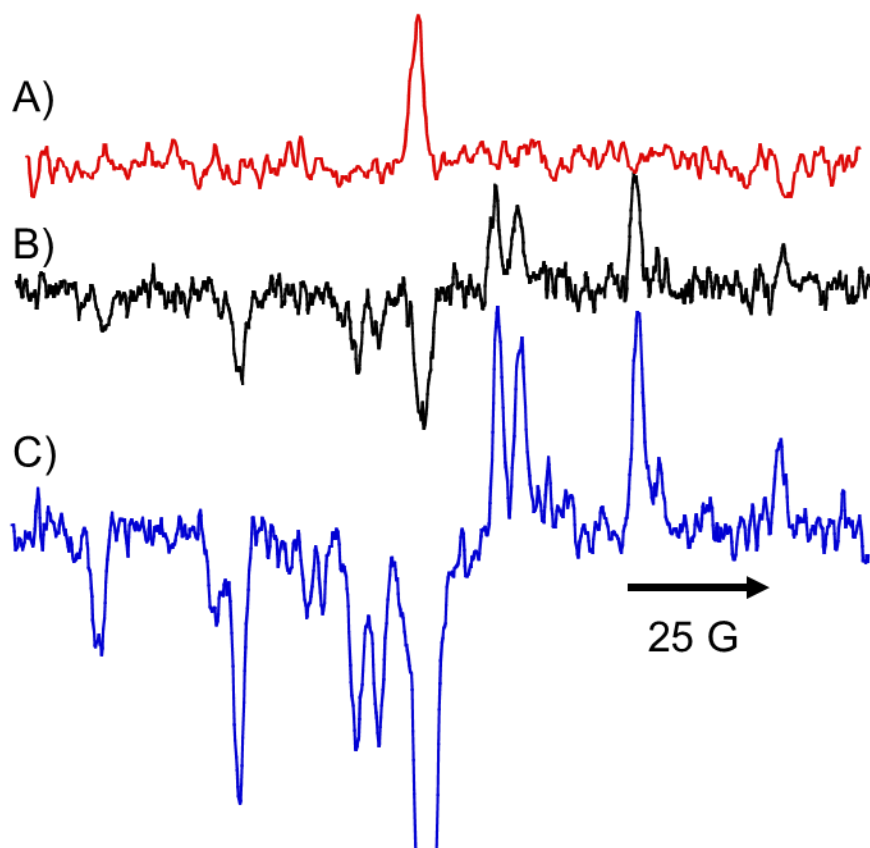
Figure 3.10: TREPR spectra collected 500ns after a 308 nm excimer laser flash in solutions of SDS with AQDS below the CMC (1mM, A), at the critical aggregate concentration (4 mM, B), and above the CMC (10 mM, C).

the micelle structure is not crucial to the diffusive behavior of the RP when there is strong electrostatic repulsion and the RP separates quickly. The absence of APS in the spectra of DTAC in 50:50 acetonitrile:water (Fig. 3.11, A. Compare to Fig. 3.1, top) indicates that the observation of APS in TREPR spectra is conditional of the formation of micelles.

An important feature to note in the disrupted micelle spectra of SDS is the relative intensities of the (1;α) and (1;β) transitions. As discussed in Section 3.3.1, these two transitions are expected to be observed in a 1:1 ratio. However, in the experimental spectra, the (1;α) transitions is less intense than the (1;β) transitions, which is the hallmark of fast escape of the SDS-AQDS RP from the micelle. It was accurately reproduced by spectral simulation in Figure 3.4. The same intensity pattern is observed in SDS-AQDS solutions when micelle formation is disrupted (Fig. 3.12, C). Fast separation of the RP has even been observed in solutions of SDS and neutral sensitizers when micelle formation is disrupted. In disrupted solutions of DTAC (Fig. 3.12, A), the intensities of the (1;α) and (1;β) are equal, which suggest slower separation of the RP. When the micelle structure is disrupted, the electrostatic attraction between the monomer DTAC and the AQDS sensitizer is too weak to maintain spin-correlation in the RP, and APS is not observed. However, electrostatic attraction between the surfactant monomer radical and the sensitizer radical still exists, resulting in slower separation of the DTAC-AQDS RP than is observed for the SDS-AQDS RP. The observation of APS in solutions of DTAC micelles must be a function of the formation of the surfactant aggregate. Because the AQDS exist preferentially in the aqueous phase, it is the large surface charge of the micelle structure that causes the restricted diffusion of the RP, and not electrostatic attraction between a single surfactant monomer and the sensitizer radical.
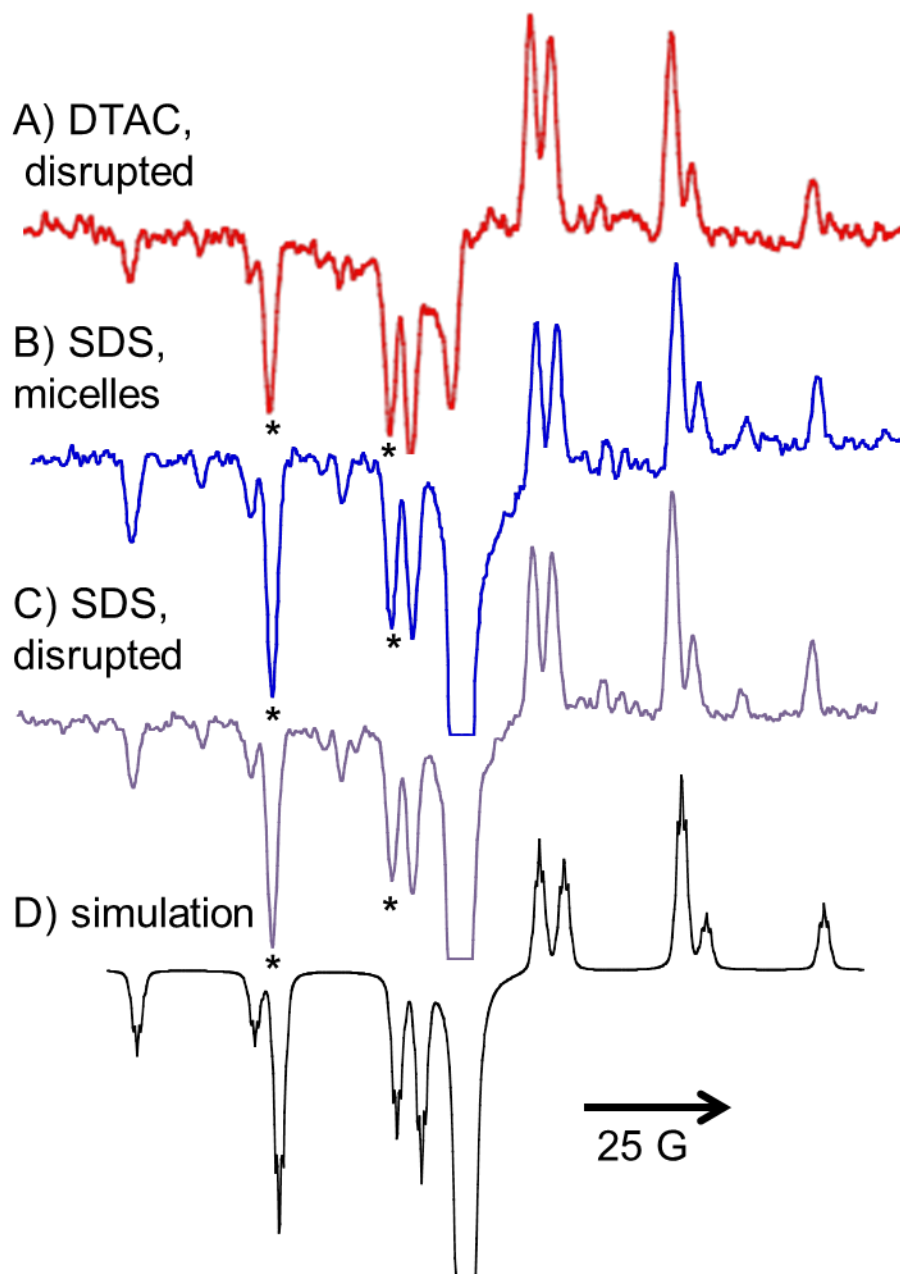
Figure 3.11 TREPR spectra collected at 500 ns after a 308 nm laser flash of DTAC and AQDS in 50:50 acetonitrile: water (A), SDS and AQDS (B), and SDS and AQDS in 50:50 acetonitrile:water (C). The transitions marked by * are expected to be equal in intensity. The simulation (d) is able to reproduce this unusual intensity pattern observed in SDS spectra by allowing for fast separation and escape of the radical pair from the micelles (2.5 ns). This occurs when there is strong electrostatic repulsion between the radical pair (B) or when there is no SDS micelle to confine the radical pair (C). When there is electrostatic attraction between the radical pair but micelle formation is disrupted (A), the expected intensity pattern is observed and separation the radical pair must be slower.

3.4 Conclusions and Future Directions

3.4.1 Conclusions

A comparison of all three anthraquinone based sensitizers in ionic surfactant solutions that differ by the head group charge and surfactant tail demonstrates that the competition between the hydrophobic and electrostatic effects in a micellized RP can dramatically alter the diffusive behavior of the RP. When there is strong electrostatic attraction between the micelle structure and a charged sensitizer in the aqueous phase, as is the case for DTAC or CTAC and AQDS, then the RP is spin-correlated and APS is observed in the TREPR. When there is strong electrostatic repulsion (SDS), only RPM polarization from escaped radicals is observed, regardless of delay time. Careful control studies above and below the CMC and CAC of the surfactant and when surfactant aggregate formation is disrupted prove that the appearance of APS is dependent on the formation of the micelle.[7a] This supramolecular structured environment provides nanoscale confinement of the RPs diffusion that is necessary for the formation of an SCRP . When the hydrophobic AQ sensitizer is employed, confinement of the RP occurs inside the hydrophobic aggregate. The competition between electrostatic repulsion and hydrophobicity in the AQS sensitizer lead to the observation of varying degrees APS in all three surfactant systems studied in this chapter. This suggests a dynamic struggle between Coulombic forces and the hydrophobic effect in the solubilization of small organic molecules by micelle structures. The interplay between these two effects could potentially be used to modulate or "tune" the diffusion of hydrophobic molecules out of surfactant-based structures, and has strong implications in conscientious design and development of controlled drug delivery systems that rely on diffusive escape of hydrophobic drugs from supramolecular surfactant structures.

3.4.2 Future Directions

The qualitative features of the DTAC spectra were discussed extensively above in relation to the SDS and CTAC spectra. At this point, only the spectral simulations of the CTAC and SDS spectra have been completed. Quantitative simulations of the features of the APS in the DTAC spectra would be most beneficial and would allow for a complete and thorough comparison of the diffusive behavior of the RPs in the SDS, DTAC, and CTAC solutions. Currently, the simulation of the DTAC spectra is hampered by poor S/N of the DTAC-AQ spectra. Because the photochemistry and photophysics of the AQ sensitizers is not as well understood as they are for BP, benchmark comparisons between the BP and AQ spectra are important to ensuring reasonable assumptions and estimations of the simulation parameters for the other AQ based sensitizers.

In the spectral simulations of the AQ sensitizer in CTAC and SDS, a difference in the relaxation rate of the triplet sublevels and in the escape rate of the RP from micellar confinement was observed. The difference in escape rate was an intuitive choice made in fitting the TREPR spectra based off of the line shape. The strong similarities in the TREPR spectra of CTAC and Zwittergent at different time delays suggest that this choice may not be a correct physical interpretation of the observed phenomena. Better measurements of the photophysical properties of the anthraquinone sensitizers are necessary to motivate this assumption and to provide a platform for comparing the simulation results to other physical measurements, as was done in Chapter 2 for the SDS-BP radical pair.

In order to more thoroughly explore the competition between the hydrophobic and electrostatic effects, it would be beneficial to compare the sulfate analogue of the CTAC surfactant (16 carbon alkyl tail). Unfortunately, sodium cetyl sulfate (SCS) could not be easily compared to

130

these surfactants at ambient temperatures. The Krafft point of the surfactant is below room temperature and the solubility of SCS is poor, so comparable concentrations of SCS could not be achieved. Although it is possible to heat the system above the Krafft point of the surfactant, the results in Chapter 2 clearly demonstrates that there is a strong temperature dependence to the observation of the APS that would precluded direct comparison of the features of the TREPR of SCS at higher temperature to the spectra of SDS, DTAC, and CTAC presented in this chapter. A more feasible solution would be to compare the TREPR spectra of shorter chain length analogues such as sodium octyl sulfate to the spectra of SDS, DTAC, and CTAC to confirm the electrostatic dependence of the observation of APS with AQDS.

Finally, only SDS was studied (Fig. 3.11) to examine the effects of micelle formation on the CIDEP of the RP. However, the results in Figure 3.4 suggest that micelle formation has a less pronounced effect on the appearance of the TREPR spectra of SDS due to strong electrostatic repulsion between SDS and AQDS. DTAC could not be studied below the CMC because of formation of a precipitate between the DTAC monomer and the AQDS sensitizer. This precipitate could be easily collected by filtration, and was solubilized by the addition of DTAC above the CMC. NMR confirmed a 2:1 ratio of DTAC:AQDS in the precipitate. This precipitation behavior has not been explored yet with CTAC. Because the identity of the counterion plays such a large role in the phase behavior of surfactant systems, it is possible that this counter ion exchange could lead to drastically different phase behavior of the DTAC surfactant. The addition of charged aromatic salts to such solutions has been shown to alter the aggregation behavior of ionic surfactants, and leads to the formation of thread like micelles.[3b] The aggregation behavior of DTAC after counterion exchange with AQDS could be investigated by SSEPR, TREPR, and other common micelle characterization techniques.

3.5 Experimental

9,10-anthraquinone (AQ) was recrystallized from benzene. 9,10-anthraquinone-2-sulfonate sodium salt (AQS), and 9,10-anthraquionone-2,6-disulfonate disodium salt (AQDS) were recrystallized from methanol. Sodium dodecyl sulfate (SDS) was purified with petroleum ether by Soxhlet extraction. Dodecyl trimethylammonium chloride (DTAC) was used as received. Cetyl trimethylammonium chloride (CTAC) was purified by Soxhlet extraction with petroleum ether. The concentration of sensitizer was 1.1 mM, and the total concentration of surfactant in all cases was 50 mM, which is well above the critical micelle concentration (CMC) of all three surfactants. Samples were prepared by dissolving the surfactant and sensitizer in ultrapure water from a Millipore filtration system, then purging the sample with nitrogen gas for 15 minutes.

Our TREPR apparatus has been described previously. A 248 nm or 308 nm excimer laser is used at a repetition rate of 60 Hz. The direct detection EPR signal is obtained from the microwave bridge using a gated boxcar average. The external magnetic field is swept over a 4 minute period using a gate width of 300 ns. Samples are flowed from a reservoir through a quartz flat cell (0.4-0.5 mm path length) using a micropump, and the sample reservoir is kept under nitrogen during the EPR experiment. All spectra have a center field of approximately 3380 G, a microwave frequency of 9.48 GHz, and a power of 10 mW.

REFERENCES

1.	Zana, R., Micellization of amphiphiles: Selected aspects. *Colloid Surf. A-Physicochem. Eng. Asp.* **1997,** *123*, 27-35.

2.	Soderman, O.; Herrington, K. L.; Kaler, E. W.; Miller, D. D., Transition from micelles to vesicles in aqueous mixtures of anionic and cationic surfactants. *Langmuir* **1997,** *13* (21), 5531-5538.

3.	(a) Lebedeva, N. V.; Shahine, A.; Bales, B. L., Aggregation number-based degrees of counterion dissociation in sodium n-alkyl sulfate micelles. *J. Phys. Chem. B* **2005,** *109* (42), 19806-19816; (b) Wang, Z. W.; Larson, R. G., Molecular Dynamics Simulations of Threadlike Cetyltrimethylammonium Chloride Micelles: Effects of Sodium Chloride and Sodium Salicylate Salts. *J. Phys. Chem. B* **2009,** *113* (42), 13697-13710; (c) Bergstrom, L. M.; Skoglund, S.; Danerlov, K.; Garamus, V. M.; Pedersen, J. S., The growth of micelles, and the transition to bilayers, in mixtures of a single-chain and a double-chain cationic surfactant investigated with small-angle neutron scattering. *Soft Matter* **2011,** *7* (22), 10935-10944.

4.	(a) Dejanovic, B.; Noethig-Laslo, V.; Sentjurc, M.; Walde, P., On the surface properties of oleate micelles and oleic acid/oleate vesicles studied by spin labeling. *Chem. Phys. Lipids* **2011,** *164* (1), 83-88; (b) Dejanovic, B.; Mirosavljevic, K.; Noethig-Laslo, V.; Pecar, S.; Sentjurc, M.; Walde, P., An ESR characterization of micelles and vesicles formed in aqueous decanoic acid/sodium decanoate systems using different spin labels. *Chem. Phys. Lipids* **2008,** *156* (1-2), 17-25.

5.	(a) Roby, A.; Erdogan, S.; Torchilin, V. P., Solubilization of poorly soluble PDT agent, meso-tetraphenylporphin, in plain or immunotargeted PEG-PE micelles results in dramatically improved cancer cell killing in vitro. *Eur. J. Pharm. Biopharm.* **2006,** *62* (3), 235-240; (b) Bramer, T.; Dew, N.; Edsman, K., Pharmaceutical applications for catanionic mixtures. *J. Pharm. Pharmacol.* **2007,** *59* (10), 1319-1334; (c) Husseini, G. A.; Pitt, W. G., The use of ultrasound and micelles in cancer treatment. *J. Nanosci. Nanotechnol.* **2008,** *8* (5), 2205-2215; (d) Li, W. T., Nanotechology-Based Strategies to Enhance the Efficacy of Photodynamic Therapy for Cancers. *Curr. Drug Metab.* **2009,** *10* (8), 851-860.

6.	(a) Yin, Q.; Shen, J. N.; Zhang, Z. W.; Yu, H. J.; Li, Y. P., Reversal of multidrug resistance by stimuli-responsive drug delivery systems for therapy of tumor. *Advanced Drug Delivery Reviews* **2013,** *65* (13-14), 1699-1715; (b) Sun, H. L.; Meng, F. H.; Cheng, R.; Deng, C.; Zhong, Z. Y., Reduction-sensitive degradable micellar nanoparticles as smart and intuitive delivery systems for cancer chemotherapy. *Expert Opinion on Drug Delivery* **2013,** *10* (8), 1109-1122.

7.	(a) Caregnato, P.; Jarocha, L. E.; Esinhart, H. S.; Lebedeva, N. V.; Tarasov, V. F.; Forbes, M. D. E., Electrostatic Control of Spin Exchange Between Mobile Spin-Correlated Radical Pairs Created in Micellar Solutions. *Langmuir* **2011,** *27* (9), 5304-5309; (b) Manju, T.; Manoj, N.; Gejo, J. L.; Braun, A. M.; Oliveros, E., Micellar control of the photooxidation pathways of 10-methyl phenothiazine: electron versus energy transfer mechanisms. *Photochem. Photobiol. Sci.* **2014,** *13* (2), 281-292.

8.	Mahmoudzadeh, M.; Fassihi, A.; Emami, J.; Davies, N. M.; Dorkoosh, F., Physicochemical, pharmaceutical and biological approaches toward designing optimized and efficient hydrophobically modified chitosan-based polymeric micelles as a nanocarrier system for targeted delivery of anticancer drugs. *Journal of Drug Targeting* **2013,** *21* (8), 693-709.

9.	(a) Rizzi, C.; Lauricella, R.; Tuccio, B.; Bouteiller, J. C.; Cerri, V.; Tordo, P., Spin-trapping of free radicals by PBN-type beta-phosphorylated nitrones in the presence of SDS micelles. *Journal of the Chemical Society-Perkin Transactions 2* **1997,** (12), 2507-2512; (b) Bales, B. L.; Ranganathan, R.; Griffiths, P. C., Characterization of mixed micelles of SDS and a sugar-based nonionic surfactant as a variable reaction medium. *J. Phys. Chem. B* **2001,** *105* (31), 7465-7473; (c) Bales, B. L.; Zana, R., Characterization of micelles of quaternary ammonium surfactants, as reaction media I: Dodeclytrimethylammonium bromide and chloride. *J. Phys. Chem. B* **2002,** *106* (8), 1926-1939; (d) Santiago, P. S.; Neto, D. D.; Barbosa, L. R. S.; Itri, R.; Tabak, M., Interaction of meso-tetrakis (4-

sulfonatophenyl) porphyrin with cationic CTAC micelles investigated by small angle X-ray scattering (SAXS) and electron paramagnetic resonance (EPR). *J. Colloid Interface Sci.* **2007,** *316* (2), 730-740; (e) Wasserman, A. M.; Motyakin, M. V.; Yasina, L. L.; Zakharova, Y. A.; Matveenko, V. N.; Shulevich, Y. V.; Rogovina, L. Z., EPR Spin Probe Study of New Micellar Systems. *Appl. Magn. Reson.* **2010,** *38* (1), 117-135.

10.   (a) McCaffrey, V. P.; Forbes, M. D. E., Energy transfer studied using spin polarized free radicals. Effect of substrate structure and a comparison between micellar confinement and free solution. *Tetrahedron* **2000,** *56* (36), 6991-6997; (b) Tarasov, V. F.; White, R. C.; Forbes, M. D. E., Photo-oxidation of diglycine in confined media relaxation of longitudinal magnetization in spin correlated radical pairs. *Spectroc. Acta Pt. A-Molec. Biomolec. Spectr.* **2006,** *63* (4), 776-783; (c) Tarasov, V. F.; Jarocha, L. E.; Avdievich, N. I.; Forbes, M. D. E., TREPR spectra of micelle-confined spin correlated radical pairs: I. Molecular motion and simulations. *Photochem. Photobiol. Sci.* **2014,** *13* (2), 439-453.

11.   Closs, G. L.; Forbes, M. D. E.; Norris, J. R., Spin-polarized electron paramagnetic resonance spectra of radical pairs in micelles - observation of electron spin-spin interactions *J. Phys. Chem.* **1987,** *91* (13), 3592-3599.

12.   (a) Sakaguchi, Y.; Hayashi, H.; Murai, H.; Ihaya, Y. J., CIDEP study of the photochemical reactions of carbonyl compounds showing the external magnetic field effect in a micelle. *Chem. Phys. Lett.* **1984,** *110* (3), 275-279; (b) Sakaguchi, Y.; Hayashi, H.; Murai, H.; Ihaya, Y. J.; Mochida, K., CIDEP study of the formation of a cyclohexadienyl type radical in the hydrogen abstraction reactions of triplet xanthone *Chem. Phys. Lett.* **1985,** *120* (4-5), 401-405; (c) Murai, H.; Sakaguchi, Y.; Hayashi, H.; Ihaya, Y. J., An anomalous phase effect in the individual hyperfine lines of the CIDEP spectra observed in the photochemical reactions of benzophenone in micelles *J. Phys. Chem.* **1986,** *90* (1), 113-118.

13.   Tarasov, V. F.; Jarocha, L. E.; Forbes, M. D. E., TREPR spectra of micelle-confined spin correlated radical pairs: II. Spectral decomposition and asymmetric line shapes. *Photochem. Photobiol. Sci.* **2014,** *13* (2), 454-463.

14.   Langevin, D., Micelles and Microemulsions. *Annu. Rev. Phys. Chem.* **1992,** *43* (1), 341-369.

15.   (a) Bales, B. L., A definition of the degree of ionization of a micelle based on its aggregation number. *J. Phys. Chem. B* **2001,** *105* (29), 6798-6804; (b) Bales, B. L.; Tiguida, K.; Zana, R., Effect of the nature of the counterion on the properties of anionic surfactants. 2. Aggregation number-based micelle ionization degrees for micelles of tetraalkylammonium dodecylsulfates. *J. Phys. Chem. B* **2004,** *108* (39), 14948-14955.

16.   Malliaris, A.; Lemoigne, J.; Sturm, J.; Zana, R., Temperature dependence of the micelle aggregation number and rate of intramicellar excimer formation in aqueous surfactant solutions *J. Phys. Chem.* **1985,** *89* (12), 2709-2713.

17.   Bergstrom, M.; Pedersen, J. S., A small-angle neutron scattering (SANS) study of tablet-shaped and ribbonlike micelles formed from mixtures of an anionic and a cationic surfactant. *J. Phys. Chem. B* **1999,** *103* (40), 8502-8513.

18.   Imae, T.; Kamiya, R.; Ikeda, S., Formation of spherical and rod-like micelles of cetyltrimethylammonium bromide in aqueous NaBr solutions Formation of spherical and rod-like micelles of cetyltrimethylammoniuim bromide in aqueous NaBr solutions.

19.   (a) Ge, M. T.; Freed, J. H., An electron spin resonance study of interactions between gramacidin-A' and phosphatidylcholine bilayers *Biophys. J.* **1993,** *65* (5), 2106-2123; (b) Bratt, P. J.; Kevan, L., Electron spin resonance line shape analysis of x-doxylstearic acid spin probes in dihexadecyl phosphate vesicles and effects of cholesterol addition *J. Phys. Chem.* **1993,** *97* (28), 7371-7374; (c) Bratt, P. J.; Kevan, L., Electron spin resonance line shape analysis of x-doxylstearic acid spin probes in dioctadecyldimethylammonium chloride vesicles. *J. Phys. Chem.* **1992,** *96* (16), 6849-6852.

20.   (a) Mangels, M. L.; Cardon, T. B.; Harper, A. C.; Howard, K. P.; Lorigan, G. A., Spectroscopic characterization of spin-labeled magnetically oriented phospholipid bilayers by EPR spectroscopy. *J. Am. Chem. Soc.* **2000,** *122* (29), 7052-7058; (b) Cassol, R.; Ge, M. T.; Ferrarini, A.; Freed, J. H., Chain dynamics and the

simulation of electron spin resonance spectra from oriented phospholipid membranes. *J. Phys. Chem. B* **1997,** *101* (43), 8782-8789.

21.   Bezzobotnoy, V. Y.; Borbely, S.; Cser, L.; Farago, B.; Gladkih, I. A.; Ostanevich, Y. M.; Vass, S., Temperature and concentration dependence of properties of sodiumdodecyl sulfate micelles determined from small angle neutron scattering experiments *J. Phys. Chem.* **1988,** *92* (20), 5738-5743.\

22.   Tarasov, V.; Jarocha, L. E.; Avdievich, N. I.; Forbes, M. D. E., TREPR Spectra of Micelle-Confined Spin Correlated Radical Pairs I. Molecular Motion and Simulations. *Photochem. Photobiol. Sci.* **2013**.

23.   (a) van Hemelrijck, C.; Muller-Goymann, C. C., Rheological characterization and permeation behavior of poloxamer 407-based systems containing 5-aminolevulinic acid for potential application in photodynamic therapy. *Int. J. Pharm.* **2012,** *437* (1-2), 120-129; (b) Tian, B.; Tao, X.; Ren, T.; Weng, Y.; Lin, X.; Zhang, Y.; Tang, X., Polypeptide-based vesicles: formation, properties and application for drug delivery. *J Mater Chem* **2012,** *22* (34), 17404-17414; (c) Parmar, A.; Parekh, P.; Bahadur, P., Solubilization and Release of a Model Drug Nimesulide from PEO-PPO-PEO Block Copolymer Core-Shell Micelles: Effect of Size of PEO Blocks. *J. Solution Chem.* **2013,** *42* (Copyright (C) 2013 American Chemical Society (ACS). All Rights Reserved.), 80-101.

24.   Bhattacharjee, J.; Verma, G.; Aswal, V. K.; Patravale, V.; Hassan, P. A., Microstructure, drug binding and cytotoxicity of Pluronic P123-aerosol OT mixed micelles. *Rsc Advances* **2013,** *3* (45), 23080-23089.

25.   Dong, R. H.; Wu, J.; Dong, S. L.; Song, S. S.; Tian, F.; Hao, J. C., Interconvertible Self-Assembly and Rheological Properties of Planar Bilayers and Vesicle Gels in Anionic/Nonionic (CF/CH) Surfactant Solutions. *Chem.-Asian J.* **2013,** *8* (8), 1863-1872.

26.   Yaroslavov, A. A.; Udalykh, O. Y.; Melik-Nubarov, N. S.; Kabanov, V. A.; Ermakov, Y. A.; Azov, V. A.; Menger, F. M., Conventional and gemini surfactants embedded within bilayer membranes: Contrasting behavior. *Chem.-Eur. J.* **2001,** *7* (22), 4835-4843.

27.   Igarashi, T.; Shoji, Y.; Katayama, K., Anomalous Solubilization Behavior of Dimyristoylphosphatidylcholine Liposomes Induced by Sodium Dodecyl Sulfate Micelles. *Anal. Sci.* **2012,** *28* (4), 345-350.

28.   Goncalves, P. J.; Correa, D. S.; Franzen, P. L.; De Boni, L.; Almeida, L. M.; Mendonca, C. R.; Borissevitch, I. E.; Zilio, S. C., Effect of interaction with micelles on the excited-state optical properties of zinc porphyrins and J-aggregates formation. *Spectroc. Acta Pt. A-Molec. Biomolec. Spectr.* **2013,** *112*, 309-317.

29.   (a) Lin, C. Y.; Zhao, J. X.; Jiang, R., Nile red probing for the micelle-to-vesicle transition of AOT in aqueous solution. *Chem. Phys. Lett.* **2008,** *464* (1-3), 77-81; (b) Muus, L. T.; Atkins, P. W., *Chemically Induced Magnetic Polarization: Proceedings from the NATO Advanced Study Institute, Sogesta/Urbino, Italy*. D. Reidel Publishing Co. : 1977; Vol. 34; (c) Wang, W.; Sande, S. A., Kinetics of Re-equilibrium of Oppositely Charged Hydrogel-Surfactant System and Its Application in Controlled Release. *Langmuir* **2013,** *29* (22), 6697-6705; (d) Chauhan, S.; Chauhan, M. S.; Kaushal, D.; Syal, V. K.; Jyoti, J., Study of Micellar Behavior of SDS and CTAB in Aqueous Media Containing Furosemide-A Cardiovascular Drug. *J. Solution Chem.* **2010,** *39* (5), 622-638.

30.   (a) Bramer, T.; Frenning, G.; Grasjo, J.; Edsman, K.; Hansson, P., Implications of regular solution theory on the release mechanism of catanionic mixtures from gels. *Colloids and Surfaces B-Biointerfaces* **2009,** *71* (2), 214-225; (b) Dew, N.; Edwards, K.; Edsman, K., Gel formation in systems composed of drug containing catanionic vesicles and oppositely charged hydrophobically modified polymer. *Colloids and Surfaces B-Biointerfaces* **2009,** *70* (2), 187-197; (c) Lee, J. H.; Gustin, J. P.; Chen, T. H.; Payne, G. F.; Raghavan, S. R., Vesicle-biopolymer gels: Networks of surfactant vesicles connected by associating biopolymers. *Langmuir* **2005,** *21* (1), 26-33; (d) Zhu, C.; Lee, J. H.; Raghavan, S. R.; Payne, G. F., Bioinspired vesicle restraint and mobilization using a biopolymer scaffold. *Langmuir* **2006,** *22* (7), 2951-2955.

31.   Prevost, S.; Gradzielski, M., SANS investigation of the microstructures in catanionic mixtures of SDS/DTAC and the effect of various added salts. *J. Colloid Interface Sci.* **2009,** *337* (2), 472-484.

32.	Ferrer-Tasies, L.; Moreno-Calvo, E.; Cano-Sarabia, M.; Aguilella-Arzo, M.; Angelova, A.; Lesieur, S.; Ricart, S.; Faraudo, J.; Ventosa, N.; Veciana, J., Quatsomes: Vesicles Formed by Self-Assembly of Sterols and Quaternary Ammonium Surfactants. *Langmuir* **2013,** *29* (22), 6519-6528.

33.	Griffiths, P. C.; Paul, A.; Heenan, R. K.; Penfold, J.; Ranganathan, R.; Bales, B. L., Role of counterion concentration in determining micelle aggregation: Evaluation of the combination of constraints from small-angle neutron scattering, electron paramagnetic resonance, and time-resolved fluorescence quenching. *J. Phys. Chem. B* **2004,** *108* (12), 3810-3816.

34.	(a) Roelants, E.; Deschryver, F. C., Parameters affecting aqueous micelles of CTAC, TTAC, and DTAC probed by fluorescence quenching *Langmuir* **1987,** *3* (2), 209-214; (b) Imae, T.; Ikeda, S., Characteristics of rodlike micelles of cetyltrimethylammonium chloride in aquous NaCl solutions - their flexibility and the scaling laws in dilute and semidilute regimes *Colloid. Polym. Sci.* **1987,** *265* (12), 1090-1098; (c) Tiefenbach, K. J.; Durchschlag, H.; Jaenicke, R., Spectroscopic and hydrodynamic investigations of nonionic and zwitterionic detergents. In *Analytical Ultracentrifugation V*, Cölfen, H., Ed. Springer Berlin Heidelberg: 1999; Vol. 113, pp 135-141.

35.	White, R. C.; Gorelik, V.; Bagryanskaya, E. G.; Forbes, M. D. E., Photoredox chemistry of AOT: Electron transfer and hydrogen abstraction in microemulsions involving the surfactant. *Langmuir* **2007,** *23* (8), 4183-4191.

36.	Moribe, S.; Ikoma, T.; Akiyama, K.; Tero-Kubota, S., Time-resolved EPR study on photoreduction of sodium anthraquinone-2-sulfate in liposomes. *Chem. Phys. Lett.* **2008,** *457* (1-3), 66-68.

37.	(a) Miura, T.; Kageyama, A.; Toru, S.; Murai, H., Photoreactions and Molecular Dynamics of Radical Pairs in a Reversed Micelle Studied by Time-Resolved Measurements of EPR and Magnetic Field Effect. *J. Phys. Chem. B* **2010,** *114* (45), 14550-14558; (b) Khudyakov, I. V.; McGarry, P. F.; Turro, N. J., A time-resolved electron spin resonance and laser flash spectroscopy investigation of the photolysis of benzaldehyde and benzoin in homogenous solvents and micellar solutions *J. Phys. Chem.* **1993,** *97* (50), 13234-13242; (c) Goez, M.; Henbest, K. B.; Windham, E. G.; Maeda, K.; Timmel, C. R., Quenching Mechanisms and Diffusional Pathways in Micellar Systems Unravelled by Time-Resolved Magnetic-Field Effects. *Chem.-Eur. J.* **2009,** *15* (24), 6058-6064.

38.	(a) Turro, N. J.; Chow, M.-F.; Chung, C.-J.; Kraeutler, B., Magnetic and micellar effects on photoreactions. 1. Carbon-13 isotopic enrichment of dibenzyl ketone via photolysis in aqueous detergent solution. *J. Am. Chem. Soc.* **1981,** *103* (13), 3886-3891; (b) Turro, N. J.; Anderson, D. R.; Chow, M.-F.; Chung, C.-J.; Kraeutler, B., Magnetic and micellar effects on photoreactions. 2. Magnetic isotope effects on quantum yields and magnetic field effects on separation efficiency. Correlation of carbon-13 enrichment parameters with quantum yield measurements. *J. Am. Chem. Soc.* **1981,** *103* (13), 3892-3896.

39.	Landolt-Bornstein, *Organic C Centered Radicals*. Springer: Berlin, 1977.

40.	Menger, F. M.; Doll, D. W., On the structure of micelles *J. Am. Chem. Soc.* **1984,** *106* (4), 1109-1113.

41.	(a) Bales, B. L.; Howe, A. M.; Pitt, A. R.; Roe, J. A.; Griffiths, P. C., A spin-probe study of the modification of the hydration of SDS micelles by insertion of sugar-based nonionic surfactant molecules. *J. Phys. Chem. B* **2000,** *104* (2), 264-270; (b) Bales, B. L.; Messina, L.; Vidal, A.; Peric, M.; Nascimento, O. R., Precision relative aggregation number determinations of SDS micelles using a spin probe. A model of micelle surface hydration. *J. Phys. Chem. B* **1998,** *102* (50), 10347-10358; (c) Lebedeva, N.; Zana, R.; Bales, B. L., A reinterpretation of the hydration of micelles of dodecyltrimethylammonium bromide and chloride in aqueous solution. *J. Phys. Chem. B* **2006,** *110* (20), 9800-9801; (d) McCarney, E. R.; Armstrong, B. D.; Kausik, R.; Han, S., Dynamic nuclear polarization enhanced nuclear magnetic resonance and electron spin resonance studies of hydration and local water dynamics in micelle and vesicle assemblies. *Langmuir* **2008,** *24* (18), 10062-10072.

42.	Bruce, C. D.; Berkowitz, M. L.; Perera, L.; Forbes, M. D. E., Molecular dynamics simulation of sodium dodecyl sulfate micelle in water: Micellar structural characteristics and counterion distribution. *J. Phys. Chem. B* **2002,** *106* (15), 3788-3793.

43.   Forbes, M. D. E.; Jarocha, L. E.; Sim, S.; Tarasov, V. F., Time-Resolved Electron Paramagnetic Resonance Spectroscopy: History, Technique, and Application to Supramolecular and Macromolecular Chemistry. In *Advances in Physical Organic Chemistry, Vol 47*, Williams, I. H.; Williams, N. H., Eds. 2013; Vol. 47, pp 1-83.

44.   Malliaris, A.; Binanalimbele, W.; Zana, R., Fluorescence Probing Studies of Surfactant Aggregation in Aqueous-Solutions of Mixed Ionic Micelles *J. Colloid Interface Sci.* **1986,** *110* (1), 114-120.

45.   Cui, X.; Mao, S.; Liu, M.; Yuan, H.; Du, Y., Mechanism of surfactant micelle formation. *Langmuir* **2008,** *24* (19), 10771-10775.

46.   Mandal, A. B.; Nair, B. U.; Ramaswamy, D., Determination of the critical micelle concentration of surfactants and the partition coefficient of an electrochemical probe by using cyclic voltammetry. *Langmuir* **1988,** *4* (3), 736-739.

CHAPTER 4: EPR Studies of Mixed Catanionic Surfactant Systems

4.1 Introduction

Mixed surfactant systems are ubiquitous in nature. Phospholipid based cell membranes, for instance, are mixtures of phospholipids, glycolipids, and sterols – with the exact composition of the membrane varying by cell type.[1] In industrial and consumer applications, surfactants are more commonly encountered in mixtures rather than pure formulations. In part, this is due to the excessive cost to rigorously purify amphiphilic surfactant molecules on a large scale, especially when high purity is not required. Surfactants may also be intentionally mixed because surfactant mixtures can have very different properties, functions, or aggregate structures than their pure components.[2]

The physical properties of mixed surfactant systems have not been explored as thoroughly in the literature as pure surfactants. In part, this is because of the sheer number of mixed surfactant systems that are possible. Additional complications can arise due to interactions between the surfactants. For instance, mixtures of cationic and anionic surfactants, known as catanionic systems,[3] display very different phase behavior than their cationic or anionic components, including the formation of vesicle structures not normally observed for single component mixtures of single tailed surfactants.[4] This varied phase behavior occurs because of electrostatic interactions between the oppositely charged head groups. While this phase behavior is of great interest, catanionic systems are particularly understudied because significant precipitation of the surfactants

can complicate physical measurements, especially with solutions containing approximately equimolar amounts of each surfactant.[4a, 5]

One of the more recent and promising applications for micelle and vesicle phases formed by catanionic mixtures has been pharmaceutical applications.[6] A significant effort has been made to find surfactant systems the self-assemble with physical properties similar to natural lipids. Ionic surfactants, such as quaternary ammonium salts, have been widely investigated for this purpose. However, pure ionic surfactants often exhibit high toxicity or dentaturing properties that make them poorly suited for in vivo applications. Catanionic mixtures of surfactants have presented a promising alternative because of the spontaneous formation of vesicle structures similar to those formed by natural lipids and because of their reduced cytotoxicity relative to their pure ionic counterparts.[6a] Thermally induced phase transitions from multilamellar vesicles to unilamellar vesicles that are much more similar in structure to biological liposomes, and the long term stability of these unilamellar structures when stored, have made some catanionic systems particularly attractive.[4c] In order to be of use in pharmaceutical applications, the performance of a catanionic mixture under physiological conditions and its response to relevant changes in environment, like pH, temperature, or salt, must be fully explored. The physiological environment can vary depending on the desired route of administration, so extensive knowledge of how catanionic mixtures react to environmental conditions is imperative.[6a]

Several possible drug delivery applications for catanionic mixtures are presently being explored, including longer encapsulation of drugs for storage and controlled release,[7] the formation of catanionic drug-surfactant complexes,[8] spontaneous formation of gels in polymer – catanionic aggregate mixtures,[9] and controlled drug release from gels.[10] Drug release by diffusion out of catanionic surfactant systems can be 1-100 times slower than release out of single component

aggregates. [8, 10b, 11]. The ability of charged drug molecules to form catanionic aggregates with ionic surfactants has also greatly increased the carrying capacity of surfactant-based drug delivery systems, leading to prolonged periods of drug delivery. More recent work has focused on pharmaceutical gels, because these systems have rheological and bioadhesive properties that promote long term contact with an application site that make them very attractive for prolonged drug release applications. However, these gels are typically greater than 95% water, which means that diffusion of drug molecules out of them is incredibly fast. Incorporating catanionic micelles into the gel matrix, or forming a gel matrix via the interaction of catanionic micelles with charged polymers, has been shown to promote prolonged release drug molecules from pharmaceutical gels.[6b, 8-9, 9c, 12] In the former systems, the inclusion of large catanionic micelles and vesicles slows the diffusion of water soluble drugs through the matrix,[9b, 10c] while in the later, drug molecules incorporated into catanionic vesicles can be released when the gel is disrupted in response to changes in environmental conditions.[9b, 10a, 10c] One final application for catanionic vesicle structures has been to serve as templates for polymerization reactions.[7b, 10a, 13] A polymerizable material can be incorporated into the catanionic mixture, or the surfactants themselves can contain polymerizable groups. These techniques have been used to successfully template the formation of hollow polymer spheres. Polymerization of catanionic vesicle structures can make them more stable to changes in environmental conditions and prolong the encapsulation time of drug molecules in the aggregates by slowing diffusive escape.[14]

Fundamentally, the ubiquitous use of surfactant mixtures and applications like the drug delivery systems described above make it important to develop an understanding of the properties that govern phase behavior in surfactant mixtures and diffusion of molecules in the micelle or vesicle. As we have already seen, EPR is particularly sensitive to different forms of diffusive

motion in micelles. This chapter reports the SSEPR and TREPR investigation of the phase behavior and radical dynamics in catanionic mixture of SDS and DTAC. Recent work on the phase diagram of the SDS-DTAC mixtures suggests that a phase transition from micelle to vesicle aggregate structures occurs as the surfactant mixing ratio approaches equimolar. Using stable nitroxide radicals as spin probes, the SSEPR experiment provides information on the radical rotational dynamics inside the surfactant aggregates. This technique can be particularly sensitive to changes in microviscosity[15] or molecular ordering,[16] which are reflected in changes to the rotational correlation time of the spin probe and the line shape of the EPR spectrum. In the TREPR experiment, a radical pair is photochemically generated inside the micelle or vesicle using a triplet sensitizer. The line shapes and widths of the resulting TREPR spectra are sensitive to the translational diffusion of the RP inside the supramolecular surfactant structure[17]. The SSEPR and TREPR experiments are sensitive to different diffusional motions and, as will be demonstrated below, give additional evidence for the understudied phase transitions in mixed surfactant systems as a function of surfactant mixing ratio and concentration.

4.2 Background

4.2.1 Catanionic Surfactant Mixtures

Mixed micellar systems have been studied sporadically as early as the 1950's,[18] but received much more attention in recent years due to new applications in drug delivery.[6a, 19] Mixed micellar aggregates are of great theoretical interest because of the variation in the physical properties of the aggregates and the deviation of these properties from those of the pure components. These systems are also of great practical interest because of their considerable use in industrial and consumer applications.[20] Such applications often exploit the desirable differences in

the physical behavior of surfactant aggregates over their pure components. Potentially desirable deviation in behavior include a decreased CMC, decreased surface tension, or increased solubilization of hydrophobic organic molecules. All these positive behaviors are attributed collectively to surfactant "synergism."[21]

Synergistic behaviors are observed because the process of mixing surfactants can have a dramatic effect on surfactant self-assembly in solution. A simplified treatment of surfactant aggregation models the micelle or surfactant aggregate as a separate pseudophase.[2a, 20b, 22] This approach works reasonably well for aggregates made up of 50 or more molecules. Surfactant aggregation that can be modeled this way is considered ideal, while systems where strong interactions between the surfactants lead to deviations from the predictions of this model are considered non-ideal. The most common model for non-ideal surfactant mixing is known as the real solution theory (RST) and was first applied to surfactant systems by Rubingh in the 1970's.[23]

For both ideal and non-ideal surfactant systems, the self-assembly of mixtures of surfactant molecules into aggregates is generally attributed to two sources: the hydrophobic effect and interactions between head groups in the surfactant aggregates.[20b] The former is caused by the spontaneous self-association of the hydrophobic chains of the surfactant monomers on the "interior" of an aggregate, leaving the hydrophilic head groups at the surface in contact with the bulk aqueous phase. This process is driven by a gain in free energy due to reduced contact between the hydrophobic tails and water. It does not depend as heavily on the identity of the hydrophobic tails, although differences in structure of the tails lead to changes in the aggregate shape.[5a, 24] Since this process depends only weakly on molecular structure, it tends to favor randomly mixed aggregates and is the basis for descriptions of ideal mixing of surfactants. Strong interactions between head groups in mixed surfactant systems are generally the cause of non-ideal behavior,

including the substantial lowering of CMCs or interfacial tension compared to unmixed surfactants.[25] For binary mixtures, the magnitude of these synergistic effects often increases with increasing asymmetry in either the tails or substantial differences in the head groups of the surfactants, with the largest synergistic effects having been observed in mixtures of two oppositely charged surfactants.[26]

The phase behavior of catanionic mixtures is complex. Morphological changes from micelles to vesicles have been observed as a function of mixing ratio between surfactants and the total concentration of surfactant in solution.[27] The size and shape of surfactant aggregates in mixed micellar systems depend on a number of factors, including the molecular structure of the surfactant. The shape of aggregates can generally be determined by the packing of surfactant monomers in the aggregate structure. A critical packing parameter, CPP, can be used to estimate aggregate phase behavior.[28] This packing parameter relates the area of the hydrophobic tail to the area of the hydrophilic head group through the expression:

$$CPP = \frac{V_t}{aL_t}$$

(1)

where V_t is the volume of the surfactant tail, a is the area per surfactant head group at the surface, and L_t is the length of the surfactant tail. It's important to note that these values are not constant for a given surfactant molecule and can be affected by various solution conditions like temperature or ionic strength. An illustration of the CPP for solutions of ionic surfactants or catanionic mixtures near equimolar mixing is shown in Figure 4.1. The larger the volume of the head group relative to the tail, the higher the curvature at the surface of the aggregate. A value of CPP between 0 and 1/3 leads to smaller, typically spherical micellar structures (Fig 4.1A). As the volume of the hydrophobic tail increases, the packing parameter approaches $1/3 \leq CPP \leq 1/2$, and rod like micelles are formed. For $1/2 \leq CPP \leq 1$, structures with an even lower curvature such as vesicles

143
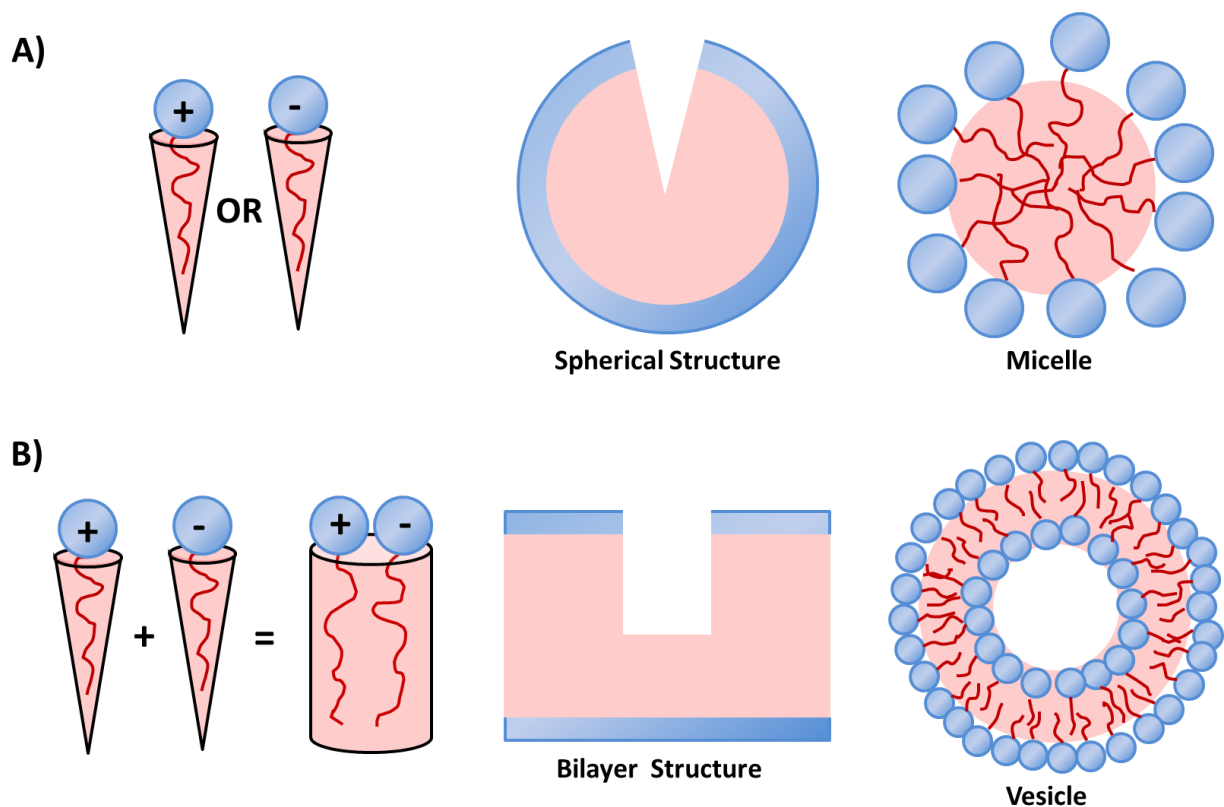
Figure 4.1: When the critical packing parameter (CPP) of pure anionic or cationic surfactants falls in the range of $0 \leq CPP \leq 1/3$ and pack together as if they have a conical shape, leading to small nanostructures with a high curvature (A). When the mixing ratio of cationic and anionic surfactants approach equimolar (B), electrostatic interactions between the oppositely charged surfactants cause the surfactant system to behave like a double tailed surfactant with $1/2 \leq CPP \leq 1$, leading to bilayer structures with a low surface curvature.

or flat lamellar phases are observed (Fig 4.1B).

Strong electrostatic interactions between the oppositely charged head groups change the packing parameter by reducing the volume between head groups. This electrostatic attraction can cause the surfactants to behave more like double tailed or gemini surfactants, especially near equimolar mixing. The formation of both multilamellar and unilamellar vesicles has been reported for systems close to the equimolar mixing ratio in binary mixtures of surfactants, and these vesicles can range in size from 20 nm to several hundreds of nanometers in diameter.[4c, 29] The symmetry of the surfactant tail length also affects micellar growth and vesicle formation.[5a, 24] A catanionic mixture with one surfactant having a short alkyl tail and one with a long alkyl tail exhibits weak micellar growth. Micelle growth and morphology changes most significantly for mixtures of two surfactants with long alkyl tails of different length. When the alkyl tails of the surfactants were of equal length, like in the binary mixture of SDS and DTAC, strong interactions between both the hydrophobic and hydrophilic portions of the surfactants lead to the formation of bilayer structures over a wide range of compositions. Salts also have a strong effect on micelle and vesicle formation in surfactant aggregates.[30] Increasing salt concentrations, including increasing the concentration of the surfactants counterions, can induce phase transitions in catanionic systems. These changes occur due to screening of head group charges by salt additives, which leads to an increase in the packing parameter that is similar to that observed for catanionic mixtures of surfactants.

The spontaneous formation of vesicles in catanionic systems has been of particular interest. It was first reported by Kaler et al. in 1989,[31] but has also been observed in many other catanionic systems since then.[2c, 4, 32] Typical vesicle preparations techniques involve sonication, thin-film hydration, high-pressure extrusion, or vortexing.[33] Vesicles prepared by these methods, even from biologically derived phosphatidylcholines, are not considered thermodynamically equilibrated

states.[34] Provided that there are no shear forces necessary for vesicle formation, the spontaneous formation of vesicles from catanionic mixtures has opened the door to the idea that, for some surfactant mixtures, vesicles may exist in a thermodynamically equilibrated state[13, 35] In fact, in some systems, vesicles are readily formed and appear to be stable over long periods of time. This question of equilibrium is still widely debated,[33-34] and studies of the effect of mixing procedure on phase behavior in catanionic systems and on equilibration of mixed surfactant aggregates are ongoing.

The most commonly employed thermodynamic model for the non-ideal behavior and composition of mixed micellar aggregates is Regular Solution Theory (RST).[23] The non-ideality of surfactant mixtures is best described by the activity coefficients of the surfactants, which represent the ratio of the effective mole fraction of each surfactant its actual mole fraction in solution.[2a, 20b, 25] In ideal mixtures or for pure surfactant solutions, the activity coefficient is equal to one, but in nonideal surfactant mixtures the activity coefficients are typically less than this.

The RST assumes the excess entropy of mixing surfactants is zero. Expressions for excess enthalpy of mixing, H_E, can then be used instead of excess free energy, G_E, to determine the properties of the mixed surfactant system. The value of H_E can be expressed as:

$$H_E = \beta_{int} x(1-x)RT \tag{2}$$

where β_{int} is a single adjustable interaction parameter to account for differences in energy between the mixed and unmixed systems that result from surfactant-surfactant interactions. The sign of β_{int} indicates the nature of the interaction between the surfactants, with a large negative β_{int} indicating strong attractive forces between the surfactants and synergism, while a large positive β_{int} indicates strong repulsive forces or antagonism. Large, negative interaction parameters have typically been

reported for catanionic mixtures of surfactants due to electrostatic attraction between the oppositely charged head groups. The activity coefficients for surfactants in a binary mixture can then be expressed in terms of this interaction parameter, β_{int}:

$$\gamma_1 = e^{\beta_{int}(1-x)^2} \tag{3}$$

$$\gamma_2 = e^{\beta_{int}x^2} \tag{4}$$

While careful calorimetry measurements have determined that the assumption $S_E = 0$ is invalid, direct physical measurements of the properties of non-ideal surfactant mixtures reveal that RST is very accurate in predicting physical properties of mixed surfactant systems. RST has been successfully used to model nonideality in a wide range of mixed surfactant systems, including mixtures of nonionic surfactants, nonionic-ionic surfactants, and catanionic surfactant systems.

The surfactant composition of the aggregates formed in mixed micellar systems are not identical to the surfactant mixing ratio and depends strongly on the total surfactant concentration.[27, 36] This effect is more pronounced in mixtures of surfactants that are asymmetric in size or volume or that have substantially different critical micelle concentrations. The molar ratio between the two surfactants in the aggregates has a strong influence on the structure of the aggregate (micelle or vesicle). In addition, abrupt transitions between bilayer and micelle structures have been observed at a constant mixing ratio but as a function of dilution in mixtures of anionic-cationic or single and double tailed charged surfactants.[32, 36-37 38]

Modifications to the RST have been made to account for electrostatic effects between charged surfactants. The magnitude of synergistic effects in mixtures of ionic surfactants and the composition of aggregates have been successfully calculated using the Poisson-Boltzmann mean field theory for electrostatic free energy of a charged interface, which treats the interfacial charges as if they were smeared out across the aggregate surface and accounts for entropic effects of

charged counterions.[36] Its application to catanionic mixtures receives thorough treatment in recent work by Bergstrom et al. for systems known to form both micelles and bilayer structures.[26-27] With these modifications, RST forms the basis for thermodynamic calculations of the activity coefficient, CMC_{mix}, and for the composition of mixed micellar aggregates for catanionic mixtures. The CMC_{mix} of a binary mixture of surfactants may be written as:

$$CMC_{mix} = a_1 CMC_1 + a_2 CMC_2 \qquad (5)$$

where CMC_1 and CMC_2 are the CMC of each pure component of the mixture and $a_1 = \gamma_1 x$ and $a_2 = \gamma_2(1-x)$ are the activities and γ_1 and γ_2 the activity coefficients for surfactant 1 and 2. The mole fractions of each surfactant in the aggregates are denoted as x for surfactant 1 and $(1-x)$ for surfactant 2.

Eq. 5 assumes ideal behavior of the surfactants, where the monomer concentration of the surfactants stays constant in solution when the total surfactant concentration C_{total} is at or above the CMC, at which point the concentration of the monomer in solution is assumed to be constant and equal to the CMC. Any additional surfactant added after the CMC is reached forms aggregates. Therefore, the monomer concentrations may be calculated using the relationship $C_1^{free} = \gamma_1 x CMC_1$ and $C_2^{free} = \gamma_2(1-x)CMC_2$. The total surfactant concentration is a sum of the surfactant in aggregates and monomeric surfactant, $C_{total} = C_{agg} + C_1^{free} + C_2^{free}$. The mole fraction of surfactant 1 in solution is given by $y = (C_1^{free} + xC_{agg})/C_{total}$. The expressions for the activity coefficients, γ_1 and γ_2, must be derived from an appropriate model for the type of surfactant mixture. Despite the expected non-ideality of catanionic systems, these simple expressions for the CMC are still generally considered valid. They are commonly used to model non-ideal systems[20b, 25] and have been shown to generate accurate values of x, C_{agg}, C_1^{free} and C_2^{free}.[26, 36]

Calculations for x, C_{agg}, and the concentration of free monomer for each surfactant begin with more general expressions for the two activity coefficients that have previously been derived by minimizing the free energy per aggregated surfactant molecule with respect to the composition at constant chemical potentials of free surfactant in solution.

$$\gamma_1(x) = \exp\left[\left(\mu_{ex}(x) - \mu_{ex}(x = 1) + (1 - x)\frac{d\mu_{ex}}{x'}(x' = x)\right)\Big/ kT\right] \tag{6}$$

$$\gamma_2(x) = \exp\left[\left(\mu_{ex}(x) - \mu_{ex}(x = 0) + (x)\frac{d\mu_{ex}}{x'}(x' = x)\right)\Big/ kT\right] \tag{7}$$

Where the excess free energy per aggregated molecule is defined as

$$\mu_{ex} \equiv \mu - kT[x lnx + (1 - x)\ln(1 - x)] \tag{8}$$

From the Poisson-Boltzmann theory, the expression for the electrostatic free energy for a mixture of anionic and cationic surfactants may be written as:

$$\mu_{ex} = |2x - 1|\mu_{el} \tag{9}$$

The free energy per charge μ_{el} of a curved interface is expressed as a first order expansion of μ_{el} with respect of H/κ, where H is the mean curvature at the surface of charge and κ is the Debye screening length:

$$\frac{\mu_{el}}{kT} = h_0 + h_1 H \tag{10}$$

where

$$h_0 = 2ln\left(s + \sqrt{s^2 + 1}\right) - 2q \tag{11}$$

$$h_1 = -\frac{4}{\kappa s}\ln\left(\frac{s}{2q}\right) \tag{12}$$

The dimensionless reduced surface charge density, s, is defined as

$$s \equiv |2x - 1| \frac{2\pi l_B}{a\kappa} \tag{13}$$

And

$$p \equiv \frac{s}{\sqrt{s^1 + 1}} \tag{13}$$

$$q \equiv \frac{s}{\sqrt{s^2 + 1} + 1} \tag{14}$$

The area per aggregated surfactant at the surface of charge is a. The Bjerrum length is:

$$l_B \equiv \frac{e_{el}^2}{4\pi \varepsilon_0 \varepsilon_r kT} \tag{16}$$

The inverse Debye screening length is:

$$\kappa = \sqrt{\frac{2N_A e_{el}^2}{\epsilon_0 \varepsilon_r kT}} \sqrt{c_s + CMC_{mix}} \tag{17}$$

where e_{el} is the elementary charge, N_A is Avogadro's number, ϵ_0 is the permittivity in vacuum, ε_r is the dielectric constant of the medium, and c_s is the concentration of any added salt. In general, l_B is about 7.15 Å and $\kappa^{-1} = 3.04/\sqrt{CMC_{mix}}$ Å for a 1:1 electrolyte in aqueous solution at 25°C.

By substituting Eqs. 6 and 7 into equations 3 and 4, γ_1 and γ_2 may be expressed as

$$\gamma_1 = \left(s + \sqrt{s^2 + 1}\right)^{2|2x-1|/(2x-1)} \left(\frac{2q}{s}\right)^j \exp\left[-2|2x - 1|q - \frac{\mu_{el}^1}{kT} - 2pq\frac{(1-x)}{2x-1}j\right] \tag{18}$$

$$\gamma_2 = \left(s + \sqrt{s^2 + 1}\right)^{-2|2x-1|/(2x-1)} \left(\frac{2q}{s}\right)^j \exp\left[2|2x - 1|q - \frac{\mu_{el}^1}{kT} + 2pq\frac{x}{2x-1}j\right] \tag{19}$$

where $\mu_{el}^1 \equiv \mu_{el}(x = 1)$ and $\mu_{el}^2 \equiv \mu_{el}(x = 0)$ are the molecular electrostatic free energies in pure solution for surfactant 1 and surfactant 2, and j is the dimensionless curvature

$$j = \frac{2aH}{\pi l_B}. \tag{20}$$

Since the Debye screening length depends on the CMC_{mix}, which in turn depends on γ_1 and γ_2, the solutions to Eqs. 18 and 19 must be calculated iteratively. These calculations were performed for mixtures of SDS and DTAC, and the results are reported in section 4.3.2.

4.2.2 Spin Probe Studies of Micelles and Vesicles

The SSEPR spin probe and spin labeling techniques have been instrumental to the study of molecular dynamics in a wide variety of systems, including isotropic fluids, ordered phases like biological membranes, surfaces, and macromolecules.[39] Detailed information about the micellar interface can be obtained at the molecular level from EPR of surfactant aggregates when spin probes are incorporated into these structures.[20a] Spin probe studies on micellar aggregates have been used extensively to characterize micellar properties related to the rotational diffusion of the spin probe. Most often, characterization has focused on obtaining rotational correlation times and microviscosity, but more recent advances in the technique have allowed spin probe studies to explore other properties of surfactant aggregates like the degree of hydration and counterion binding.[15b, 40] In biological membranes and vesicles, these techniques provide information about the types and rates of motion in the structure, the degree of organization of the lipids or surfactants, and the dynamic behavior of bilayers at the molecular level, which differ noticeably from the dynamic behavior of micelles.[41]

The most important information extracted from the SSEPR spectra concern rotational correlation times (τ_c), ordering parameters (S_{eff}), partitioning of spin probes between multiple environments, polarity, and hydration. Rotational correlation times are uniquely sensitive to the microviscosity of the local environment of the probe. Components of the hyperfine or g-factor tensors have likewise been shown to be sensitive to polarity and hydration. This sensitivity makes

it possible to study spin probe partitioning, for instance, between a micelle and the bulk aqueous phase, for small, hydrophilic spin probes because the properties of the local environment of the probe will be reflected in changes to the magnetic or dynamic parameters observable in the EPR spectrum.[42] Such partitioning is more often observed for smaller, more hydrophilic spin probes, while larger hydrophobic spin probes have been shown to incorporate preferentially or even exclusively in hydrophobic surfactant aggregates over the bulk water. Comparisons of spin probes that differ in size, hydrophobicity, or probe location have been regularly undertaken in attempts to characterize different environments in surfactant solutions. The structure of some commonly used spin probes for SSEPR investigations of micelles and vesicles are shown in Scheme 4.1.

The differing size and location of spin probes in supramolecular aggregates can be inferred from an analysis of the line shape of the SSEPR spectra. The rotational motion of the spin probe is generally classified according to three different motional regimes: the rigid limit, slow motion, and fast or isotropic motion. The rigid limit applies to spin probe measurements where the rotational motion of the spin probe is essentially frozen on the timescale of the EPR measurement. In such cases, the anisotropies of the g-factor and hyperfine coupling can be directly extracted from the positions of the EPR transitions. On the other end of the motional regime, small spherical molecules in isotropic fluids can undergo isotropic rotational motion. When this isotropic motion is fast on the EPR timescale, any anisotropies in the g-factor or hyperfine splitting will be averages of the principle tensor components. In general, motion faster than $\tau_c \approx 10^{-9}$ s can be considered fast motion for the standard EPR experiment at 9.5 GHz. The rate of rotational motion in the isotropic limit determines the relative width of the EPR transitions, which are narrower for faster rotational motion and broaden as the rotational motion slows. In the case of fast motion, information on the rotational correlation time of nitroxide spin probes can be directly extracted from the line width

Scheme 4.1

5-DSA

5-DSE

16-DSA

16-DSE

4-HTB
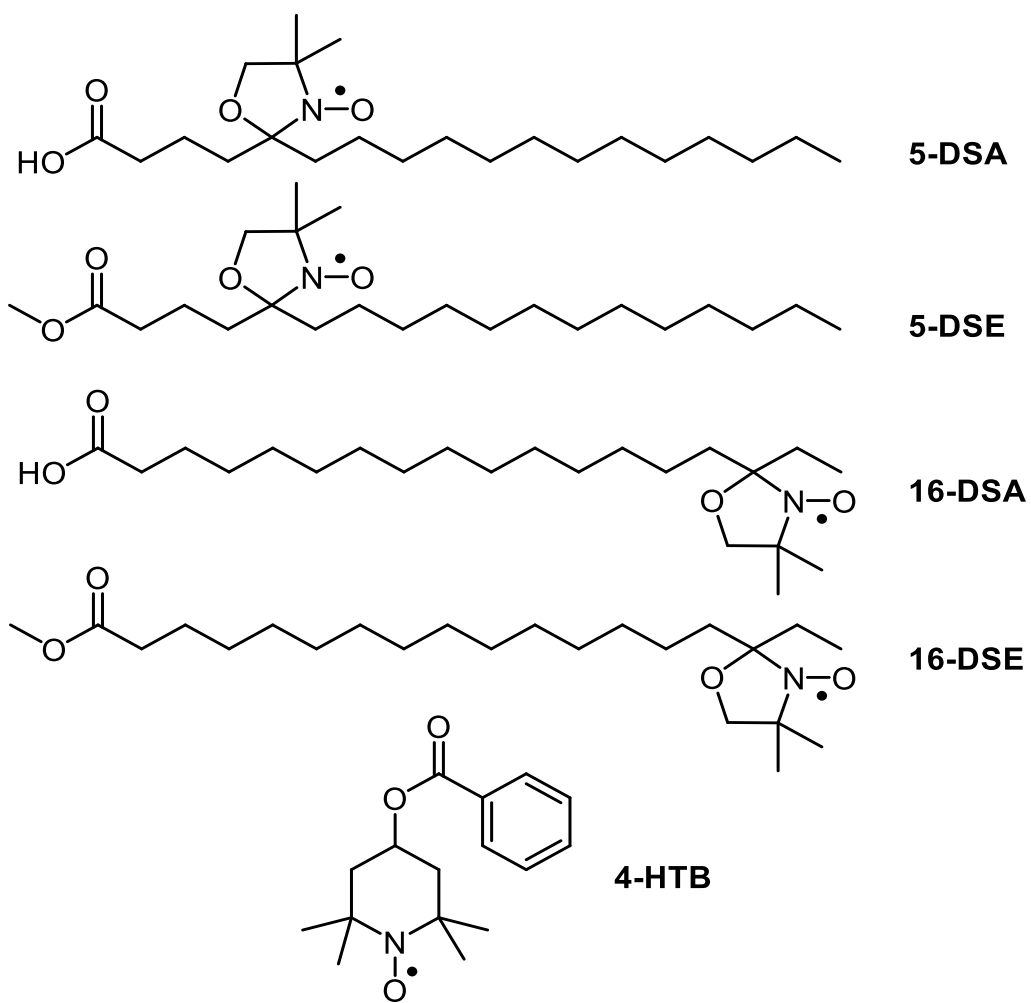
and line height of the transitions.[41c] For the doxyl stearic acid (DSA) spin probes like 5-DSA and 16-DSA in Scheme 4.1, the rotational correlation time can be obtained using the following equation:[43]

$$\tau_c = 6.65 \ x \ 10^{-10} \Delta H_{(+1)} \left(\sqrt{\frac{I_{(+1)}}{I_{(-1)}}} \right) \tag{21}$$

where $I_{(+1)}$ and $I_{(-1)}$ are the height of the low and high field lines, $\Delta H_{(+1)}$ is the line width of the low field line, and the constant is derived from the magnetic parameters of the spin probe. This equation has been used to extract τ_c values from SSEPR spectra of spin probes in micellar solutions. It was a standard method before the development and improved accessibility of more sophisticated computer-based fitting procedures to cover a wider range of τ_c values.

The slow motion regime is most relevant to the discussion of spin probes in surfactant-based aggregates. Spin probes are said to undergo slow motion when the rotational diffusion of the probe is slow enough that the rate of averaging of the g-factor and hyperfine tensors is comparable to their anisotropy. SSEPR in the slow motion regime often exhibit very complicated or irregular line shapes that are a convolution of the magnetic parameters and the dynamic rotational motion of the probe.[41a, 41c] At X-band for the more commonly used spin probes, this region encompasses rotational motions in the range of $\tau_c \approx 10^{-7} - 10^{-9}$ s.

The rate of rotation of a spin probe in its local environment is directly related to two physical properties: the molecular structure of the probe and the viscosity of the environment. Local viscosity measurements obtained from spin probe studies are referred to as microviscosities, since the rotational motion of the probe is primarily affected by the viscosity in the surfactant aggregate and not the viscosity of the bulk solution. The microviscosity of the probe environment can be calculated from the rotational correlation time using the Stokes-Einstein equation:[15b]

$$\tau_c = \frac{4\pi\eta R_h^3}{3kT} \tag{22}$$

where R_h is the hydrodynamic radius of the probe and η is the viscosity of the local environment.

One additional and very important point concerning the rotational correlation time is that spin probes often undergo anisotropic rotation, even in isotropic media. This anisotropic motion is related to the probe structure and is obviously much stronger for more structurally anisotropic spin probes. The most commonly employed spin probes for characterizing hydrophobic micelle and vesicle structures are based of stearic acid, including DSA and doxyl stearic acid methyl esters (DSE), like those shown in Scheme 4.1. These molecules are axially symmetric, and rotational diffusion around the axis parallel to the axis of molecular symmetry is expected to be much faster than rotation around perpendicular axis. Accurate analysis of the SSEPR spectra of these spin probes should account for this anisotropy, which is typically accomplished by extracting separate values for the rotational diffusion or rotational correlation time along the parallel ($R_\parallel$ or $\tau_\parallel$) or perpendicular ($R_\perp$ or $\tau_\perp$) axes.

Even if the average τ_c is greater than 10^{-9} s, if the rotational correlation time of one axis of the molecule falls into the region of slow motion, quantitative information can only be extracted from a full line shape analysis.[41c] In many instances where Eq. 21 has been applied to micelles, the rotational correlation time is incorrect because the rotational anisotropy of the spin probe was not taken into account. For instance, in the study of CTAC micelles incorporating a 5-DSA probe, calculations of the rotational correlation time were obtained from both Eq. 21 and a computational program.[44] The authors found a discrepancy between the two methods, with results from the line width/line height calculations a factor of two larger than those obtained from simulations that included the anisotropic rotational motion of the probe. When the simulation program was forced

to calculate the rotational correlation time under the assumption of isotropic motion, the results converged with those obtained from Eq. 21.

In general, the rate of rotational motion, the anisotropy of the probe, and any inhomogeneous broadening (for instance, due to unresolved hyperfine splittings) are sufficient to fit the SSEPR spectra of spin probes in micellar solutions.[45] The average τ_c values reported for micellar environment are on the order of $10^{-9} - 10^{-10}$ s. The τ_c of 5-DSA of SDS as measured from Eq. 21 and corrected for inhomogeneous broadening is reported between 0.6 x 10^{-9} s and 8.4 x 10^{-9} s,[46] and the τ_c of SDS and DTAC for 16-DSA are both on the order of 10^{-12} s.[15b, 15d, 40a, 47] The 5- and 16-DSA probes explore slightly different environments in the micelle structure, leading to these very different rotational correlation times as a function of probe location.

One additional parameter that can be considered in spin probe measurements of micelle properties is the variation in hyperfine splitting. For nitroxides, the value of A_N is known to be sensitive to local polarity[48] and directly related to solution properties like solvent dielectric constant,[49] dipolar moment of the solvent,[50] and hydrogen bonding ability.[48c] A decrease in local polarity will cause a corresponding decrease in the value of A_N. Above the CMC of a surfactant, a decrease in polarity of nitroxide probes has been observed that corresponds with the solubilization of the probe in micellar aggregates. A similar decrease has been observed by the addition of salt to micellar solutions,[51] which is due to a decrease in the polarity of the local environment of the spin probe and related to expulsion of water molecules from the micellar surface. These changes to polarity directly correlated with the level of hydration at the location of the spin probe, with values of A_N =14.5 considered effectively anhydrous and A_N = 15.7 fully hydrated for the DSA spin probes. Differences is measurements of the isotropic hyperfine splitting between the low field and center field lines of both 5- and 16-DSE probes have been used as a measure of aggregation

number, because this splitting (denoted as A+) has been found to vary monotonically with N_{agg}, which in turn has been shown to correlate with the degree of counterion binding α for both SDS and DTAC.[15a, 15b, 40c, 52] Bales et al. have demonstrated very accurate measurements of the counterion binding for both SDS and DTAC, with $\alpha = 0.277$[15a] and $\alpha = 0.365$, [15b] respectively. For measurements that rely on either A_N or A+, the quality of a spectral fit is often improved by allowing for variation in A_{zz}, which is the component of the hyperfine tensor most sensitive to local polarity. [53]

An additional parameter must be considered to adequately explain the line shape of SSEPR spectra of bilayers and vesicles, which are far more ordered than their micelle counterparts due to tighter packing of the surfactant tails and greater exclusion of water. In these systems, anisotropic spin probes will often assume a preferred orientation relative to the ordered bilayer structure. Calculation of rotational correlation times from Eq. 21 are impossible in systems exhibiting molecular ordering, regardless of the rate of rotational motion.[41c] Molecular ordering can be observed and calculated directly in the EPR spectrum as long as the timescale for preferential distribution of the probe is at least 10^{-7} s at X-band, so that it is longer than the inverse of the orientation dependent part of the spin Hamiltonian. For systems experiencing fast motion and molecular ordering, the order parameter, S_{eff}, can be calculated directly from the high and low field extrema of the spectra – which will show additional splitting due to probe ordering. However, if the rate of probe motion is slower than 10^{-9} s, the line positions are a function of both S_{eff} and τ_c, and the order parameter can only be calculated from spectral simulation. Spectral fitting is also necessary if the splitting of the high and low field lines are not well resolved. In the event that S_{eff} cannot be measured directly from the spectrum, it is not possible to obtain a unique value of S_{eff} and τ_c to fit the experimental spectra.

A final complication occurs in the analysis of SSEPR spectra of spin probes in vesicles. While the spin probe is ordered when incorporated into the bilayer, the distribution vesicles is random and isotropic with respect to the magnetic field in the laboratory frame.[44] On a microscopic level, an axially symmetric spin probe like DSA is oriented normal to the bilayer and the concentration of spin probe is kept low such that there is no more than one probe molecule incorporated into each vesicle structure. Because the vesicles are isotropically distributed relative to the laboratory frame, on the macroscopic level, the spin probe is also oriented isotropically relative to the applied magnetic field, which is coincident with the z-axis of the laboratory frame, z_L. On a microscopic level, however, the rotation of the probe is not isotropic. The resulting EPR spectrum is a sum of EPR spectra for all possible orientations of the bilayer normal with respected to the z_L. This behavior is referred to as microscopic order, macroscopic disorder (MOMD), and must be accounted for in order to fit experimental SSEPR spectra of vesicle solutions.

Spectral fitting of nitroxides exhibiting slow rotational motion or ordering are regularly carried out using a fitting program described extensively by Budil et al.[44] Commonly referred to as the Freed program, it is based on least-squares fitting of experimental spectra using the stochastic Liouville equation. Model parameters for the calculation of slow motion spectra include the magnetic and structural parameters of the radical, dynamic parameters including rates of rotational diffusion, and ordering potentials that describe the influence of anisotropic fluids like liquid crystals or membranes. On the whole, this makes the program useful for examining the dynamic motion of nitroxide radicals in micelle and vesicle structures. However, because a large number of parameters can contribute to the observed line shape of a slow motion EPR spectrum and least-squares fitting is particularly sensitive to over fitting, it is common practice to obtain the

magnetic parameters for a spin probe from a rigid limit spectrum and fit only the dynamic parameters and ordering potential.

There are several important coordinate systems to model nitroxide diffusional motion in supramolecular aggregates. These include the magnetic tensor frame of the molecule (x_M, y_M, z_M), the rotational diffusion tensor frame (x_R, y_R, z_R), the director frame (x_D, y_D, z_D), and the laboratory frame of reference (x_L, y_L, z_L). The relationship between these frames of reference is illustrated in Figure 4.2. The first two coordinate systems are based on the molecular frame of reference, and describe the orientation of the magnetic tensor and the rotational diffusion tensor of the molecule relative to the molecular geometry. In the case of a nitroxide molecule like those studied here, the magnetic frame and rotational diffusion frame are identical for axially symmetric spin probes like DSA. However, if necessary, the two frames of reference can be related to each other through a set of Euler angles, $\Omega_D = (\alpha_D\ \beta_D\ \gamma_D)$. In some cases, the magnetic frame and rotational frame of DSA spin probes are offset, and the inclusion of a value of β_D is necessary to relate the two frames of reference and more accurately fit the experimental data. This angle has been related to the presences of gauche bonds in the alkyl chain of the spin probe,[16b] which alters the rotational diffusion of the molecule and the orientation of the nitroxide moiety relative to the axis of molecular symmetry. When included in the calculations, values of β_D have been reported for DSA either between 27° to 40° in micelles and bilayers.[16b, 16d, 54]

The final two frames of reference are both related to the laboratory axis system.[44] The director frame describes the orientation of the molecule in anisotropic fluids, and the laboratory frame describes the direction of the applied magnetic field, which lies along the z_L axis. The director frame is related to the laboratory frame by a series of angles $\Psi=(0,\psi,0)$. Only one angle is required to relate the two reference frames because the orienting potential is axially symmetric.
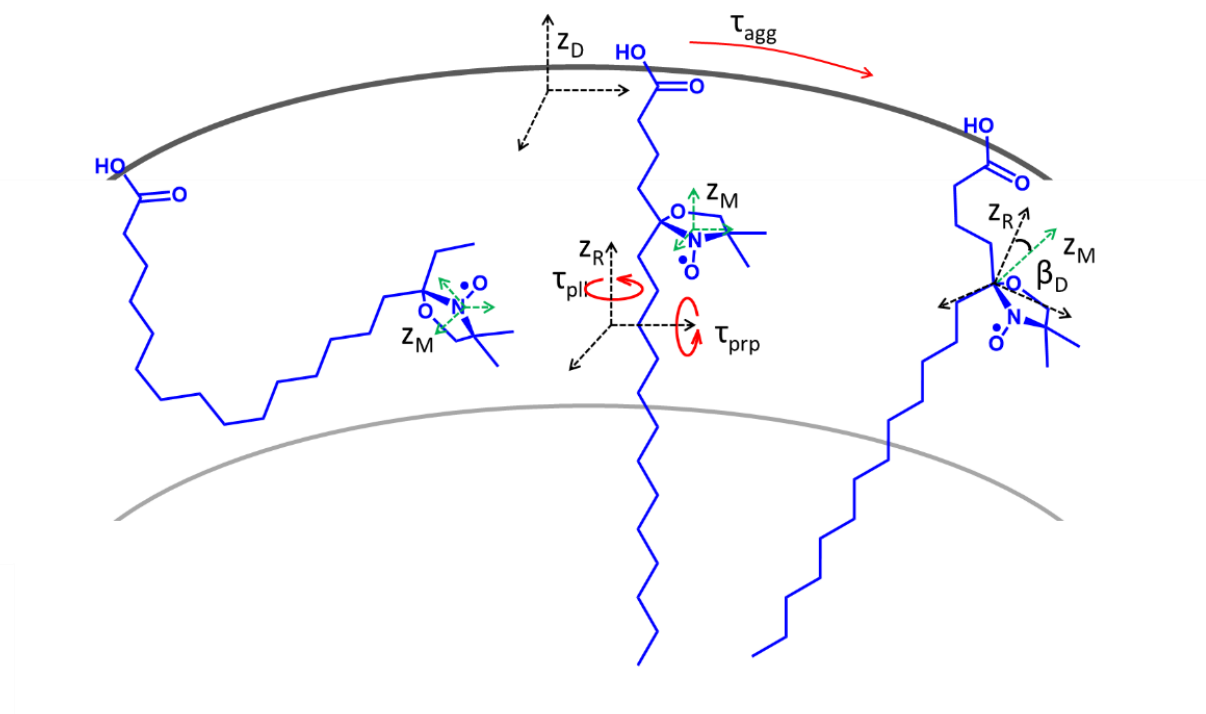
Figure 4.2 Schematic representation of the bilayer surface illustrating some of the relevant reference frames of the MOMD model for 16-DSA (left) and 5-DSA. The director frame (z_D) is normal to the bilayer. The rotational frame Z_R and the magnetic frame z_M of reference are both molecular frames and can be coincident (center) or offset (left, right) due to the conformation of the DSA chain. Rotational motion along the long axis of the spin probe is denoted by τ_{pll} and around the other axes as τ_{prp}. When fast enough, the rotational motion of the aggregate, τ_{agg} , which moves the director frame relative to the laboratory frame, z_L,can also be considered. The laboratory frame is related to the director frame by the director tilt angle, ψ. The laboratory frame is not shown, because the director frame can assume all possible orientations relative to the laboratory frame. A sum over these possible orientations of z_D relative to z_L is performed during MOMD model based simulations.

This angle ψ is referred to as the director tilt angle, and represents the angle between the director imposing the ordering in an anisotropic fluid and magnetic field.

In terms of simulating experimental spectra in vesicle or lamellar phases, the director tilt angle is particularly important because they exhibit microscopic order with macroscopic disorder (MOMD). In vesicles and bilayers there are domains of local ordering of the spin probes, but these ordered domains are distributed randomly and isotropically with respect to the laboratory frame. Because the EPR experiment is sensitive to the ordering of a spin probe, it is necessary to account for this local ordering to accurately reproduce the experimental spectrum. This is accomplished by integrating the spectral line shapes over the director tilt angle ψ. This MOMD model has been extensively and successfully applied to numerous vesicle forming systems, where the bilayer has been shown to impose a preferential orientation on axially symmetric spin probes like DSA. The application of the MOMD model to the catanionic SDS-DTAC systems is reported in greater detail in section 4.3.2

4.2.3 TREPR Studies of Micelles and Vesicles

As discussed extensively in the previous chapters, TREPR studies of RPs that have been photochemically generated in micelle surfactant aggregates are numerous.[17a, 17c, 55] The CFN model[56] for the SCRP mechanism of CIDEP was specifically developed to explain the observation of APS for RPs generated in SDS micelles.[57] The details of RP diffusion under nanoscale confinement in micelle structures can be directly extracted from the TREPR line shape, and in many cases TREPR studies of these systems provide information that is not easily obtainable by other spectroscopic methods. The fundamental features of RP diffusion in mixed surfactant systems should not differ substantially from the features of micellized RPs discussed in the

previous chapters, as long as the system is examined at a point in the phase diagram where micellar aggregates form.

To date, there are few TREPR investigations of RPs confined to vesicle structures. The only known study conducted on the TREPR of photochemically generated radicals in bilayer surfactant structures was performed by Moribe et al,[58] in which the TREPR of the photoreduction of anthraquinone-2-sulfate in phosphatidylcholine-based liposomes was examined. The AQS undergoes a hydrogen atom abstraction reaction with the phospholipid tails that is identical to the reaction between the BP or anthraquinone sensitizers with the alkyl tails of ionic surfactants discussed previously (Chapters 2 and 3). However, in liposome solutions, only a large, broad transition is observed at a g-factor that corresponds to the g-factor of the semi-anthraquinone (AQSH·) radical. Any radicals formed by phosphatidylcholine observed as very weak wings on the broad AQSH· signal. The weak signal and substantial broadening of the alkyl radical signal in the TREPR spectra are attributed to the significantly restricted motion of the RP inside the liposome bilayer.

4.2.4 The SDS-DTAC Catanionic Surfactant System

One of the earliest studies of the SDS-DTAC system was done by Malliaris et al.,[59] which examined the aggregation number (N_{agg}) for this system using conductivity and fluorescence measurements of a pyrene probe solubilized in the micelle structure for a total surfactant concentration ($C_{total} = $ [SDS]+[DTAC]) of 0.3 M. Measurements were not made in the region of $\chi_{SDS} = 0.22$-0.86 due to precipitation. A significant increase in N_{agg} was observed as the mixing ratio approached equimolar, and this increase was much faster for SDS rich micelles, where N_{agg} increased to approximately 400 by $\chi_{SDS} = 0.8$, than for DTAC-rich micelles, where N_{agg} was just

under 200 at $\chi_{SDS} = 0.2$. This behavior is interpreted in the context of the degree of ionization of the SDS and DTAC micelles relative to the mixed micelle. The counterion binding at a micelle surface is denoted by α, and represents the fraction of counterions that associate with the aggregate surface relative to number of molecules in the aggregate.[15a] The degree of ionization ($1-\alpha$) of the SDS micelle is less than the degree of ionization of the DTAC micelle. The association between the oppositely charged head groups of the surfactants causes the degree of ionization of SDS-rich micelles to decrease even further following surfactant mixing. The reduction in the degree of ionization of SDS allows for a greater increase in surfactant packing and N_{agg} with small additions of DTAC, and this effect is more pronounced for SDS-rich micelles because the initial degree of ionization is lower for SDS ($\alpha = 0.277$)[15a] than DTAC ($\alpha = 0.365$).[15b]

Composition dependent changes in the packing of DTAC and SDS monomers in mixed micelles of SDS-DTAC were examined by Weers and Scheuing using Fourier transform infrared spectroscopy (FT-IR) at 0.3M total surfactant concentration.[60] Because of the formation of strong ion-pair precipitates of dodecyl trimethylammonium-dodecyl sulfate ($DTA^+–DS^-$), FT-IR were not examined in the range of χ_{SDS}=0.23-0.85. The spectra were collected and examined on the SDS-rich ($\chi_{SDS} \geq 0.85$) and DTAC-rich ($\chi_{SDS} \leq 0.23$) side of the phase diagram for a total surfactant concentration of 0.3 M. This study found systematic shifts in the frequency of the CH_2 stretching bands of both SDS and DTAC in mixed micelles to lower frequencies than those observed in either pure SDS or pure DTAC micelles. The frequency and width of the CH_2 stretching bands are known to be sensitive to the ratio of gauche/trans conformers in the alkyl tails, which is a measure of the disorder of these tails in the micellar environment. This increase in order of the alkyl tails corresponds to the significant increase in aggregation number observed by Malliaris et al. [59] The authors argue that this correlation between ordering of the surfactant tails and the increase in N_{agg}

is indicative of changes in micelle structure from small spherical micelles to larger nonspherical ones. The effect is also more pronounced on the SDS-rich side of the phase diagram. Additional observations of the S—O stretching band of the SDS head group and the CH_3—N^+ stretching band of the DTAC head group indicate strong interactions between the oppositely charged head groups in mixed micelles and release of the associated Na^+ and Cl^- counterions with as χ_{SDS} approaches equimolar.

The first EPR study of the mixed SDS-DTAC system was carried out by Baglioni et al.,[20a] which reported the electron spin echo envelope modulation (ESEEM) and SSEPR measurements of doxyl stearic acid spin probes (x-DSA, x=5,7,10,12, and 16) in mixed surfactant solutions of SDS-DTAC as a function of mixing ratio.[20a] The SSEPR results were analyzed to obtain τ_c using the line width/line height equation (Eq. 21) for $\tau_c < 3$ ns or the Freed program for $\tau_c > 3$ ns. The ESEEM results were analyzed to obtained the deuterium modulation depth, which is a direct measure of the strength of the nitroxide-deuterium interaction when micelles were formed in D_2O.[20a] The total surfactant concentration was 0.05 M and the x-DSA concentration was 10^{-4} M. Significant precipitation was observed in the range of $\chi_{SDS} = 0.35$-0.65. SSEPR measurements were not obtained in this region, but ESEEM measurements were acquired by heating the samples overnight to obtain a homogenous solution followed by rapid freezing.

A decrease in the A_N was observed by SSEPR for the x-DSA probes from 15.8 G in pure water to 15.3G for SDS and 15.1 G for DTAC micelles (Table 4.1). Mixing of the two surfactants lead to a further decrease in the value of A_N that was concentration dependent, but reached a minimum of 14.7 G for measurements made closest to equimolar mixing ($\chi_{SDS} = 0.25$ or 0.75). This is indicative of a decrease in surface polarity for the mixed micelles. The authors suggest that electrostatic interactions between the SDS and DTAC head groups result in the expulsion of water

molecules from the head group region of the aggregates. Analysis of the rotational correlation times was performed as a function of the composition of the mixed micelles. As the mixing ratio of the two surfactants approached equimolar, τ_c increased for all x-DSA spin probes, which indicates an increase in microviscosity within the aggregates. The increase in τ_c was greater when the doxyl was positioned closer to the head group 5-DSA > 7-DSA > 10-DSA > 12-DSA > 16-DSA. This suggests that changes in microviscosity inside the micelle aggregates is greater near the head groups on the surface of the mixed micelle than in the inner part of the mixed micelle. The measured τ_c increases faster on the DTAC-rich side of the phase diagram than the SDS-rich side. For 5-DSA, an increase in τ_c from approximately 1.2 ns to 5.6 ns is observed as χ_{SDS} approaches 0.35, but on the SDS-rich side of the phase diagram this value only increases to approximately 4.8 ns as χ_{SDS} approaches 0.65. The τ_c for 10-DSA, 12-DSA, and 16-DSA do not

Table 4.1 Literature values for the physical properties of the SDS-DTAC system as a function of mole fraction SDS at 50 mM total surfactant concentration

X_{SDS}	N_{agg}[a]	A_N[b]	a (nm^2)[a]	R (nm)[c]
0.0	48	15.1	83	1.8
0.1	98	14.9	59	2.1
0.2	117		55	2.3
0.3	157		51	2.5
0.4				47[d]
0.5				
0.6				56[d]
0.7	3744		36	10.4
0.8	279		41	3.0
0.9	129	15.1	47	2.2
1.0	77	15.3	58	1.9

[a] from Prevost et al.,[4b] [b] from Baglioni et al.,[20a] [c] calculated from N_{agg} and a,
[d] volume weighted average radius for vesicle fitting of SANS data reported in Prevost et al.[4b]

exhibit such a pronounced difference in τ_c between SDS-rich and DTAC-rich micelles.

ESEEM is a version of pulsed EPR that measures the intensity of the signal from the refocusing of the electron spins known as the spin "echo." The echo intensity is measured as a function of the delay time between pulses to provide information of the decay of the echo due to relaxation. The echo intensity is sensitive to weak dipolar interactions between neighboring paramagnetic species or magnetic nuclei within a close range (0.2-0.6 nm). Mixed micelle solutions were created in deuterated water, then rapidly frozen. Measurements of the electron spin echo modulation were analyzed as a function of the position of the doxyl group on the stearic acid chain. Greater contact between the doxyl group and the D_2O solvent is inferred from the deuterium modulation depth, which can include contact with a greater number of deuterium atoms or a closer distance between the D_2O and the spin probe.

The normalized deuterium modulation depth measured by ESEEM for SDS, DTAC, and mixed micelle solutions was greatest for 5-DSA and smallest for 10-DSA. It increases again for 16-DSA. The trend in deuterium modulation depth relative to the position of the doxyl group along the stearic acid chain suggests that the 16-DSA and 12-DSA adopt a bent or U-shaped conformation of the stearic acid chain, with the hydrophilic doxyl group closer to the micelle surface than the micelle interiors. This is consistent with more recent reports on the behavior of the 16-DSA spin probe in micellar environments in SSEPR measurements.[52] In addition, the modulation depth is smaller for mixed micelle solutions when compared to pure SDS or DTAC for all the x-DSA probes. The decrease in modulation depth as the surfactant mixing ratio approaches equimolar suggests electrostatic attraction between the surfactant head groups cause a decrease in the number of water molecules with access to the alkyl tails of the surfactant at the

micelle surface, which is consistent with the conclusions drawn from the SSEPR results and with the previously reported FT-IR results.[60]

There are three features of the study conducted by Baglioni et al. [51a] that merit substantial scrutiny and criticism. First, the expression for τ_c in Eq. 21 is typically considered reliable for rotational correlation times faster than 1 ns, but was used in their work up to 3 ns. The value of τ_c obtained from Eq. 21 is known to be inaccurate for spin probes experiencing anisotropic motion, and SSEPR studies of the x-DSA spin probes have shown substantial differences in the anisotropy of the spin probe rotation as a function of the position of the doxyl moiety along the stearic acid chain. Second, no mention is made whether or not the MOMD model was used for simulations of the x-DSA spin probes. Ordering of the x-DSA probes would require the use of the MOMD model for accurate simulation of the spectra. Although Baglioni et al.[51a] do not report precipitation in solutions of DTAC-rich micelles and $C_{total} = 50$ mM until $\chi_{SDS} = 0.35$, other studies have reported noticeable precipitation at lower mixing ratios. If precipitation occurred, it is possible that the EPR spectra could be broadened by Heisenberg spin exchange between the doxyl spin probes that would lead to an overestimation of the τ_c. Finally, in the ESEEM measurements, there is no guarantee that the equilibrium structure of the surfactant aggregates in the heated samples ($\chi_{SDS} = 0.35$-0.65) is analogous to the equilibrium structures of the aggregates at room temperature. Phase transitions are known to occur in mixed micelle systems upon heating, particularly in systems that can form lamellar phases.

Despite the fact that the SDS-DTAC system had been previously studied, a phase diagram of the system was not published until 2004 by Stenstam et al,[61] although it was based strictly on visual observation of solutions of SDS-DTAC. Earlier studies of the SDS-DTAC system refer to their results only in the context of micellar phases, but the phase diagram suggests the existence

of vesicle or bilayer structures in this catanionic system. The first experimental evidence for the formation of vesicle structures in catanionic mixtures of SDS/DTAC was reported by Prevost and Gradzielski in 2009,[4b] some of which is shown in Figure 4.3A. Prevost's published phase diagram was also constructed on visual observation of the solutions in the range of 4 mM to 200 mM total surfactant concentration, with the presence of bluish turbidity used as an indication of vesicle formation. However, SAXS and SANS measurements were obtained for two different concentrations of surfactant (50 mM and 200 mM) and at two different temperatures (25 ° and 50 °C). The "pure micelle" data from both experiments could be fit as monodisperse core-shell triaxial ellipsoids. This same model could be applied to mixed micellar results on the SDS-rich and DTAC-rich sides of the phase diagram. Visual observation at 50 mM surfactant concentration and 25 °C suggested the formation of vesicles from χ_{SDS} = 0.1-0.7. SANS measurements under these conditions could be fit with a model for densely packed vesicles for a range of χ_{SDS} = 0.4-0.6. Precipitation of the surfactant ion-pair was also observed over a range of χ_{SDS} = 0.1-0.6, which is slightly larger than the range reported for Baglioni et al.[20a] for the same concentration. Heating of the surfactant mixtures above 40-50 ° C resulted in the disappearance of any precipitate, suggesting that these temperatures are above the Krafft temperature of the mixed surfactant system.[4b] These experimental measurements allowed for an estimation of the size of the surfactant aggregates, the area per surfactant head group at the surface, and the aggregation number, which was calculated assuming the composition of the surfactant in the micelles was identical to the mixing ratio of surfactants in solution. A summary of these results is shown in Table 4.1. These values of N_{agg} are not directly comparable to those reported by Malliaris et al.[59] because the two studies were performed at different concentrations and make different assumptions about the composition of the micellar aggregates; however, the general trend in N_{agg} observed in both is identical, with N_{agg}
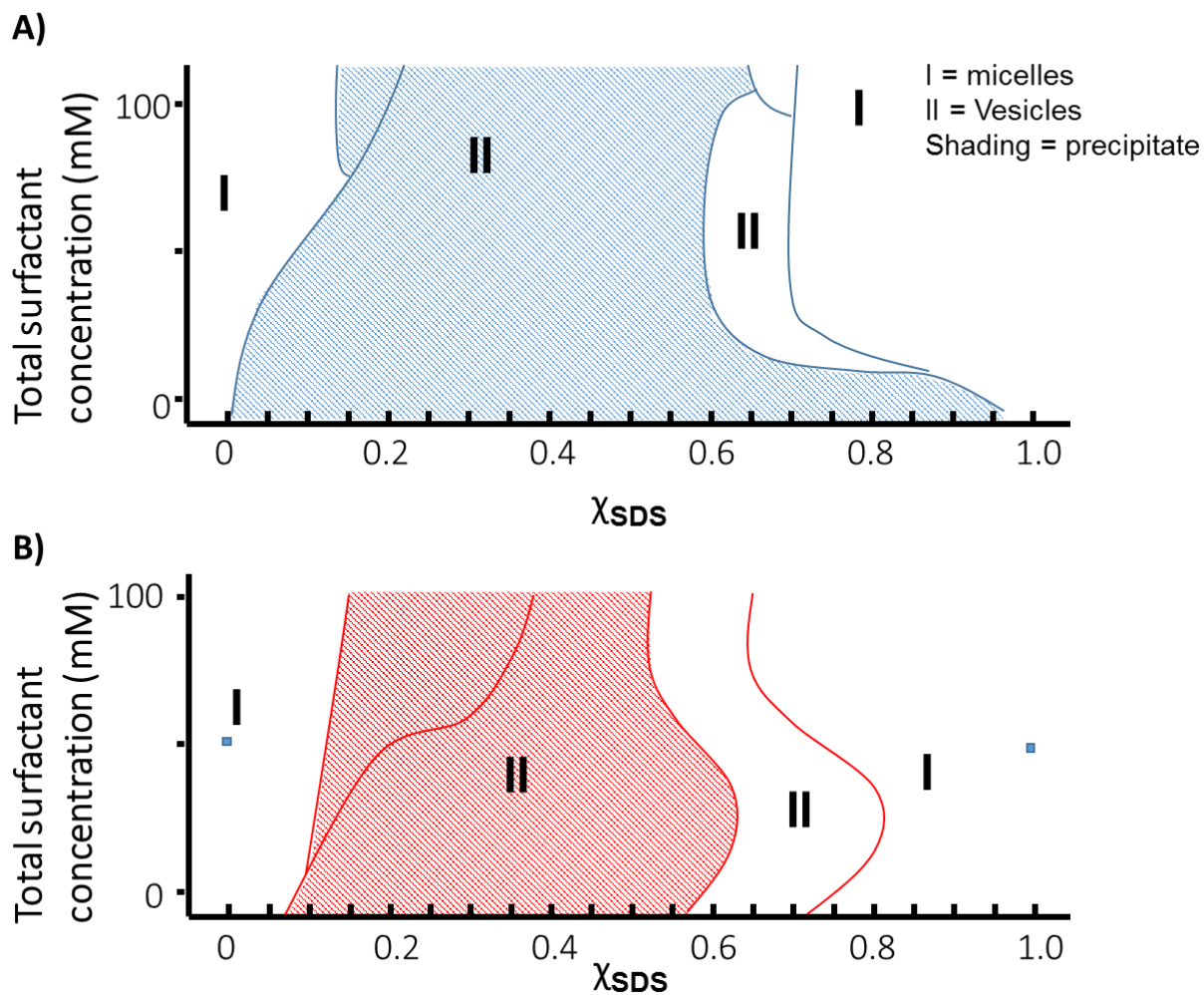
Figure 4.3 Comparison of the published phase diagram from Prevost et al.[4b] (A) constructed from visual observation of solutions of SDS-DTAC for total surfactant concentrations between 4 mM and 100 mM and the phase diagram constructed based on experimental results (B) reported in section 4.3.1 for total surfactant concentrations between 10-100 mM. Regions of the phase diagram that are shaded denote mixing ratios at which precipitate is observed. **I** denotes micelle formation and **II** indicates vesicle formation.

increasing faster for SDS-rich micelles than DTAC-micelles as the mixing ratio approaches equimolar. To date, the SANS measurements of Prevost and Gradzielski[4b] appear to be the only experimental measurements of the properties of the catanionic SDS-DTAC system for solutions near equimolar mixing and under ambient conditions where vesicle formation might be expected. The experimental work reported in this chapter seeks to further characterize the SDS-DTAC system across the entire range of χ_{SDS} using SSEPR and TREPR spectroscopies.

4.3 Results and Discussion

4.3.1 Characterization of the Phase Behavior of SDS-DTAC

Characterization of the phase behavior of the SDS-DTAC system was undertaken by visual observation, UV-vis measurements of turbidity, [62] and DLS measurements of aggregate size. [63] Additional evidence for the phase behavior obtained from the SSEPR and TREPR measurements described in section 4.3.3 and 4.3.4 were also considered. Samples were examined at concentrations of 10 mM, 25 mM, 50 mM, 75 mM, and 100 mM over a period of one month from their creation, in order to ensure that observations were being made on an equilibrated sample. The phase diagram constructed from these measurements is shown in Figure 4.3B. Micelle formation occurs on the SDS and DTAC-rich sides of the phase diagram, separated by a vesicle or lamellar phase. Vesicle formation appears to occur over a wider range at a concentrations for $C_{total} = 10$ mM or 25 mM. At 50 mM, vesicle formation is expected from $\chi_{SDS} = 0.3\text{-}0.7$, while at high C_{total} this range is reduced to $\chi_{SDS} = 0.4\text{-}0.7$, which is generally in good agreement with the phase diagram and SANS measurements reported by Prevost and Gradzielski.[4b] One reason for the possible discrepancies between these two phase diagrams is the presence of precipitation, which can significantly impair the visual observation of turbidity in the solutions.

Precipitation is observed from approximately $\chi_{SDS} = 0.1$ for all concentrations, and extends to χ_{SDS} of approximately 0.6 at low surfactant concentrations and ends more abruptly at $\chi_{SDS} = 0.5$ at higher values of C_{total}. Noticeable precipitation was observed in the region of $\chi_{SDS} = 0.1$-0.6 for $C_{total} = 50$ mM. An approximation of the degree of precipitation was obtained by filtering mixed surfactant solutions after their equilibration and weighing the filtered precipitate. Table 4.2 shows the measured degree of precipitation as a function of surfactant mixing ratio for solutions where $C_{total} = 50$ mM. Precipitation is most significant from $\chi_{SDS} = 0.2$ to $\chi_{SDS} = 0.6$, with a maximum at equimolar mixing that is consistent with the theory describing the precipitation behavior for catanionic surfactants. Only a small amount of precipitate is observed at $\chi_{SDS} = 0.1$. Table 4.2 also shows the adjusted concentration of surfactant in solution that is in equilibrium with the precipitate.

DLS measurements are frequently employed to evaluate the size of surfactant–based aggregates that are either biologically or synthetically based.[63] Results from the DLS sizing experiments provide information on the hydrodynamic radius of the resulting nanostructures, which confirmed a significant increase in size of the aggregate structures as mixing ratios approached equimolar, from $R_h \approx 1.2$-1.5 nm for pure SDS and DTAC to $R_h \approx 35$-38 nm at $\chi_{SDS} = 0.4$ or 0.6. There is generally good agreement between the DLS measurements and the values of the radius of the aggregate structure calculated using the SANS data in Prevost and Gradzielski[4b] that are reported in Table 4.2. In order to obtain more accurate measurements of the size of the aggregate structures, samples were passed through a 0.2 μm syringe filter before measurement. Despite filtration, some anomalous peaks were observed in the DLS measurements with average values of $R_h \approx 1000$ nm. In catanionic surfactant solutions, the precipitate exists in equilibrium with the surfactant aggregates and monomer. Filtering out the precipitate disturbs this equilibrium,

so the large particulate measured by DLS is most likely due to the formation of new precipitate in the filtered solution, which occurs quickly following filtration when χ_{SDS} is near equimolar.

4.3.2 Synergism in Mixed Micelles of SDS-DTAC

Iterative solutions for the activity coefficients in the mixed micelle solutions from Eqs. 18 and 19 and the degree of precipitation observed as a function of the mixing ratio reported in Table 4.2 allows for the calculation of the concentration of aggregates and the composition of surfactants in the aggregates. Table 4.2 shows the results of these calculations, including the value of the CMC of the mixed surfactant systems, *CMC_mix*, as a function of the mixing ratio. The general trend in the *CMC_mix* reveals that the mixed surfactant solutions generally have a lower value for the CMC than either of the pure surfactants (CMC < 20.3 mM on the DTAC-rich side and CMC < 8.2 mM on the SDS-rich side. This is consistent with the expectation that the SDS-DTAC system would exhibit strong synergism and non-ideal behavior due to electrostatic interactions between the

Table 4.2 Degree of precipitation, effective concentration of surfactant after precipitation, mole fraction of SDS in aggregates (x), concentration of surfactant incorporated in aggregates (C_{agg}), concentration of free monomer of SDS and DTAC, and CMC of the mixed systems as a function of the total mole ratio of SDS in solution, χ_{SDS}

χ_{SDS}	Degree of precipitation (wt %)	Effective C_{TOTAL} (mM)	x	C_{agg}	C_{SDS}^{free}	C_{DTAC}^{free}	CMC_{mix}
0.0	0.0	50	0.0	29.70	0.0	20.30	20.30
0.1	2.2	48.9	2.2	29.35	0.24	19.30	19.55
0.2	19.0	40.5	19.0	24.85	0.65	14.99	15.64
0.3	46.8	26.6	46.8	15.33	1.35	9.93	11.27
0.4	28.4	35.8	28.4	26.08	1.73	7.98	9.72
0.5	77.3	11.4	77.3	4.24	3.25	3.92	7.16
0.6	68.3	15.8	68.3	8.92	4.01	2.87	6.88
0.7	0	50	0.0	42.83	5.67	1.42	7.17
0.8	0	50	0.0	42.15	7.18	0.66	7.85
0.9	0	50	0.0	41.18	8.58	0.23	8.82
1.0	0	50	0.0	41.80	8.2	0.0	8.20
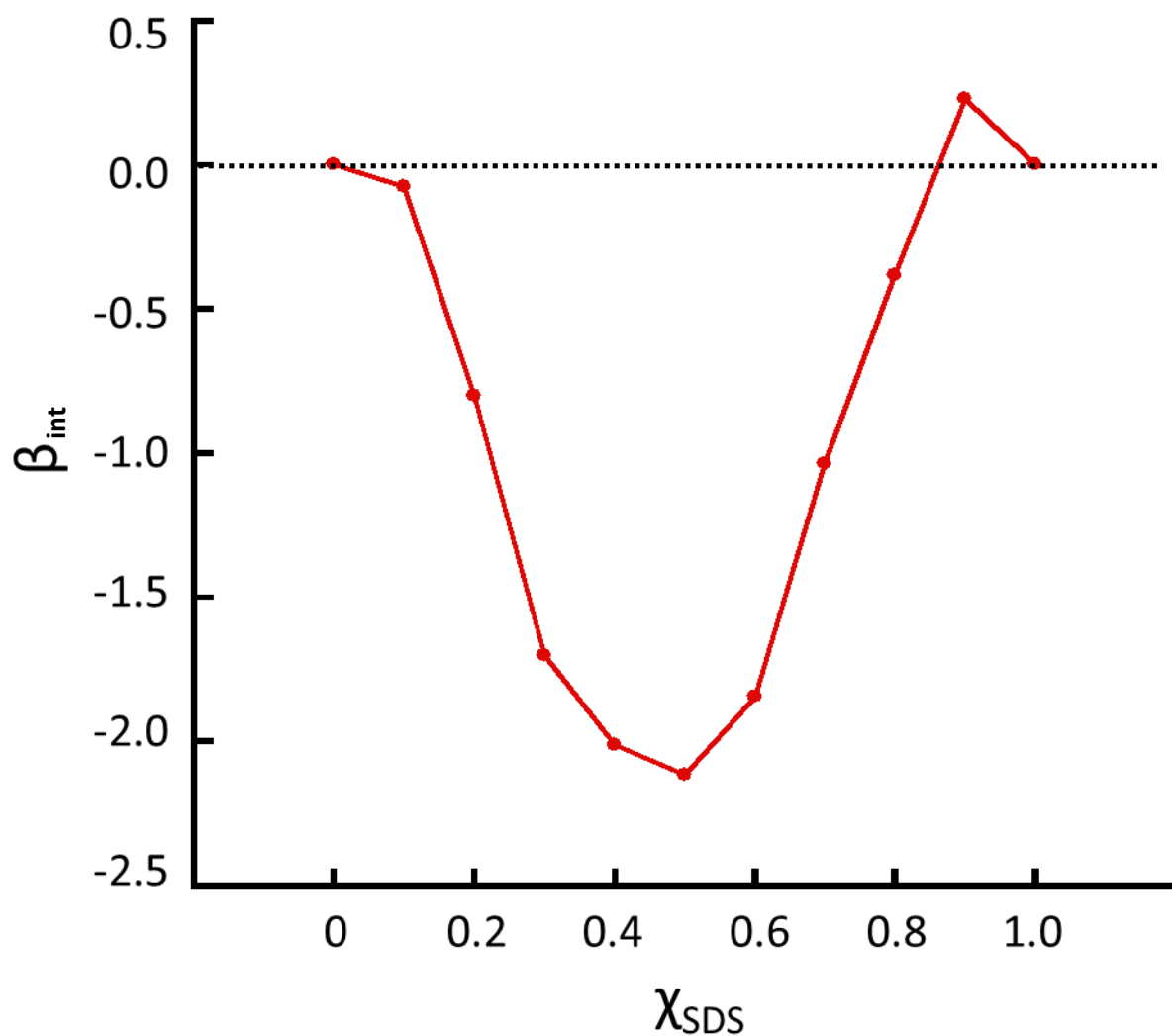
Figure 4.4 The calculated deviations from ideal behavior, as quantified by the model-independent thermodynamic parameter, β_{int}, for solutions of 50 mM SDS-DTAC after accounting for the degree of precipitation reported in Table 4.2. $\beta_{int} < 0$ corresponds to a negative deviation from ideal behavior (synergism), while $\beta_{int} > 0$ corresponds to a positive deviation from ideal behavior (antagonism).

surfactant head groups.

One interesting anomaly in this general trend is the value for the CMC_{mix} at $\chi_{SDS} = 0.9$, where the CMC_{mix} is slightly larger than the CMC of pure SDS. Figure 4.4 shows the value of the interaction parameter, β_{int}, for SDS as a function of mixing ratio. In general, the value of β_{int} negative, as expected for a catanionic system. However, around $\chi_{SDS} = 0.9$ the interaction parameter is slightly positive, suggesting that the incorporation of DTAC into SDS micelles is initially antagonistic. Antagonism in mixed surfactant systems has been previously reported for catanionic is mixtures of gemini surfactants, mixtures of nonionic surfactants with sodium alkyl sulfonates,[64] mixtures of surfactants with hydrocarbon and perfluorinated chains,[2b] and mixtures of cationic surfactants with identical head groups but different tail lengths.[65] In the latter two cases, the antagonistic behavior was attributed to strong effects of stearic hindrance and a mismatch in the hydrophobicity of the alkyl tails. In mixtures of double tailed ionic and non-ionic surfactants, antagonism has been attributed to differences in the CPP.[66] It has also been attributed to stearic effects for surfactants that have bulky head groups, where the interaction was observed to be synergistic on one side of the phase diagram and antagonistic on the other.[64] The most likely explanation for the slight antagonism observed with the addition of DTAC to SDS is steric effects between the head groups and the difference in CPP between the two surfactants. The volume of the hydrophobic portion of the molecule and the length of the alkyl tail in SDS and DTAC should be identical. This suggests that only a difference in volume of the head groups is responsible for differences in the CPP. The molecular volume for the sulfate head group of SOS has been measured as 0.0472 nm^3, while the molecular volume of the DTAC head group is more than twice this value at 0.1090 nm^3.[4b] The more bulky CH_3 groups of the DTAC head group may be responsible for stearic hindrance that make its incorporation into SDS-rich micelles less

energetically favorable when the molar ratio of DTAC in the mixtures is low, but this effect is obviously overcome by the addition of more DTAC.

Another important feature of the data in Table 4.2 is the concentration of aggregated surfactant, C_{agg}. At mixing ratios where there is a significant degree of precipitation, the total concentration of surfactant dissolved in solution is much lower than the total surfactant concentration. Surfactant aggregates must also be at equilibrium with surfactant monomers in solution, so the surfactant incorporated into aggregate structures is even lower still. At this point, it is also important to consider information on N_{agg} for the SDS-DTAC system[4b, 59] For solutions where vesicles are formed and N_{agg} is high, the total concentration of aggregates in solution will be very low. For example, at $\chi_{SDS} = 0.3$, C_{agg} is only 15.3 mM. The N_{agg} measured by Prevost and Gradzielski.[4b] at this mixing ratio is 157. The resulting concentration of aggregates structures 0.1 mM, almost two orders of magnitude lower than C_{agg} and substantially lower than C_{total}. The degree of precipitation and N_{agg} are both higher for χ_{SDS} closer to equimolar mixing, which explains why previous studies of the SDS-DTAC system avoided these mixing ratios or were generally unable to detect very small concentrations of aggregates at room temperature.

4.3.3 SSEPR Spin Probe Studies of Surfactant Aggregate Structure

4.3.3a Rotational Correlation Time

Solutions of SDS-DTAC at mixing ratios over the full range of χ_{SDS} were studied with three different spin probes, 5-DSA, 16-DSA, and 4-hydroxy tempo benzoate (4-HTB) for C_{total} between 25 mM and 100 mM. Figure 4.5 shows a comparison of the SSEPR spectra collected from all three spin probes at $C_{total} = 50$ mM and a point in the phase diagram where the formation of micelles ($\chi_{SDS} = 0$) and mixed micelles ($\chi_{SDS} = 0.3$) is expected. The rotational correlation times for all
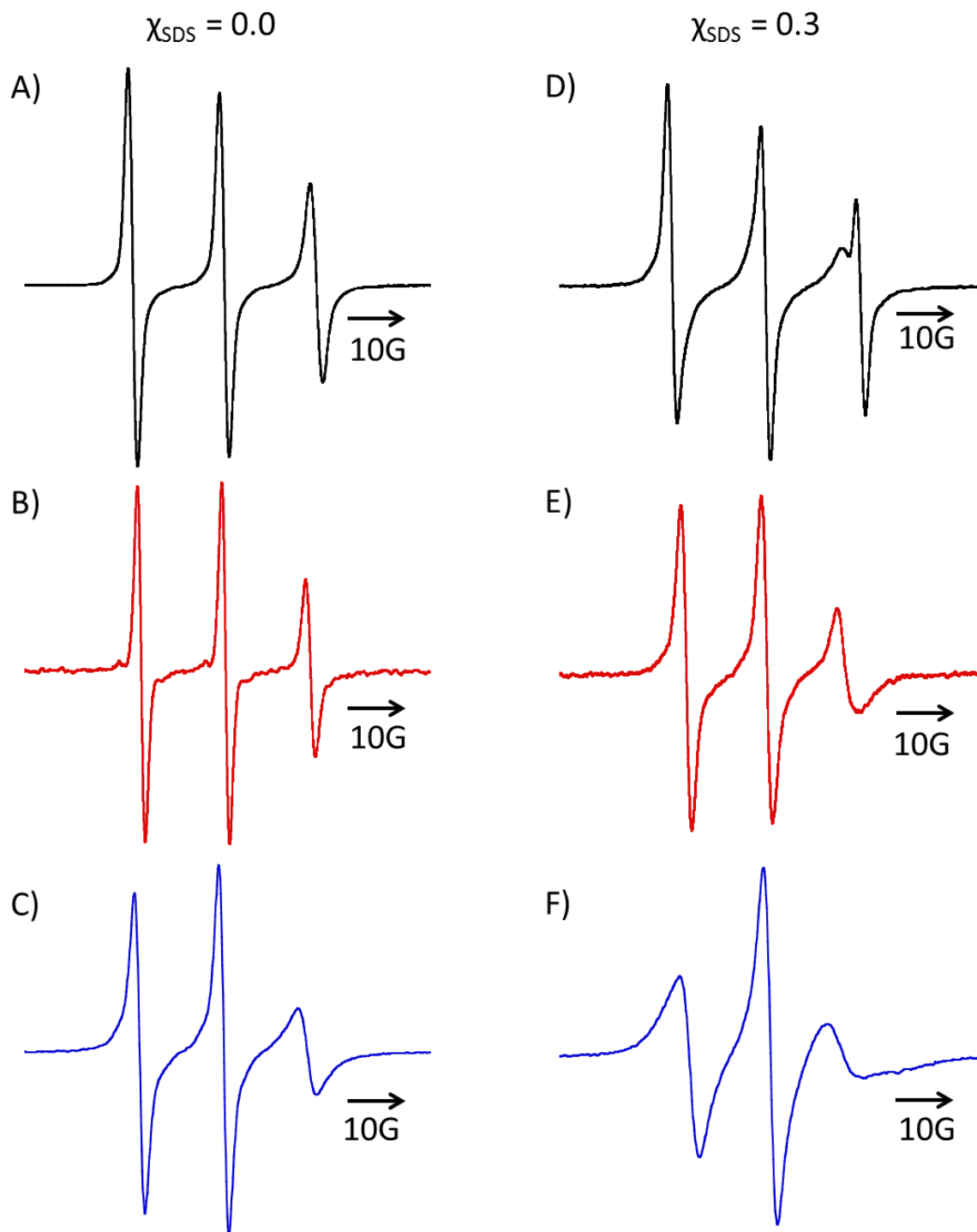
Figure 4.5 SSEPR of solutions of SDS-DTAC with a total surfactant concentration of 50 mM at a mixing ratio of $\chi_{SDS} = 0.0$ with (A) 4-HTB, (B) 16-DSA, and (C) 5-DSA or $\chi_{SDS} = 0.3$ with (D) 4-HTB, (E) 16-DSA, and (F) 5-DSA. Spin probe concentrations were 0.2 mM for all spin probes.

values of χ_{SDS} and 5-DSA and 4-HTB are reported in Table 4.3. The line shape of the 4-HTB appears complicated and asymmetric at both $\chi_{SDS} = 0$ and $\chi_{SDS} = 0.3$. For Figure 4.5A, where the 4-HTB is incorporated into DTAC micelles, the low-field line is significantly more intense than the center-field line. This intensity pattern can be reproduced if we assume that there is a mismatch between the principle axes for the rotational diffusion and the magnetic tensors of the 4-HTB. Simulations were carried out to obtain the rotational correlation time of 4-HTB in these samples assuming a value of β_D, which relates z_R to z_M, of $65°$. It is clear from Figure 4.5D that the 4-HTB spectra for some mixing ratios are a superposition of the SSEPR spectra of the spin probe experiencing at least two different motional regimes – one fast motion spectra with sharp transitions, and one slow motion spectra with broader transitions from the spin probe incorporated into a less polar environment. The rotational correlation times collected for the 4-HTB using the Freed program are reported in Table 4.3, with the rotational correlation time for both sites reported as necessary. Partitioning of small spin probes is commonly observed in both micelles and vesicles; however, only the fast motion spectrum is observed when $\chi_{SDS} = 0.4$-0.6. This is the same region where SANS measurements suggest the formation of vesicles. The exclusive observation of a fast motion SSEPR spectrum for 4-HTB in this region suggests that the spin probe does not incorporate well into the vesicle structure. Because the probe is relatively hydrophilic, it is possible that it is expelled from the aggregate structure as water is forced from the aggregate surface during the micelle to vesicle phase transition. From the values of τ_c in Table 4.3, it is clear that the fast motion component of the spectrum corresponds quite well with the rotational correlation time and hyperfine values of 4-HTB in pure water.[67]

When comparing the DSA based spin probes, the line shape of the 5-DSA probe (Fig 4.5C, F) is broader and the high field peak much shorter than for the related 16-DSA spin probe (Fig

Table 4.3 Rotational correlation times obtained from spectral fittings of slow motion SSEPR spectra with spin probes 4-HTB, as a function of χ_{SDS} for a total surfactant concentration of 50 mM

χ_{SDS}	τ_c 4-HTB (x 10^{-10} s)
0.0	3.7
0.1	4.2
0.2	4.7
0.3	6.6, 0.53
0.4	0.53
0.5	0.53
0.6	0.53
0.7	8.35, 0.53
0.8	6.6, 0.53
0.9	4.2, 0.53
1.0	3.3

4.5B, E). The shortening of the high-field transition relative to the others is indicative of anisotropic rotational motion, but the reduced line width of the 16-DSA spectra suggest that this probe experience faster rotational motion than 5-DSA. Simulations of the SSEPR spectra of the DSA probes in solutions of pure SDS or DTAC reveal that the anisotropic of the spin probe, measured by the ratio $R_{\parallel} / R_{\perp}$, is greater for 5-DSA ($R_{\parallel}/R_{\perp} \approx 25$) than for 16-DSA ($R_{\parallel}/R_{\perp} \approx 6$), and the τ_c of 5-DSA is approximately twice that of 16-DSA. Historically in micelle solutions, this it was assumed that the faster rotational motion of 16-DSA was observed because the radical moiety was located in the more fluid, hydrophobic interior of the aggregate. Careful measurements of the DSA and related DSE spin probes by ESEEM and calculation of the degree of hydration as a function of position of the doxyl moiety on the stearic acid chain reveals that the doxyl group at the 16-position often inhabits an environment that is more polar and more accessible to water than the 5-position. The faster rotational motion observed in Figure 4.5 A, B, and C is actually due to

"hairpinning" of the flexible stearic acid chain that allows the polar nitroxide to exist in the more polar regions of the micelle surface, which is reflected in the faster τ_c value. The fast rotational correlation time of 16-DSA and 5-DSA obtained in solutions of SDS or DTAC support the conclusion that the 5-DSA is more closely associated with the interior of the micelle and more sensitive to changes in aggregate structure caused by differences in the surfactant mixing ratio. For this reason, an extended discussion of the features and the spectral fitting of the 5-DSA spectra will be undertaken here.

Spectral simulations of the DSA probes in mixed surfactant solutions of SDS and DTAC were carried out using the MOMD model[16b, 68] for all values of χ_{SDS}. The MOMD model is not required to fit the micelle spectra, since micellar structures are highly disordered. However, the exact location of the micelle to vesicle phase transition is unclear, and the quality of the fits was not significantly improved by switching to a non-ordered simulation model. The uniform application of the MOMD model to the entire data set avoided some discontinuities the fitted parameters in regions where transitions between micelle and vesicle structures were expected. As these discontinuities appeared unphysical, a continuous application of the MOMD model across the data set was deemed more appropriate for analyzing the general qualitative trends in the fitting parameters. Considering the relatively slow motion of the spin probe and the ordering of the probe in the vesicle environments, a truly unique fit to the experimental data cannot be expected or obtained. However, the dynamic information obtained in the pure micelle systems is close to reports in the literature for the rotational correlation times of these spin probes in SDS and DTAC micelles. If the rotational anisotropy of the probe is omitted from the spectral fittings, the value of τ_c obtained from the Freed program for pure SDS micelles converges with the literature value reported for the τ_c of SDS (~0.6 ns) obtained from the line width/line height expression in Eq. 21.

[46] In addition, the criteria for the quality of the fit between the experimental and simulated spectra, as measured by the residual index, correlation coefficient, and reduced χ^2 test, were highest across board for the results reported here. Therefore, we are confident that a qualitative discussion of the observed trends is physically relevant and meaningful.

Simulations were carried out with the magnetic parameters for the spin probe fixed from rigid limit measurements reported in the literature.[69] The only magnetic parameter that was allowed to vary in the fits was the A_{zz} component of the hyperfine tensor, because this parameter is known to be sensitive to the polarity of the local environment of the spin probes.[53] Variation of both the parallel ($R_∥$) and perpendicular ($R_⊥$) components of an axial diffusion tensor can lead to large uncertainties and strong correlations between parameters in the fit. Better fits could be obtained by varying the isotropic rotational diffusion tensor ($\bar{R}$) but specifying the anisotropy of the molecular diffusion using the value N, where $N = R_∥ / R_⊥$.[44] This is common for slow motion spectra exhibiting significant anisotropic motion. As the rate of rotation slows, the fitting procedure becomes less and less sensitive to the slower component of the rotational diffusion. Furthermore, the values of N have been reported previously for these spin probes in similar systems in the literature, which allows us to make an intuitive choice for the starting parameters of both $\bar{R}$ and N based on these measurements.

In addition to these rotational diffusion parameters, spectra were also fit by varying the ordering potential via its coefficients, the homogenous broadening of the spectra, and the rate of Heisenberg spin exchange, if applicable. The best fit results for the experimental SSEPR spectra at $C_{total} = 50$ mM are shown in Figure 4.6, while the exact values obtained for these parameters are contained in Table 4.4. It is clear that a substantial difference is observed between spectra collected in pure micelles ($\chi_{SDS} = 1.0$ and 0.0) than those collected close to equimolar mixing. The spectra
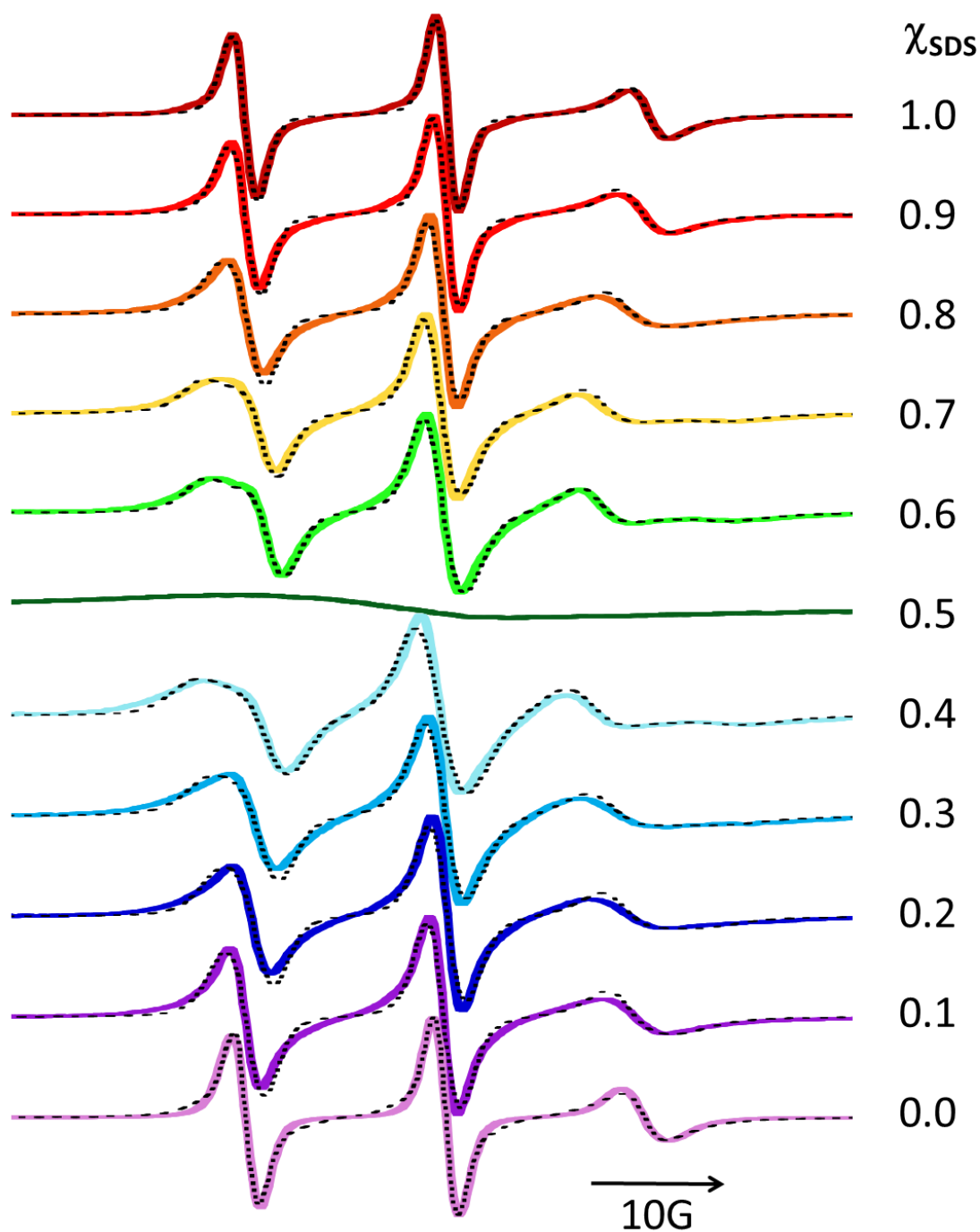
Figure 4.6 SSEPR of solutions of SDS-DTAC with a total surfactant concentration of 50 mM and 0.2 mM 5-DSA as a function of the mole ratio of SDS, χ_{SDS}. Black dotted lines represent the best fit of the experimental data obtained from the Freed program for slow motion SSEPR using the MOMD model. Fitting parameters can be found in Table 4.4.

Table 4.4 Parameters for rotational correlation times, order parameter, and isotropic hyperfine obtained from MOMD fitting of 5-DSA in solutions of C_{total} = 50 mM as a function of χ_{SDS}

χ_{SDS}	τ_{agg} (x 10^{-9} s)	τ_c (x 10^{-10} s)	$\tau_{\parallel}$ (x 10^{-10} s)	$\tau_{\perp}$ (x 10^{-10} s)	τ_{doxyl} (x 10^{-10} s)	S_{eff}	A_N (G)
1.0	6.99	3.29	0.39	9.62	3.45	0.07	15.2
0.9	10.85	3.27	0.38	9.57	3.37	0.11	15.1
0.8	27.52	3.98	0.47	11.6	4.04	0.16	15.0
0.7	1.02×10^3	4.25	0.50	12.4	4.25	0.28	14.7
0.6	1.79×10^5	3.64	0.43	10.6	3.64	0.30	14.5
0.4	1.06×10^5	4.40	0.52	12.9	4.40	0.35	14.5
0.3	15.92	4.83	0.57	14.1	4.98	0.24	14.9
0.2	12.40	4.42	0.52	12.9	4.58	0.19	14.9
0.1	10.85	4.10	0.48	12.0	4.26	0.13	14.9
0.0	5.94	3.65	0.43	10.7	3.89	0.08	15.0

of pure SDS and pure DTAC micelles exhibit slight anisotropy in the rotation of the 5-DSA probe, which is evident from the shortening and broadening of the high field line. This anisotropy and the observed broadening in the micelle spectra in Figure 4.6 suggest that the rotational motion of the spin probe may be slow and requires a full line shape analysis to extract quantitative information about the dynamic behavior of the spin probe in these micellar systems.

At mixing ratios of χ_{SDS} = 0.2 and 0.8, the high and low field lines of the EPR spectra become shorter and broader. The broadening of the high field transition appears much more substantial than the low field transition, but both transitions appear to become asymmetric. This behavior is characteristic of slow motion, suggesting that the rotational correlation time of at least one axis of the 5-DSA is slowing as the two surfactants are mixed. Near equimolar mixing (χ_{SDS} = 0.4, 0.6), the line shape of the EPR spectra differs substantially from those at lower mixing ratio. The high-field transition exhibits "double peaking," in that it appears to be a superposition of two EPR transitions at slightly different positions and with slightly different widths. Figure 4.7 shows

an expansion of the spectra at $\chi_{SDS} = 0.4$ and 0.6. This characteristic line shape has been interpreted in the literature in two different fashions: either the spin probe is sampling two different motional environments[54, 70] or it is experiencing molecular ordering[16d, 16e, 71] that is affecting the line shape of the EPR spectrum. In some spectra, double peaking of the low field line can be observed, too, but the separation of the components of the transition is not as pronounced as the high field line. It could be argued that, under these conditions, the SDS-DTAC system is forming both micelles, which would have a faster rotational correlation time, and vesicles – which would exhibit a slower rotational correlation time. The double peaking of the SSEPR spectrum would then be caused by a superposition of these faster and slower components. Intuitively, in order for the experimental spectra in Figure 4.7 to be a superposition of two EPR spectra from spin probes in different types of aggregate structures, substantial differences in the g-factor, hyperfine, and rotational correlation time between 5-DSA in micelles and vesicles would be expected. Such large differences are not supported by the literature or by measurements made in pure DTAC or SDS micelles. A two–component micelle-vesicle explanation of the line shape seems untenable; however, simulations of the spectra as two component systems using the Freed program were undertaken. These simulations returned unrealistic values for the rotational correlation time, g-factor, or hyperfine tensor components – but often the quality of the fits were poor or completely unsuccessful. It is more likely, therefore, that the line shape of the $\chi_{SDS} = 0.4$ and $\chi_{SDS} = 0.6$ spectra is due to molecular ordering of the spin probe in the surfactant aggregate. In fact, this behavior has been observed in a number of other SSEPR studies of vesicle systems that have been successfully analyzed with the MOMD model.

The parameters extracted from the best fits of the data in Figure 4.6 are presented in Table 4.4. The spectrum collected at $\chi_{SDS} = 0.5$ was not simulated. The rotational correlation time of the
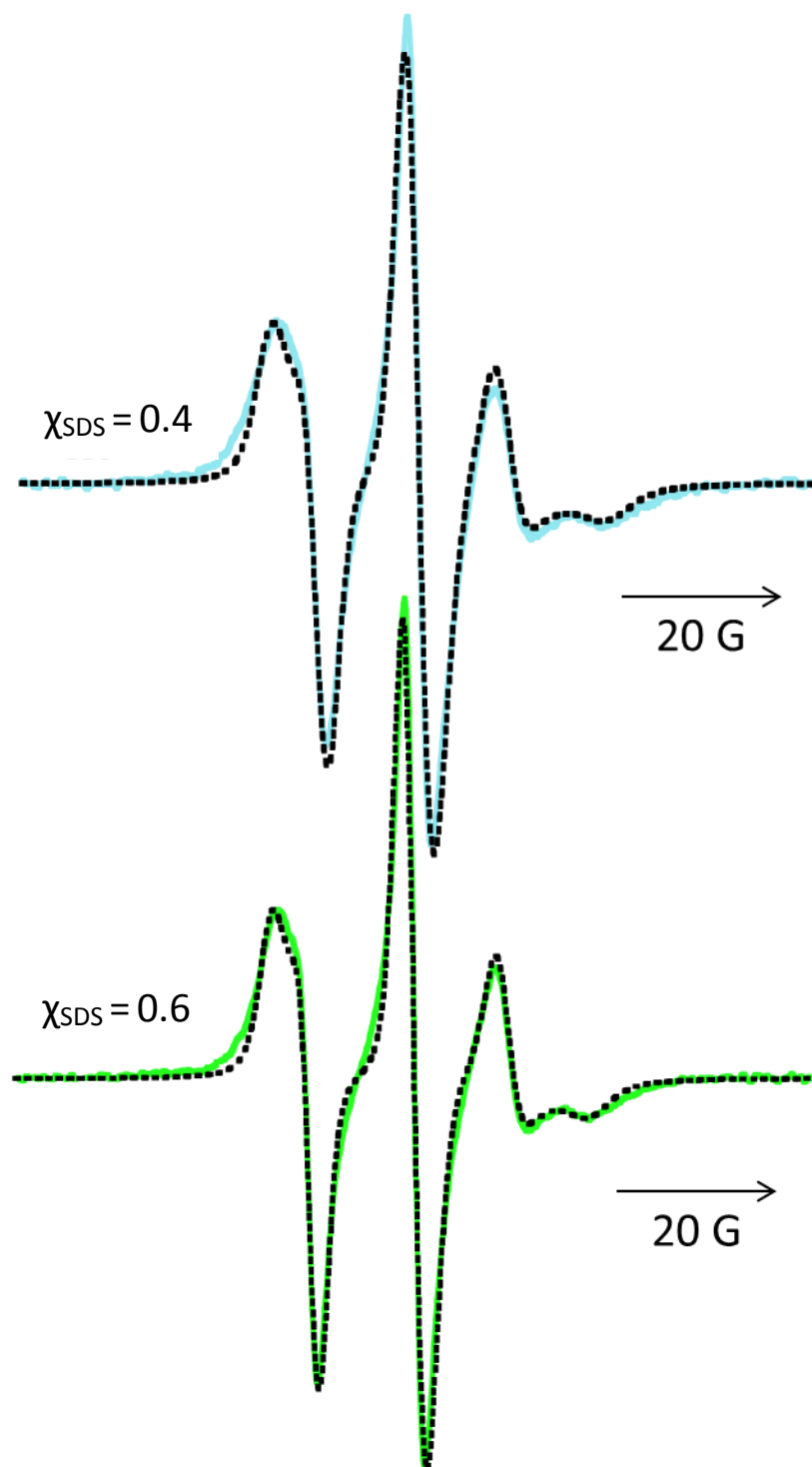
Figure 4.7 SSEPR of solutions of SDS-DTAC with a total surfactant concentration of 50 mM with 0.2 mM 5-DSA for χ_{SDS} = 0.4 (top) and χ_{SDS} = 0.6 (bottom). Black dotted lines represent the best fit of the experimental data obtained from the Freed program for slow motion EPR using the MOMD model. Fitting parameters are listed in Table 4.4. The low-field and high-field transitions exhibit an additional splitting due to molecular ordering of the spin probe in the surfactant aggregates.

aggregate structures, τ_{agg}, was calculated from the size of the aggregates obtained from SANS measurements. The rotational correlation time of the spin probe, τ_{doxyl}, can be obtained from the measured τ_c by the relationship

$$:\frac{1}{\tau_c} = \frac{1}{\tau_{agg}} + \frac{1}{\tau_{doxyl}}$$
(23)

A general trend in the rotational correlation time and the order parameter is observed in relation to χ_{SDS}. The rotational correlation times for the 5-DSA in SDS and DTAC are somewhat faster than those reported in the literature as calculated from the line-width, line height expression in Eq. 21. In fact, the rotational correlation time calculated from computer simulation is approximately half the literature value. This difference by a factor of two between the two methods has a president in literature for CTAC micelles.[72] The slow rotational motion along at least one axis of the 5-DSA make us confident that the rotational correlation time obtained computationally is reasonable and more accurate than that obtained from the line width and line height. The rotational correlation time decreases slightly as the mixing ratio approaches equimolar from either side of the phase diagram by roughly 1.5-2. This is consistent with the findings in the literature, where the rotational correlation time was observed to decrease by a factor of 1-3 for the transition from micelles to vesicles.[73]

The order parameter is also observed to increase gradually as the mixing ratio approaches equimolar. For the pure micelles, the order parameter is low, and removing this parameter from the simulations does not substantially change the results or quality of the spectral fits. However, near equimolar mixing ratios, the order parameter is significant; values of 0.3-0.6 have been reported previously for vesicle structures.[54] The gradual increase of the order parameter as it approaches an equimolar mixing ratio likely reflects and increasing ordering of the surfactant molecules as the size of the micelle or vesicle structure increases, with the largest values of the

order parameter observed in vesicle structures. This increase in order has been attributed to close packing of the surfactant tails and the corresponding expulsion of water from the polar shell of the surfactant aggregate. The more moderate increase in the order parameter at intermediate mixing ratios like $\chi_{SDS} = 0.2$ or $\chi_{SDS} = 0.8$ could be due to the formation of large, non-spherical micelles rather than vesicles. Like the reports of the $\tau_{c\,for}$ x-DSA in SDS/DTAC mixed micelles, the order parameter increases much more sharply on the DTAC-rich side of the phase diagram than on the SDS-rich side, with trends that are nearly identical to the increase in τ_c reported by Baglioni et al.[20a] This suggests that the very slow τ_c reported for this system may be due to broadening of the SSEPR spectra caused by increasing ordering, rather than any substantial change in the rotational correlation times.

From Table 4.4 it is also clear that there is a trend in the value of the isotropic hyperfine coupling constant measured from these EPR spectra. The hyperfine was calculated from the simulation results, in which only the A_{zz} component of the tensor was varied, from the equation:

$$A_N = (A_{xx} + A_{yy} + Azz)/3 \qquad (24)$$

This is in good agreement with the values of A_N reported by Baglioni et al.[20a] The value of the isotropic hyperfine coupling constant is related to the polarity of the environment, which for surfactant structures has been directly related to the extent of hydration of the polar shell. A decrease in A_N corresponds with a decrease in water content in the shell and is often observed with tighter packing of the surfactant molecules. The trend in the hyperfine coupling constant reveals that the polar shell of the SDS micelle is more accessible to water than that of DTAC. This correlates well with the known hydration behavior and degree of ionization of the SDS and DTAC micelles. A substantial decrease in the value of A_N occurs near the equimolar mixing ratio, where A_N is close to the values reported for nonpolar environments where water has been completely

excluded from the environment surrounding the spin probe. This exclusion of water inferred from the decrease in polarity and decrease in A_N is also consistent with the formation of vesicle structures.

One additional feature that is important to note is that the spectrum collected at $\chi_{SDS} = 0.5$ appears as a single, broad EPR transition. At equimolar mixing ratio, catanionic mixtures of surfactants exhibit very strong precipitation. In many cases, characterization of the surfactant aggregates when there is such strong precipitation is impossible, and it is often unclear if aggregate structures form at all. The substantial broadening of the EPR transitions observed at $\chi_{SDS} = 0.5$ is most likely due to strong Heisenberg spin exchange broadening as the spin probe becomes increasingly concentrated. [74,75] The question remains as to whether or not the spin probe is concentrated to this extent because it is located in the crystalline precipitate or whether it is being concentrated inside a very small number of aggregates. To address this question, the concentration of 5-DSA was significantly reduced. Figure 4.8 shows the concentration dependence of the EPR spectrum of $\chi_{SDS} = 0.5$ as a function of 5-DSA concentration. If the spin probe were aggregating in the precipitate, we expect the rotational motion of the spin probe to be severely restricted by the crystalline environment, which would lead to the observation of a rigid limit EPR spectrum. Instead, as the concentration of 5-DSA was lowered, the line shape of the EPR spectrum appears much more similar to the line shape of 5-DSA at other mixing ratios. Thus, it appears that at equimolar mixing ratio, the precipitate is still in equilibrium with a very small number of surfactant aggregates.

4.3.3b Solution Equilibrium

The SSEPR spectra of 5-DSA in solutions of SDS-DTAC reveal the experimental
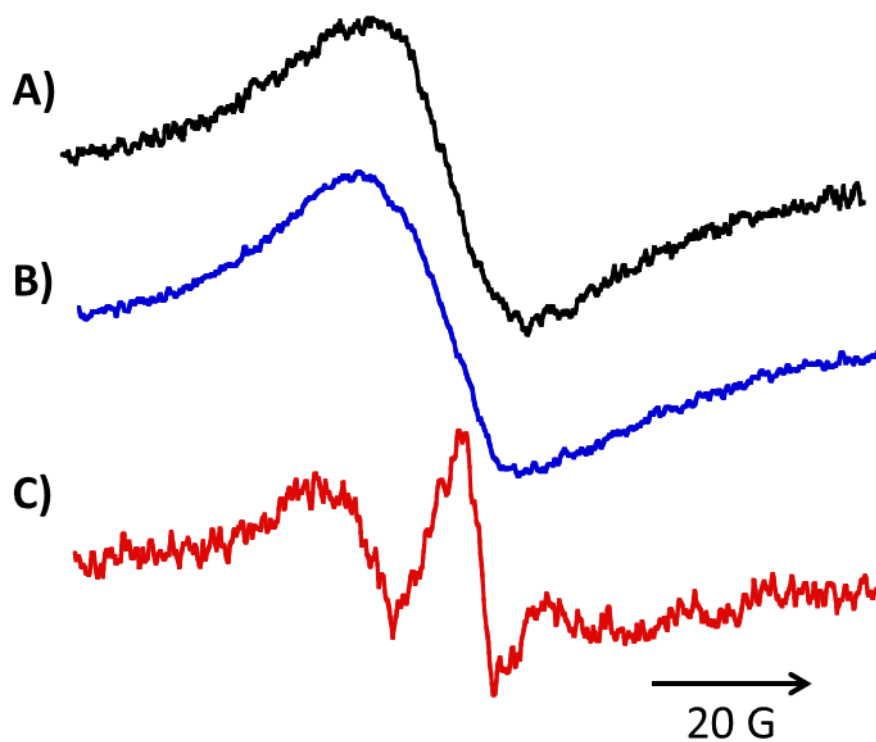
Figure 4.8 SSEPR of solutions of SDS-DTAC with a total surfactant concentration of 50 mM for $\chi_{SDS} = 0.5$ and varying concentrations of 5-DSA: (A) 1 mM, (B) 0.2 mM, and (C) 0.04 mM

technique to be particularly sensitive to changes in surfactant aggregate structure through line shape analysis and the observation of molecular ordering. In addition, broadening of the SSEPR signal was observed for $\chi_{SDS} = 0.5$ as a function of the concentration of spin probe that appears to be related to the formation of precipitate. As demonstrated by Table 4.4, strong precipitation occurs across a wide range of mixing ratios between the two surfactants, which suggests that changes to the line width of SSEPR spectra may potentially be used to monitor the precipitation behavior of mixed surfactant systems. Because very long equilibration times have been reported in mixed and ionic surfactant systems for the formation of aggregate structures, the sensitivity of the SSEPR technique to both aggregate structure and precipitation give it great potential as an experimental tool for monitoring these equilibria.

In an attempt to determine the time frame for equilibration of the aggregates, the SSEPR spectrum was monitored over the course of a month at a moderate concentration of 5-DSA (0.2 mM) after mixing of stock solutions of SDS and DTAC. Figure 4.9 shows the SSEPR collected at one day, one week, and one month after these samples for pure micelles, at an intermediate mixing ratio, and at a mixing ratio near equimolar where vesicle formation is expected. The spectra for the micelle solutions ($\chi_{SDS} = 0.0$) do not change as a function of the time of observation. At intermediate mixing ratios, some changes in line shape as a function of time are observed for χ_{SDS} on the DTAC-rich side of the phase diagram, but the same changes are not observed for $\chi_{SDS} = 0.8$ on the SDS-rich side. Because the precipitation is more pronounced in DTAC-rich solutions, the changes in the spectra are most likely a reflection of precipitation processes rather than structural changes. This is also true for the spectrum near equimolar mixing ($\chi_{SDS} = 0.4$ or $\chi_{SDS} = 0.7$), where the substantial changes in time observed for the SSEPR spectrum at $\chi_{SDS} = 0.4$ are almost certainly
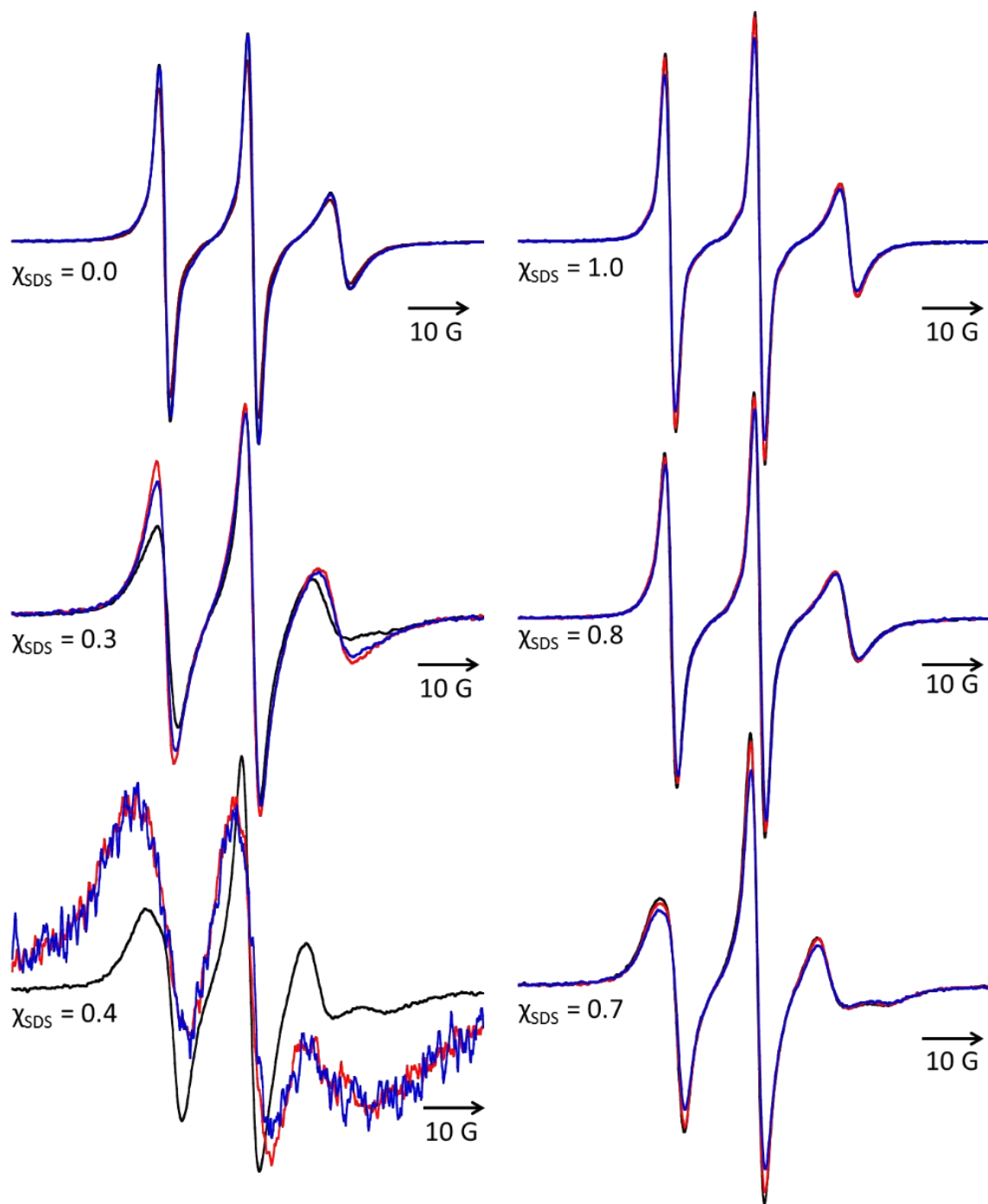
Figure 4.9 SSEPR of solutions of SDS-DTAC with 0.2 mM 5-DSA and a total surfactant concentration of 50 mM for the DTAC rich side of the phase diagram (left) where strong precipitation is observed and the SDS-rich side (right) where no precipitation is observed. A comparison is made samples at a period of 1 day (black), 1 week (red), and 1 month (blue) after mixing SDS and DTAC for mixing ratios that form pure micelles (top), mixed micelles (middle), and vesicle structures (bottom).

due to Heisenberg spin exchange broadening after substantial precipitation. On the DTAC-rich side of the phase diagram, these measurements were repeated with an even lower concentration of 5-DSA, which confirmed that the SSEPR spectra do not change substantially with time after mixing. In all cases where the spin probe concentration is low enough that it is not affected by precipitation, there are no substantial changes to the molecular ordering or rotational motion of the spin probe in the surfactant aggregates that would indicate significant changes in aggregate structure over time. In general, it can be safely assumed that this mixed surfactant system reaches an equilibrium structure for the aggregates in less than 24 hours

The small changes in the SSEPR that were attributed to precipitation of the surfactants suggest that the equilibrium between precipitate and dissolved surfactant is a much slower process. In order to increase the sensitivity of the SSEPR experiment to the precipitation behavior of the mixed surfactant system, the concentration of 5-DSA was increased an order of magnitude to 1 mM. This concentration is generally considered high for spin probe characterization of aggregates. Figure 4.10 shows a comparison of the SSEPR collected over a period of 1 month for several different mixing ratios. For pure micelles (top), it is clear from a comparison with Figure 4.9 that the concentration of spin probe is high because the micelle spectrum is broadened. However, in the pure micelles and for vesicles at $\chi_{SDS} = 0.7$, where little or no precipitation is observed, the SSEPR spectra do not change much as a function of time after mixing. However, for spectra where the extent of precipitation was large ($\chi_{SDS} = 0.3$, 46 wt. % or $\chi_{SDS} = 0.4$, 28 wt. % precipitation), there are significant changes to the spectra over time. The transitions broaden substantially, to the point that for $\chi_{SDS} = 0.4$, they almost appear as a single broad transition. The broadening is likely more significant for $\chi_{SDS} = 0.4$ than $\chi_{SDS} = 0.3$ because, even though the extent of precipitation is smaller, N_{agg} is much larger.[4b] This leads to the formation of fewer aggregate structures with more
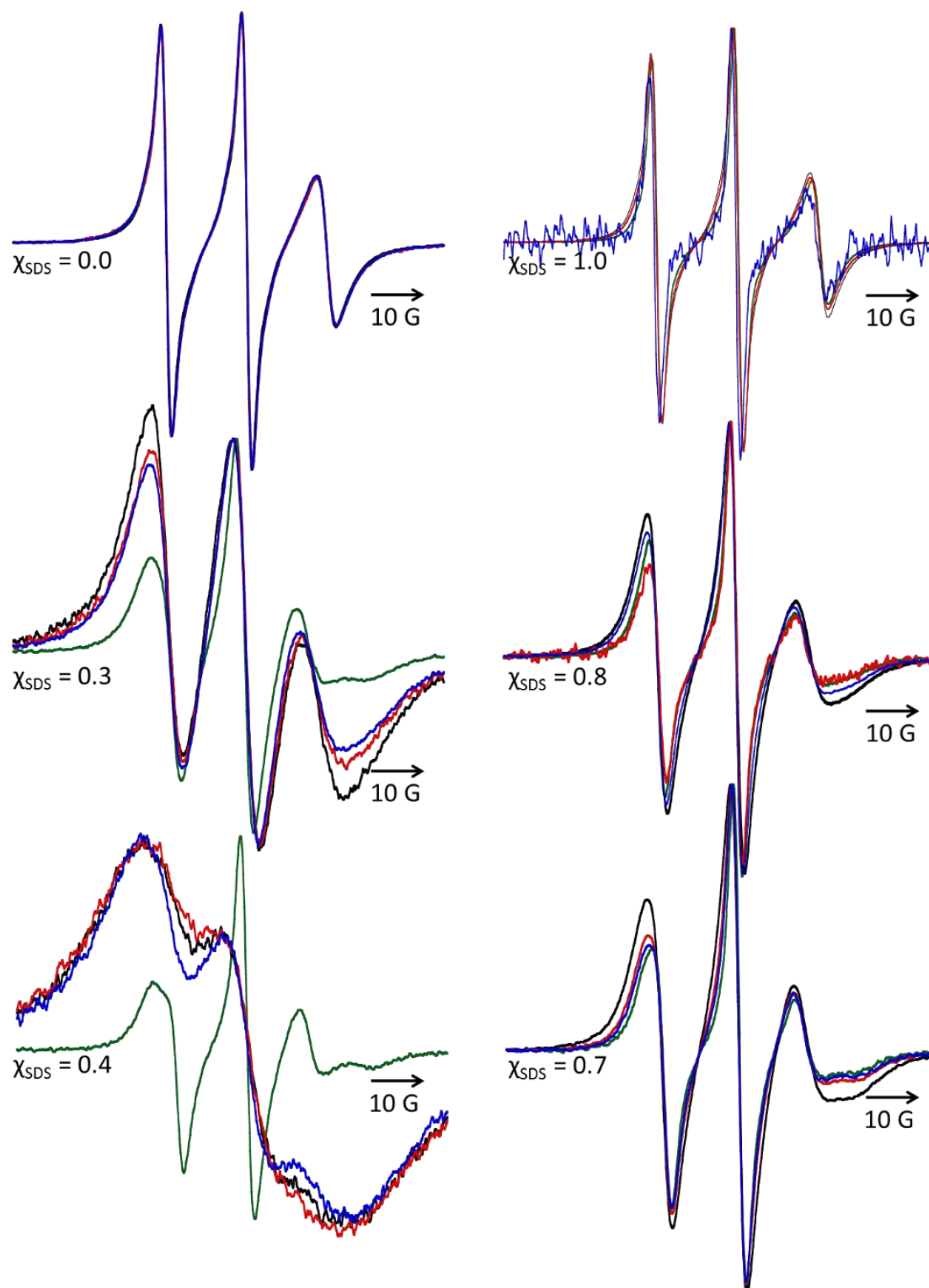
Figure 4.10 SSEPR of solutions of SDS-DTAC with 1 mM 5-DSA and a total surfactant concentration of 50 mM for the DTAC rich side of the phase diagram (left) where strong precipitation is observed and the SDS-rich side (right) where no precipitation is observed. A comparison is made samples at a period of 30 minutes (green), 1 day (black), 1 week (red), and 1 month (blue) after mixing SDS and DTAC for mixing ratios that form pure micelles (top), mixed micelles (middle), and vesicle structures (bottom).
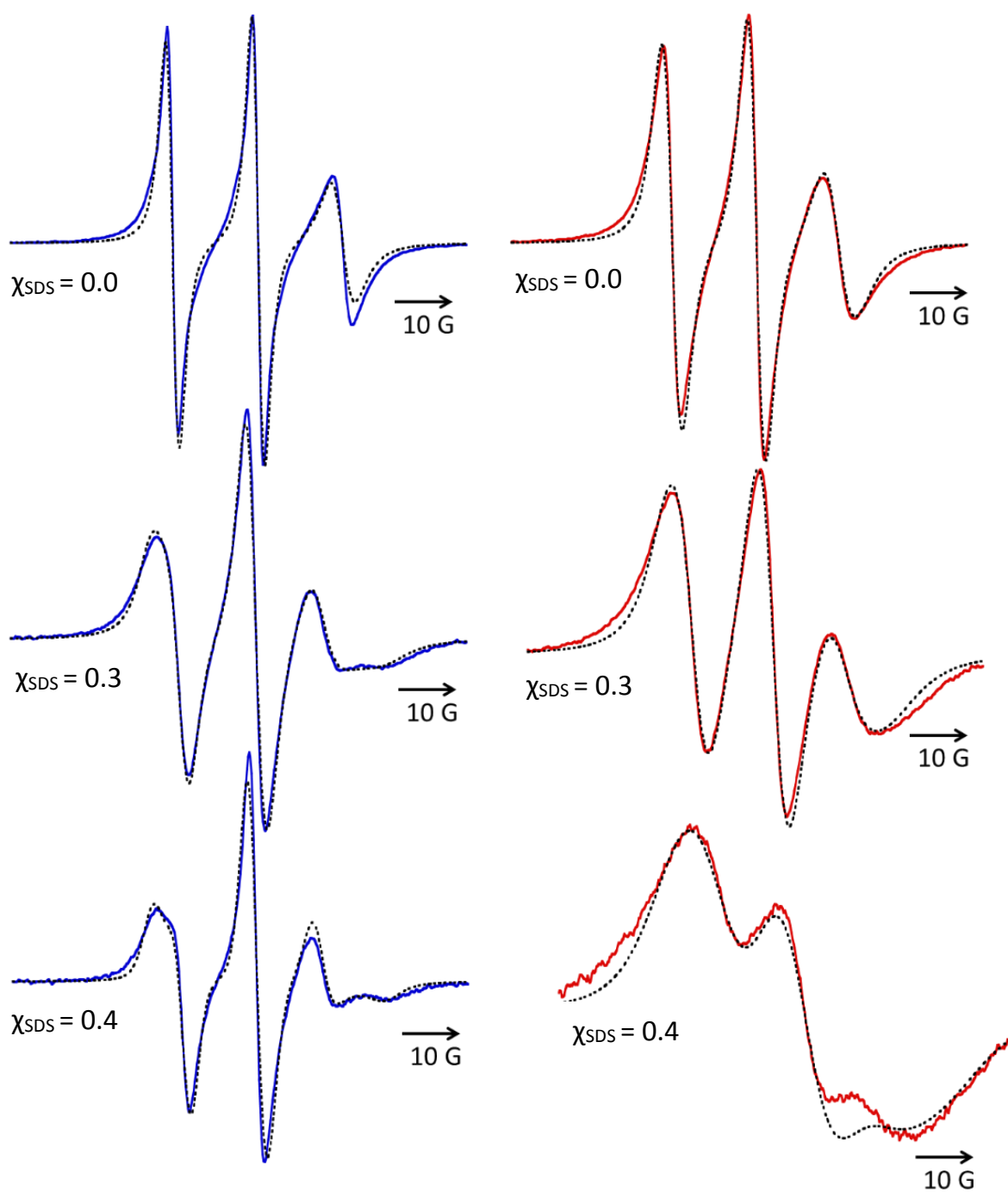
Figure 4.11 SSEPR of solutions of SDS-DTAC with 1 mM 5-DSA and a total surfactant concentration of 50 mM for the DTAC rich side of the phase diagram where strong precipitation is observed. A comparison is made samples at a period of 30 minutes (left) and 1 month (right) after mixing. Black dotted lines indicate the best fit obtained from MOMD fitting of the experimental data using the Freed Program and including the frequency of Heisenberg spin exchange as a fitting parameter.

Table 4.5 Parameters for rotational correlation times, order parameter, and frequency of Heisenberg spin exchange obtained from MOMD fitting of 5-DSA in solutions of $C_{total} = 50$ mM as a function of χ_{SDS} and measured 1 month after initial sample preparation.

χ_{SDS}	τ_c (x 10^{-10} s)	$\tau_{\parallel}$ (x 10^{-10} s)	$\tau_{\perp}$ (x 10^{-10} s)	wt % precipitate	ω_{ex} (MHz)	S_{eff}
1.0	3.33	0.39	9.73	0	8.7	0.02
0.9	3.35	0.39	9.8	0	10.1	0.08
0.8	4.79	0.56	14.0	0	5.8	0.16
0.7	4.76	0.56	13.9	0	4.5	0.28
0.6	4.42	0.52	12.9	68.3	37.6	0.29
0.5	5.81	0.68	17.0	77.3	215	0.39
0.4	4.49	0.53	13.1	28.4	105	0.40
0.3	4.97	0.58	14.5	46.8	81.1	0.23
0.2	4.06	0.46	11.9	19.0	36.9	0.17
0.1	3.80	0.44	11.1	2.2	31.8	0.10
0.0	3.48	0.41	10.2	0	17.1	0.04

spin probes per aggregate and, consequently, a greater degree of Heisenberg spin exchange broadening.

Simulations of the exchange broadened spectra were performed with the MOMD model.[44] these fits at 30 minutes after mixing and one month after mixing for the DTAC-rich side of the phase diagram when including a Heisenberg spin exchange broadening. The frequency of exchange or the whole data set at one month is reported in Table 4.5. All of the spectra could be fit just with the addition of Heisenberg spin exchange broadening except for $\chi_{SDS} = 0.4$ and 0.5. These two spectra also required approximately 8-9 G of additional inhomogenous broadening to adequately fit the spectra. In general, higher frequencies of Heisenberg spin exchange correlate with higher degrees of precipitation in the sample, with the highest rates observed for the two mixing ratios that exhibited the most pronounced broadening in the EPR spectra.

4.3.4 TREPR Studies of Radical Pair Dynamics in Mixed Micellar Aggregates

The TREPR spectrum acquired after laser flash photolysis of deuterated BP in mixed surfactant solutions of SDS-DTAC are shown in Figure 4.12 as a function of the mixing ratio. A hydrogen atom abstraction reaction is expected to take place following the excitation of the triplet sensitizer. Figure 4.11 shows the results of sensitizer molecule, producing a BP ketyl radical and alkyl radicals identical to those discussed in the previous two chapters for SDS and DTAC. On the extremes of the SDS and DTAC-rich sides of the phase diagram, the signal from the alkyl radicals is clearly visible. This signal becomes weaker as the mixing ratio approaches equimolar (for example, compare $\chi_{SDS} = 0.9$ and $\chi_{SDS} = 0.7$), and eventually disappears entirely. For mixing ratios close to equimolar, the TREPR spectrum consists only of one large, emissive peak at a g-factor consistent with a BP-based radical. This region in which the alkyl radicals are not visible extends from $\chi_{SDS} = 0.2\text{-}0.6$, much further to the DTAC-rich side of the dataset than the SDS-rich side. It is also interesting to note that the intensity of the central signal in the spectra from $\chi_{SDS} = 0.2\text{-}0.6$ increases as the mole fraction of SDS decreases. One possible explanation for this is the significant precipitation of the system in this region. It is important to note that the weakest TREPR signal comes from solutions with a mixing ratio of $\chi_{SDS} = 0.5$ and 0.6, which also exhibited the greatest degree of precipitation. The broadening of the central BP ketyl radical signal and the SDS alkyl radicals to the point that they are hardly visible is consistent with the spectral features of the TREPR of RPs in liposomes reported by Moribe et al.[58]

In examining the TREPR for mixing ratios in which mixed micelle formation is clearly expected, the line shape of the TREPR spectra agrees well with the expected line shapes and features for both radicals of the RP. The alkyl radicals are clearly observed for mixing ratios of $\chi_{SDS} = 0.7\text{-}1.0$ and $\chi_{SDS} = 0.0\text{-}0.1$. It is interesting to note that the signal from the alkyl radicals is
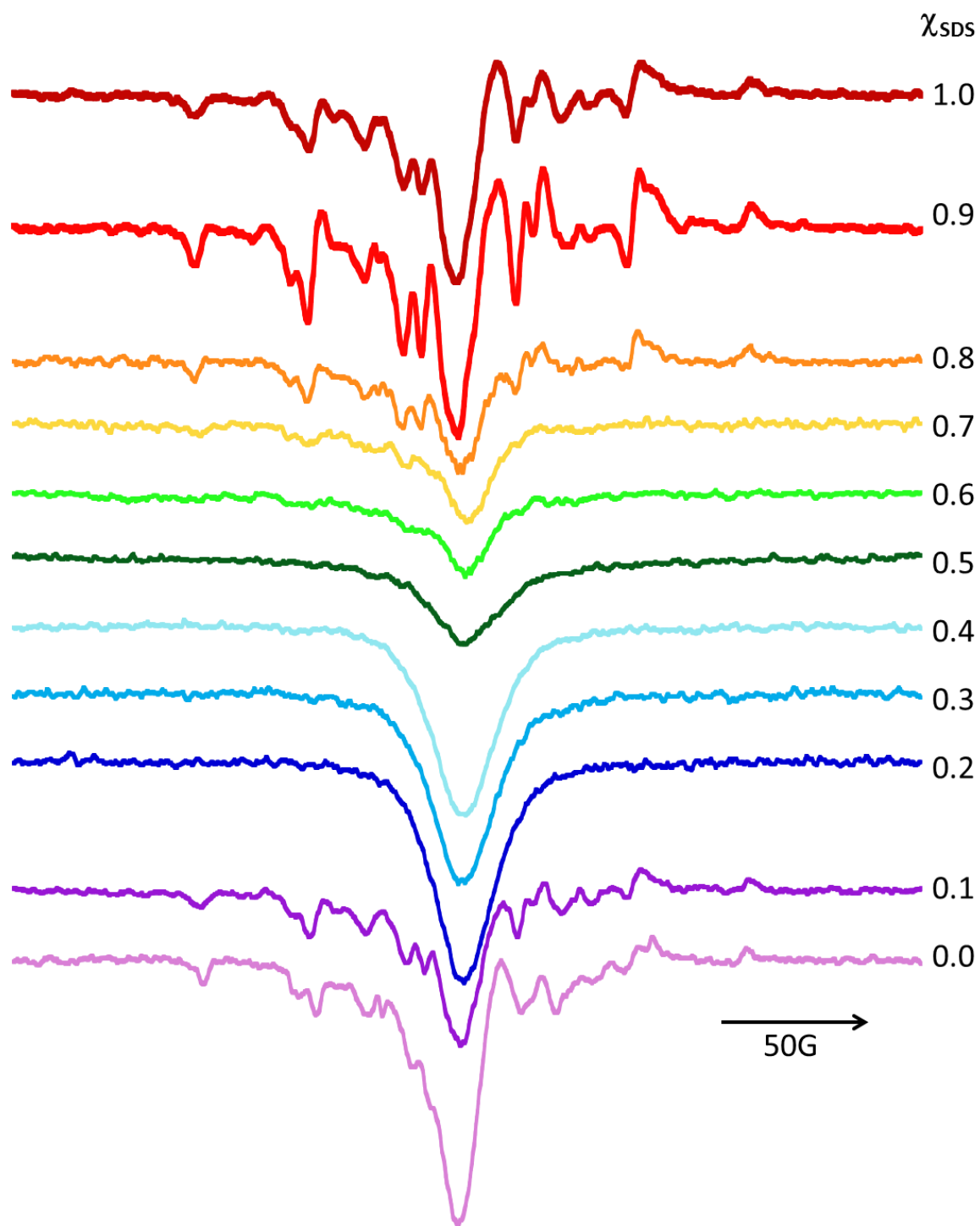
Figure 4.12 TREPR of solutions of SDS-DTAC as a function of χ_{SDS}. Spectra were collected at a delay time of 500 ns following excitation of deuterated BP at 308 nm. Total surfactant concentration was 50 mM and BP concentration was approximately 1 mM.
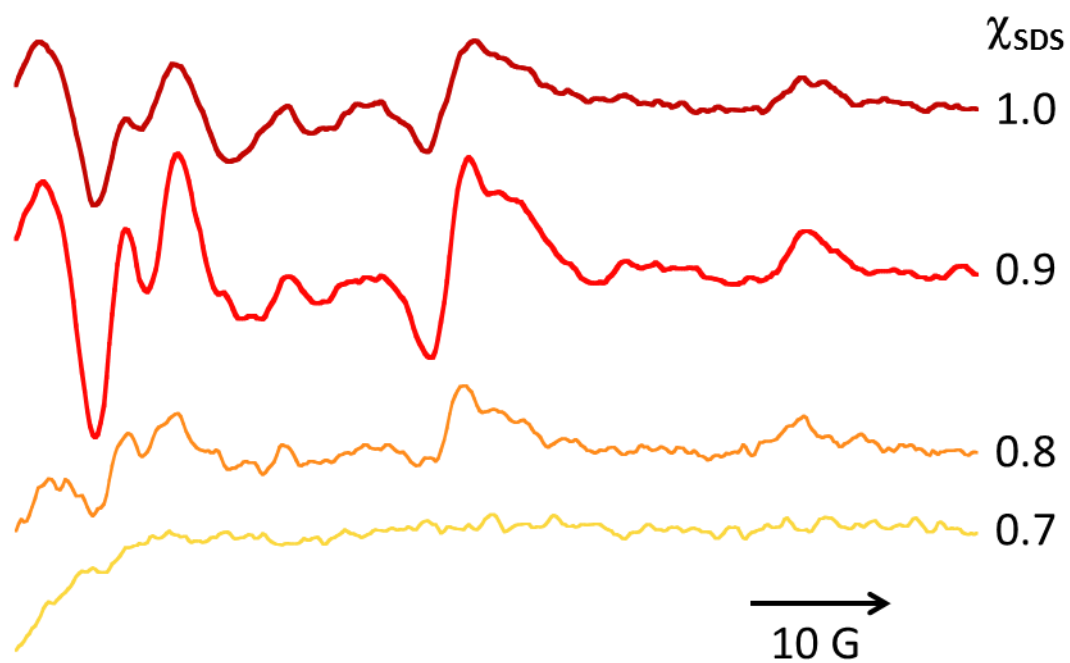
Figure 4.13 High-field portion of the TREPR of solutions of SDS-DTAC on the SDS-rich side of the phase diagram for the catanionic mixture. Spectra were collected at a delay time of 500 ns following excitation of deuterated BP at 308 nm. Total surfactant concentration was 50 mM and BP concentration was approximately 1 mM.

observed over a shorter range of χ_{SDS} for DTAC-rich solutions. It was in DTAC-rich solutions that Baglioni et al.[20a] reported a sharper increase in rotational correlation time and a greater expulsion of water from the micelle surface, and this correlates well with the faster disappearance of the alkyl radical signal in the TREPR spectrum. Comparison of the signals from the alkyl radicals in the SDS-rich or DTAC-rich solutions reveals subtle differences in the contribution and asymmetry of the APS to the spectral shape. This is most clearly seen by a comparison of the spectra for χ_{SDS} = 1.0-0.7 in Figure 4.13. The APS appears slightly asymmetric and the transitions less broad for χ_{SDS}= 0.9. For χ_{SDS} = 0.8, the APS is clearly asymmetric and the line width appears to broaden. It is possible that there is a greater contribution of escaped radicals to the spectrum, leading to this observed asymmetry. However, given that the time dependence of the TREPR measurements for these mixing ratios appear to be fairly similar, it is more likely that these differences arise from differences in characteristics of the two micelles. The size of the micelles increases dramatically with the addition of small amounts of DTAC (Table 4.1).[4b] Similar to the comparison of SDS and CTAC with an AQ sensitizer made in Chapter 3, the increased size of the micelles formed in solutions where χ_{SDS} = 0.9 and χ_{SDS} = 0.8 provides a larger space for the mutual diffusion of the SCRPs. This larger micellar volume likely reduces the forced reencounter rate of the RPs, leading to substantial differences in the contribution of APS to the TREPR spectra.

The primary differences between the SDS-rich and DTAC-rich spectra can be explained by a different polarization mechanism. The DTAC-rich spectra appear to have a much greater net emissive contribution to the signal from the TM. This conclusion is supported by the very strong, purely TM polarization observed for mixing ratios between X_{SDS} = 0.2-0.5, where larger aggregate formation is expected. TM polarization contributes more significantly to TREPR spectra as the viscosity of the solution increases. Slowing of the rotational tumbling of the triplet causes this

increase, since faster rotational motion can average out the population difference generated between the triplet energy levels by spin-selective ISC. This greater TM polarization is most likely related to the increased microviscosity in the DTAC-rich micelles, as evidenced by the slower rotational correlation times for DTAC micelle versus the SDS micelle in Table 4.2.

4.4 Conclusions and Future Directions

4.4.1 Conclusions

Investigations of the phase behavior of catanionic mixtures of SDS and DTAC reported here by UV-vis, DLS, SSEPR, and TREPR are in generally good agreement with the previously published visual observations of the phase behavior for this surfactant systems.[4b, 61] Thermodynamically based calculations for the behavior of this system predict strong non-ideality and synergism between the surfactant monomers due to electrostatic attraction between the oppositely charged head groups. Furthermore, it has been demonstrated that SSEPR experiments employing spin probes can be used to characterize catanionic aggregate structures despite the formation of precipitate near equimolar mixing, which has proved to be a barrier in other experimental studies of these mixtures. Careful choice of surfactant and spin probe concentrations are necessary to ensure measurements are made on the surfactant aggregates. By choosing higher spin probe concentrations, the SSEPR experiment can also characterize the slow formation of this precipitate by monitoring changes in the line shape of the EPR spectra. The prevailing opinion for mixed surfactant systems has been that they reach equilibrium states rather quickly, but in a handful of surfactant mixtures where the equilibrium of aggregate formation has been monitored, this has not been the case.[76] Because of the high sensitivity of the SSEPR experiment to both the aggregate structure and slower formation of precipitate demonstrated for mixtures of SDS-DTAC,

spin probe studies represent a promising, relatively simple avenue for characterizing the equilibration of both processes in other mixed surfactant systems. TREPR investigations of RP dynamics in solutions of SDS-DTAC as a function of mixing ratio also exhibited strong changes in the appearance and observation of the members of the RP as a function of surfactant mixing ratio that correlated well to both the line shape changes in the SSEPR experiment and to the expected phase transitions between micelles and vesicles. These pronounced changes in the TREPR spectra reflect changes in the translational diffusion of the RP between the micelle and vesicle environment. To the best of our knowledge, this is the first time the TREPR experiment has been used to examine phase changes in surfactant aggregate structures for micelle to vesicle transitions. Results from these two complimentary experiments allow for a direct comparison of changes in rotational and translational diffusion of radicals in SDS-DTAC aggregates and represents a novel methodology for characterizing phase changes in surfactant nanostructures using both types of motion.

4.4.2 Future Directions

There are a wide variety of potentially interesting surfactant systems exhibiting novel phase changes that could be explored using both of these techniques. The SSEPR experiment represents a promising experimental technique to determine, at least quantitatively, the timescale for these mixtures to reach equilibrium. Although the aggregate structures of the SDS-DTAC system appeared to reach equilibrium quite quickly, care should be taken not to extend this assumption to other mixed micelle or even pure surfactant systems. For the SDS-DTAC case, the structures of the surfactants are very similar, and it is not surprising that their association and equilibration in solution should be rapid. For surfactants of very different size or structure, SSEPR represents one

avenue by which the question of micelle and vesicle formation and equilibria can be studied, and has potential to address lingering questions about catanionic vesicles as thermodynamically equilibrium states.

The TREPR spectroscopy of radical pairs confined to vesicles and liposomes is still remarkably understudied. Understanding the mobility of small molecules in vesicles and liposomes is critical to developing better drug delivery applications,[6a, 77] and the TREPR experiment is very sensitive to this translational diffusion. However, the rather broad and featureless TREPR of BP in SDS-DTAC micelles or in the liposomes studied by Moribe et al.[58] may explain why these systems are so understudied. The question remains whether or not the TREPR line shape is a function of the physical characteristics of this particular RP or is intrinsic to RP diffusion in these bilayer environments. TREPR polarization transfer from a triplet sensitizer incorporated in a bilayer to a small, hydrophilic spin probe like TEMPO may provide more insight into the diffusive properties of organic molecules in a bilayer than a photochemically generated RP this those presented here. In addition, it is unclear if the strong, net emissive signal for mole fractions of SDS between 0.2 and 0.6 is from the same photochemical process that forms the RP in micelles. It is possible that some other chemical process, for instance, and electron transfer event, may be forming the sensitizer radical. The process responsible for forming the radicals in vesicle solutions deserves further study. Even so, the sensitivity of the TREPR of photochemically generated sensitizer-surfactant RP to phase changes from small micelles to larger mixed micelles and surfactants represents a new technique for characterizing phase transitions in surfactant structures.

Calculations of the non-ideality of the SDS-DTAC system, at this point, are purely theoretical. Experimental measurements of the CMC_{mix} by UV-vis,[78] conductivity,[79] or surface

tension[80] could be done to confirm the validity of the model and the small region of antagonistic behavior between SDS and DTAC. Likewise, the actual structures formed at different mixing ratios of SDS and DTAC are still not well understood, with the SSEPR and TREPR results here providing only the third set of experimental measurements for the SDS-DTAC system near equimolar mixing. While these measurements and the ESEEM measurements of Baglioni et al.[20a] support the conclusions made by Stenstam et al.[61] and Prevost and Gradzielski[4b] that vesicles are formed in mixtures of SDS-DTAC, they do not confirm the structure of the aggregate. Visual characterization techniques like cryo-TEM would provide more definitive confirmation of the aggregate structures.[5b, 27, 81] In terms identifying micelle and vesicle phases conclusively, this may also be accomplished by SSEPR using the excluded volume technique described in Dejanovic et al.[73b, 82]

4.5 Experimental

UV-vis measurements of turbidity were carried out on a Shimazdu UV-vis spectrometer, monitoring absorbance at 300 nm and 360 nm.[62] Stock solutions of SDS and DTAC were prepared at 100 mM in MilliQ filtered water. Samples for UV-vis measurements were created by mixing the appropriate amount of surfactant stock solution and MilliQ water to achieve the desired concentration and surfactant mixing ratio. Samples were prepared at total surfactant concentrations of 10 mM, 25 mM, 50 mM, 75 mM, and 100 mM in a volume of 5 mL. Samples were allowed to equilibrate for 1 week prior to measurements. To measure the UV-vis spectrum, 3 mL were filtered through a 0.2 μm syringe filter into a quartz cuvette. Samples were run immediately after filtration to avoid the formation of additional precipitate. Large absorbance values at the monitored

wavelengths were considered indicative of the formation of large surfactant aggregates. Visual observation of sample appearance before and after filtrations were recorded.

DLS measurements were obtained on a Zetasizer Nano Z from Malvern Instruments. Samples were prepared from stock solutions of SDS and DTAC (50 mM) in MilliQ water. Samples were examined only at $C_{total} = 50$ mM, and were prepared 24 hours before data was collected. To obtain more accurate measurements of the surfactant aggregate size, samples were passed through a 0.2 μm syringe filter as they were loaded into the sample cell. To confirm that the incorporation of the spin probe or triplet sensitizer was not disrupting or altering the formation of surfactant aggregates, samples were also run at $\chi_{SDS} = 0.4$ and $\chi_{SDS} = 0.6$ with 0.2 mM 5-DSA or 1 mM BPd10 dissolved in solution. Solubilization of both caused a small decrease ($\approx$1-2.5 nm) in the measured hydrodynamic radius of the aggregates as measured by DLS.

SSEPR measurements were recorded on a JEOL FA-100 spectrometer with a digital variable temperature control unit. For measurements of SSEPR spectra of 4-HTB, 5-DSA, and 16-DSA in solutions of SDS-DTAC, stock solutions of the spin probe in acetone were generated. An aliquot of the stock solution was introduced to a sample vial such that the total concentration of the spin probe in the final sample prior to measurement would be approximately 0.1-0.2 mM. The solvent was evaporated off, leaving a thin film of the spin probe at the bottom of the vial. Stock solutions of SDS and DTAC (50 mM) were then pipetted into the vials in the appropriate ratio for a final sample volume of 1 or 5 mL. Samples were allowed to equilibrate for 24 hours after mixing prior to measurement. Samples examined as a function of DSA concentration were treated in the same fashion, but the aliquot of stock solution was increased or decreased according to the final desired concentration of spin probe. Samples of varying SDS-DTAC concentration were obtained from 100 mM stock solutions of SDS and DTAC, which were diluted with MilliQ water to obtain

concentrations of C_{total} = 10 mM, 25 mM, 50 mM, 75 mM, and 100mM. Samples were degassed for 15-30 minutes prior to the experiment. Samples were loaded into quartz capillaries with an ID of 0.5 mm. For all SSEPR measurements made at room temperature, the instrument parameters are as follows: center field approximately 3360 , sweep width 100 G, modulation frequency 100 kHz, modulation amplitude 0.1 mT, microwave power 1 mW.

Simulations of the SSEPR spectra were carried out using the Freed program[44] and the MOMD model.[16b, 83] Best fits of the experimental data were obtained by varying the components of the rotational diffusion tensor, the anisotropy parameter N, the inhomogeneous broadening, the A_{zz} component of the hyperfine tensor, and the coefficients of the ordering potential. Samples at high concentrations of spin probe (1 mM) were also fit using the frequency of Heisenberg spin exchange. MOMD model calculations were allowed to sum over 20 orientations of ψ. The hyperfine and g-factor tensor components of the 4-HTB were taken from the literature to be: A_{xx} = 6.30 G, A_{yy} = 5.80 G, A_{zz} = 33.6 G and g_{xx} = 2.0088, g_{yy} = 2.0061, g_{zz} = 2.0027. Spectra for 4-HTB also required the inclusion of a fixed value of the Euler angle, β_D, of 65°. The best fits were obtained for a probe anisotropy parameter of N = 2.5. Hyperfine and g-factor tensor parameters of 5-DSA and 16-DSA taken from the literature to be: A_{xx} = 6.40 G, A_{yy} = 5.90 G, A_{zz} = 33.5 G and g_{xx} = 2.0089, g_{yy} = 2.0062, g_{zz} = 2.0027. Best fits were obtained using a probe anisotropy of N=6.5 for 16-DSA and N=25 for 5-DSA. Including β_D did not improve the quality of the fits for the DSA spin probes.

TREPR measurements were obtained on a modified JEOL, USA, Inc. JES RE-1X X-band spectrometer outfitted with a fast preamplifier and a low noise GaAs FET microwave amplifier. The spectrometer is fitted with a rectangular Varian TE_{103} cavity that allows for optical transmission. Samples are flowed through a quartz flat cell with a path length of 0.4 mm using a

micropump connected to a sample reservoir with Teflon tubing. Flowing of the sample prevents degradation and heating. Laser excitation occurs at 308 nm using a Lambda-Physik LPX 100i excimer laser. Pulse energy hitting the sample is approximately 20 mJ. Spectra are recorded at a fixed time after the laser shot by positioning the gate of a Stanford Research Systems boxcar integrator at the desired time point after the pulse trigger. The external magnetic field is swept over a specified time period, and successive averages are taken at each magnetic field point across the sweep.   Instrument settings for the TREPR measurements were as follows: Center field approximately 3390 G, sweep width 150 G, sweep time 4 minutes, boxcar gate width 300 ns, boxcar averages 30, boxcar delay time 500 ns, excitation wavelength 308 nm, pulse frequency 60 Hz, and incident microwave power of 10 mW.

Samples for TREPR experiments were prepared by mixing 50 mM stock solutions of SDS and DTAC to achieve the desired mole ratio between the two surfactants and dissolving 1-5 mM deuterated benzophenone in the mixed surfactant solutions. Water for the stock solutions was obtained from a Millipore Milli-Q water purification system. The samples were degassed by bubbling with nitrogen gas for 30 minutes prior to each experiment. The reservoir and flow system was sealed and kept under a flow of nitrogen gas during the experiment.

Benzophenone-d_{10} was prepared from benzene-d_6 (Aldrich, 99.5%-d) according to literature methods and was purified by recrystallization from hexane.[84] SDS (Aldrich 98.5%) was purified by Soxhlet extraction with petroleum ether.[85] DTAC, 4-HTB, 16-DSA, and 5-DSA were all obtained from Sigma-Aldrich and used as received.

REFERENCES

1.   Boesze-Battaglia, K.; Schimmel, R. J., Cell membrane lipid composition and distribution: Implications for cell function and lessons learned from photoreceptors and platelets. *J. Exp. Biol.* **1997,** *200* (23), 2927-2936.

2.   (a) Holland, P. M.; Rubingh, D. N., Mixed surfactant systems - an overview *ACS Symp. Ser.* **1992,** *501*, 2-30; (b) Hoffmann, H.; Possnecker, G., The mixing behavior of surfactants *Langmuir* **1994,** *10* (2), 381-389; (c) Kronberg, B., Surfactant mixtures. *Curr. Opin. Colloid Interface Sci.* **1997,** *2* (5), 456-463.

3.   Jokela, P.; Joensson, B.; Khan, A., Phase equilibria of catanionic surfactant-water systems. *J. Phys. Chem.* **1987,** *91* (12), 3291-3298.

4.   (a) Talhout, R.; Engberts, B. F. N., Self-assembly in mixtures of sodium alkyl sulfates and alkyltrimethylammonium bromides: Aggregation behavior and catalytic properties. *Langmuir* **1997,** *13* (19), 5001-5006; (b) Prevost, S.; Gradzielski, M., SANS investigation of the microstructures in catanionic mixtures of SDS/DTAC and the effect of various added salts. *J. Colloid Interface Sci.* **2009,** *337* (2), 472-484; (c) Andreozzi, P.; Funari, S. S.; La Mesa, C.; Mariani, P.; Ortore, M. G.; Sinibaldi, R.; Spinozzi, F., Multi- to Unilamellar Transitions in Catanionic Vesicles. *J. Phys. Chem. B* **2010,** *114* (24), 8056-8060.

5.   (a) Filipovicvincekovic, N.; Bujan, M.; Dragcevic, D.; Nekic, N., Phase behavior in mixtures of cationic and anionic surfactants in aqueous solutions *Colloid. Polym. Sci.* **1995,** *273* (2), 182-188; (b) Wolf, C.; Bressel, K.; Drechsler, M.; Gradzielski, M., Comparison of Vesicle Formation in Zwitanionic and Catanionic Mixtures of Hydrocarbon and Fluorocarbon Surfactants: Phase Behavior and Structural Progression. *Langmuir* **2009,** *25* (19), 11358-11366.

6.   (a) Bramer, T.; Dew, N.; Edsman, K., Pharmaceutical applications for catanionic mixtures. *J. Pharm. Pharmacol.* **2007,** *59* (10), 1319-1334; (b) Dew, N.; Edwards, K.; Edsman, K., Gel formation in systems composed of drug containing catanionic vesicles and oppositely charged hydrophobically modified polymer. *Colloids and Surfaces B-Biointerfaces* **2009,** *70* (2), 187-197.

7.   (a) Chung, M. H.; Chung, Y. C.; Chun, B. C., Highly pH-sensitive ion pair amphiphile vesicle. *Colloids and Surfaces B-Biointerfaces* **2003,** *29* (1), 75-80; (b) Chung, M. H.; Park, J. H.; Chun, B. C.; Chung, Y. C., Polymerizable ion-pair amphiphile that has a polymerizable group at cationic ammonium chain. *Colloids and Surfaces B-Biointerfaces* **2004,** *39* (4), 165-170.

8.   (a) Bramer, T.; Paulsson, M.; Edwards, K.; Edsman, K., Catanionic drug-surfactant mixtures: Phase behavior and sustained release from gels. *Pharm. Res.* **2003,** *20* (10), 1661-1667; (b) Bramer, T.; Dew, N.; Edsman, K., Catanionic mixtures involving a drug: A rather general concept that can be utilized for prolonged drug release from gels. *J. Pharm. Sci.* **2006,** *95* (4), 769-780.

9.   (a) Ashbaugh, H. S.; Boon, K.; Prud'homme, R. K., Gelation of "catanionic" vesicles by hydrophobically modified polyelectrolytes. *Colloid. Polym. Sci.* **2002,** *280* (9), 783-788; (b) Lee, J. H.; Gustin, J. P.; Chen, T. H.; Payne, G. F.; Raghavan, S. R., Vesicle-biopolymer gels: Networks of surfactant vesicles connected by associating biopolymers. *Langmuir* **2005,** *21* (1), 26-33; (c) Medronho, B.; Antunes, F. E.; Lindman, B.; Miguel, M. G., Gels of catanionic vesicles and hydrophobically modified poly(ethylene glycol). *J. Dispersion Sci. Technol.* **2006,** *27* (1), 83-90.

10.   (a) Chung, M. H.; Park, C.; Chun, B. C.; Chung, Y. C., Polymerized ion pair amphiphile vesicles with pH-sensitive transformation and controlled release property. *Colloids and Surfaces B-Biointerfaces* **2004,** *34* (3), 179-184; (b) Paulsson, M.; Edsman, K., Controlled drug release from gels using lipophilic interactions of charged substances with surfactants and polymers. *J. Colloid Interface Sci.* **2002,** *248* (1), 194-200; (c) Zhu, C.; Lee, J. H.; Raghavan, S. R.; Payne, G. F., Bioinspired vesicle restraint and mobilization using a biopolymer scaffold. *Langmuir* **2006,** *22* (7), 2951-2955.

11.   Osth, K.; Paulsson, M.; Bjork, E.; Edsman, K., Evaluation of drug release from gels on pig nasal mucosa in a horizontal Ussing chamber. *J. Controlled Release* **2002,** *83* (3), 377-388.

12. Bramer, T.; Frenning, G.; Grasjo, J.; Edsman, K.; Hansson, P., Implications of regular solution theory on the release mechanism of catanionic mixtures from gels. *Colloids and Surfaces B-Biointerfaces* **2009,** *71* (2), 214-225.

13. McKelvey, C. A.; Kaler, E. W.; Zasadzinski, J. A.; Coldren, B.; Jung, H. T., Templating hollow polymeric spheres from catanionic equilibrium vesicles: Synthesis and characterization. *Langmuir* **2000,** *16* (22), 8285-8290.

14. (a) Chung, M. H.; Chung, Y. C., Polymerized ion pair amphiphile that shows remarkable enhancement in encapsulation efficiency and very slow release of fluorescent markers. *Colloids and Surfaces B-Biointerfaces* **2002,** *24* (2), 111-121; (b) Mueller, A.; O'Brien, D. F., Supramolecular materials via polymerization of mesophases of hydrated amphiphiles. *Chem. Rev.* **2002,** *102* (3), 727-757.

15. (a) Lebedeva, N. V.; Shahine, A.; Bales, B. L., Aggregation number-based degrees of counterion dissociation in sodium n-alkyl sulfate micelles. *J. Phys. Chem. B* **2005,** *109* (42), 19806-19816; (b) Bales, B. L.; Zana, R., Characterization of micelles of quaternary ammonium surfactants, as reaction media I: Dodeclytrimethylammonium bromide and chloride. *J. Phys. Chem. B* **2002,** *106* (8), 1926-1939; (c) Fukuda, H.; Goto, A.; Yoshioka, H.; Goto, R.; Morigaki, K.; Walde, P., Electron spin resonance study of the pH-induced transformation of micelles to vesicles in an aqueous oleic acid/oleate system. *Langmuir* **2001,** *17* (14), 4223-4231; (d) Bales, B. L.; Ranganathan, R.; Griffiths, P. C., Characterization of mixed micelles of SDS and a sugar-based nonionic surfactant as a variable reaction medium. *J. Phys. Chem. B* **2001,** *105* (31), 7465-7473.

16. (a) Polnaszek, C. F.; Freed, J. H., Electron spin resonance studies of anisotropic ordering, spin relaxation, and slow tumbling in liquid crystalline solvents. *J. Phys. Chem.* **1975,** *79* (21), 2283-2306; (b) Ge, M. T.; Freed, J. H., An electron spin resonance study of interactions between gramacidin-A' and phosphatidylcholine bilayers *Biophys. J.* **1993,** *65* (5), 2106-2123; (c) Nakagawa, K., ESR spin probe investigation of chain ordering of a triglycerol membrane. *Bull. Chem. Soc. Jpn.* **2004,** *77* (2), 269-273; (d) Wasserman, A. M.; Motyakin, M. V.; Yasina, L. L.; Zakharova, Y. A.; Matveenko, V. N.; Shulevich, Y. V.; Rogovina, L. Z., EPR Spin Probe Study of New Micellar Systems. *Appl. Magn. Reson.* **2010,** *38* (1), 117-135; (e) Smith, A. K.; Freed, J. H., Dynamics and ordering of lipid spin-labels along the coexistence curve of two membrane phases: An ESR study. *Chem. Phys. Lipids* **2012,** *165* (3), 348-361.

17. (a) Caregnato, P.; Jarocha, L. E.; Esinhart, H. S.; Lebedeva, N. V.; Tarasov, V. F.; Forbes, M. D. E., Electrostatic Control of Spin Exchange Between Mobile Spin-Correlated Radical Pairs Created in Micellar Solutions. *Langmuir* **2011,** *27* (9), 5304-5309; (b) White, R. C.; Gorelik, V.; Bagryanskaya, E. G.; Forbes, M. D. E., Photoredox chemistry of AOT: Electron transfer and hydrogen abstraction in microemulsions involving the surfactant. *Langmuir* **2007,** *23* (8), 4183-4191; (c) Chaney, E. E.; Forbes, M. D. E., Dynamics of spin-correlated radical pairs in non-ionic surfactant solutions. *J. Phys. Chem. B* **2003,** *107* (18), 4464-4469.

18. (a) Anacker, E. W., Light scattering by solutions of octyltrimethylammonium octanesulfonate and octyltrimethylammonium decanesulfonate. *Journal of Colloid Science* **1953,** *8* (4), 402-413; (b) Collison, R.; Lawrence, A. S. C., The solubility of organic substantces in aqueous soap solutions. 9. The sodium dodecyl sulphate+water+normal oxtalamine system *Transactions of the Faraday Society* **1959,** *55* (4), 662-666.

19. Rupp, C.; Steckel, H.; Muller, B. W., Mixed micelle formation with phosphatidylcholines: The influence of surfactants with different molecule structures. *Int. J. Pharm.* **2010,** *387* (1-2), 120-128.

20. (a) Baglioni, P.; Dei, L.; Kevan, L.; Rivara-Minten, E., Interface of Mixed Micelles Formed of Anionic?Cationic and Ionic?Nonionic Surfactants. In *Mixed Surfactant Systems*, American Chemical Society: 1992; Vol. 501, pp 180-193; (b) Paul, M. H.; Donn, N. R., Mixed Surfactant Systems. In *Mixed Surfactant Systems*, American Chemical Society: 1992; Vol. 501, pp 2-30.

21. Khan, A.; Marques, E. F., Synergism and polymorphism in mixed surfactant systems. *Curr. Opin. Colloid Interface Sci.* **1999,** *4* (6), 402-410.

22. Holland, P. M., Nonideal mixed micellar solutions *Adv. Colloid Interface Sci.* **1986,** *26* (2-4), 111-129.

23. Rubingh, D. N., In *Solution Chemistry of Surfactants*, Plenum Press: New York, 1979; Vol. 1, pp 337-354.

24. Raghavan, S. R.; Fritz, G.; Kaler, E. W., Wormlike micelles formed by synergistic self-assembly in mixtures of anionic and cationic Surfactants. *Langmuir* **2002,** *18* (10), 3797-3803.

25.   Holland Paul, M., Modeling Mixed Surfactant Systems. In *Mixed Surfactant Systems*, American Chemical Society: 1992; Vol. 501, pp 31-44.

26.   Bergstrom, L. M.; Bramer, T., Synergistic effects in mixtures of oppositely charged surfactants as calculated from the Poisson-Boltzmann theory: A comparison between theoretical predictions and experiments. *J. Colloid Interface Sci.* **2008,** *322* (2), 589-595.

27.   Bergström, L. M.; Skoglund, S.; Edwards, K.; Eriksson, J.; Grillo, I., Self-Assembly in Mixtures of an Anionic and a Cationic Surfactant: A Comparison between Small-Angle Neutron Scattering and Cryo-Transmission Electron Microscopy. *Langmuir* **2013,** *29* (38), 11834-11848.

28.   Nagarajan, R., Molecular Packing Parameter and Surfactant Self-Assembly: The Neglected Role of the Surfactant Tail†. *Langmuir* **2001,** *18* (1), 31-38.

29.   (a) Adrian, F. J., Role of diffusion controlled reaction in chemically induced nuclear spin polarization *J. Chem. Phys.* **1970,** *53* (8), 3374-&; (b) Rodríguez-Abreu, C.; Shrestha, L. K.; López Quintela, M. A., Unusual formation of small aggregates by mixing giant multilamellar vesicles. *J. Colloid Interface Sci.* **2007,** *312* (1), 108-113.

30.   (a) Wan, L. S. C.; Poon, P. K. C., Effect of salts on surface/interfacial tension and critical micelle concentration of surfactants *J. Pharm. Sci.* **1969,** *58* (12), 1562-&; (b) Mazer, N. A.; Benedek, G. B.; Carey, M. C., Investigation of micellar phase of sodium dodecyl sulfate in aqueous sodium chloride solutions using quasi-elastic light scattering spectroscopy. *J. Phys. Chem.* **1976,** *80* (10), 1075-1085; (c) Hoffmann, H.; Rehage, H.; Platz, G.; Schorr, W.; Thurn, H.; Ulbricht, W., Investigations on a detergen system with rodlike micelles. *Colloid. Polym. Sci.* **1982,** *260* (11), 1042-1056; (d) Khatory, A.; Lequeux, F.; Kern, F.; Candau, S. J., Linear and nonlinear viscoelasticity of semidilute solutions of wormlike micelles at high salt content. *Langmuir* **1993,** *9* (6), 1456-1464; (e) Hassan, P. A.; Raghavan, S. R.; Kaler, E. W., Microstructural changes in SDS micelles induced by hydrotropic salt. *Langmuir* **2002,** *18* (7), 2543-2548; (f) Raghavan, S. R.; Edlund, H.; Kaler, E. W., Cloud-point phenomena in wormlike micellar systems containing cationic surfactant and salt. *Langmuir* **2002,** *18* (4), 1056-1064.

31.   Kaler, E. W.; Murthy, A. K.; Rodriguez, B. E.; Zasadzinski, J. A. N., Spontaneous Vesicle Formation in Aqueous Mixtures of Single-Tailed Surfactants. *Science* **1989,** *245* (4924), 1371-1374.

32.   Marques, E. F.; Regev, O.; Khan, A.; da Graça Miguel, M.; Lindman, B., Vesicle Formation and General Phase Behavior in the Catanionic Mixture SDS−DDAB−Water. The Anionic-Rich Side. *The Journal of Physical Chemistry B* **1998,** *102* (35), 6746-6758.

33.   Marques, E. F., Size and stability of catanionic vesicles: Effects of formation path, sonication, and aging. *Langmuir* **2000,** *16* (11), 4798-4807.

34.   (a) Almgren, M.; Rangelov, S., Spontaneously formed nonequilibrium vesicles of cetyltrimethylammonium bromide and sodium octyl sulfate in aqueous dispersions. *Langmuir* **2004,** *20* (16), 6611-6618; (b) Laughlin, R. G., Equilibrium vesicles: fact or fiction? *Colloid Surf. A-Physicochem. Eng. Asp.* **1997,** *128* (1-3), 27-38.

35.   (a) Morgan, J. D.; Johnson, C. A.; Kaler, E. W., Polymerization of equilibrium vesicles. *Langmuir* **1997,** *13* (24), 6447-6451; (b) Villeneuve, M.; Kaneshina, S.; Imae, T.; Aratono, M., Vesicle-micelle equilibrium of anionic and cationic surfactant mixture studied by surface tension. *Langmuir* **1999,** *15* (6), 2029-2036.

36.   Bergstrom, L. M.; Aratono, M., Synergistic effects in mixtures of two identically charged ionic surfactants with different critical micelle concentrations. *Soft Matter* **2011,** *7* (19), 8870-8879.

37.   (a) Bergstrom, L. M.; Skoglund, S.; Danerlov, K.; Garamus, V. M.; Pedersen, J. S., The growth of micelles, and the transition to bilayers, in mixtures of a single-chain and a double-chain cationic surfactant investigated with small-angle neutron scattering. *Soft Matter* **2011,** *7* (22), 10935-10944; (b) Bergstrom, M.; Pedersen, J. S., A small-angle neutron scattering study of surfactant aggregates formed in aqueous mixtures of sodium dodecyl sulfate and didodecyldimethylammonium bromide. *J. Phys. Chem. B* **2000,** *104* (17), 4155-4163.

38.   Bergstrom, M.; Pedersen, J. S., A small-angle neutron scattering (SANS) study of tablet-shaped and ribbonlike micelles formed from mixtures of an anionic and a cationic surfactant. *J. Phys. Chem. B* **1999,** *103* (40), 8502-8513.

39.   (a) Shelke, S. A.; Sigurdsson, S. T., Site-Directed Spin Labelling of Nucleic Acids. *Eur. J. Org. Chem.* **2012,** (12), 2291-2301; (b) Klare, J. P., Site-directed spin labeling EPR spectroscopy in protein research. *Biol. Chem.* **2013,** *394* (10), 1281-1300; (c) Klare, J. P.; Steinhoff, H. J., Spin labeling EPR. *Photosynth. Res.* **2009,** *102* (2-3), 377-390; (d) Hommel, H., Developments of the spin labelling study of polymers at interfaces. *Adv. Colloid Interface Sci.* **2008,** *141* (1-2), 1-23; (e) Subczynski, W. K.; Widomska, J.; Feix, J. B., Physical properties of lipid bilayers from EPR spin labeling and their influence on chemical reactions in a membrane environment. *Free Radical Biol. Med.* **2009,** *46* (6), 707-718; (f) Hommel, H., Polymers at solid interfaces - a spin labeling approach *Adv. Colloid Interface Sci.* **1995,** *54,* 209-277.

40.   (a) Bales, B. L.; Howe, A. M.; Pitt, A. R.; Roe, J. A.; Griffiths, P. C., A spin-probe study of the modification of the hydration of SDS micelles by insertion of sugar-based nonionic surfactant molecules. *J. Phys. Chem. B* **2000,** *104* (2), 264-270; (b) Griffiths, P. C.; Paul, A.; Heenan, R. K.; Penfold, J.; Ranganathan, R.; Bales, B. L., Role of counterion concentration in determining micelle aggregation: Evaluation of the combination of constraints from small-angle neutron scattering, electron paramagnetic resonance, and time-resolved fluorescence quenching. *J. Phys. Chem. B* **2004,** *108* (12), 3810-3816; (c) Lebedeva, N.; Zana, R.; Bales, B. L., A reinterpretation of the hydration of micelles of dodecyltrimethylammonium bromide and chloride in aqueous solution. *J. Phys. Chem. B* **2006,** *110* (20), 9800-9801.

41.   (a) Hubbell, W. L.; McConnel.Hm, Molecular motion in spin-labeled phospholipids and membranes. *J. Am. Chem. Soc.* **1971,** *93* (2), 314-&; (b) Ernandes, J. R.; Schreier, S.; Chaimovich, H., Spin label studies of micellar and pre-micellar aggregates *Chem. Phys. Lipids* **1976,** *16* (1), 19-30; (c) Schreier, S.; Polnaszek, C. F.; Smith, I. C. P., Spin labels in membranes-problems in practice *Biochim. Biophys. Acta* **1978,** *515* (4), 375-436.

42.   (a) Peric, M.; Alves, M.; Bales, B. L., Precision parameters from spin-probe studies of membranes using a partitioning technique. Application to two model membrane vesicles. *Biochim. Biophys. Acta-Biomembr.* **2005,** *1669* (2), 116-124; (b) Rizzi, C.; Lauricella, R.; Tuccio, B.; Bouteiller, J. C.; Cerri, V.; Tordo, P., Spin-trapping of free radicals by PBN-type beta-phosphorylated nitrones in the presence of SDS micelles. *Journal of the Chemical Society-Perkin Transactions 2* **1997,** (12), 2507-2512; (c) Kurzbach, D.; Reh, M. N.; Hinderberger, D., Nanoscale Inhomogeneities in Thermoresponsive Triblock Copolymers. *ChemPhysChem* **2011,** *12* (Copyright (C) 2013 American Chemical Society (ACS). All Rights Reserved.), 3566-3572.

43.   Keith, A.; Bulfield, G.; Snipes, W., Spin labeled neurospora mitochondria *Biophys. J.* **1970,** *10* (7), 618-&.

44.   Budil, D. E.; Lee, S.; Saxena, S.; Freed, J. H., Nonlinear-least-squares analysis of slow-motion EPR spectra in one and two dimensions using a modified Levenberg-Marquardt algorithm. *J. Magn. Reson., Ser A* **1996,** *120* (2), 155-189.

45.   Bales, B., Inhomogeneously Broadened Spin-Label Spectra. In *Spin Labeling*, Berliner, L.; Reuben, J., Eds. Springer US: 1989; Vol. 8, pp 77-130.

46.   (a) Bales, B. L.; Stenland, C., Statistical distributions and collision rates of additive molecules in compartmentalized liquids studied by EPR spectroscopy. 1. sodium dodecylsulfate micelles, 5-doxylstearic acid ester, acid aster, and cobalt(II). *J. Phys. Chem.* **1993,** *97* (13), 3418-3433; (b) Wasserman, A. M.; Kasaikin, V. A.; Timofeev, V. P., EPR spin probe and spin label studies of some low molecular and polymer micelles. *Spectroc. Acta Pt. A-Molec. Biomolec. Spectr.* **1998,** *54* (14), 2295-2308; (c) Bales, B. L.; Messina, L.; Vidal, A.; Peric, M.; Nascimento, O. R., Precision relative aggregation number determinations of SDS micelles using a spin probe. A model of micelle surface hydration. *J. Phys. Chem. B* **1998,** *102* (50), 10347-10358.

47.   Griffiths, P. C.; Cheung, A. Y. F.; Farley, C.; Paul, A.; Heenan, R. K.; King, S. M.; Pettersson, E.; Stilbs, P.; Ranganathan, R., Small-angle neutron scattering, electron paramagnetic resonance, electrophoretic NMR, and time-resolved fluorescence quenching studies of sodium dodecyl sulfate and tetra(ethylene oxide) dodecyl ether mixed surfactant micelles. *J. Phys. Chem. B* **2004,** *108* (4), 1351-1356.

48.   (a) Knauer, B. R.; Napier, J. J., Nitrogen hyperfine splitting constant of nitroxide functional group as a solvent polarity parameter - relative importance for a solvent polarity parameter of its being a cybotatic probe vs its being a model process *J. Am. Chem. Soc.* **1976,** *98* (15), 4395-4400; (b) Abe, T.; Tero-Kubota, S.; Ikegami, Y., Theory of solvent effects on the hyperfine splitting constants in ESR spectra of free radicals. *The Journal of Physical Chemistry* **1982,** *86* (8), 1358-1365; (c) Stout, G.; Engberts, J. B. F. N., Medium effects on the electron spin resonance hyperfine splitting constants of tert-butyl nitroxide in mixed aqueous solvents. *The Journal of Organic Chemistry* **1974,** *39* (25), 3800-3802.

49.   Umemoto, K.; Deguchi, Y.; Takaki, H., Electron spin resonance hyperfine spectra of di-p-anisyl nitric oxide *Bull. Chem. Soc. Jpn.* **1963,** *36* (5), 560-563.

50.   Mukai, K.; Nishiguc.H; Ishizu, K.; Deguchi, Y.; Takaki, H., Solvent effects in electron spin resonance spectra of some phenoxyl nitroxide and anilino radicals *Bull. Chem. Soc. Jpn.* **1967,** *40* (12), 2731-&.

51.   (a) Baglioni, P.; Rivaraminten, E.; Dei, L.; Ferroni, E., ESR study of sodium dodecyl sulfate and dodecyltrimethylammonium bromide micellar solutions - effect of urea *J. Phys. Chem.* **1990,** *94* (21), 8218-8222; (b) Baglioni, P.; Ottaviani, M. F.; Martini, G., Micellar solutions of sulfate surfactants studied by electron spin resonance of nitroxide radiccals. 3. Effects of added electrolytes *J. Phys. Chem.* **1986,** *90* (22), 5878-5882.

52.   Lebedeva, N.; Bales, B. L., Location of spectroscopic probes in self-aggregating assemblies. I. The case for 5-doxylstearic acid methyl ester serving as a benchmark spectroscopic probe to study micelles. *J. Phys. Chem. B* **2006,** *110* (20), 9791-9799.

53.   Owenius, R.; Engstrom, M.; Lindgren, M.; Huber, M., Influence of solvent polarity and hydrogen bonding on the EPR parameters of a nitroxide spin label studied by 9-GHz and 95-GHz EPR spectroscopy and DFT calculations. *J. Phys. Chem. A* **2001,** *105* (49), 10967-10977.

54.   Bratt, P. J.; Kevan, L., Electron spin resonance line shape analysis of x-doxylstearic acid spin probes in dioctadecyldimethylammonium chloride vesicles. *J. Phys. Chem.* **1992,** *96* (16), 6849-6852.

55.   (a) McCaffrey, V. P.; Forbes, M. D. E., Energy transfer studied using spin polarized free radicals. Effect of substrate structure and a comparison between micellar confinement and free solution. *Tetrahedron* **2000,** *56* (36), 6991-6997; (b) Tarasov, V. F.; White, R. C.; Forbes, M. D. E., Photo-oxidation of diglycine in confined media relaxation of longitudinal magnetization in spin-correlated radical pairs. *Spectroc. Acta Pt. A-Molec. Biomolec. Spectr.* **2006,** *63* (4), 776-783; (c) Tarasov, V. F.; Jarocha, L. E.; Avdievich, N. I.; Forbes, M. D. E., TREPR spectra of micelle-confined spin-correlated radical pairs: I. Molecular motion and simulations. *Photochem. Photobiol. Sci.* **2014,** *13* (2), 439-453; (d) Tarasov, V. F.; Jarocha, L. E.; Forbes, M. D. E., TREPR spectra of micelle-confined spin-correlated radical pairs: II. Spectral decomposition and asymmetric line shapes. *Photochem. Photobiol. Sci.* **2014,** *13* (2), 454-463.

56.   Closs, G. L.; Forbes, M. D. E.; Norris, J. R., Spin-polarized electron paramagnetic resonance spectra of radical pairs in micelles - observation of electron spin-spin interactions *J. Phys. Chem.* **1987,** *91* (13), 3592-3599.

57.   (a) Sakaguchi, Y.; Hayashi, H.; Nagakura, S., Laser photolysis study of the external magnetic field effect upon the photochemical processes of carbonyl compounds in micelles *J. Phys. Chem.* **1982,** *86* (16), 3177-3184; (b) Sakaguchi, Y.; Hayashi, H.; Murai, H.; Ihaya, Y. J., CIDEP study of the photochemical reactions of carbonyl compounds showing the external magnetic field effect in a micelle. *Chem. Phys. Lett.* **1984,** *110* (3), 275-279; (c) Sakaguchi, Y.; Hayashi, H.; Murai, H.; Ihaya, Y. J.; Mochida, K., CIDEP study of the formation of a cyclohexadienyl type radical in the hydrogen abstraction reactions of triplet xanthone *Chem. Phys. Lett.* **1985,** *120* (4-5), 401-405.

58.   Moribe, S.; Ikoma, T.; Akiyama, K.; Tero-Kubota, S., Time-resolved EPR study on photoreduction of sodium anthraquinone-2-sulfate in liposomes. *Chem. Phys. Lett.* **2008,** *457* (1-3), 66-68.

59.   Malliaris, A.; Binanalimbele, W.; Zana, R., Fluorescence Probing Studies of Surfactant Aggregation in Aqueous-Solutions of Mixed Ionic Micelles *J. Colloid Interface Sci.* **1986,** *110* (1), 114-120.

60.   Scheuing, D. R.; Weers, J. G., A fourier transform infrared spectroscopic study of dodecyltrimtehylammonium chloride-sodium dodecyl sulfate surfactant mixtures. *Langmuir* **1990,** *6* (3), 665-671.

61. Stenstam, A.; Khan, A.; Wennerstrom, H., Lysozyme in catanionic surfactant mixtures. *Langmuir* **2004,** *20* (18), 7760-7765.

62. Cano-Sarabia, M.; Angelova, A.; Ventosa, N.; Lesieur, S.; Veciana, J., Cholesterol induced CTAB micelle-to-vesicle phase transitions. *J. Colloid Interface Sci.* **2010,** *350* (1), 10-15.

63. (a) Lapinski, M. M.; Castro-Forero, A.; Greiner, A. J.; Ofoli, R. Y.; Blanchard, G. J., Comparison of liposomes formed by sonication and extrusion: Rotational and translational diffusion of an embedded chromophore. *Langmuir* **2007,** *23* (23), 11677-11683; (b) Bhattacharjee, J.; Aswal, V. K.; Hassan, P. A.; Pamu, R.; Narayanan, J.; Bellare, J., Structural evolution in catanionic mixtures of cetylpyridinium chloride and sodium deoxycholate. *Soft Matter* **2012,** *8* (39), 10130-10140; (c) Barbetta, A.; Pucci, C.; Tardani, F.; Andreozzi, P.; La Mesa, C., Size and Charge Modulation of Surfactant-Based Vesicles. *J. Phys. Chem. B* **2011,** *115* (44), 12751-12758.

64. Jackson, L. P.; Townsend, C.; Grady, B. P., Mixtures of Nonionic Surfactants made from Renewable Resources with Alkyl Sulfates and Sodium n-Alkanecarboxylates: Comparison of Mixing Behavior using Rubingh's Treatment. *J. Surfactants Deterg.* **2013,** *16* (6), 893-902.

65. Prasad, M.; Moulik, S. P.; Palepu, R., Self-aggregation of binary mixtures of alkyltriphenylphosphonium bromides: a critical assessment in favor of more than one kind of micelle formation. *J. Colloid Interface Sci.* **2005,** *284* (2), 658-666.

66. Akbar, J.; Tavakoli, N.; Gerrard Marangoni, D.; Wettig, S. D., Mixed aggregate formation in gemini surfactant/1,2-dialkyl-sn-glycero-3-phosphoethanolamine systems. *J. Colloid Interface Sci.* **2012,** *377* (1), 237-243.

67. Aizawa, M.; Komatsu, T.; Nakagawa, T., Spin-probe study of aqueous soap and polysoap solutions. *Bull. Chem. Soc. Jpn.* **1977,** *50* (12), 3107-10.

68. (a) Xu, D. J.; Budil, D. E.; Ober, C. K.; Freed, J. H., Rotational diffusion and order parameters of a liquid crystalline polymer studied by ESR: Molecular weight dependence. *J. Phys. Chem.* **1996,** *100* (39), 15867-15872; (b) Pilar, J.; Labsky, J.; Marek, A.; Budil, D. E.; Earle, K. A.; Freed, J. H., Segmental rotational diffusion of spin-labeled polystyrene in dilute toluene solution by 9 and 250 GHz ESR. *Macromolecules* **2000,** *33* (12), 4438-4444.

69. Wikander, G.; Eriksson, P. O.; Burnell, E. E.; Lindblom, G., ESR line shapes in lyotropic systems - the micellar and liquid crystalline phases of the dodecyltrimethylammonium chloride in waters system

J. Phys. Chem. **1990,** *94* (15), 5964-5972.

70. Forbes, M. D. E.; Yashiro, H., Initiator addition to methyl methacrylate studied in liquid and supercritical carbon dioxide. *Macromolecules* **2007,** *40* (5), 1460-1465.

71. (a) Vasilescu, M.; Caragheorgheopol, A.; Caldararu, H.; Bandula, R.; Lemmetyinen, H.; Joela, H., Micropolarity and order in the reverse micelles of L62 and L64 pluronic copolymers, as studied by molecular probe techniques. *J. Phys. Chem. B* **1998,** *102* (40), 7740-7751; (b) Lou, Y.; Ge, M. T.; Freed, J. R., A multifrequency ESR study of the complex dynamics of membranes. *J. Phys. Chem. B* **2001,** *105* (45), 11053-11056.

72. Tabak, M.; Neto, D. D.; Salmon, C. E. G., On the interaction of bovine serum albumin (BSA) with cethyltrimethyl ammonium chloride surfactant: Electron paramagnetic resonance (EPR) study. *Braz. J. Phys.* **2006,** *36* (1A), 83-89.

73. (a) Deo, N.; Somasundaran, P.; Subramanyan, K.; Ananthapadmanabhan, K. P., Electron Paramagnetic Resonance Study of the Structure of Lipid Bilayers in the Presence of Sodium Dodecyl Sulfate. *J. Colloid Interface Sci.* **2002,** *256* (1), 100-105; (b) Dejanovic, B.; Mirosavljevic, K.; Noethig-Laslo, V.; Pecar, S.; Sentjurc, M.; Walde, P., An ESR characterization of micelles and vesicles formed in aqueous decanoic acid/sodium decanoate systems using different spin labels. *Chem. Phys. Lipids* **2008,** *156* (1-2), 17-25.

74. Budil, D. E.; Earle, K. A.; Lynch, B.; Freed, J. H., Electron Paramagnetic Resonance at 1 Millimeter Wavelengths. In *Advanced EPR: Applications in Biology and Biochemistry*, Hoff, A. J., Ed. 1989.

75.   (a) Bales, B. L., Simple, accurate method to correct for unresolved hyperfine broadening in the EPR of nitroxide spin probes to determine the heisenberg spin exchange frequency. *Bulletin of the American Physical Society* **1979,** *24* (3), 427-427; (b) Bales, B. L., A simple, accurate method of correcting for unresolved hyperfine broadening in the EPR of nitroxide spin probes to determine the intrinsic linewidth and heisenberg spin exchange frequency. *Journal of Magnetic Resonance (1969)* **1980,** *38* (2), 193-205; (c) Peric, M.; Bales, B. L., Lineshapes of spin exchange broadened EPR spectra. *Journal of Magnetic Resonance* **2004,** *169* (1), 27-29.

76.   (a) Zemb, T.; Dubois, M.; Deme, B.; Gulik-Krzywicki, T., Self-assembly of flat nanodiscs in salt-free catanionic surfactant solutions. *Science* **1999,** *283* (5403), 816-9; (b) Kopetzki, D.; Michina, Y.; Gustavsson, T.; Carriere, D., Fatty acid-cationic surfactant vesicles: counter-ion self-encapsulation. *Soft Matter* **2009,** *5* (21), 4212-4218; (c) Naderi, A.; Claesson, P. M.; Bergstrom, M.; Dedinaite, A., Trapped non-equilibrium states in aqueous solutions of oppositely charged polyelectrolytes and surfactants: effects of mixing protocol and salt concentration. *Colloid Surf. A-Physicochem. Eng. Asp.* **2005,** *253* (1-3), 83-93; (d) Jung, H. T.; Coldren, B.; Zasadzinski, J. A.; Iampietro, D. J.; Kaler, E. W., The origins of stability of spontaneous vesicles. *Proc. Natl. Acad. Sci. U. S. A.* **2001,** *98* (4), 1353-1357; (e) Coldren, B.; van Zanten, R.; Mackel, M. J.; Zasadzinski, J. A.; Jung, H. T., From vesicle size distributions to bilayer elasticity via cryo-transmission and freeze-fracture electron microscopy. *Langmuir* **2003,** *19* (14), 5632-5639.

77.   (a) Wang, W.; Sande, S. A., Kinetics of Re-equilibrium of Oppositely Charged Hydrogel-Surfactant System and Its Application in Controlled Release. *Langmuir* **2013,** *29* (22), 6697-6705; (b) Serra, L.; Domenech, J.; Peppas, N. A., Drug transport mechanisms and release kinetics from molecularly designed poly(acrylic acid-g-ethylene glycol) hydrogels. *Biomaterials* **2006,** *27* (31), 5440-5451.

78.   Dominguez, A.; Fernandez, A.; Gonzalez, N.; Iglesias, E.; Montenegro, L., Determination of critical micelle concentration of some surfactants by three techniques. *J. Chem. Educ.* **1997,** *74* (10), 1227-1231.

79.   Shanks, P. C.; Franses, E. I., Estimation of micellization parameters of aqueous sodium dodecyl sulfate from conductivity data *J. Phys. Chem.* **1992,** *96* (4), 1794-1805.

80.   Hines, J. D.; Thomas, R. K.; Garrett, P. R.; Rennie, G. K.; Penfold, J., Investigation of mixing in binary surfactant solutions by surface tension and neutron reflection: Anionic/nonionic and zwitterionic/nonionic mixtures. *J. Phys. Chem. B* **1997,** *101* (45), 9215-9223.

81.   Kamenka, N.; Chorro, M.; Talmon, Y.; Zana, R., Study of mixed aggregates in aqueous solutions of sodium dodecyl sulfate and dodecyltrimethylammonium bromide *Colloids and Surfaces* **1992,** *67*, 213-222.

82.   Dejanovic, B.; Noethig-Laslo, V.; Sentjurc, M.; Walde, P., On the surface properties of oleate micelles and oleic acid/oleate vesicles studied by spin labeling. *Chem. Phys. Lipids* **2011,** *164* (1), 83-88.

83.   Earle, K. A.; Budil, D. E.; Freed, J. H., 250-GHz EPR of nitroxides in the slow-motional regime - models of rotational diffusion. *J. Phys. Chem.* **1993,** *97* (50), 13289-13297.

84.   *Organic Syntheses*. Wiley and Sons: New York, 1989; Vol. 1.

85.   Armarego, W. L.; Chai, C., *Purification of laboratory chemicals*. Butterworth-Heinemann: 2012.

CHAPTER 5: EPR Investigations of Nonionic Surfactants

5.1 Introduction

The most versatile and ubiquitous commercial surfactants are non-ionic and polymer based. They have a wide range of applications, and are regularly encountered in cosmetics,[1] cleaning formulations,[2] medial products,[3] and even food preparation.[4] Their lack of charge makes them much more stable to environmental changes, and they are generally much less toxic than their charged counterparts.[5] Many nonionic surfactants are based on the polymer polyethylene oxide (PEO). These include core-shell surfactants, where a block of PEO units serves as a hydrophilic shell and is covalently attached to a hydrophobic alkyl chain or other tail structure, which is buried much deeper in the micelle core. For example, modified phosphatidylcholine covalently attached to PEO is used extensively in FDA approved formulations for drug delivery[6] and ultrasound imaging contrast agents.[7] Other common PEO-based, core-shell surfactants include the Brij and Triton surfactant lines – where a hydrophilic PEO structure is attached to an alkyl chain or 4-(1,1,3,3-tetramethylbutyl)-phenyl group, respectively.

Another common class of PEO surfactants are block copolymers with amphiphilic characteristics. The Pluronic line of surfactants from BASF are triblock copolymers consisting of two identical end blocks and a unique center block consisting of polypropylene oxide (PPO), while surfactants known as reverse Pluronics have a PPO-PEO-PPO structure.[8] Both are being widely studied for drug delivery applications because of their thermoresponsive behavior,[9] effect on cellular adhesion,[10] and ability to alter cell permeability.[11] This behavior is highly dependent on

block size and organization (PEO-PPO-PEO vs PPO-PEO-PPO), but some structure have shown promising affinity for and high toxicity to cancerous cell lines.[11a, 12]

From a magnetic resonance perspective, these PEO-based surfactants are of great interest because micellar structures formed by these surfactants can be used to restrict free radical diffusion.[13] The core-shell or block copolymer aggregates differ greatly in aggregate formation, size, and viscosity from their ionic surfactant counterparts. Because nonionic surfactants are so regularly employed for solubilizing hydrophobic drug targets,[3a, 5a, 14] and in diffusion controlled drug delivery applications,[3b, 5c, 15] characterization of the diffusive motion of small organic molecules in these structures is important. SSEPR and TREPR are both quite sensitive to the regimes of diffusive motion accessible in surfactant aggregate structure; however, to date, many of these nonionic surfactants have not been fully characterized by EPR spectroscopies.

5.2 Background

5.2.1 Nonionic Core-Shell Surfactants

The structures of some of the nonionic surfactants relevant to the experimental work presented in this chapter can be seen in Scheme 5.1 The Brij surfactant series are poly(oxyethylene) alkyl ethers, often denoted with a C_nE_m surfactants, where n is the number of carbons in the alkyl chain and m is the number of ethylene oxide (EO) units. Triton surfactants are poly(oxyethylene) alkylphenyl ethers. Both the Brij and Triton surfactants form core-shell micelles, with the polyethylene oxide serving as the hydrophilic "head group" of the surfactant.[16] Nonionic surfactants are of significant biological interest because they have been very successful in solubilizing membrane proteins.[17] Their wide range of structures lead to varied aggregation behavior, and they are also used extensively in industrial and household cleaning products.[18]

Scheme 5.1

Brij 35

Brij 97

Brij 700

Triton X-405

Triton X-100

Pluronic L61

Pluronic L64

Pluronic F68

Pluronic 17R4
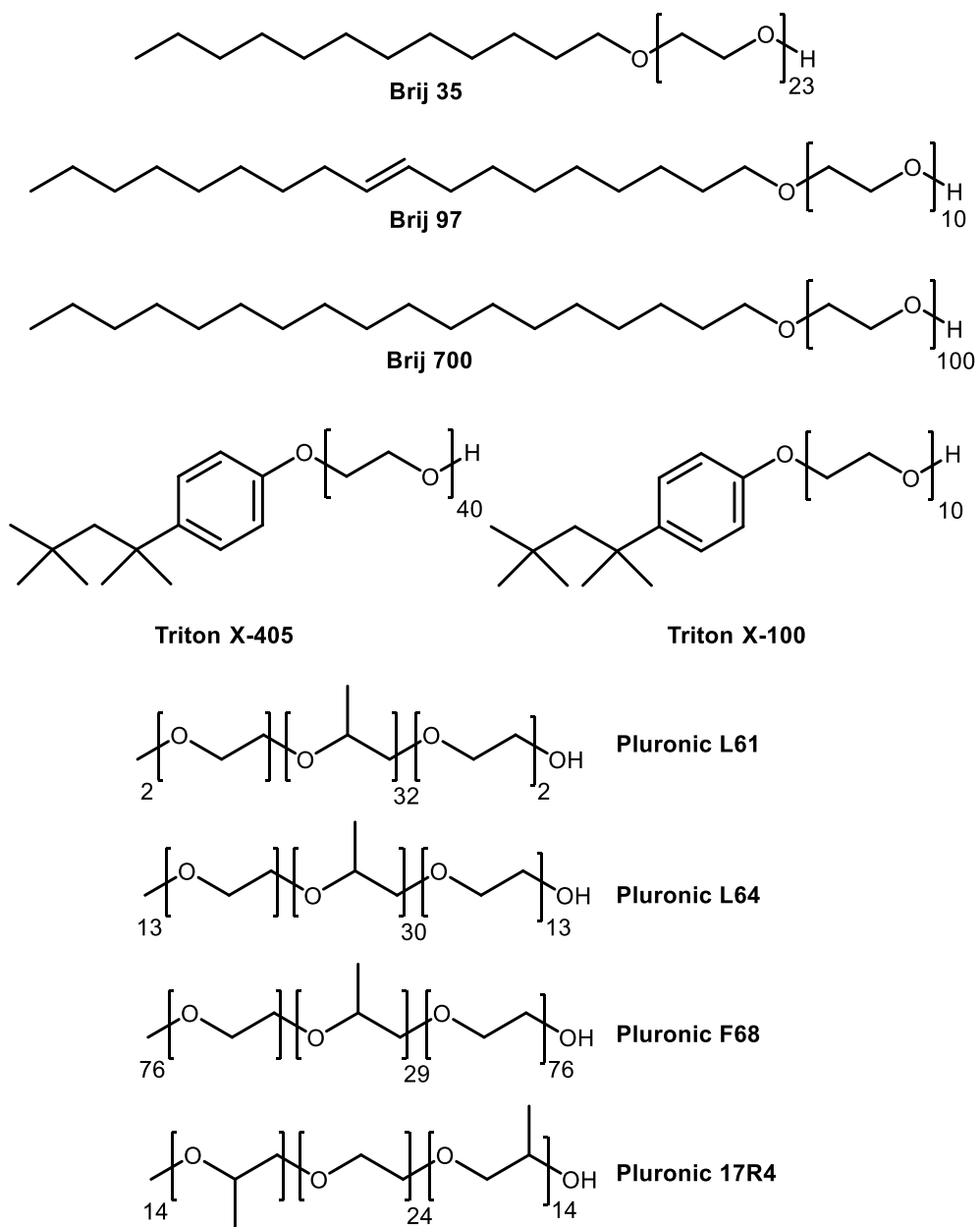
The sizes and shapes of nonionic surfactant aggregates have been characterized by light scattering and small angle neutron scattering (SANS). Triton X-100 micelles appear to be disk-like with a major semiaxis of 35 Å and a minor axis of 10 Å for the core, and a radius of 50 Å for the shell.[20] Early characterization of C_nE_m surfactants described the Brij 35 micelle with a semiaxis radius 35 Å for the shell and 16.6 Å for the core.[19] More recent studies of the Brij micelle suggests that Brij 35 forms spherical micelles with a central anhydrous core, a hydrated outer core that is viscous and obstructs solvent flow, and an outer shell or corona.[21] The total micelle hydrodynamic radius is approximately 44 Å, with and aggregation number of about 40. The size of the shell is temperature dependent, decreasing from 13 Å at 10 °C to 7 Å at 70°C. The hydration degree of the whole PEO segment of the micelle decreases over this same range from 8 water molecules per EO unit to 4. Therefore, the contraction of the PEO shell is intimately relate to the expulsion of water from the micelle interior.

Magnetic resonance studies of photochemically generated RPs in the Brij and Triton micelles primarily focused on how these structures affected product yields of radical reactions.[22] Their large size and viscous nature made them ideal candidates for altering spin-selective product formation of radical reactions. The structure and nature of the micellar RP in these systems was reported relatively recently by Chaney and Forbes.[13] The photochemistry leading to the generation of a RP in neat PEO and core-shell surfactants with a BP triplet sensitizer is shown in Scheme 5.2. Hydrogen atom abstraction occurs selectively at the α-alkoxyalkyl position of EO subunits. The PEO radical spectrum consists of a series triplets with an isotropic g-factor of 2.0026 from three different hyperfine coupling constants: one α-hyperfine coupling of 17.7G, two β-hyperfine couplings of 9.3 G, and two γ-hyperfine couplings of 2.0 G in solutions of PEO in water. The hyperfine coupling was observed to be dependent on the radical environment, with slightly small

Scheme 5.2

10 G
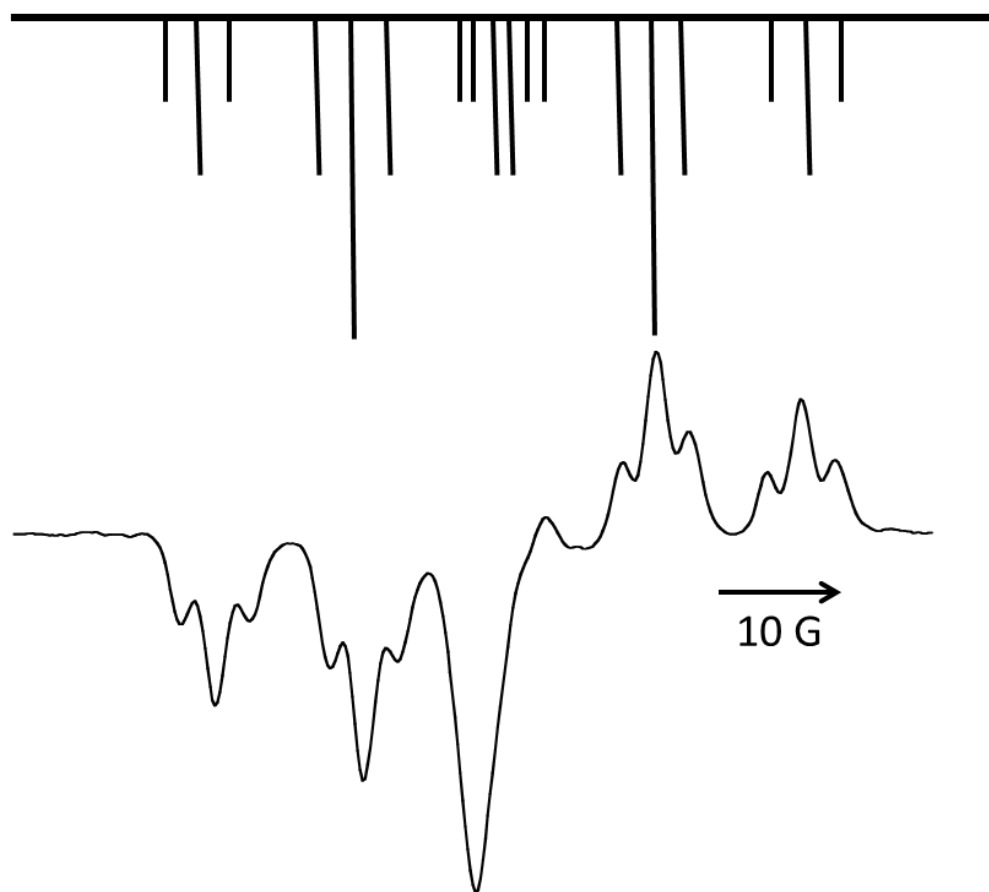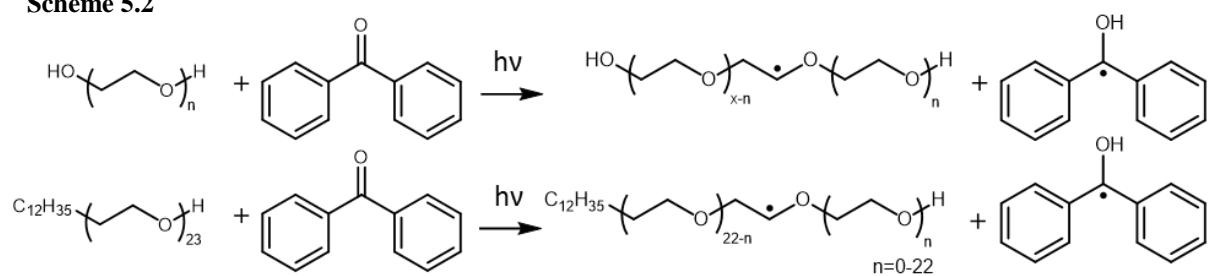
values of the α- and β-hyperfine coupling constants measured in micellar solutions of Brij 35. Scheme 5.2 also shows a stick plot of the EPR transitions of the PEO radical structure, shown in net emission caused by the TM for clarity. Below that is an experimental spectrum collected for a solution of PEO (MW= 2000) in 50:50 acetonitrile:water at a 500 ns delay time and room temperature. The intense emissive peak in the center of the spectrum is due to the sensitizer radical.

The polarization pattern for the PEO radicals in Scheme 5.2 is dominated by the RPM, with a low field E, high field A pattern. Some degree of TM contributes to the spectrum, resulting the high field transitions appearing less intense than their low field counterparts. The CIDEP polarization is more complex for the Brij surfactant series. Figure 5.1 shows a time dependence of the TREPR spectra of solutions of Brij 35 and a deuterated benzophenone (BPd10). First, it is important to note that the spectrum appears to arise almost exclusively from BPd10 and PEO. At short delay times, Chaney and Forbes[13] observed that the polarization of the PEO radicals appeared primarily from the RPM, but the APS of the central component from the BPd10 radical suggests that this spectrum is a superposition of RPM and SCRP polarization. The time dependence reveals that the contribution of the APS to the spectrum increases with delay time after photolysis. It was also observed to increase even more substantially with increasing temperatures. This delayed growth of APS is a direct result of the large size and high internal viscosity of the core-shell micelle. The process of "filling out" the micelle volume (Figure 2.3) takes more time under these conditions, so at short delay times the line shape of the SCRP appears qualitatively identical to RPM polarization. At longer time delays, the effect of the micellar confinement and the spin correlation can be observed as APS.

An anomalous feature was observed in the TREPR spectra of Brij-35 micelles. Additional transitions are observed just next to the transitions of the PEO radicals, which are marked with an
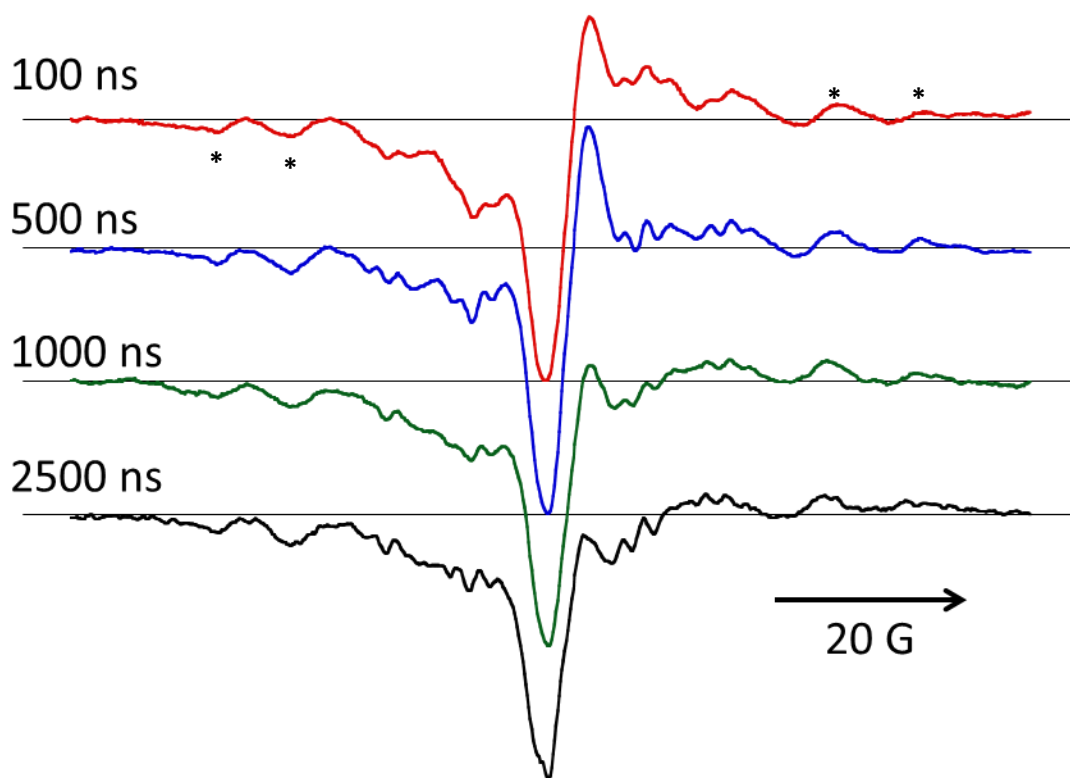
Figure 5.1 The time dependence of the TREPR spectra of 0.1 M Brij 35 with 1.1 mM BPd10. Spectra were collected during 4 minute scans, with a gate width of 300 ns, at the delay times indicated next to each spectra, after photolysis at 308 nm and a repetition rate of 60 Hz. The large central transitions arises from the ketyl radical of the deuterated benzophenone. The transitions marked in the top spectrum with an asterisk are unidentified, but tentatively assigned as alkyl radicals from the micelle core.

asterisk in Figure 5.1.. The anomalous transitions are also much weaker and broader than the PEO radical signal. Chaney and Forbes [13] attributed this signal to an alkyl core radical. The weaker intensity of the TREPR signal of the radical was explained by the preferential location of the BPd10 sensitizer in the PEO shell over the alkyl core, resulting in an overall greater production of the PEO-based surfactant radical.

Although Chaney and Forbes[13] assigns the additional radical signal in Figure 5.1 to alkyl core radicals, because of broadening and the low S/N in the spectra, hyperfine coupling constants could not be determined with enough precision to identify the structure of the unknown radical signal. Additional transitions are also obscured because they are superimposed underneath the signal of the PEO and BPd10 radical. As a consequence, the structure of the unidentified radical could not be determined, and it could not be definitely identified as arising from the micelle core. Furthermore, PEO is known to degrade following γ-irradiation or H-atom abstraction reactions initiated by H_2O_2 or the Fenton reaction, which produce the same PEO radical as H-atom abstraction by a triplet sensitizer, through a series of radical mechanisms.[23] Therefore, it is possible that the transitions marked in Figure 5.1 are not from the core radical. The lower intensity of the unidentified signal carrier could be due to low production of the radical or to decay of the spin polarization during a secondary degradation process that leads to its formation.

The sonochemical and photochemical degradation of ionic and nonionic PEO-based micelles has also been carried out by SSEPR spin trapping studies.[24] In these experiments, a "trap" molecule is included in solution that is known to react with short lived radicals of interest to form a more stable radical adduct. Sostaric and Riesz[25] employed the spin trap 3,5-dibromo-4-nitrosobenzene sulfonic acid (DBNBS) to trap short lived alkyl radicals produced by during sonolysis and UV photolysis of H_2O_2 in surfactant solutions, including SDS and polyoxyethelene-
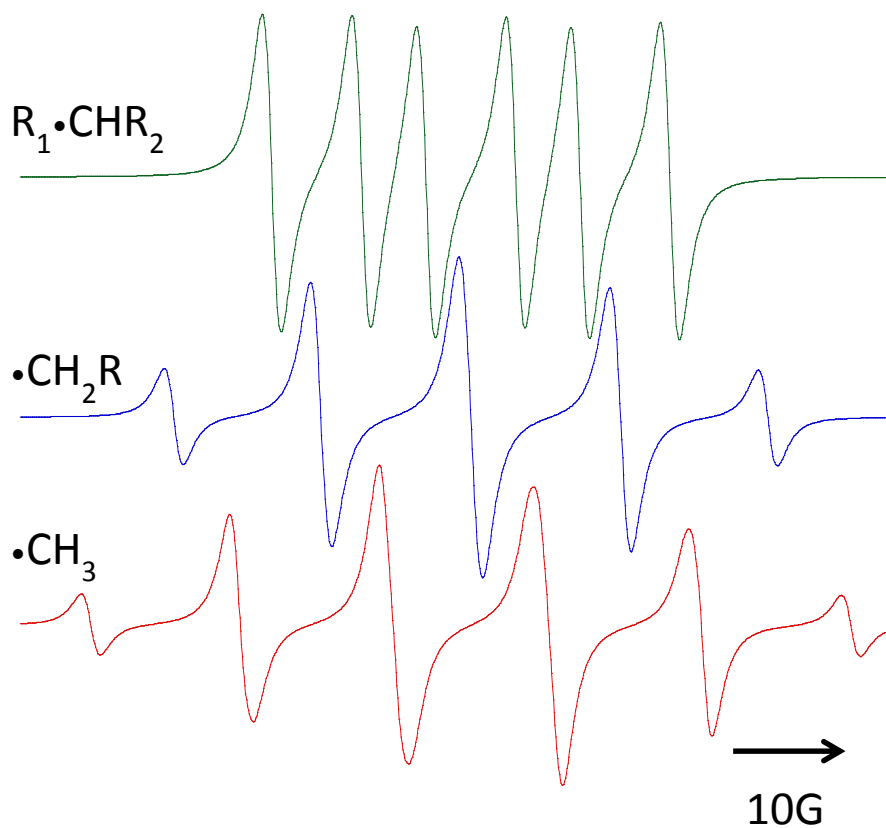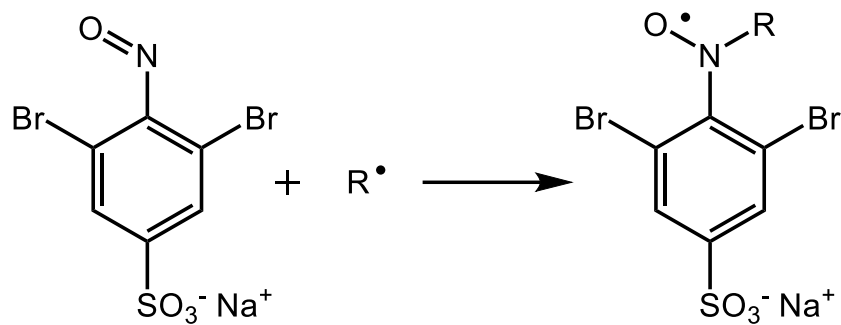
Figure 5.2 Simulations of the secondary (-·CH-), primary (·CH$_2$), and methyl (·CH$_3$) radical adducts of DBNBS.

8-decyl ether. Three alkyl radical adducts of DBNBS were observed, each with different hyperfine coupling constants (Figure 5.2). For both sonolysis and UV photolysis in solutions of nonionic PEO-based surfactants, the primary product was the $-\cdot CH-$ adduct with a minor contribution to the EPR signal from the $-\cdot CH_2$ adduct. The methyl radical ($\cdot CH_3$) was observed only during sonolysis. The formation of the minor products was attributed to the degradation of the PEO chain after H-atom abstraction. Spin trapping proved remarkably successful in detecting alkyl radicals in surfactant solutions; however, it was only applied to PEO-based surfactants that had a very small number of PEO units at concentrations below their CMC.

The goal of our studies of nonionic surfactants is twofold: 1) extend the previous work of Chaney and Forbes[13] to a wider range of structurally related nonionic core-shell micelles to understand the correlation between molecular structure and the diffusion of RPs inside the micellar environment, and 2) identify the unknown radical previously assigned to the alkyl core. To this end, variation in the hydrophobicity of the sensitizer could change the location of H-atom abstraction and radical formation in the micelle. In addition, extending the spin trapping study of Sostaric and Reisz[25] to micellar solutions of larger PEO-alkyl ether surfactants could help identify the structure of the unknown radical.

5.2.2 Triblock Copolymer Surfactants

5.2.2a Background

Triblock copolymers consisting of blocks of polypropylene oxide (PPO) and polyethylene oxide (PEO) are available commercially under the trade names Synperonics, Pluronics, or Poloxamers, and commonly denoted as either PEO-PPO-PEO or $EO_nPO_mEO_n$ to indicate the arrangement and size of the blocks.[8] The structure of these surfactants can be found in Scheme

5.1. These polymers are available in a wide range of molecular weights and varying ratios of PEO/PPO. As water soluble copolymers, Pluronics have attracted considerable attention because they exhibit diverse, temperature and concentration dependent phase behavior. Aggregate structures formed by these surfactants include micelles and reverse micelles, random polymer networks, cubic, lamellar, and hexagonal phases, isotropic phase separation, and thermally induced gelation.[8, 26] This highly variable phase behavior and the ease of tuning the copolymer properties by changing the molecular structure of the copolymer have made these systems very attractive for applications in detergents,[2, 27] emulsifiers,[28] lubricants, cosmetics,[1] inks,[29] bioprocessing,[11b, 30] separations and purification.[31] They are also extensively used in pharmaceutical applications for drug solubilization or controlled release,[3, 32] and have been shown to either enhance or decrease cell membrane permeability as a function of PEO/PPO block ratio.[33]

For ease of reference, PEO-PPO-PEO block copolymer surfactants will be referenced using the nomenclature for the BASF line of products under the trade name Pluronic. The name of the surfactant begins with a letter that denotes the physical state of the polymer at ambient conditions, "L" for liquid, "P" for paste, and "F" for flake, followed by 2-3 numbers.[8] The last number in the surfactant name indicates the weight percentage of the PEO content relative to the average molecular weight M_w of the polymer. The remaining digits indicate the M_w of the PPO block, which is roughly determined by multiplying by 300. For example, Pluronic F68 indicates a solid PEO-PPO-PEO polymer with a PPO block of M_w~1800 and 80 wt. % PEO. Pluronic L64 is a liquid with an identical block size, but a PEO content of 40 wt. %. "Reverse Pluronics" have a slightly different nomenclature. For instance, Pluronic 17R4 describes a reverse Pluronic surfactant – where the R indicates the reverse block ordering, the first two digits indicate the total M_w of PPO in the polymer (M_w of PPO ~1700), and the last digit represents the weight percent of

PEO (40 wt. %). Due to their similar block sizes, Pluronic 17R4 is the structural analogue of the conventional Pluronic L64.

Because of their availability, low toxicity, considerable structural variation, and aggregation behavior, Pluronic copolymers have found wide use in many applications common to other ionic surfactants. Like the related poly(oxyethylene) alkyl ethers (Brij) discussed above, amphiphilic copolymers can self-assemble in aqueous solution to form micelles. Aggregation of PEO-PPO-PEO block copolymers occurs because of differences in the hydrophobicity of the PEO and PPO blocks.[34] Water is a selective solvent for the PEO blocks, meaning that it is a thermodynamically favorable solvent for solubilizing the PEO. On the other hand, PPO becomes insoluble in water at temperatures as low as 290 K.[26] The insoluble PPO block comprises the core of the micelle and is surrounded by a shell comprised of the hydrated PEO block.

PEO-PPO-PEO copolymers exist as unimers at low temperature or low concentration, but will aggregate at increased temperatures or at higher concentrations.[8] For example, early formation of aggregates is detectible in solutions of L64 by light scattering starting at 6 wt. % polymer in solution at a temperature of 25°C, representing the CAC of this surfactant.[35] Pluronics can also be characterized by a critical micelle temperature (CMT), the temperature at which micelles begin to form given a constant concentration. For a 10 wt. % solution of Pluronic L64, the CMT has been reported at approximately 34.5°C.[36] Below this temperature, the polymer exists as coiled unimers or as premicellar aggregates of a smaller size. However, the CMC and CMT of block copolymers are not well defined.[8, 37] Polydispersity exists, even for samples of a relatively uniform M_w that causes the CMC and CMT to vary over a range of 10 wt. % or 10 °C.[8, 26]

The micellization of PEO-PPO-PEO copolymers depends most strongly on the size of the PPO block.[8, 26, 34] If the PPO block is too large then the copolymer may not dissolve at all, but in

general, the large the hydrophobic block, the lower the onset of micellization as measured by both the CMC and CMT. There is a small increase in the CMC and CMT for surfactants with increasing PEO content. This effect on the CMC and CMT is not as strong as the effect of the PPO block size, which indicates that hydrophobic interactions between the PPO blocks are the driving force behind micelle formation. For Pluronics that are less hydrophobic, either due to low molecular weight or high PEO content, micellization is not observed at room temperature, but may be observed when the temperature is increased because water becomes a poorer solvent for both the PPO and PEO blocks as the temperature decreases. The dehydration of the PPO block is more pronounced and begins at a lower temperature, which is why the size of the PPO block exerts greater control over the phase behavior of the polymer.

The size and shape of Pluronic micelles seems to be relatively independent of the surfactant structure. Unimers are detected by light scattering techniques with a hydrodynamic radius of 1-2 nm.[8, 35-36] Aggregates begin to form with increasing temperature and concentration with low aggregation numbers of 4-10 molecules.[38] Micellar structures typically have hydrodynamic radii of approximately 10 nm and aggregation numbers on the order of 50 molecules.[8, 39] The radii of the micellar structures are constant with increasing temperature, but the aggregation number increases substantially. For the micelle size to stay constant but the aggregation number to increase, deswelling of the PPO and PEO blocks must be substantial. Observations of tighter packing of the copolymer in the aggregate[40] and dehydration of both parts of the polymer,[36, 41] confirm this behavior.

One final point of interest in the phase behavior of these block copolymer surfactants is the formation of novel aggregates and phases observed in solutions of C_nE_m core-shell surfactants. In addition to unimer and micellar phases, triblock copolymer surfactants form flower-like micelles,

polymer and micellar networks, gels, and separate, isotropic phases.[8, 26, 42] The formation of gels and the observation of isotropic phase separation are particularly unique to nonionic copolymer surfactants. SANS measurements reveal that the formation of gels is the result of hard sphere crystallization of the micelles.[34b, 34c, 43] Gel formation occurs at lower temperatures for polymers with higher molecular weight and is typically observed for Pluronics with high PEO content.[8, 44] Phase separation is observed many different Pluronic surfactants, although the PEO content is usually lower than surfactants known to form thermoresponsive gels. Ranges of temperature and concentration where phase separation is observed are also larger for reverse Pluronics relative to their conventional analogues of the same molecular weight and PEO/PPO content.[36]

5.2.2b Spin Probe Studies of Pluronic Micelles

The micellar phase of some Pluronic surfactants have been examined by SSEPR by using a wide range of spin probes.[26, 45] Extensive structural variation of the spin probes allowed for the investigation of mobility of the probe and polarity of the local environment in different regions of the aggregate structure, including the PPO core and varying depths of the PEO shell. Spin probes included in the study were primarily large and hydrophobic to ensure association with the micelle, but included cationic and anionic head groups attached to alkyl chains, spin labeled PEO-PPO-PEO polymer, and the commonly used doxyl stearic acids (DSA). The main objective of these spin probe studies is to obtain local information on the hydration of the hydrophobic and hydrophilic domains, on the degree of order in the aggregates, the effects of temperature on aggregate structure, and on the solubilization and diffusion of guests in the system.

The assumption is made that the DSA spin probe is located preferentially in the polymer

aggregates.[45a] Experimental spectra in solutions containing Pluronic surfactants above the CMC or CMT differ from the spectra of DSA in pure water. The absence of a sharp, isotropic line shape in the experimental spectra of 5-DSA in micellar solutions of Pluronics support the assumption that the spin probe associates closely with the micelle. The hyperfine value for the 5-DSA probe in L64 is closer to the value measured in neat PPO than neat PEO or water, suggesting that the probe is most likely sampling the PPO core or is at least in a hydrophobic environment where the hydration is low.[46] The order parameter, S_{eff}, measured from the spectra also decreases gradually as a function of the doxyl position along the alkyl chain. Assuming that there is no hairpinning for the 10-DSA or 12-DSA probes, this suggests a gradual decrease in ordering from the PEO-PPO interface toward to the PPO core. Caldararu et al. have also used DSA in alkali solutions, which leads to the deprotonation of the carboxylic acid and increases the polarity of the DSA probe, to investigated ordering in the more polar micellar shell.[26, 45] If the solution is not basic, SSEPR spectra of 5-DSA in 10% aqueous solutions of Pluronic P85 show two components. A slow motion component is attributed to the deprotonated form of 5-DSA in the PEO core, while the fast motion component has a A_N of 14.3 G, identical to the value of A_N in neat PPO.

Kurzbach et al.[47] examined the partitioning of the small, hydrophilic spin probe TEMPO in Pluronic micelles, which revealed temperature dependent partitioning of the spin probe between at least two-sites in solution – one that appeared hydrophobic and the other hydrophilic. Changes in the hyperfine coupling and isotropic g-factor of TEMPO were indicative of changes in polarity that were used to identify a more hydrated, hydrophilic region and a more anhydrous, hydrophobic environment occupied by the spin probe. For Pluronics with a PEO fraction less than 50%, the two-sites appeared to be static with little or no exchange between the sites. For surfactants with a PEO fraction of greater than 70%, the A_N for the hydrophobic species of TEMPO changed with

increasing temperature – becoming larger and approaching the value of A_N assigned to the hydrophilic TEMPO species. This behavior is interpreted by the authors as site exchange between the hydrophobic and hydrophilic TEMPO species. The observation of exchange of TEMPO between the hydrophobic PPO core and bulk water with increasing PEO content is attributed to one of two sources: 1) the smaller size of the PPO core for Pluronic surfactants with larger PEO content allows for faster diffusion of the TEMPO out of the core and into the aqueous bulk or 2) increasing penetration of the PPO core by PEO and water occurs for Pluronic surfactants with a larger PEO content.[48] Regardless of the PEO content, TEMPO partitioning revealed the formation of hydrophobic regions at much lower concentrations than observed with DSA or other hydrophobic spin probes. The observation of TEMPO in a hydrophobic environment below the CMC of the surfactant is attributed to the formation of small, hydrophobic cavities due to the collapse of the PPO block of several molecules prior to micelle formation. The small size of the TEMPO molecule allows it to be solubilized in these premicellar aggregates, making it a good indicator of the CAC of the surfactant rather than the CMC.

Although some attempts have been made to compare the phase behavior of structurally related Pluronics by light scattering or viscosity measurements, [45b] no comprehensive comparison has been undertaken using EPR - although the few Pluronics that have been characterized by SSEPR have been given a very thorough treatment.[26, 45-46] In addition, TREPR spectroscopy of transient radicals in these surfactant systems has never been carried out. Given the diverse range of structures formed by Pluronic surfactants and the questions raised concerning water penetration into the shell and core by partitioning experiments, TREPR could provide valuable information about the accessibility of the hydrophobic and hydrophilic blocks to aqueous and hydrophobic

sensitizers, as well as additional information about the formation and physical characteristics of the hydrophobic aggregates themselves.

5.2.2c Electron Spin Polarization (ESP) of Nitroxides in Supramolecular Systems

One additional TREPR experiment that could provide valuable information about the polymer aggregates involves electron spin polarization (ESP) or polarization transfer from excited organic molecules to stable nitroxide radicals in solution. Stable free radicals like nitroxides are typically not observed in TREPR experiments because they exist with Boltzmann spin distributions, but under particular circumstances, these stable radicals can become spin polarized. ESP has been well documented following the interaction of triplet sensitizers like benzophenone and nitroxides in solution. This type of polarization occurs by two different mechanisms: the Radical Triplet Pair Mechanism (RTPM) or Electron Spin Polarization Transfer (ESPT)[49] which are shown in Scheme 5.3. In supramolecular systems like host guest complexes or surfactant aggregates, polarization transfer can occur between radicals or triplet sensitizers confined to the supramolecular structure to another molecule outside the structure. Like most other CIDEP mechanism, ESP in these systems provide information about the nature and physical properties of any confining supramolecular structure that affects the diffusion of the triplet or nitroxide radical.

The two forms of ESP of nitroxides observed by TREPR occur by slightly different mechanisms. In RTPM, a quartet state (Q) and doublet state (D) must make repeated, diffusive reencounters – similar to the diffusive reencounters that generate RPM and SCRPM polarization.[50] This CIDEP mechanism was proposed to explain electron spin polarization produced from the quenching of triplet excited states by free radicals.[51] The diffusive encounters of a molecular triplet state (Q) and a free radical (D) can lead to spin state selective mixing of the quartet-doublet pair

(QD) through either the electron spin dipolar interaction or the hyperfine interaction. Mixing involving the $Q_{\pm 3/2}$ results in a net E or A polarization pattern that appears similar to TM polarization. RTPM polarization and has been observed in a wide variety of chemical systems, including single crystals containing free radical impurities,[52] covalently linked triplet precursors and nitroxides,[53] and host-guest complexes.[53b, 54]

It's important to note that neither the Q nor D state must be spin polarized when the QD pair begins to make diffusive reencounters for spin polarization to develop. This is not true for ESPT. As we have seen with other CIDEP mechanisms, the ISC process of an excited organic molecule solubilized in a micelle is highly dependent on the local environment of the sensitizer molecule and can result in strong spin polarization.[49a, 55] In the TREPR experiments described previously, the triplet sensitizer interacts with the surfactant molecule, participating in a chemical reaction that forms a RP that is spin polarized. However, if the triplet sensitizer is chosen such that it will not react with other molecules in solution, the spin polarization of the excited triplet state will simply decay, and no TREPR signal will be generated. In systems where a free radical may encounter the polarized triplet during its lifetime, some of the spin polarization can be transferred from the excited triplet state to the stable radical species.[49b, 56] The result is a spin polarized nitroxide radical that can be observed by TREPR. The spectra will appear with net E or A polarization according to the polarization of the excited triplet state.[56a, 57]

For RTPM polarization, the development of a spin polarized nitroxide depends on restricted diffusion the QD pair. RTPM polarization is maximized in systems where diffusion of the QD pair is severely restricted by covalent bonding, but any supramolecular confinement like a micelle that would restrict the QD pair diffusion will affect the observation of an RTPM polarized

Scheme 5.3
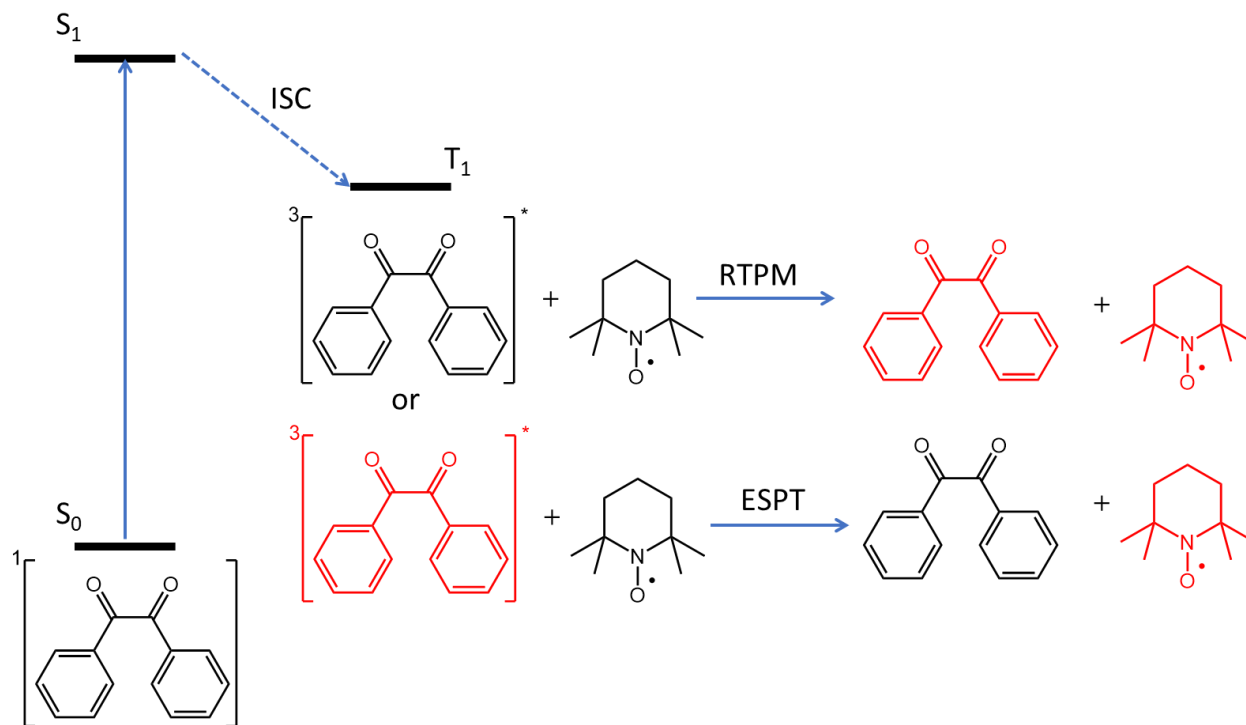
spectra. The nature of the ESPT polarization is directly related to the polarization of the triplet molecule because that polarization is dependent on the local environment of the triplet and is not a consequence of the environment of the free radical. In some ways, polarization transfer in micelle or vesicle structures can be considered a TREPR experiment analogous to SSEPR spin probe studies, because the polarization of the free radical observed in the TREPR spectra reflects properties of the triplet sensitizer. If the sensitizer is confined to the hydrophobic regions of a surfactant aggregate, any effect the aggregate structure has on the polarization of the triplet sensitizer due to properties like hydration of viscosity will be reflected in the TREPR spectra of the spin polarized free nitroxide.

Triplet sensitizers like BP or AQ are known to be spin polarized in the micellar environment, which is required for ESPT but not RTPM. Fundamentally, both ESP mechanisms will produce a spin polarized nitroxide visible by TREPR in micellar solutions. Often, only the nitroxide radical is observed, especially in cases where the triplet state of the sensitizer is quenched by its encounter with the radical. So long as the RTPM produces a net polarization and not a multiplet pattern due to interactions of the nitroxide with the $Q_{\pm 1/2}$ states, it is very difficult or impossible to distinguish between the two polarization mechanisms from the TREPR spectrum of the nitroxide alone – although some careful pulsed EPR experiments have been able to distinguish between the mechanisms from time dependent changes in the EPR spectrum and an examination of the kinetic time-trace.[54a] Both RTPM and ESPT have been reported for nitroxides in micellar solutions, where the restricted diffusion, charge, or viscosity have played a role in the observation of ESP.[58] ESP phenomena have recently been observed in block copolymer surfactants in solutions when nitroxide probes have been covalently attached to the polymer chain, which provides useful information about the dynamic motion of the polymer in solution.[59] A similar methodology can be

applied to Pluronic surfactant solutions, which may provide additional information about the hydrophobic phases in these systems.

5.3 Results and Discussion

5.3.1 TREPR of Core-Shell Surfactants

Initial experiments focused on extending the work of Chaney and Forbes[13] to other nonionic core-shell surfactants and varying the polarity of the triplet sensitizer. Two additional Brij surfactants, Brij 97 and Brij 700, and one additional Triton surfactant, Triton X-405, were examined with a BP sensitizer. The TREPR spectra of Brij 97 and Triton X-405 were relatively unremarkable, and consisted primarily of strong, broad net emissive TM polarized signals. The TREPR spectra of Brij 700 is shown in Figure 5.3. Brij 700 has a slightly longer alkyl tail than Brij 35, but the primary difference between the two surfactants is size of the PEO shell (23 monomer units for Brij 35 and 100 monomer units for Brij 700). The time evolution of the Brij 700 spectra differ substantially from Brij 35. The E/A RPM polarization pattern of the PEO radical signal is clearly visible at the shortest delay time (100ns), but at other delay times, the spectra show a strong contribution of emissive TM polarization and considerable broadening of the BP ketyl radical signal. At longer delay times than those shown in Figure 5.3, the PEO radical signal is not visible and the TREPR spectrum appears as a single, emissive peak. There is no noticeable contribution of the SCRPM to the PEO radical signal, which is observed for Brij 35 at long time delays (< 2 μs).

TM polarization is viscosity dependent,[60] and the strong, net TM polarization is likely due to increased viscosity of the Brij 700 micelles relative to Brij 35. An increase in the viscosity of Brij 700 micelles relative to Brij 35 micelles is expected due to the increase PEO content, but an
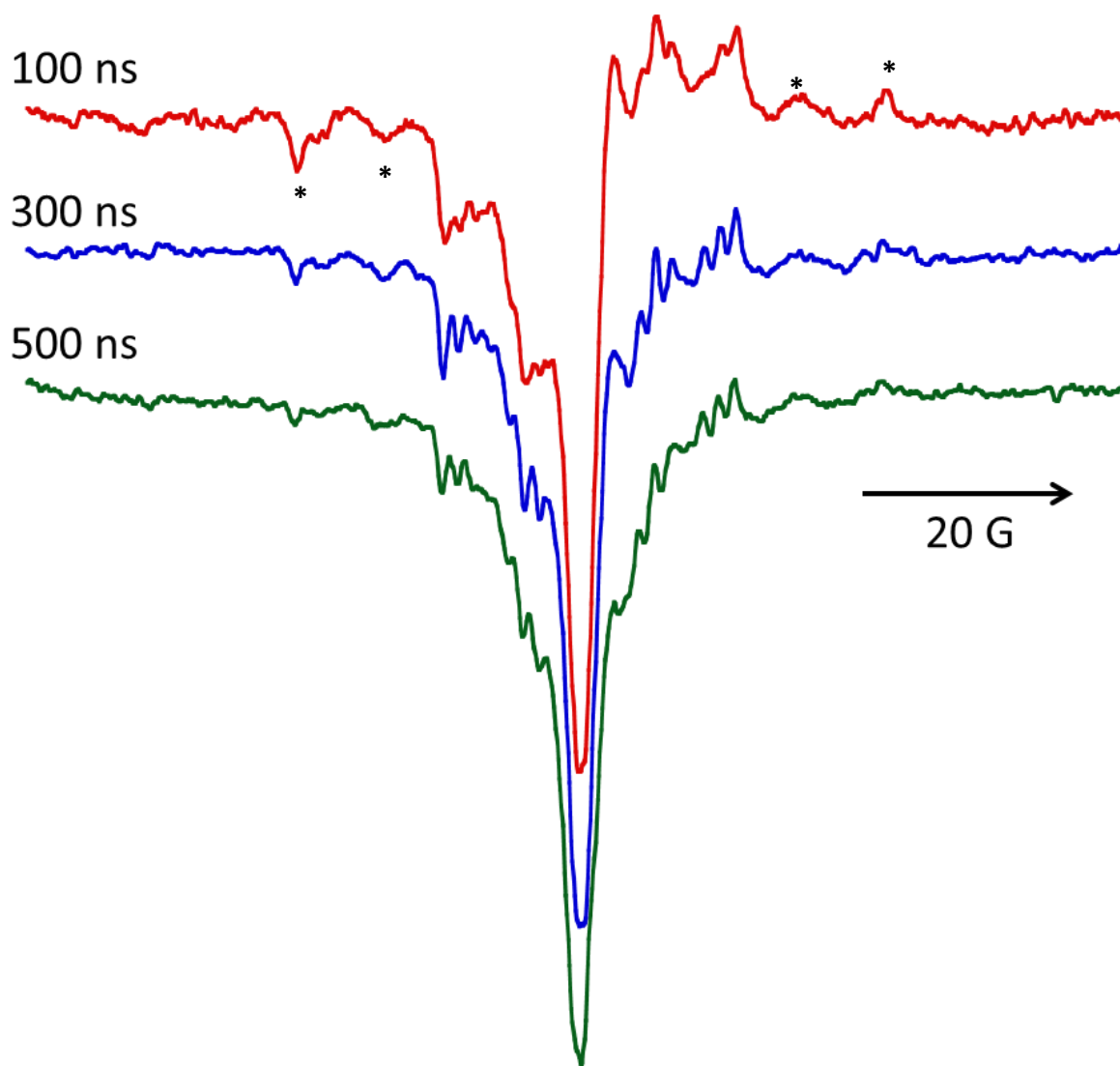
Figure 5.3 The time dependence of the TREPR spectra of 0.05 M Brij 700 with 1.1 mM BP-d10. Spectra were collected during 4 minute scans, with a gate width of 300 ns, at the delay times indicated next to each spectra.

increase in emissive TM polarization alone is not enough to explain the line shape of the spectra in Figure 5.3. The intensity of the PEO transitions does not match the predictions for a superposition of RPM and TM. In highly viscous solutions, where separation of the RP is slow, it is possible for the RP to spend a significant amount of time at short distances where $2J$ is strong. If $2J$ is approximately equal to the energy difference between the S and either to T_+ or T_- RP states, mixing between these states can occur instead of the more routine ST_0 mixing.[61] The polarization of the Brij 700 TREPR spectra appears more similar to the polarization pattern observed in Triton X-100 micelles by Chaney and Forbes,[13] where the high-field PEO transitions appeared to become more emissive with increasing delay time. This is attributed to ST_- mixing of the SCRP and has been observed for other radicals in highly viscous media and at long delay times.[61]

The TREPR of Brij surfactants was also examined with AQ, AQS, and AQDS sensitizers. Previous results for these sensitizers in ionic surfactants suggest that these sensitizers increase in hydrophobicity with decreasing charge; therefore, the doubly charged AQDS exists at the edge of the PEO shell or even outside of the micelle,[62] while the neutral and hydrophobic AQ is closer to or inside of the micelle core. Figure 5.4 shows the TREPR spectra of all three sensitizers in solutions of 0.1 M Brij 35 collected at a delay time of 500 ns. The TREPR spectra of AQ and AQS look remarkably similar, suggesting that these two sensitizers sample similar environments within the micelle. The unidentified "core" radical is visible in both systems. The correlation between the hydrophobicity of the sensitizer and the observation of transitions from the unidentified radical strengthens the argument that these transitions originate from a radical in the micelle core. Both spectra show strong net emissive character. It is difficult to determine if the line shape of the PEO radicals is due to SCRPM or ST_- based polarization of the SCRP. A distinction between the two could be made by examining the time dependence of the polarization of the PEO
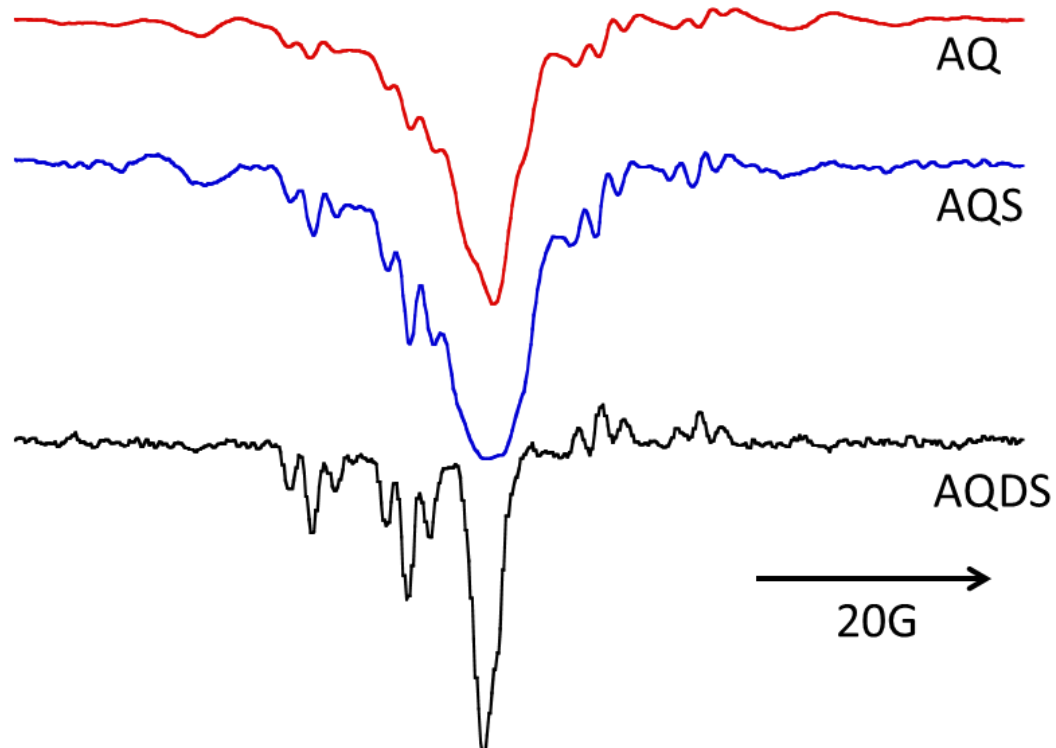
Figure 5.4 Comparison of the TREPR spectra of 0.1 M Brij 35 with 1.1 mM AQ (red), AQS (blue) and AQDS (black). Spectra were collected during 4 minute scans, with a gate width of 300 ns positioned 500 ns after the laser flash. Photolysis was at 308 nm and a repetition rate of 60 Hz. The large central transitions arises from the sensitizer radical.

radical, but the TREPR signal of the PEO radicals are only discernable until a delay time of roughly 500ns. In the spectrum of Brij 35-AQDS (Figure 5.4, black), polarization of the PEO based radicals is primarily due to the ST_0 RPM, with small contributions from net emissive TM. This suggests that the H-atom abstraction by AQDS is occurring on the outside of the PEO shell, where the local environment of the PEO radical is more hydrated and less viscous than AQS or AQ.

Figure 5.5 shows a comparison of the TREPR spectra two different neutral, hydrophobic sensitizers in solutions of Brij 35 micelles. The TREPR spectra of Brij 35-AQ has broader line shapes and a greater contribution of emissive TM polarization than the TREPR spectrum of Brij 35-BPd10. The APS of the BPd10 radical and SCRP polarization of the PEO radicals is clearly visible, while these features are lacking or obscured by other polarization mechanism in the spectrum of Brij 35-AQ. This suggests that the Brij 35-AQ radical pair is much more restricted in its diffusive motion than the Brij 35-BPd10 radical pair. Whether the increased emissive character of the spectra is due to stronger TM polarization caused be differences in the photophysics and rate of the H-atom abstraction reaction of AQ and BP, the effects of microviscosity on spin state selective ISC of the sensitizers, or slower translational diffusion leading to ST_- mixing is presently unclear.

Despite the fundamental differences between the CIDEP in the spectra of Figure 5.5, both clearly show the unidentified "core" quite clearly. The transitions from this radical appear broad and seem to be of a similar intensity. This radical is not discernable in the Brij-AQDS spectrum of Figure 5.4(bottom), which strengthens the argument that this radical is produced near or in the micelle core. The substantial broadening of these transitions suggests that the motion of this radical is severely restricted, and it even appears that the line shape is exhibit APS.

Disrupting micelle formation destroys the confinement responsible for the appearance of

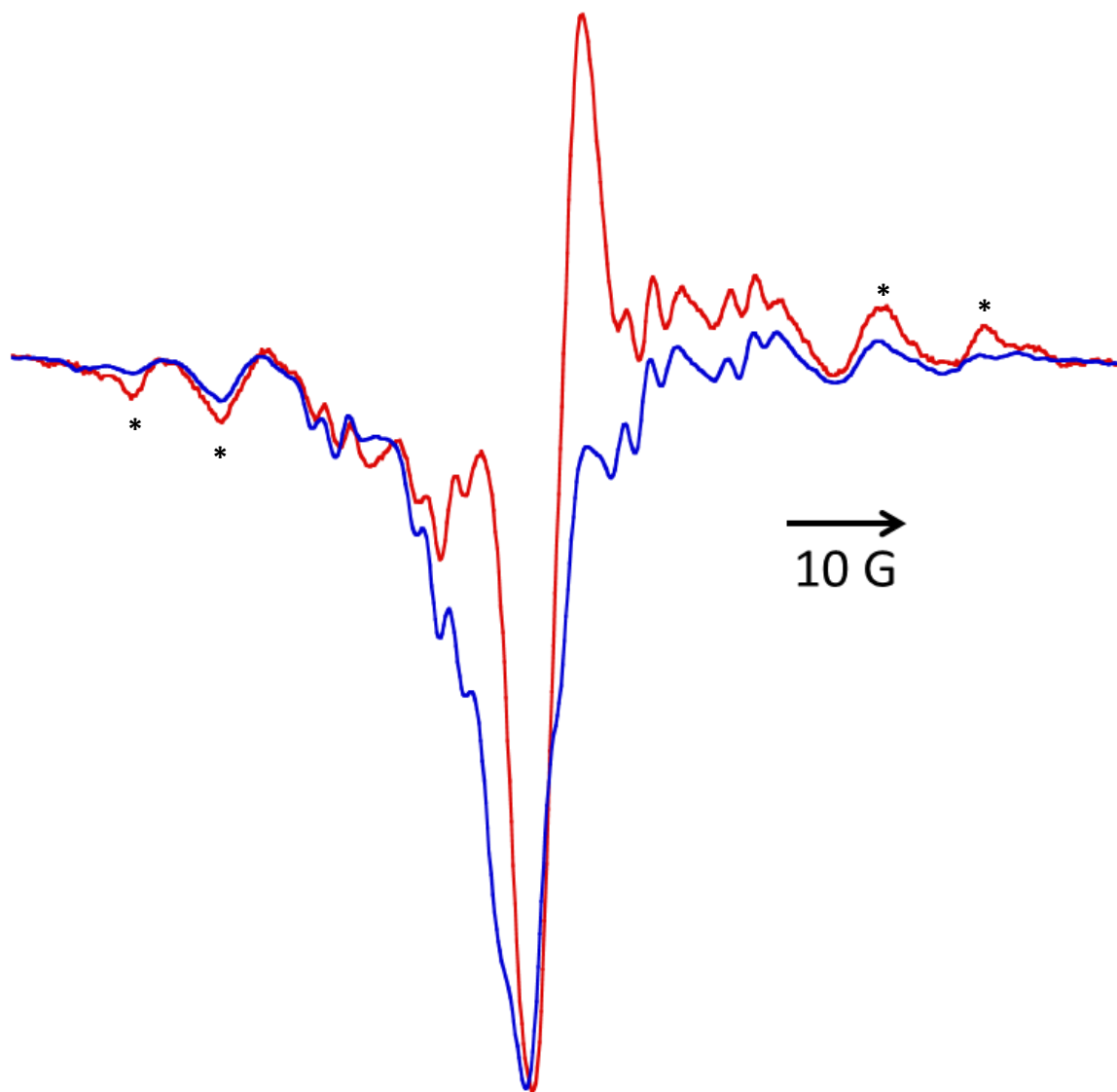**Figure 5.5** Comparison of the TREPR spectra of 0.1 M Brij 35 with 1.1 mM BPd10 (red) and AQ (blue). Spectra were collected at a delay time of 500ns during 4 minute scans, with a gate width of 300 ns after photolysis at 308 nm. The large central transitions arises from the sensitizer radical. The transitions marked with an asterisk are unidentified, but tentatively assigned as alkyl radicals from the micelle core.

the APS and could also increase the mobility of the radical. Decreasing the broadening or eliminating any APS could help resolve additional hyperfine splittings and allow the radical to be identified. Figure 5.6 shows the TREPR spectra of PEO with AQDS, Brij 35 with BP, and Brij 35 with AQDS in 50:50 acetonitrile:water to disrupt micelle or aggregate formation. In the solution containing only PEO, no signal from the unidentified radical is observed. This radical is observed in the TREPR spectra of Brij 35 with both BP and AQDS. The observation of the unidentified radical in the disrupted Brij 35-AQDS spectra is surprising, given that this radical is not observed in micellar solutions of Brij 35-AQDS (Figure 5.4). It is possible that, when micelle formation is disrupted, portions of the surfactant normally inaccessible to the hydrophilic AQDS become accessible and participate in H-atom abstraction reactions. This finding is also logically consistent with the assignment of the radical to the micelle core. Unfortunately, disrupting the micelle does not significantly improve the resolution of the unidentified radical, in part due to poor S/N in this solvent system. Brij surfactants are relatively large molecules, and the motion of the surfactant radical may still be slow enough to cause broadening of the radical signal even when micelle formation is disrupted.

To overcome this problem and obtain better resolution, signal averaging of the Brij 35-BPd10 system was performed for the low field side of the TREPR spectra at room temperature and approximately 50 °C. Experiments were also conducted on decaethylene glycol monododecyl ether, the 10 PEO unit analogue to Brij 35, in the hope that the reduced size of the surfactant or increased temperature would allow for faster motion of the RP. A comparison of the low-field side of the TREPR spectra of both surfactants in 50:50 acetonitrile water is shown in Figure 5.7. The signal from the unidentified radical is present and of a similar intensity in solutions of both surfactants. Decreasing surfactant size and increasing temperature did not significantly improve

239
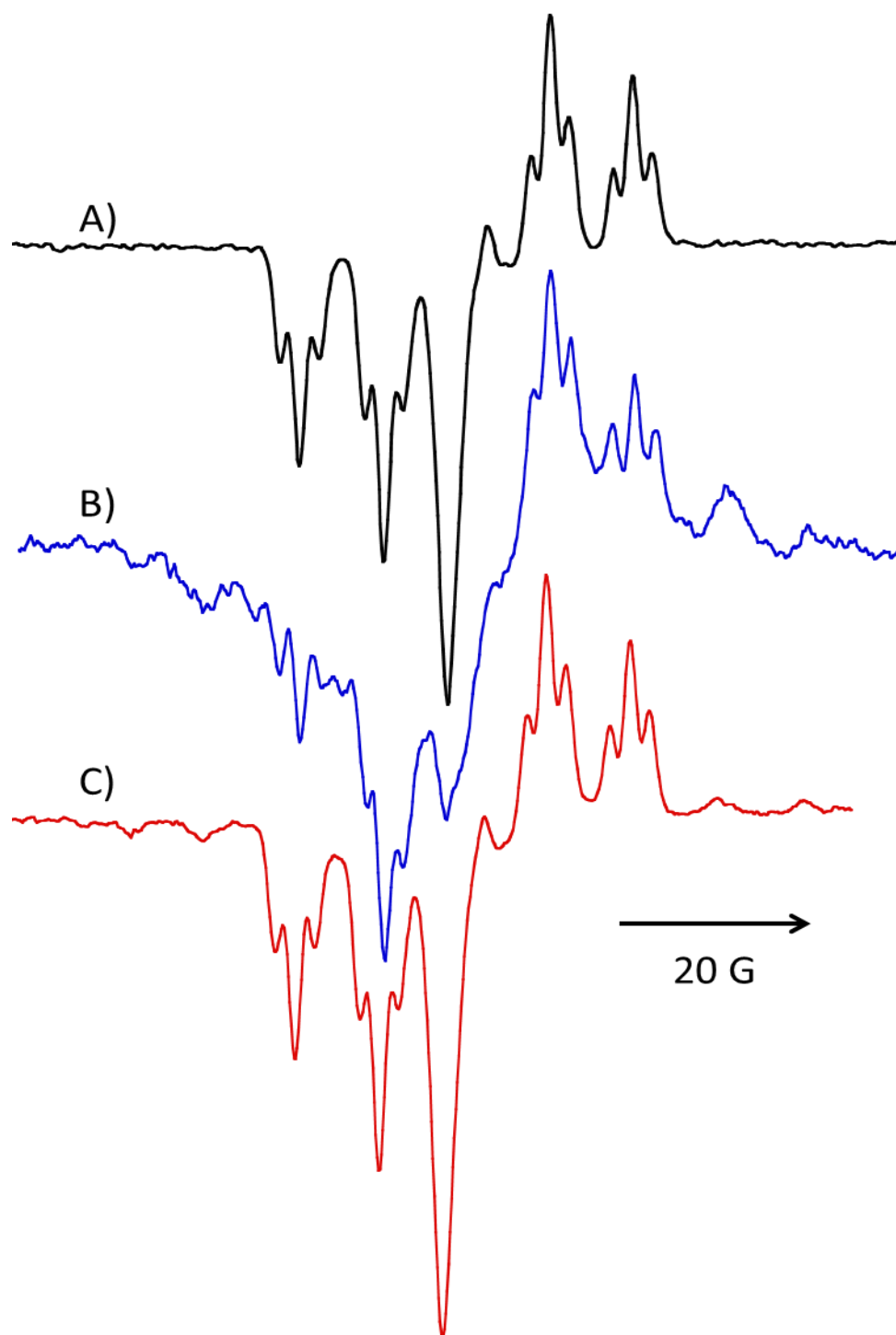
Figure 5.6 Comparison of the TREPR spectra PEO (M_w= 2000) and 1.1 mM AQDS in 50:50 acetonitrile:water to 0.1 mM Brij 35 in the same solvent but with sensitizers BPd10 (B) or AQDS (C) Delay time for all spectra is 500 ns. Spectra were collected during 4 minute scans, with a gate width of 300 ns, after photolysis at 308 nm at a repetition rate of 60 Hz. The unidentified radicals are marked with an asterisk, and are observed in solutions containing surfactant, but not in solutions of pure PEO (A). Spectra in (B) and (C) are an average of 4 scans.
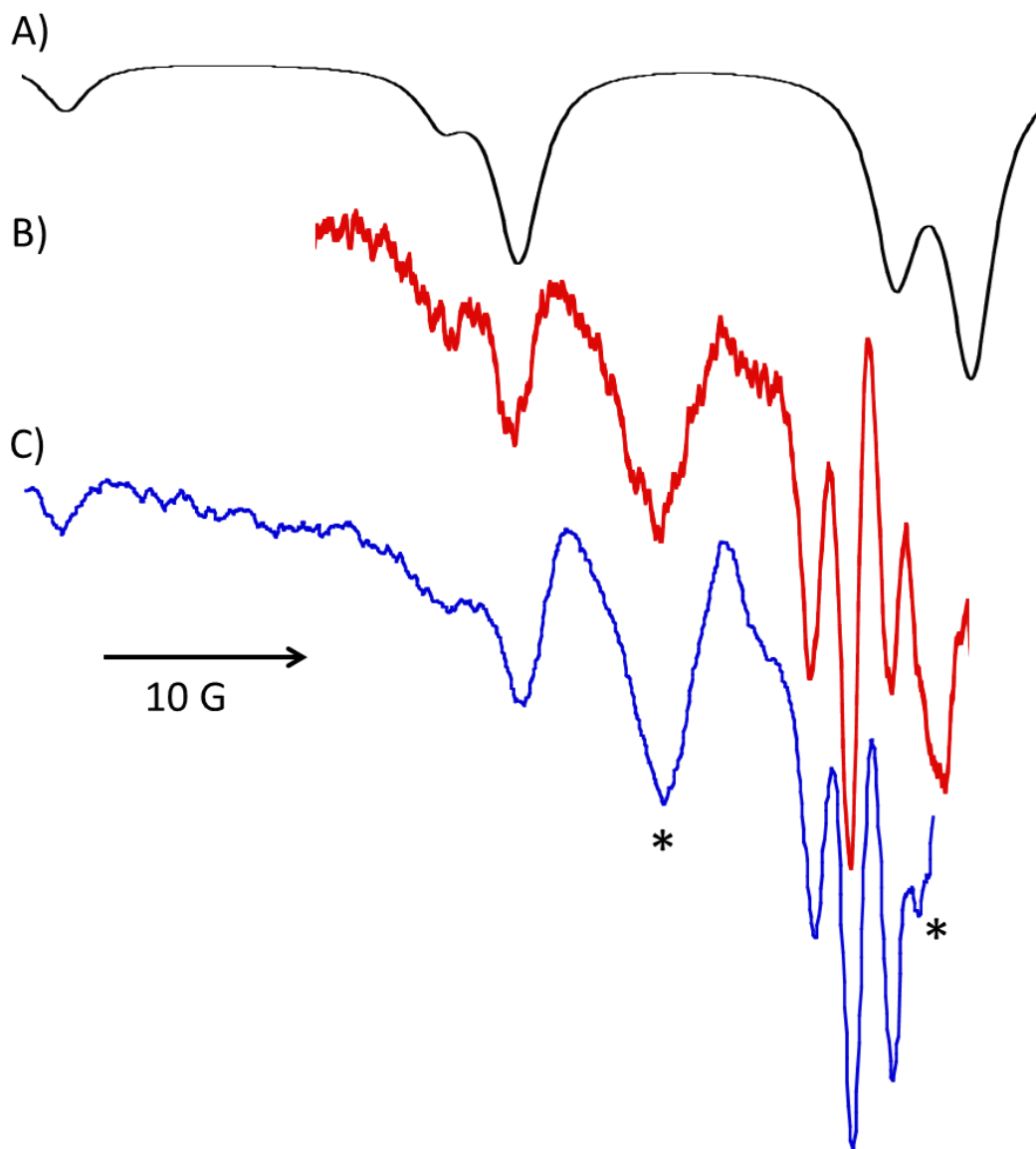
Figure 5.7 Comparison of the low field side of the TREPR spectra micellar solutions of decaethylene glycol monododecyl ether in H_2O (50 mM, B) and disrupted Brij 35 in 1:1 acetonitrile:water (100 mM, C) with 1 mM BPd10. At the top (A) is a simulation of the expected alkyl radical from the micelle core with a line width of 3 G. Transitions marked with an asterisk do not match the radical simulated in (A). Spectra were collected at a delay time of 500 ns during 4 minute scans, with a gate width of 300 ns after photolysis at 308 nm at a repetition rate of 60 Hz. Spectra in (B) and (C) are an average of 10-20 scans.

the resolution of the hyperfine splitting or narrow the radical signal. With signal averaging, it was possible to resolve an additional, weaker signal from this radical on the far high/low field extremes and to resolve a weak shoulder another transitions. There appears to be some additional transitions from the unidentified radical underneath the PEO radical signals, but because of the complicated superposition of CIDEP polarization of the surfactant radical and the weaker S/N ratio of the unidentified radical, spectral subtraction of the PEO radicals to observe the underlying transitions was not successful.

Both Brij 35 and decaethylene glycol monododecyl ether have identical, 12 carbon alkyl tails. The alkyl tail in the core is identical to the alkyl tail of the ionic surfactants, SDS and DTAC, which were discussed in the previous chapters. If the unidentified radical were coming from the Brij surfactant core, the most likely structure is identical to the alkyl surfactant radicals observed in ionic surfactants. The spectrum at the top of Figure 5.7 is a simulation of this alkyl radical with a line width of approximately 3 G and hyperfine coupling constants of 20.6 G for the α-hydrogen and 24.4 G for the four β-hydrogens.[63] The simulation shows that this radical matches the outer transitions reasonably well, but closer to the center of the spectra the fit is not as compelling. The simulation of the most likely alkyl radical of the core also does not account for the most intense transitions from an unidentified radical in the spectra.

5.3.2 Spin Trapping of Alkyl Radicals in Micellar Solutions of Core-Shell Surfactants

In order to identify any minor alkyl radical products from the photolysis of Brij surfactants and triplet sensitizers that could be the source of the unidentified radical signal, spin trapping experiments were performed using the DBNBS spin trap. Spin trapping alkyl radicals formed in SDS (50 mM) at concentrations above the CMC were used as control experiments to judge the

success of the trapping method in micelle solutions and to compare the results to the spin trapping

of Stostaric and Riesz[25] in dilute solutions of SDS (0.3 mM). SSEPR spectra were collected before

photolysis, after 4 minutes of photolysis with a 308 nm excimer laser under conditions identical to

those used for a TREPR measurement, and after 15 minutes of photolysis. As an additional control,

a 15 minute photolysis at 308 nm for solutions containing AQDS was compared to the results of

photolysis in a solution containing only SDS and H_2O_2. UV photolysis of H_2O_2 produces hydroxyl

radicals, which can also abstract hydrogen from the alkyl chain of the surfactant.[64] It is clear from

the results in Figure 5.8 that, in the absence of photolysis, no SSEPR signal is observed. For short

photolysis times, the SSEPR spectra appears to be a superposition of a $-\cdot CH-$ adduct with a small

contribution from a methyl radical adduct. The spin trapping of $-\cdot CH-$ is not surprising, given that

the primary product of the photolysis as observed by TREPR is a $-\cdot CH-$ radical of the surfactant

alkyl chain. The formation of the methyl radical was unexpected because it was not reported as a

product of photolysis of solutions of SDS by Sostaric and Riesz.[25] However, the photolysis in that

study was conducted with a much lower intensity Xenon lamp, and the methyl radical adduct was

observed following sonolysis of SDS. The production of the methyl radical was attributed to local

heating during sonolysis followed by surfactant degradation. Given the much higher intensity of

the excimer laser photolysis, heating and degradation are likely the source of the methyl radical

adduct in Figure 5.8.

The differences in the line shape between the short photolysis (4 min, blue) and the long

photolysis (15 min, green) with AQDS are caused by differences in the rotational motion of the

spin adduct. At short photolysis times, the line shape suggests relatively isotropic motion of the

spin adduct. The asymmetry in the line shape for longer photolysis, particularly the shortening and

broadening of transitions due to the $m_I = -1$ spin state of nitrogen, are indicative of slower,

Figure 5.8 SSEPR of the radical adducts formed with DBNBS in 50 mM solutions of SDS after photolysis with a radical or triplet sensitizers. DBNBS concentration was 8 mM in all samples. Photolysis was carried out with and excimer laser operating at 308 nm and a 60 Hz repetition rate. AQDS was used as a triplet sensitizer or H_2O_2 (bottom, black) as a source of hydroxyl radicals, which undergo hydrogen atom abstraction with the surfactant in solution. Photolysis times were 0 min (red), 4 min (blue) or 15 min (green, black).

anisotropic rotation. Considering that the primary radical product of the photolysis is a surfactant-based PEO radical, which is a large anisotropic molecule, slow and anisotropic rotational motion is expected. Most likely, this anisotropy is not as evident at shorter photolysis times because the concentration of radicals produced is much lower, and AQDS is a relatively hydrophilic sensitizer that will abstract from portions of the surfactant closer to the micelle-water boundary. In addition, the relatively hydrophilic nitroxide spin adduct probably exists preferentially closer to the micelle surface, allowing for more isotropic motion. The similarity between the SSEPR spectrum produced by photolysis of AQDS and the spectrum produced by photolysis of H_2O_2 is strong evidence that the spin trapping experiment of Sostaric and Riesz[25] can be applied to study alkyl radical products in micellar solutions of radicals photochemically generated by H-atom abstraction using triplet sensitizers.

Figure 5.9 shows the extension of this spin trapping technique to the Brij 35 micelle. When the photolysis is carried out for 4 minutes in a solution of 50 mM Brij 35 with 1 mM AQDS and run immediately after photolysis, there is a strong contribution to the spectra of the methyl radical, with a smaller contribution from the $-\cdot CH-$ surfactant radical. The methyl radical adduct does not appear to be stable. Figure 5.9B is a spectrum of the same sample, but taken 1 hour after the photolysis. The signal from the methyl radical adduct appears less intense than the secondary alkyl radical adduct. The line shape is also anisotropic, which suggests that the trapped $-\cdot CH-$ radical is a large anisotropic surfactant radical rather than a smaller degradation product. Figure 5.9C shows the SSEPR spectrum of the same sample after it has been diluted in a 3:1 ratio with 1-propanol, which is known to disrupted nonionic micelles. The line shape is much more symmetric and isotropic than Figure 5.9B. In Figure 5.9B, the surfactant radical adduct is incorporated in large micelle structures, which effectively slows its rotational diffusion. When the micelle
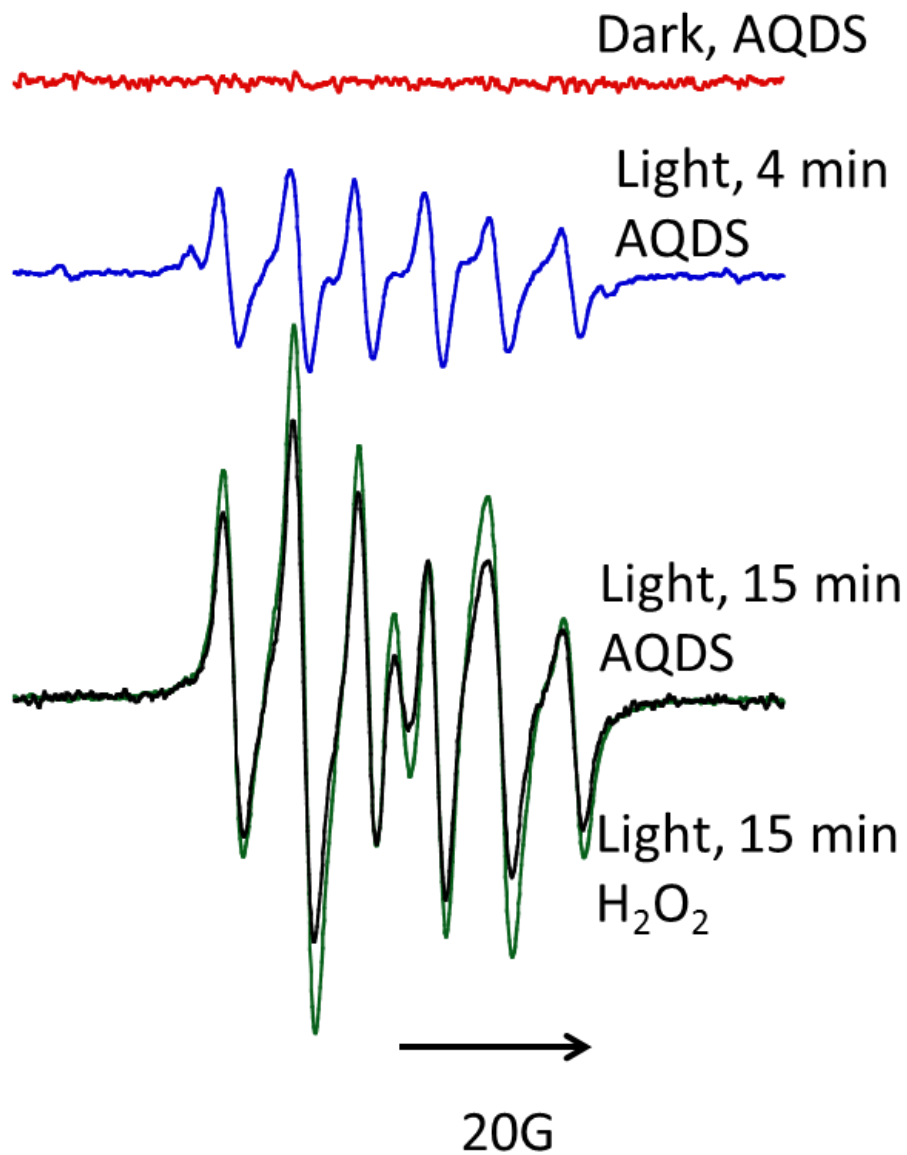
Figure 5.9 SSEPR of the radical adducts formed with DBNBS in 50 mM solutions of Brij 35 after photolysis with a triplet sensitizers AQDS. DBNBS concentration was 8 mM in all samples. Photolysis was carried out with and excimer laser operating at 308 nm and a 60 Hz repetition rate, with a photolysis time of 4 minutes. Spectra were collected immediate after photolysis (red), 1 hour after photolysis (blue), and 1 hour after photolysis followed by the addition of 1-propanol to disrupt micelle formation (green)

formation is disrupted (Figure 5.9C), the rotational motion of the spin adduct is no longer affected by a larger aggregate structure, leading to the difference between the spectra in Figure 5.9. Figure 5.10 shows the results of the spin trapping study using the BP sensitizer in solutions of Brij 35. Only the $-\cdot$CH$-$ radical adduct is observed. The SSEPR spectra in micellar solutions (50 mM Brij 35) containing BP shows an even slower rotational correlation time and greater anisotropy than observed for micellar solutions containing AQDS. This is consistent with AQDS existing preferentially in the bulk aqueous phase and abstracting only those hydrogen atoms of the surfactant near the micelle surface, and BP existing much deeper in the PEO shell. As the sensitizer abstracts from a position closer and closer to the micelle core, the packing of the PEO subunits must become tighter and viscosity increases. When the micelle structure is disrupted by the addition of 1-propanol, the line shape becomes much more isotropic, and it becomes clear that the spectrum is due to the $-\cdot$CH$-$ radical adduct. Figure 5.10B is an 8 hour average of the SSEPR spectrum in 3:1 n-propanol:water, which demonstrates that the surfactant radical adduct with DBNBS is incredibly stable. From the improved S/N, it is clear that the rotational motion of the radical product is still anisotropic.

Unfortunately, only the $-\cdot$CH$-$ radical was trapped in solutions of Brij 35-BPd10, making it unlikely that the methyl radical observed in the spin trapping of solutions containing AQDS is responsible for the unidentified radical signal in the TREPR spectrum. Furthermore, the hyperfine coupling of the methyl radical does not match the position of the unidentified transitions in the TREPR of solutions of Brij 35-BP,[63] and the small size of this radical makes it more likely that any spin polarization of the methyl radical would relax by the time of observation. The unidentified radical is either not a primary $\cdot$CH$_2$$-$ radical created by degradation of the PEO chain, or the concentration of any primary radical product is too low to detect by trapping. It is unlikely,
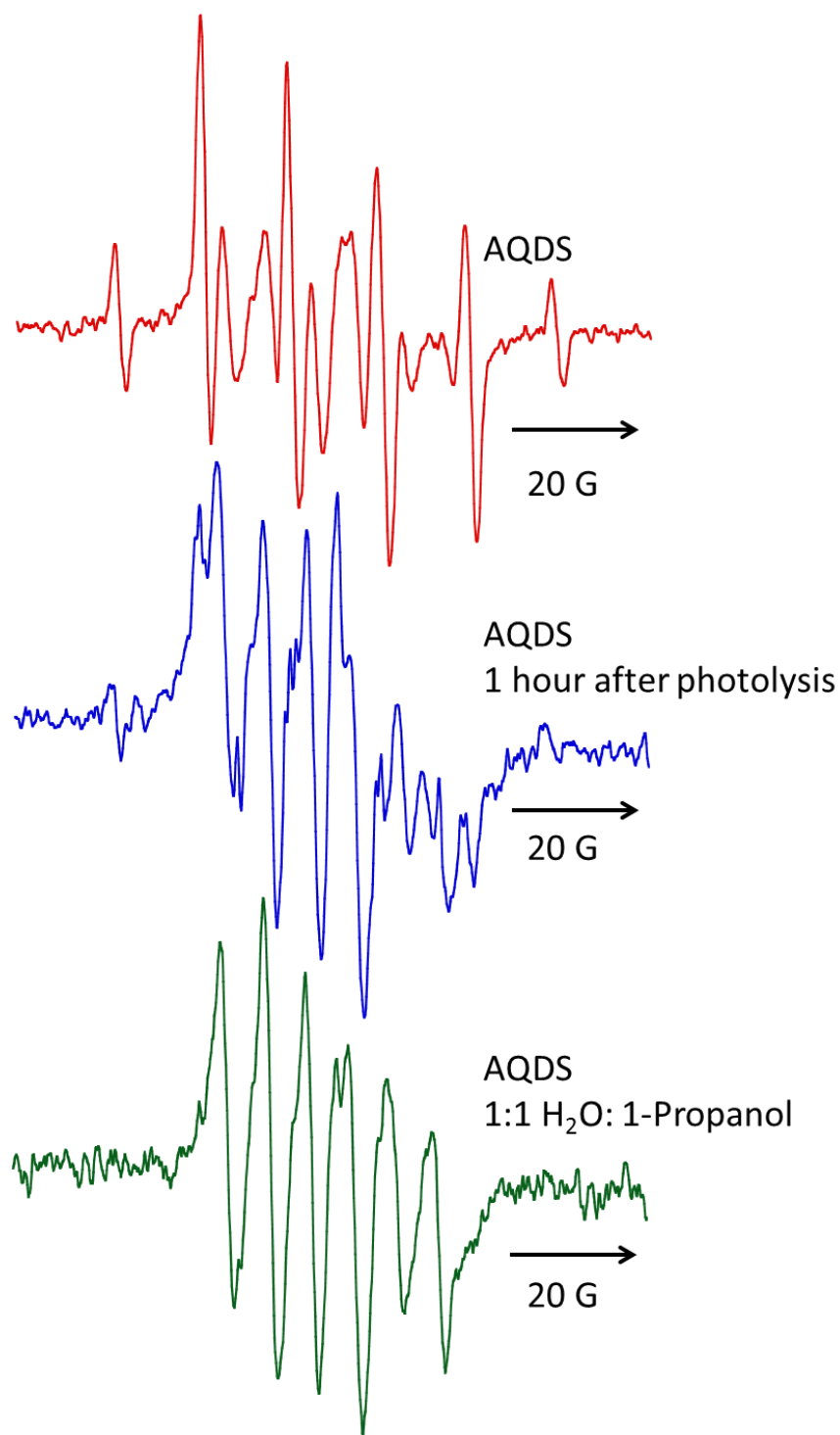
247
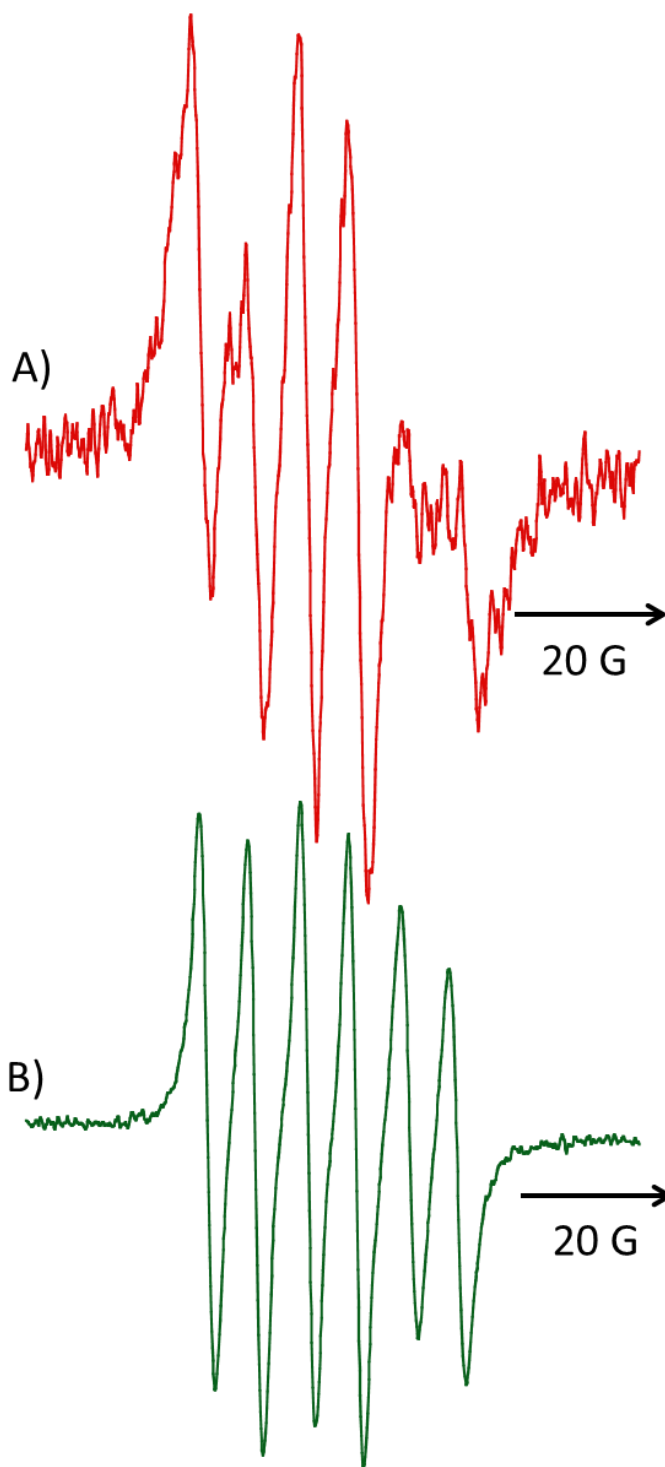
Figure 5.10 SSEPR of the radical adducts formed with DBNBS in 50 mM solutions of Brij 35 after photolysis with a triplet sensitizers BPd10. DBNBS concentration was 8 mM in all samples. Photolysis was carried out with and excimer laser operating at 308 nm and a 60 Hz repetition rate, with a photolysis time of 4 minutes. Spectra were collected immediate after photolysis (A) in micellar solutions with a solvent of H_2O or were signal averaged for 6 hours (green) after the addition of 1-propanol to disrupt micelle formation (B). Solvent for spectrum (B) is 3:1 1-propanol:water.

though not impossible, for a primary or methyl radical to be the source of the TREPR signal. As it stands, DBNBS is unable to distinguish between a $-\cdot CH-$ radical from PEO and one from the alkyl chain of the core because of the broadening and anisotropy observed in the SSEPR signals for micellar solutions and the lack resolution of any long range coupling hyperfine coupling in the DBNBS trap under these conditions.

5.3.3 SSEPR of the Thermoresponsive Behavior of Pluronic Surfactants

Surfactant solutions of Pluronic L61, L64, F68, and 17R4 were examined by SSEPR using 5-DSA and TEMPO spin probes. Concentrations of Pluronic were 1 mM, 10 mM, and 50 mM in solutions. This corresponds to approximately 0.2, 2 and 10 wt. % for L64 and 17R4. In F68 solutions, these concentrations correspond to approximately 0.6, 6, and 30 wt. %. An additional concentration of 20 mM F68 was included to correlate with the 10 wt. % solutions of L64 and 17R4.

Characterization of Pluronic L61 was particularly problematic because, at room temperature and the concentrations mentioned above, the surfactant is typically below the cloud point where phase separation is observed in aqueous solution. Pluronic L64 has already been characterized with DSA spin probes by Zhou and Schlick[46] and with TEMPO by Kurzbach et al.,[47] but it is reinvestigated here in light of its structural similarities to 17R4. F68 was also studied by Kurzbach et al.,[47] but has not been characterized by DSA. To the best of our knowledge, this is the first time that a reverse Pluronic surfactant has been investigated by EPR. For this reason, the remaining discussion will focus on the features of the SSEPR of Pluronic 17R4, with comparisons to L64 and F68 where appropriate.

Figure 5.11 shows the temperature dependence of the SSEPR of TEMPO (left) and 5-DSA
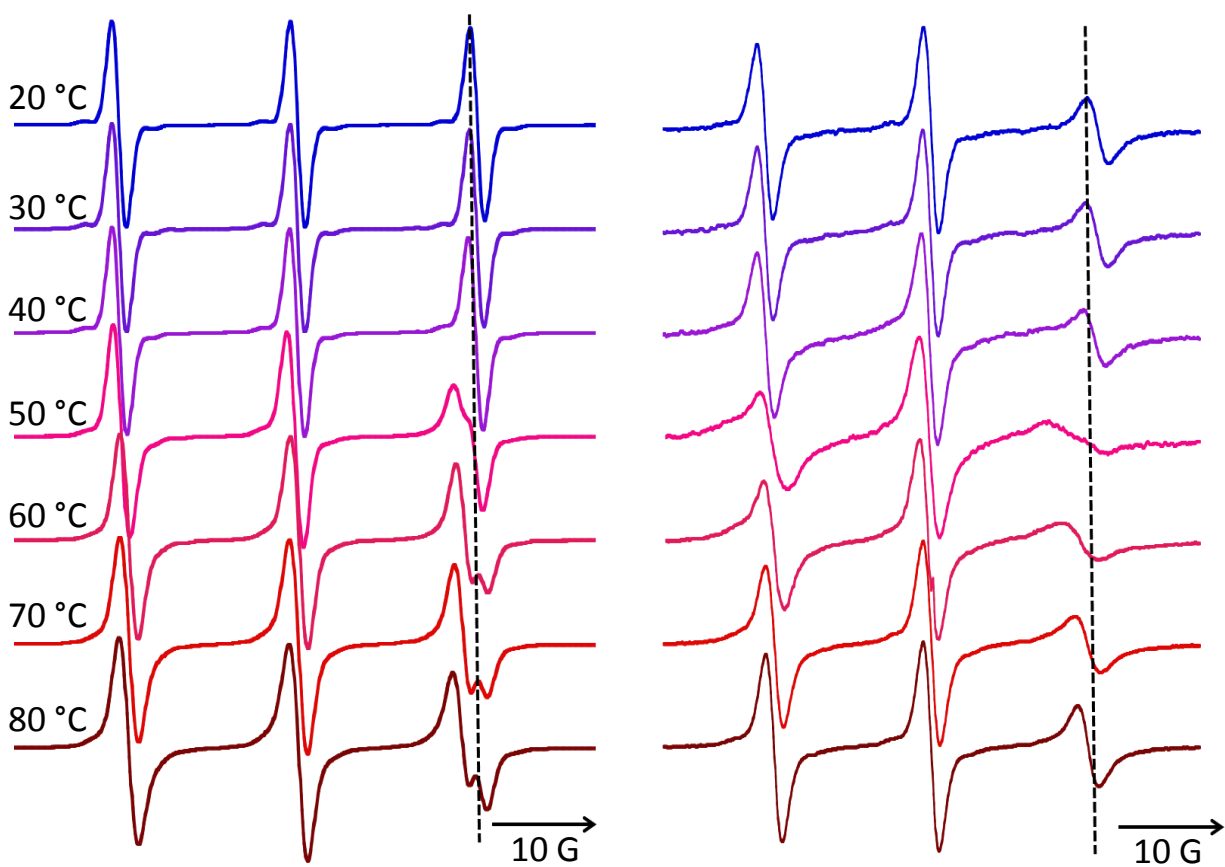
Figure 5.11 Temperature dependence of the SSEPR of 10 wt. % solutions of Pluronic 17R4 with TEMPO (left) and 5-DSA (right). The vertical dotted line is a guide for the eye indicating the peak of the SSEPR from the spin

(right) in solutions of 10 wt. % 17R4. At 20 °C, the SSEPR spectrum of TEMPO appears isotropic and fast motion, with all three transitions of equal height and line width. The isotropic HFC is 17 G, consistent with the value of A_N for TEMPO in pure water.[65] An obvious change in the line shape of the SSEPR spectra of both spin probes is clearly visible at a temperature of 50°C. In the solutions containing TEMPO, the high field transition appears to be asymmetric. At higher temperatures it is clear that this asymmetry is due to a superposition of transitions, one with a smaller A_N value indicative of a less polar environment and one that remains consistent with the A_N of TEMPO in pure water. The intensity of the new, hydrophobic TEMPO signal is weaker at 50°C, but the ratio between the aqueous and hydrophobic species appears constant at higher temperatures. Spectral decomposition reveals that both species appear to be relatively fast motion, with the hydrophobic species exhibiting a A_N of 15.6 G. This change in A_N is identical to that observed for TEMPO partitioning in Pluronics L64, P84, and P105 reported by Kurzbach et al.[47] Because the superposition of the hydrophobic and hydrophilic species is only visible for the $m_I = -1$ transition, the g-factor of the hydrophobic species must also have shifted relative to TEMPO in the aqueous phase, from g= 2.0059 to g= 2.0062.

In the 5-DSA spectrum, there is a slightly broader line width and a shortening of the high field, $m_I = -1$ transitions that is indicative of slower, axially symmetric rotation of a spin probe. This is expected given the molecular structure of 5-DSA. Like the TEMPO spectrum at this temperature, the value of A_N is equivalent to the literature value for A_N of 5-DSA in water at 15.3 G.[66] At 50°C, the spectra appear to be a superposition of a weak signal from a slow motion component and the faster component that is consistent with aqueous 5-DSA. At 60°C, the spectrum appears to be primarily a single component, but with a smaller A_N than was measured at lower temperatures. As the temperature continues to increase, the transitions become sharper, indicating

faster, anisotropic rotational motion of the 5-DSA. The A_N also decreases to 14.5 G. DSA spin probes are generally poorly soluble in water, and are assumed to exist preferentially in micellar structures. The decrease in A_N is consistent with that observed by Caldararu et al.[26, 45a] and Zhou and Schlick[46] for 5-DSA in other Pluronic solutions, which suggests that the probe is sampling the PPO core of the surfactant aggregate. Comparisons to spectra of TEMPO and 5-DSA at surfactant concentrations of 0.2 and 2 wt. % indicate that at a lower concentration, the onset for the appearance of signal of the spin probe in the hydrophobic environment occurs at increasingly higher temperatures.

The phase diagram of Pluronic 17R4 was obtained from dynamic and static light scattering measurements and published by Zhou and Chu.[36] While micellization is observed for this surfactant, it is generally only seen at surfactant concentrations greater than 7.5%. The region of micelle formation is also very small. The window for micelle formation in 10 wt. % solutions is limited to temperatures of 35-40°C. Below this temperature, the polymer exists in solution as unimers. The SSEPR observations of TEMPO and 5-DSA both support this behavior, since the A_N of both probes are in an aqueous environment below 50°C. Above 40°C, Zhou and Chu[36] report isotropic phase separation of the solutions of Pluronic 17R4. Although the SSEPR results indicate that this phase separation begins at a slightly higher temperature, a 10°C discrepancy is within reason for these polydisperse systems.[8, 26] The changes in the line shape of the EPR spectra of TEMPO and 5-DSA at temperatures above 60 °C are due to the incorporation of the spin probes into this isotropic, polymer-based phase. In the case of TEMPO, the spin probe partitions between the two phases, and site exchange for the probe must be slow on the EPR timescale. The strong partitioning of the probes is supported by visual observation of the samples upon heating. When TEMPO is added to solutions of 17R4, the solution appears pale yellow. After heating the sample,

two isotropic phases can be observed, with a supernatant phase that appears completely clear and a second phase that is bright yellow. While it cannot be confirmed visually, the SSEPR of 5-DSA suggests that the probe also exists exclusively in the hydrophobic polymer phase at high temperatures. The only exception to this is at 50°C, where the spectrum appears to be a superposition of a fast and slow component. The slow motion component is most likely related to the temperature dependent phase separation of the solution, but it is also possible that this arises from micellar aggregates formed in between the transitions from unimers to separate phases. At 0.2 and 2 wt. % in spectra of both TEMPO and 5-DSA, double peaking or a spectral superposition is not observed until 60°C. This is also consistent with the reported phase behavior of this surfactant, which exhibits a higher CMT at lower concentrations.

For comparison, Figure 5.12 shows the SSEPR spectra of 10 wt. % L64 and 30 wt. % F68. In L64 solutions of this concentration, the CMT is 34.5°C.[36] The SSEPR spectra reflect this transition, as the line shape begins to broaden and the $m_I = -1$ transitions shifts toward lower frequencies starting at 40°C. The temperature range for micelle formation in L64 is substantially larger than 17R4. Zhou and Chu[36] do not report isotropic phase separation until the temperature exceeds 60°C. This is in excellent agreement with the SSEPR spectra, as TEMPO partitioning only becomes visible for spectra collected at 70°C or higher. In these spectra, the magnetic parameters of the spin probe in the hydrophobic environment are identical to those measured at temperatures where micelle formation was observed, but a small contribution from a TEMPO species with a g-factor and A_N identical to TEMPO in water can be seen in the high field transition.

The CMT for F68 at 30 wt. % is reported around 30 °C.[35] In addition, thermal induced gelation of this surfactant has been reported above temperatures of 300 K due to cubic packing of the micellar structures at concentrations starting around 30 wt. %. At 20 °C, the A_N of TEMPO is
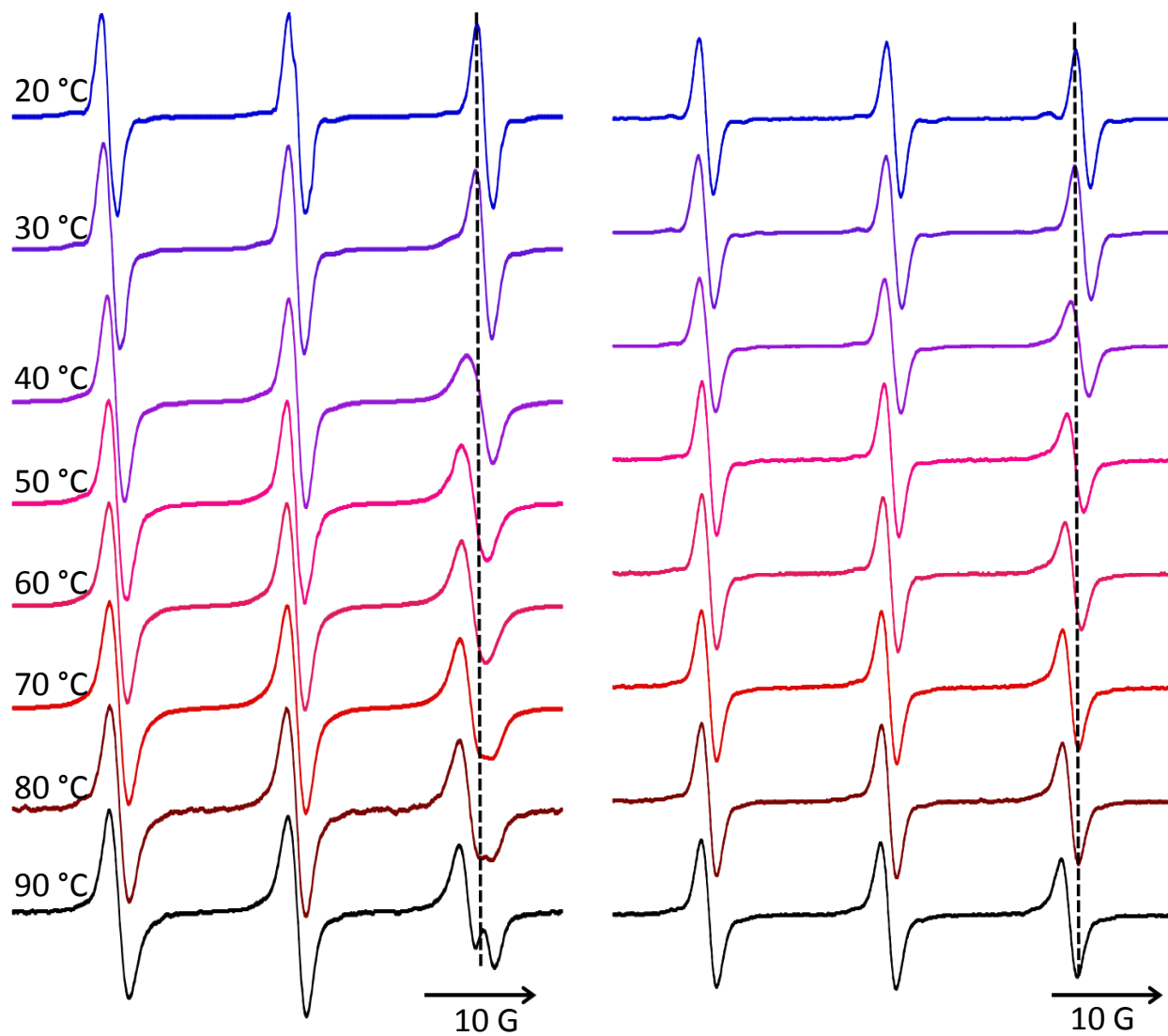
Figure 5.12 Temperature dependence of the SSEPR of a 10 wt. % solution of Pluronic L64 (left) and a 30 wt. % solution of Pluronic F68 (right) with 1 mM TEMPO. Temperatures were varied in increments of 10 °C, and the

17 G, consistent with TEMPO in water.[65] At higher temperatures, the A_N is 16.3 G. Although there is some broadening in the SSEPR starting at 30 °C where the shift of A_N to lower values begins, there appears to be no partitioning of the TEMPO in this solution. A hyperfine coupling of 16.3 G also indicates the spin probe is in a more polar environment than the dehydrated PPO core, where A_N is expected to be closer to 15.6 G.[46] Visual observations of the solutions confirm the formation of a viscous gel with increased temperature. Because the A_N is higher than expected for TEMPO in anhydrous PPO, when gel formation occurs the TEMPO spin probe does not appear to partition to the PPO core of the micelle or the PPO core is more hydrated and, therefore, more polar than in Pluronic L64 or 17R4. This could be due to incorporation of PEO into the PPO core, increasing its accessibility to water. For F68 at 10 wt. %, the trend in the SSEPR spectra is identical to that at 30 wt. %. Solutions of F68 at this lower concentration have a CMT of 40°C and do not exhibit thermal gelation,[35, 67] but the A_N at temperatures of 50-90°C is also 16.3 G. This suggests that the more polar environment of the TEMPO is an intrinsic feature of F68 aggregates and not a consequence of gel formation. It is most likely, given the large PEO fraction in this surfactant, that TEMPO is located in the hydrated PEO shell of the F68 micelles.

5.3.4 Hydrogen Atom Abstraction Reactions in Pluronic Solutions Studied by TREPR

Hydrogen atom abstraction reactions between aqueous AQDS and the Pluronic copolymer were observed by TREPR for all concentrations and all surfactants at room temperature and at 60°C. This appears to be near or above the CMT in most cases. The only exception was Pluronic F68 at 30 wt. %, which formed a highly viscous gel at high temperature that could not be pumped through the TREPR flow system. The H-atom abstraction reaction between the PEO blocks and the sensitizers is expected to mimic the TREPR of PEO based Brij surfactants.[13] The magnetic

parameters characterizing the main chain radical resulting from this photochemistry in PPO do not appear to be reported in the literature. If the reaction occurs preferentially at the same position as in PEO, the resulting radical should be easily distinguishable from the PEO radical by its different hyperfine coupling. Control experiments to observe H-atom abstraction in neat PPO or PPO in water were unsuccessful, as AQDS is not soluble in neat PPO, and PPO of a similar M_w to the Pluronic surfactants is insoluble in water at room temperature. It is unclear if H-atom abstraction would be preferential for the PEO or PPO block, but given their similar structures, this seems unlikely. Therefore, the assumption is made that any preferences in abstraction between the PEO and PPO blocks observed in the TREPR of Pluronic solutions and AQDS is a consequence of differences in hydration and accessibility of that particular block to the aqueous sensitizer.

Figure 5.13 shows the TREPR of solutions of Pluronic 17R4 and F68 at 10 wt. % at low and high temperature. In the spectra of 17R4, there appears to be an overlapping signal from two distinct radicals. The first matches the hyperfine and spectral pattern of PEO.[13] The second is consistent the PPO radical. Figure 5.14 shows a simulation of the PPO radical from the spectra of 0.2 wt. % Pluronic 17R4 at 60°C, where the hyperfine appears best resolved. This radical could be fit with one α-hydrogen HFC of 16.9 G, one β-hydrogen HFC of 9.3 G, and two γ-hydrogen HFCs of approximately 1.1 G. In all cases, the spectra show strong TM polarization, likely due to high viscosity, superimposed on RPM polarization. This results is all transitions for PPO appearing in net emission, but with greater intensity of the low field transitions than the high field ones.

There is little difference between the 20°C and 60°C spectra of Pluronic 17R4. The relative intensity of the PEO and PPO based radicals differs slightly with temperature, although the PPO radical appears broader at lower temperatures. The sharpening of the transitions is due to increasing radical mobility at increasing temperatures. The slight decrease in intensity of the PPO

256
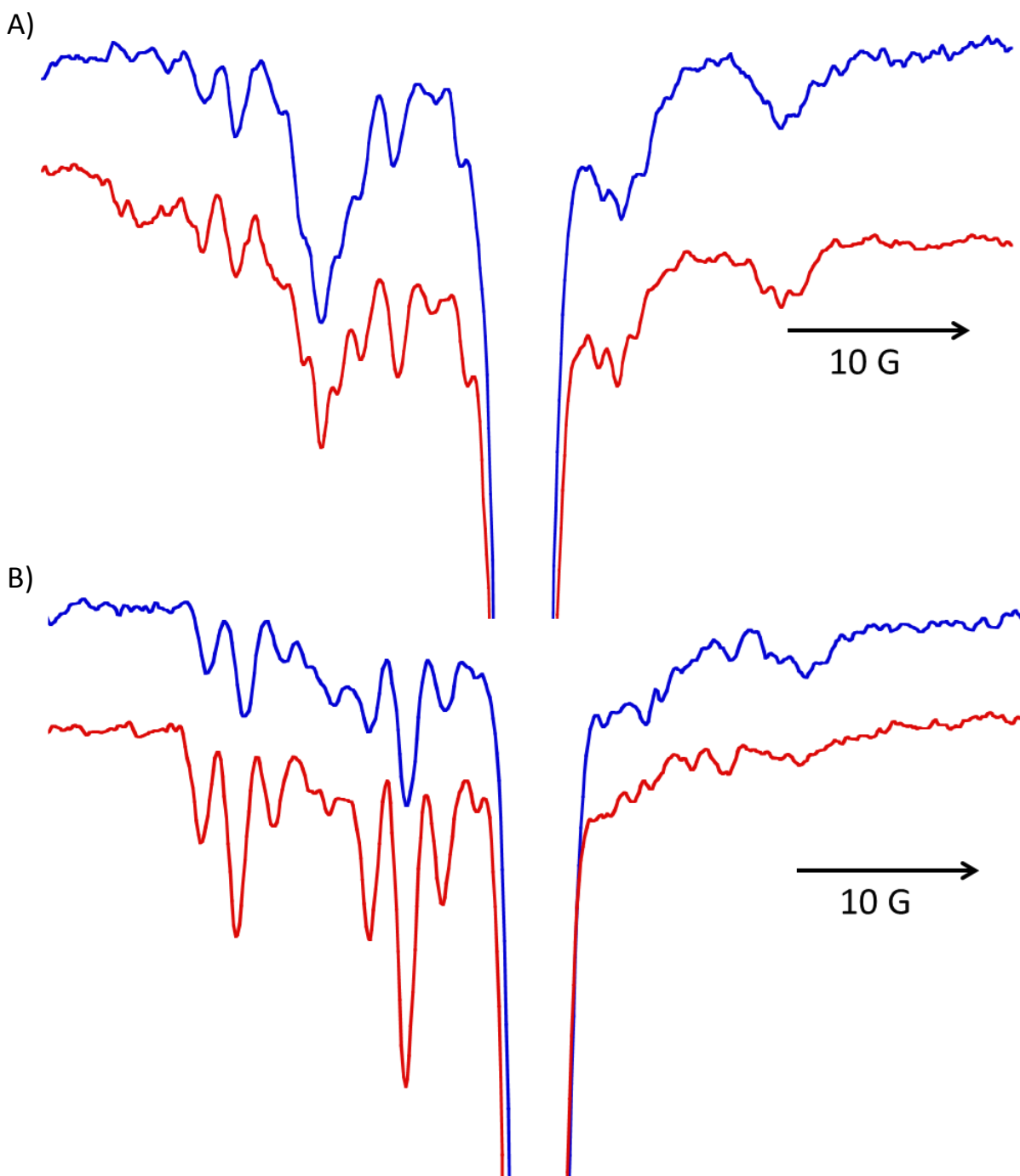
Figure 5.13 TREPR of solutions of 10 wt. % 17R4 (A) and F68 (B) and 1 mM AQDS following photolysis with an excimer laser at 308 nm. Spectra in blue were collected at room temperature and spectra in red were collected
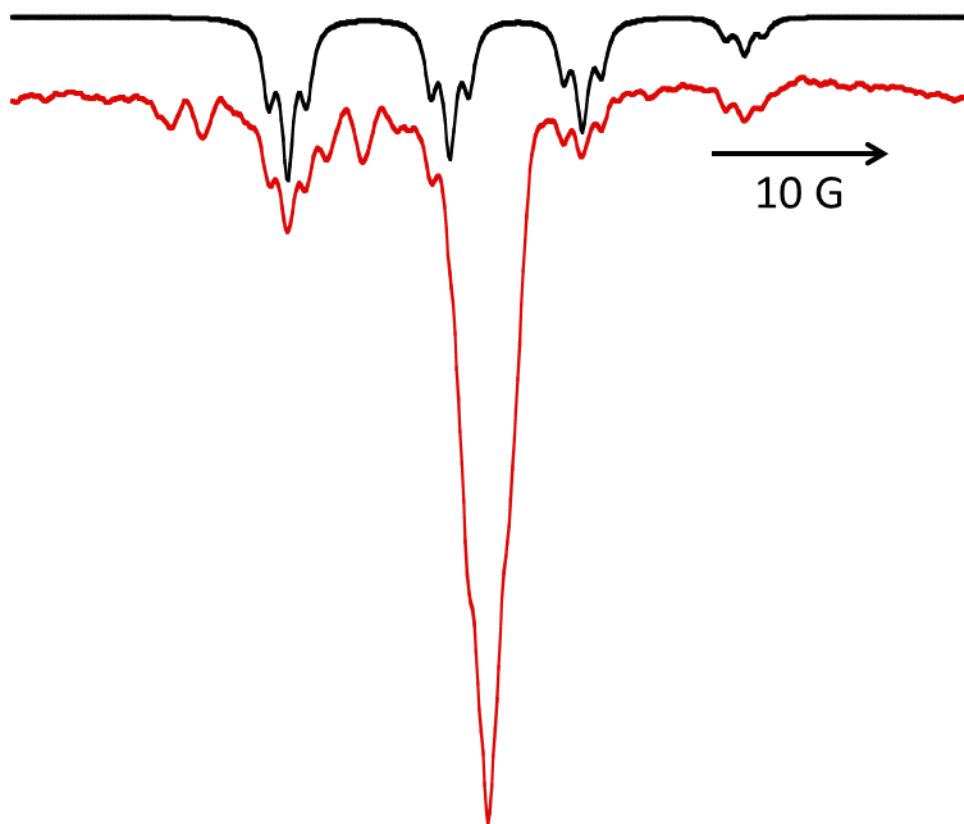
Figure 5.14 TREPR of solutions of 0.2 wt. % 17R4 (bottom) and 1 mM AQDS at 60°C following photolysis with an excimer laser at 308 nm, and simulation of the PPO radical (top). Delay time for the experimental spectrum is 500 ns, with a 4 minute scan time and a gate width of 300 ns. PPO radical is simulated with hyperfine coupling constants of 16.9 G (H_α), 9.3 H (H_β), and 1.1 G ($2H_\gamma$), and a superposition of TM and RPM polarization.

Signal relative to the PEO signal is consistent with reports of increasing dehydration of Pluronic surfactants with increasing temperature, which would make the PPO blocks less accessible to an aqueous sensitizer. At room temperature, 17R4 exists as unimers, and the aqueous sensitizer appears to have reasonable access to both blocks of the copolymer. At 60°C, 17R4 phase separates into two isotropic liquids. The sample had to be stirred and flowed at a slightly faster rate to unsure that this phase separation did not lead to preferential sampling of only one of the two phases. It is unclear whether the TREPR signal comes from the aqueous or separated polymer phase, but the similarity between the two spectra suggests that, regardless of the phase separation, the AQDS sensitizer has similar access to both blocks of the Pluronic 17R4 copolymer.

For Pluronic F68 (Figure 5.13B), there is a noticeable difference between the TREPR spectra at 20°C and 60°C. At low temperatures, abstraction can be seen from both the PEO and PPO block .The signal from the PPO radical is less intense than in solutions of 17R4, but the larger PEO block size in F68 provides a much higher likelihood of abstraction from PEO than PPO for this surfactant. Still, the PPO radical is clearly visible on both the high and low field sides of the TREPR spectrum. At high temperatures, the TREPR signal of the PPO radical is significantly less intense, although it can just barely be seen between the PEO radical transitions on the low field side of the spectrum. The reduced relative intensity of the PPO radical is consistent with micellization of F68 at higher temperatures, which would cause the PPO block to be buried in the hydrophobic core of the micelle. There are two possible explanations for the fact that the PPO radical is not absent from the TREPR spectrum. First, there may be a considerable number of unimers in solution, giving the aqueous sensitizer access to the PPO block.[68] Second, the PPO core of the F68 may be accessible the AQDS surfactant because it is at least somewhat accessible to water.[69] Similar results are observed for Pluronic L64, but Pluronic L61 shows almost exclusive

abstraction from PPO at room temperature. Extensive phase separation of L61 at high temperature results in poor S/N in the spectra to the point that the polymer-based radicals cannot be easily distinguished from each other.

Attempts were also made to study the TREPR spectra of the more hydrophobic BP sensitizer in neat PPO or in Pluronic solutions, with the expectation that this sensitizer may show preferential abstraction from the hydrophobic regions of polymer aggregates. Formation of a viscous, secondary photoproduct was observed in solutions of PPO and Pluronic surfactants with BP. This photoproduct aggregated significantly on the inside of the quartz flat cell at the site of photolysis. Formation of this secondary photoproduct caused detuning of the resonator and blocked transmission of the excitation wavelength through the optical cavity. This behavior was not observed for aqueous solutions of Pluronics with AQDS. Because this behavior is observed in solutions of PPO and Pluronic surfactants but not in solutions of PEO, the formation of the secondary photoproduct is attributed to secondary chemical processes of the PPO radicals.

5.3.5 ESP of nitroxides in solutions of Pluronic Surfactants

Examination of electron spin polarization of TEMPO in solutions of Pluronic surfactants can be compared to the SSEPR measurements of the same spin probe in these solutions to provide additional information about the aggregate structures and physical properties as a function of temperature or surfactant concentration. TEMPO is known to partition between the hydrophobic and hydrophilic environments in solutions of Pluronic surfactants. By incorporating a hydrophobic triplet sensitizer into these solutions, ESP of the nitroxide can be generated by either RTPM or ESPT. Only those TEMPO molecules that can make diffusive encounters with the sensitizer can become spin polarized, so the TREPR spectrum may preferentially reflect the properties of

TEMPO partitioned in the hydrophobic phase. Polarization transfer can also occur to nitroxides in the aqueous phase, so long as the hydrophobic sensitizer is accessible to water. In both cases, the features of the CIDEP in the TREPR spectrum originate from the diffusive motion and photophysical behavior of the sensitizer in its local environment.

In order to study ESP processes, the chemically inert triplet sensitizer benzil and TEMPO were incorporated into solutions of Pluronic surfactants. The benzil sensitizer is relatively hydrophobic, and like BP, is expected to exist preferentially in copolymer aggregates. Generally speaking, the solubility of benzil in Pluronic solutions was poor at room temperature, but increased substantially as the sample was heated. Excitation of the benzil at 308 nm is followed by fast ISC to the benzil triplet state. Any polarization transfer to TEMPO in solution was observed by TREPR, and the temperature dependence of the polarized TEMPO signal was examined. No TREPR signal from the benzil sensitizer was observed. Figure 5.15 shows the temperature dependent TREPR signal of TEMPO in 2 wt. % solutions of L64 and 17R4. The spectra of the spin polarized TEMPO is net emissive, consistent with TM polarization transferred from the triplet excited state of the benzil or RTPM polarization due to interactions between the nitroxide and the $Q_{\pm 3/2}$ states of the excited triplet.. For both surfactants, the TREPR signal at low temperature exhibits sharp line widths and distinctive transitions consistent with TEMPO in water. At higher temperatures, the line width increases substantially, and there is an apparent shift in the hyperfine coupling of the TEMPO suggesting polarization was transferred from benzil in a hydrophobic local environment than was observed at lower temperatures.

A comparison of the TREPR spectra of spin polarized TEMPO to the SSEPR spectra of TEMPO partitioning in solutions of Pluronic surfactants may potentially shed some light on the differences between the high and low temperature spectra in Figure 5.15. Figure 5.16 shows an
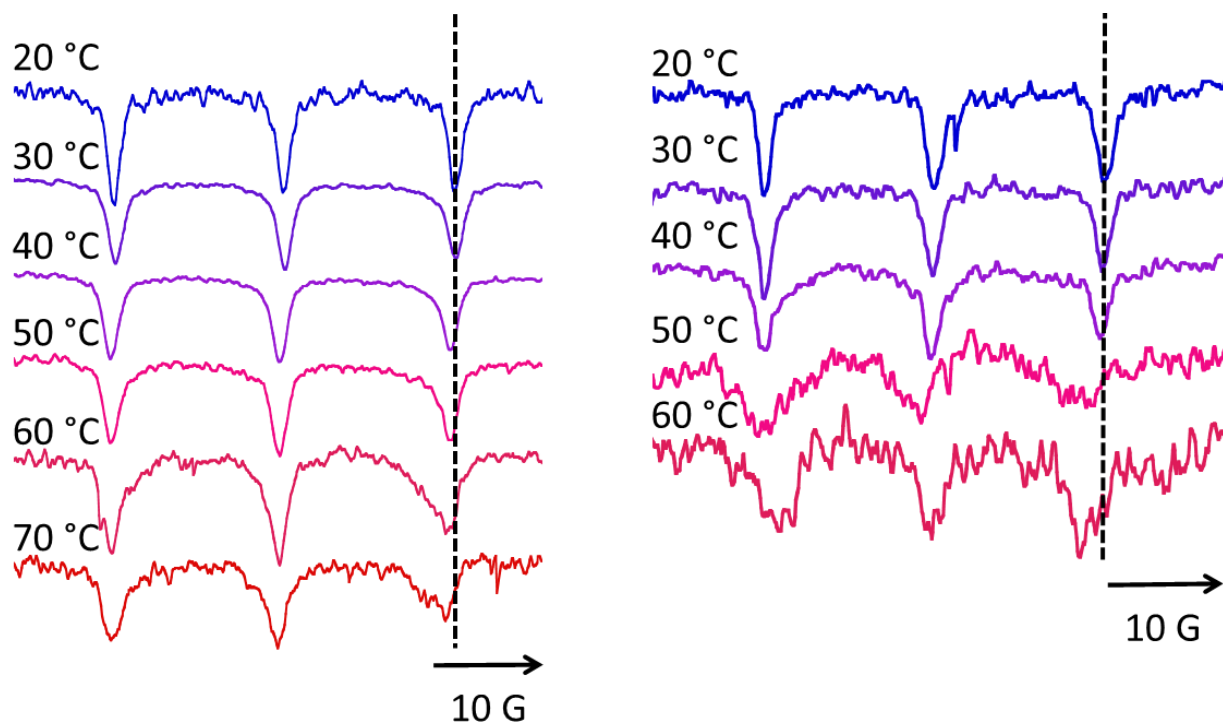
Figure 5.15 Temperature dependence of the TREPR spectra for polarization transfer between benzil (1 mM) and TEMPO (3 mM) in a 2 wt. % solution of Pluronic L64 (left) and Pluronic 17R4 (right). Temperatures were varied
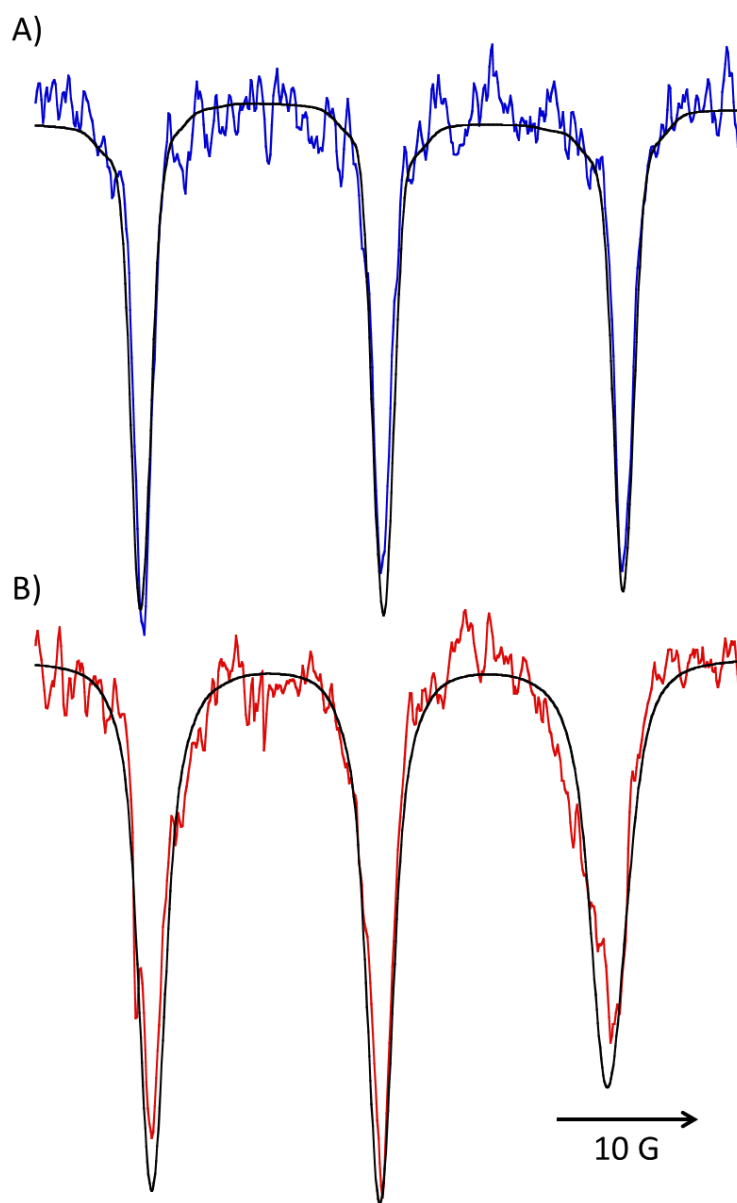
Figure 5.16 Comparison of the integral of the SSEPR (black) of TEMPO (1 mM) in a solution of Pluronic L64 (10 wt. %) to the TREPR of spin polarized TEMPO (3 mM) in identical solutions at 20 °C (A) and 60 °C (B). TREPR spectra were collected at a delay time of 500 ns following photolysis at 308 nm with a repetition rate of 60 Hz.

overlay of the TREPR spectra of 2 wt. % L64 at 20 °C and 60 °C with an integration of the curve

of the SSEPR spectra of 2 wt. % L64 at the same temperature. These two points correspond to

regions of the L64 phase diagram where the polymer exists as unimers in solutions or as micelles,

respectively. There is excellent agreement between the position of the transitions, the line width,

and the normalized line height of the SSEPR and TREPR spectra. This is not terribly surprising,

given that polarization transfer to TEMPO has been observed in polymer, polymer aggregate, and

micelle spectra previously. Figure 5.17 shows a comparison of the SSEPR spectrum of 17R4 at 60

°C and its integral to the TREPR spectra of spin polarized TEMPO at 20 °C and 60 °C. In the

SSEPR spectrum, partitioning was observed between the aqueous phase and the polymer-based

isotropic phase. In Figure 5.17, the aqueous TEMPO species is marked with a red dotted line for

clarity. It is clear that the A_N for the spin polarized spectrum at 60 °C (Figure 5.17D) is smaller

than that of the aqueous species. The high field transition at 60 °C in the TREPR spectra appears

to line up closely with the shoulder on the high field transition of the SSEPR in 5.16B, which is

caused by the slower motion of TEMPO in a hydrophobic TEMPO environment. The TREPR

signal and broadening in Figure 5.16D is the result of polarization transfer between benzil in the

more viscous, hydrophobic phase of these solutions at high temperature to TEMPO, which may

then escape the surfactant structure into solution.

5.4 Conclusions and Future directions

For both nonionic core shell and block copolymer surfactants, the work presented here is

still largely preliminary or, in some cases, inconclusive. In regard to the Brij surfactants, there are

two pressing concerns. First, the TREPR results for the hydrogen atom abstraction reaction

between Brij surfactants and triplet sensitizers are somewhat inconsistent. A more thorough
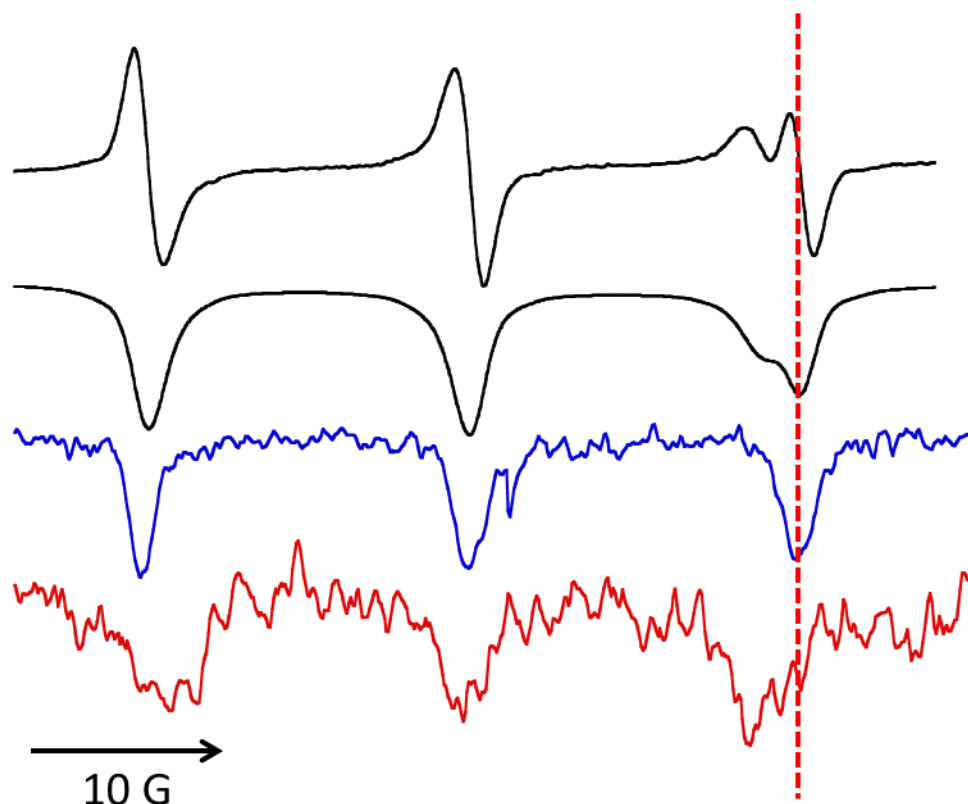
Figure 5.17 Comparison of the SSEPR of TEMPO (1 mM) in a solution of Pluronic 17R4 (2 wt. %) at 60 °C (A) and its integral (B) to the TREPR spectrum of spin polarized TEMPO (3 mM) in the same surfactant solution at 20 °C and 60 °C . The vertical dotted line is a guide for the eye indicating the location of the peak of the TREPR spectrum at the lowest temperature.

study of the surfactants as a function of structure – particularly in regard to the core and shell size – is warranted. The CIDEP of the PEO radicals was found to be very sensitive to concentration of both the surfactant and the sensitizer. Issues encountered with net emission of the TREPR signal or exceptionally broad TREPR transitions, particularly with the Triton X-405 and Brij 97 surfactants, may be related concentration rather than surfactant structure. Furthermore, the exact nature of the CIDEP needs to be explored with respect to surfactant structure and surfactant concentration through spectral simulations using the microreactor model.

The second concern with the TREPR of the PEO-based, core-shell surfactants is related to the identification of the unknown radical signal, which has been previously assigned as the core radical.[13] Some of the transitions of the unidentified radical clearly resemble the expected location of a core alkyl radical.[62-63, 70] However, the HFC constants of the most likely radical product from the core do not fit all of the observed transitions. The remarkably similar CIDEP, including the virtually identical line broadening of all of the unidentified transitions, suggest that they are either from the same radical or very closely related radicals. The identity of this radical still needs to be determined. If a truly nonpolar triplet sensitizer can be found, it might exist preferentially in the core and could be used to confirm the assignment of this radical to the alkyl core of the micelle. Another possible avenue is looking at SSEPR adducts of oxygen -based degradation products – these cannot be trapped by DBNBS. Another possible approach involves examining the TREPR of model compounds for the suspected radicals. This was already attempted with ethoxybenzene, but was unsuccessful. If reasonable model compounds that mirror the suspected structure of the unknown radical can be found, TREPR spectra can be used to obtain the necessary HFC constants for identification of the unknown radical product. Finally, it is possible that the signal is not from

a core radical, but may be due to some secondary photoproduct or degradation product, and this avenue should also be explored.

SSEPR and TREPR investigations of Pluronic surfactants reveal rich phase behavior that is dependent on the triblock copolymer structure, concentration, and solution temperature. Careful examination of the SSEPR of TEMPO and 5-DSA in these solutions can distinguish between the formation of micelles and isotropic liquid phases, including phase separation at higher temperature. These spin probes are also sensitive to the degree of hydration in the local environment of the probe, revealing different levels of hydration for probes in copolymers of varying PEO content. Though extensive investigations of the SSEPR of some Pluronic surfactants have already been conducted,[26, 45a, 46] the TREPR of these molecules is completely novel. TREPR studies further elucidate the temperature dependent structure of Pluronic aggregates and the accessibility of the copolymer blocks to the aqueous bulk. Direct comparisons between SSEPR of spin probes incorporated into these aggregates with TREPR of spin polarized probes show remarkable similarities and confirm the formation of a hydrophobic phase into which small spin probes like TEMPO can partition.[47, 71]

At this stage, SSEPR and TREPR investigations of the Pluronic surfactants discussed here are still ongoing. There are some discrepancies between the partitioning of TEMPO observed by Kurzbach et al.[47, 71] and the experimental results reported here. Question remain about the location of the TEMPO when it partitions and the nature of the site exchange between the hydrophobic and hydrophilic sites in different types of Pluronic aggregate structures. Considering that dehydration of both the PEO and PPO blocks of the copolymer is expected at higher temperature,[36, 72] it is possible that partitioning is occurring between the PPO core and PEO shell. The observation of TEMPO with a hyperfine coupling of 16.3 G, which is smaller than aqueous TEMPO but larger

than TEMPO in PPO, [46, 65] in solutions of Pluronic surfactants of high PEO content (F68), suggest that partitioning to the PEO shell is a possibility not fully explored in previous studies. Careful examinations of the temperature and concentration dependence of the SSEPR is currently being repeated to ensure the accuracy of these observations, since the ultimate goal is to compare them directly to the spin polarized TREPR signal of TEMPO. To this end, the concentration of TEMPO in the SSEPR experiment (1 mM) does not match the concentration in the TREPR experiment (3 mM). Partitioning of TEMPO is concentration dependent. For samples where partitioning occurs – especially if it may be occurring between the shell and core of the copolymer aggregates – it may be particularly important to repeat the SSEPR experiments with a higher concentration of TEMPO. Polarization transfer using other spin probes, including 5-DSA, may also be of interest. Finally, in all cases, this work could be extended to a comparison of structurally related Pluronics that vary in PPO block size.

5.5 Experimental

All Pluronic surfactants were obtained from Aldrich and were used as received. Stock solutions of the samples were prepared by weighing out the polymer sample and adding MilliQ water to achieve the desired concentration. Stock solutions were prepared at the highest weight percent for each sample and stirred overnight to ensure the Pluronic polymer dissolved. Initial stock solutions of 10 wt. % (L64, 17R4) or 30 wt. % (F68) were diluted to obtain stock solutions at 2 wt. % and 0.2 wt. % or 10 wt. %, 6 wt. %, and 0.6 wt. % respectively. For SSEPR measurements, the spin probe TEMPO or 5-DSA (Aldrich) were dissolved in acetone to form a stock solution of 1 M TEMPO or 10 mg /3.25 mL 5-DSA. Spin probe stock solutions were aliquotted into vials and the solvent was allowed to evaporate off under flow of nitrogen. Stock

solution of the Pluronic were added to the vials in 1 mL total volume. Samples were stirred and degassed for 15 minutes prior to being run by SSEPR. For TREPR measurements, 25 mL aliquots of stock solution were taken. For H-atom transfer studies, AQDS (Aldrich) was added directly to the samples for a total concentration of 1.1 mM. For polarization transfer studies, benzil and TEMPO were added directly to the samples for a total concentration of 1 mM benzil and 3 mM TEMPO. Samples were stirred and gently heated to dissolve the benzil. Samples were cooled to room temperature, then bubbled with nitrogen gas for 15-30 minutes before being run by TREPR.

SSEPR measurements were collected on a JEOL-FA 100 X-band (9.5 GHz) spectrometer with a digital variable temperature control unit. Field modulation was 100 kHz with a modulation amplitude of 1 G. Typical spectrometer settings were: microwave power 1 mW, sweep width 100G, center field 3362 G, time constant 0.3 s, sweep time 4 min. Temperature was controlled between 20-50 °C by the DVT using the liquid nitrogen set up for low temperature. Data collection on the same sample was repeated at 50 °C and over the range of 50 °C to 90 °C with the DVT set -up for high temperatures using a compressor and blast heater to flow warm nitrogen gas through the cavity.

TREPR measurements were obtained on a modified JEOL JES RE-1X X-band spectrometer outfitted with a fast preamplifier and a low noise GaAs FET microwave amplifier. The spectrometer is fitted with a rectangular Varian TE_{103} cavity that allows for optical transmission. Samples are flowed through a quartz flat cell with a path length of 0.4 mm using a micropump connected to a sample reservoir with Teflon tubing. Flowing of the sample prevents degradation and heating. The reservoir and flow system was sealed and kept under a flow of nitrogen gas during the experiment. Laser excitation occurs at 308 nm using a Lambda-Physik LPX 100i excimer laser. Pulse energy hitting the sample is approximately 20 mJ. Spectra are

recorded at a fixed time after the laser shot by positioning the gate of a Stanford Research Systems boxcar integrator at the desired time point after the pulse trigger. The external magnetic field is swept over a specified time period, and successive averages are taken at each magnetic field point across the sweep. Instrument settings for the TREPR measurements were as follows: center field approximately 3390 G, sweep width 150 G, sweep time 4 minutes, boxcar gate width 300 ns, boxcar averages 30, boxcar delay time 500 ns, excitation wavelength 308 nm, pulse frequency 60 Hz, and incident microwave power of 10 mW.

REFERENCE

1.   Schmolka, I. R., Gel cosmetics. *Cosmetics & Toiletries* **1984,** *99* (11), 69-&.

2.   Schmolka, I. R., Review of block polymer surfactants *J. Am. Oil Chem. Soc.* **1977,** *54* (3), 110-116.

3.   (a) Lin, S. Y.; Kawashima, Y., The influence of three poly(oxyethylene)-poly(oxypropylene) surface active block copolymers on the solubility behavior of indomethacin *Pharmaceutica Acta Helvetiae* **1985,** *60* (12), 339-344; (b) Serra, L.; Domenech, J.; Peppas, N. A., Drug transport mechanisms and release kinetics from molecularly designed poly(acrylic acid-g-ethylene glycol) hydrogels. *Biomaterials* **2006,** *27* (31), 5440-5451; (c) Parmar, A.; Parekh, P.; Bahadur, P., Solubilization and Release of a Model Drug Nimesulide from PEO-PPO-PEO Block Copolymer Core-Shell Micelles: Effect of Size of PEO Blocks. *J. Solution Chem.* **2013,** *42* (Copyright (C) 2013 American Chemical Society (ACS). All Rights Reserved.), 80-101; (d) Mahmoudzadeh, M.; Fassihi, A.; Emami, J.; Davies, N. M.; Dorkoosh, F., Physicochemical, pharmaceutical and biological approaches toward designing optimized and efficient hydrophobically modified chitosan-based polymeric micelles as a nanocarrier system for targeted delivery of anticancer drugs. *Journal of Drug Targeting* **2013,** *21* (8), 693-709; (e) Henry, R. L.; Schmolka, I. R., Burn wound coverings and the use of poloxamer preparations *Critical Reviews in Biocompatibility* **1989,** *5* (3), 207-220.

4.   Bridgeford, D. J. Celluslose-containing Food Wrapper. 1984.

5.   (a) Kabanov, A. V.; Batrakova, E. V.; Meliknubarov, N. S.; Fedoseev, N. A.; Dorodnich, T. Y.; Alakhov, V. Y.; Chekhonin, V. P.; Nazarova, I. R.; Kabanov, V. A., A new class of drug carriers - micelles of poly(oxyethylene)-poly(oxypropylene) block copolymers as microcontainers for drug targeting from blood in brain *J. Controlled Release* **1992,** *22* (2), 141-157; (b) Osth, K.; Paulsson, M.; Bjork, E.; Edsman, K., Evaluation of drug release from gels on pig nasal mucosa in a horizontal Ussing chamber. *J. Controlled Release* **2002,** *83* (3), 377-388; (c) Paulsson, M.; Edsman, K., Controlled drug release from gels using lipophilic interactions of charged substances with surfactants and polymers. *J. Colloid Interface Sci.* **2002,** *248* (1), 194-200; (d) Dong, R. H.; Wu, J.; Dong, S. L.; Song, S. S.; Tian, F.; Hao, J. C., Interconvertible Self-Assembly and Rheological Properties of Planar Bilayers and Vesicle Gels in Anionic/Nonionic (CF/CH) Surfactant Solutions. *Chem.-Asian J.* **2013,** *8* (8), 1863-1872.

6.   B., S.; V., N.; G.V., B., Insoluble drug delivery technologies: Review of health benefits and business potentials. *OA Drug Design & Delivery* **2013,** *1* (1).

7.   Streeter, J. E.; Gessner, R.; Miles, I.; Dayton, P. A., Improving Sensitivity in Ultrasound Molecular Imaging by Tailoring Contrast Agent Size Distribution: In Vivo Studies. *Molecular Imaging* **2010,** *9* (2), 87-95.

8.   Alexandridis, P.; Hatton, T. A., Poly(ethylene oxide)-poly(propylene oxide)-poly(ethylene oxide) block copolymer surfactants in aqueous solutions and at interfaces - thermodynamics, structure, dynamics, and modeling *Colloid Surf. A-Physicochem. Eng. Asp.* **1995,** *96* (1-2), 1-46.

9.   (a) Qiu, Y.; Park, K., Environment-sensitive hydrogels for drug delivery. *Advanced drug delivery reviews* **2001,** *53* (3), 321-339; (b) Bromberg, L. E.; Ron, E. S., Temperature-responsive gels and thermogelling polymer matrices for protein and peptide delivery. *Advanced drug delivery reviews* **1998,** *31* (3), 197-221; (c) Ruel-Gariepy, E.; Chenite, A.; Chaput, C.; Guirguis, S.; Leroux, J.-C., Characterization of thermosensitive chitosan gels for the sustained delivery of drugs. *Int. J. Pharm.* **2000,** *203* (1), 89-98.

10.   (a) Hersel, U.; Dahmen, C.; Kessler, H., RGD modified polymers: biomaterials for stimulated cell adhesion and beyond. *Biomaterials* **2003,** *24* (24), 4385-4415; (b) Park, A.; Wu, B.; Griffith, L. G., Integration of surface modification and 3D fabrication techniques to prepare patterned poly (L-lactide) substrates allowing regionally selective cell adhesion. *Journal of Biomaterials Science, Polymer Edition* **1998,** *9* (2), 89-110; (c) Liu, V. A.; Jastromb, W. E.; Bhatia, S. N., Engineering protein and cell adhesivity using PEO-terminated triblock polymers. *Journal of biomedical materials research* **2002,** *60* (1), 126-134.

11.   (a) Redhead, M.; Mantovani, G.; Nawaz, S.; Carbone, P.; Gorecki, D. C.; Alexander, C.; Bosquillon, C., Relationship between the Affinity of PEO-PPO-PEO Block Copolymers for Biological Membranes and Their Cellular Effects. *Pharm. Res.* **2012,** *29* (Copyright (C) 2013 American Chemical Society (ACS). All Rights Reserved.), 1908-

1918; (b) Zhang, Z.; Alrubeai, M.; Thomas, C. R., Effect of Pluronic F68 on the mechanical properties of mammalian cells. *Enzyme Microb. Technol.* **1992,** *14* (12), 980-983.

12.   (a) Roby, A.; Erdogan, S.; Torchilin, V. P., Solubilization of poorly soluble PDT agent, meso-tetraphenylporphin, in plain or immunotargeted PEG-PE micelles results in dramatically improved cancer cell killing in vitro. *Eur. J. Pharm. Biopharm.* **2006,** *62* (3), 235-240; (b) Krupka, T. M.; Weinberg, B. D.; Wu, H. P.; Ziats, N. P.; Exner, A. A., Effect of intratumoral injection of carboplatin combined with pluronic P85 or L61 on experimental colorectal carcinoma in rats. *Experimental Biology and Medicine* **2007,** *232* (7), 950-957; (c) Bhattacharjee, J.; Verma, G.; Aswal, V. K.; Patravale, V.; Hassan, P. A., Microstructure, drug binding and cytotoxicity of Pluronic P123-aerosol OT mixed micelles. *Rsc Advances* **2013,** *3* (45), 23080-23089.

13.   Chaney, E. E.; Forbes, M. D. E., Dynamics of spin-correlated radical pairs in non-ionic surfactant solutions. *J. Phys. Chem. B* **2003,** *107* (18), 4464-4469.

14.   (a) Yokoyama, M., Block copolymers as drug carriers *Critical Reviews in Therapeutic Drug Carrier Systems* **1992,** *9* (3-4), 213-248; (b) Guzman, M.; Garcia, F. F.; Molpeceres, J.; Aberturas, M. R., Polyoxyethylene-polyoxypropylene block copolymer gels as sustained release vehicles for subcutaneous drug administration *Int. J. Pharm.* **1992,** *80* (2-3), 119-127.

15.   (a) Paulsson, M.; Edsman, K., Controlled drug release from gels using surfactant aggregates. II. Vesicles formed from mixtures of amphiphilic drugs and oppositely charged surfactants. *Pharm. Res.* **2001,** *18* (11), 1586-1592; (b) Wang, W.; Sande, S. A., Kinetics of Re-equilibrium of Oppositely Charged Hydrogel-Surfactant System and Its Application in Controlled Release. *Langmuir* **2013,** *29* (22), 6697-6705.

16.   (a) Phillies, G. D. J.; Hunt, R. H.; Strang, K.; Sushkin, N., Aggregatopm number acid hydrodynamic hydration levels of Brij 35 micelles from optical probe studies *Langmuir* **1995,** *11* (9), 3408-3416; (b) Kumbhakar, M.; Goel, T.; Mukherjee, T.; Pal, H., Role of micellar size and hydration on solvation dynamics: A temperature dependent study in Triton-X-100 and Brij-35 micelles. *J. Phys. Chem. B* **2004,** *108* (50), 19246-19254.

17.   (a) Luche, S.; Santoni, V.; Rabilloud, T., Evaluation of nonionic and zwitterionic detergents as membrane protein solubilizers in two-dimensional electrophoresis. *Proteomics* **2003,** *3* (3), 249-253; (b) le Maire, M.; Champeil, P.; Møller, J. V., Interaction of membrane proteins and lipids with solubilizing detergents. *Biochimica et Biophysica Acta (BBA)-Biomembranes* **2000,** *1508* (1), 86-111.

18.   (a) Motson, H. R., Cleaning surfaces. Google Patents: 2006; (b) Adams, J.; Allgaier, J.; Frank, C., Mixture comprising an alkyl polyglucoside, a cosurfactant and a polymer additive. Google Patents: 2013.

19.   Preu, H.; Zradba, A.; Rast, S.; Kunz, W.; Hardy, E. H.; Zeidler, M. D., Small angle neutron scattering of D2O-Brij 35 and D2O-alcohol-Brij 35 solutions and their modelling using the Percus-Yevick integral equation. *PCCP* **1999,** *1* (14), 3321-3329.

20.   Yuan, H. Z.; Cheng, G. Z.; Zhao, S.; Miao, X. J.; Yu, J. Y.; Shen, L. F.; Du, Y. R., Conformational dependence of triton X-100 on environment studied by 2D NOESY and H-1 NMR relaxation. *Langmuir* **2000,** *16* (7), 3030-3035.

21.   Phillies, G. D. J.; Hunt, R. H.; Strang, K.; Sushkin, N., Aggregation number acid hydrodynamic hydration levels of Brij 35 micelles from optical probe studies *Langmuir* **1995,** *11* (9), 3408-3416.

22.   (a) Batchelor, S. N.; McLauchlan, K. A.; Shkrob, I. A., Reaction yield detected magnetic resonance and magnetic field effect studies of radical pairs containing electronically excited organic molecules *Mol. Phys.* **1992,** *77* (1), 75-109; (b) Ortica, F.; Elisei, F.; Favaro, G., Photophysics of 3-phenyl and 4-phenyl pyridyl ketones in submicellar and micellar solutions of ionic and nonionic surfactants *Journal of the Chemical Society-Faraday Transactions* **1995,** *91* (19), 3405-3413.

23.   (a) Prousek, J.; Duriskova, I., Oxidative degradation of poly(ethylene glycol)s (PEG) by the Fenton and photo-Fenton reactions. *Chem. Listy* **1998,** *92* (3), 218-220; (b) Santos, L. C.; Schmitt, C. C.; Poli, A. L.; Neumann, M. G., Photo-Fenton Degradation of Poly(ethyleneglycol). *Journal of the Brazilian Chemical Society* **2011,** *22* (3), 540-545; (c) Dorati, R.; Colonna, C.; Tomasi, C.; Genta, I.; Modena, T.; Faucitano, A.; Buttafava, A.; Conti, B.,

gamma-irradiation of PEGd,lPLA and PEG-PLGA multiblock copolymers: II. effect of oxygen and EPR investigation. *AAPS PharmSciTech* **2008,** *9* (4), 1110-8.

24.   (a) Janzen, E. G.; Coulter, G. A., Spin Trapping in SDS micelles. *J. Am. Chem. Soc.* **1984,** *106* (7), 1962-1968; (b) Janzen, E. G.; Haire, D. L.; Coulter, G. A.; Stronks, H. J.; Krygsman, P. H.; Towner, R. A.; Hilborn, J. W., Locating spin trapos in heterogenous media by C13 NMR spectroscopy - investigations in SDS micelles, DMPC vesicles, and rat liver microsomes *J. Org. Chem.* **1989,** *54* (12), 2915-2920; (c) Rizzi, C.; Lauricella, R.; Tuccio, B.; Bouteiller, J. C.; Cerri, V.; Tordo, P., Spin-trapping of free radicals by PBN-type beta-phosphorylated nitrones in the presence of SDS micelles. *Journal of the Chemical Society-Perkin Transactions 2* **1997,** (12), 2507-2512.

25.   Sostaric, J. Z.; Riesz, P., Sonochemistry of Surfactants in Aqueous Solutions: An EPR Spin-Trapping Study. *J. Am. Chem. Soc.* **2001,** *123* (44), 11010-11019.

26.   Caldararu, H., Structural aspects in self-assembled systems of polyoxyethylene surfactants, as studied by the spin probe technique. *Spectroc. Acta Pt. A-Molec. Biomolec. Spectr.* **1998,** *54* (14), 2309-2336.

27.   Holmberg, K., Applications of block copolymers. In *Amphiphilic block copolymers : self-assembly and applications*, Alexandridis, P.; Lindman, B., Eds. Elsevier: Amsterdam ;New YOrk, 2000.

28.   Pons, R., Polymeric Surfactants as Emulsion Stabilizers. In *Amphiphilic block copolymers : self-assembly and applications*, Alexandridis, P.; Lindman, B., Eds. Elsevier: Amsterdam ;New YOrk, 2000.

29.   (a) Winnik, F. M.; Brenton, M. P.; Riske, W. Ink compositions. 1992; (b) Winnik, F. M.; Davidson, A. R.; Lin, J. W.-P.; Croucher, M. D., Inks containing block copolymer micelles. *U.S. Patent 5145518* **1992**.

30.   Murhammer, D. W.; Goochee, C. F., Structural features of nonionic polyglycol polymer molecules responsible for the protective effect in sparged animal cell bioreactors *Biotechnol. Progr.* **1990,** *6* (2), 142-148.

31.   (a) Hurter, P. N.; Hatton, T. A., Solubilization of polycyclic aromatic hydrocarbons by poly(ethylene oxide-propylene oxidde) block copolymer micelles - effects of polymer on structure *Langmuir* **1992,** *8* (5), 1291-1299; (b) Hurter, P. N.; Alexandridis, P.; Hatton, T. A., Solubilization in amphiphilic copolymer solutions. In *Solubilization in Surfactant Aggregates*, Christian, S. D.; Scamehorn, J. F., Eds. CRC Press: 1995; Vol. 55; (c) Nagarajan, R.; Barry, M.; Ruckenstein, E., Unusual selectivity in solubilization by block copolymer micelles *Langmuir* **1986,** *2* (2), 210-215; (d) Svensson, M.; Johansson, H.-O.; Tjerneld, F., Applilcations of Amphiphilic Copolymers in Separations. In *Amphiphilic block copolymers : self-assembly and applications*, Alexandridis, P.; Lindman, B., Eds. Elsevier: Amsterdam ;New YOrk, 2000.

32.   (a) Kavanov, A. V.; Alkhov, V. Y., Micelles of amphiphilic block copolymers as vehicles for drug delivery. In *Amphiphilic block copolymers : self-assembly and applications*, Alexandridis, P.; Lindman, B., Eds. Elsevier: Amsterdam ;New YOrk, 2000; (b) Malmsten, M., Block copolymers in pharmaceuticals. In *Amphiphilic block copolymers : self-assembly and applications*, Alexandridis, P.; Lindman, B., Eds. Elsevier: Amsterdam ;New YOrk, 2000.

33.   (a) Nawaz, S.; Redhead, M.; Mantovani, G.; Alexander, C.; Bosquillon, C.; Carbone, P., Interactions of PEO-PPO-PEO block copolymers with lipid membranes: a computational and experimental study linking membrane lysis with polymer structure. *Soft Matter* **2012,** *8* (Copyright (C) 2013 American Chemical Society (ACS). All Rights Reserved.), 6744-6754; (b) Wang, J.-Y.; Marks, J.; Lee, K. Y. C., Nature of Interactions between PEO-PPO-PEO Triblock Copolymers and Lipid Membranes: (I) Effect of Polymer Hydrophobicity on Its Ability to Protect Liposomes from Peroxidation. *Biomacromolecules* **2012,** *13* (Copyright (C) 2013 American Chemical Society (ACS). All Rights Reserved.), 2616-2623.

34.   (a) Alexandridis, P.; Holzwarth, J. F.; Hatton, T. A., Micellization of poly(ethylene oxide)-poly(propylene oxide)-poly(ethylene oxide triblock copolymers in aqueous solutions - thermodynamics of copolymer association. *Macromolecules* **1994,** *27* (9), 2414-2425; (b) Mortensen, K.; Pedersen, J. S., Structural study on the micelle formation of poly(ethylene oxide)-poly(propylene oxide)-poly(ethylene oxide) triblock copolymer in aqueous solution *Macromolecules* **1993,** *26* (4), 805-812; (c) Mortensen, K.; Brown, W., Poly(ethylene oxide)-poly(propylene oxide)-poly(ethylene oxide) triblock copolymers in aqueous solution - the influence of relative block size *Macromolecules* **1993,** *26* (16), 4128-4135.

35.   Alsaden, A. A.; Whateley, T. L.; Florence, A. T., Poloxamer association in aqueous solution *J. Colloid Interface Sci.* **1982,** *90* (2), 303-309.

36.   Zhou, Z.; Chu, B., Phase behavior and association properties of poly(oxypropylene)-poly(oxyethylene)-poly(oxypropylene) triblock copolymer in aqueous solution *Macromolecules* **1994,** *27* (8), 2025-2033.

37.   (a) Chu, B.; Zhou, Z., Physical Chemistry of Polyoxyalkylene Block Copolymer Surfactants. In *Non-ionic surfactants: polyoxyalkylene block copolymers*, Nace, V. M., Ed. Marcel Dekker, Inc.: New York, 1996; Vol. 60; (b) *Amphiphilic block copolymers : self-assembly and applications*. Elsevier: Amsterdam ;New YOrk, 2000.

38.   Almgren, M.; Bahadur, P.; Jansson, M.; Li, P. Y.; Brown, W.; Bahadur, A., Static and dynamic properties of a PEO-PPO-PEO block coplymer in aqueous solution *J. Colloid Interface Sci.* **1992,** *151* (1), 157-165.

39.   (a) Alexandridis, P.; Zhou, D. L.; Khan, A., Lyotropic liquid crystallinity in amphiphilic block copolymers: Temperature effects on phase behavior and structure for poly(ethylene oxide)-b-poly(propylene oxide)-b-poly(ethylene oxide) copolymers of different composition. *Langmuir* **1996,** *12* (11), 2690-2700; (b) Zhou, S. Q.; Su, J.; Chu, B., Water-induced micellar structure change in pluronic P103/water/o-xylene ternary system. *Journal of Polymer Science Part B-Polymer Physics* **1998,** *36* (5), 889-900; (c) Wu, G. W.; Zhou, Z. K.; Chu, B., Water induced micelle formation of block copoly(oxyethylene oxypropylene oxyethylene) in o-xylene *Macromolecules* **1993,** *26* (8), 2117-2125; (d) Wu, G. W.; Chu, B., Light scattering studies of a blcok poly(oxyethylene oxypropylene oxyethylene) copolymer in water o-xylene mixtures. *Macromolecules* **1994,** *27* (7), 1766-1773; (e) Wanka, G.; Hoffmann, H.; Ulbricht, W., The aggregation behavior of poly(oxyetheylene)-poly(oxypropylene)-poly(oxyethylene) block copolymers in aqueous solution *Colloid. Polym. Sci.* **1990,** *268* (2), 101-117.

40.   (a) Alexandridis, P.; Nivaggioli, T.; Holzwarth, J. F.; Hatton, T. A., Characterization of block copolymer micellar solutions - thermodynamics and microenvironment

Abstr. Pap. Am. Chem. Soc. **1994,** *207*, 234-POLY; (b) Nakashima, K.; Anzai, T.; Fujimoto, Y., Fluorescence studies on the properties of a pluronic F68 micelle

Langmuir **1994,** *10* (3), 658-661; (c) Nakashima, K.; Anzai, T.; Fujimoto, Y., Fluorescence studies on the properties of a pluronic F68 micelle *Langmuir* **1994,** *10* (3), 658-661.

41.   Nivaggioli, T.; Tsao, B.; Alexandridis, P.; Hatton, T. A., Microviscosity in pluronic and tetronic poly(ethylene oxide)-poly(propylene oxide) block copolymer micelles *Langmuir* **1995,** *11* (1), 119-126.

42.   Larraneta, E.; Isasi, J. R., Phase Behavior of Reverse Poloxamers and Poloxamines in Water. *Langmuir* **2013,** *29* (4), 1045-1053.

43.   Mortensen, K., Phase behavior of poly(ethylene oxide)-poly(propylene oxide)-poly(etheylene oxide(triblock copolymer dissolved in water

Europhys. Lett. **1992,** *19* (7), 599-604.

44.   Su, Y. L.; Wang, J.; Liu, H. Z., FTIR spectroscopic investigation of effects of temperature and concentration on PEO-PPO-PEO block copolymer properties in aqueous solutions. *Macromolecules* **2002,** *35* (16), 6426-6431.

45.   (a) Caragheorgheopol, A.; Caldararu, H.; Dragutan, I.; Joela, H.; Brown, W., Micellization and micellar structure of a poly(ethyleneoxide)/poly(propyleneoxide)/poly(ethyleneoxide) triblock copolymer in water solution, as studied by the spin probe technique. *Langmuir* **1997,** *13* (26), 6912-6921; (b) Vasilescu, M.; Caragheorgheopol, A.; Caldararu, H.; Bandula, R.; Lemmetyinen, H.; Joela, H., Micropolarity and order in the reverse micelles of L62 and L64 pluronic copolymers, as studied by molecular probe techniques. *J. Phys. Chem. B* **1998,** *102* (40), 7740-7751.

46.   Zhou, L.; Schlick, S., Electron spin resonance (ESR) spectra of amphiphilic spin probes in the triblock copolymer EO13PO30EO13 (Pluronic L64): hydration, dynamics and order in the polymer aggregates. *Polymer* **2000,** *41* (12), 4679-4689.

47.   Kurzbach, D.; Reh, M. N.; Hinderberger, D., Nanoscale Inhomogeneities in Thermoresponsive Triblock Copolymers. *ChemPhysChem* **2011,** *12* (Copyright (C) 2013 American Chemical Society (ACS). All Rights Reserved.), 3566-3572.

48.   (a) Turro, N. J.; Chung, C., Photoluminescent probes for water soluble polymers. Pressure and temperature effects on a polyol surfactant. *Macromolecules* **1984,** *17* (10), 2123-2126; (b) Andersson, M.; Karlstrom, G., Conformational structure of 1,2-dimethoxyethane in water and other dipolar solvents, studied by quantum mechanical, reaction field, and statistical mechanical techniques *J. Phys. Chem.* **1985,** *89* (23), 4957-4962; (c) Hurter, P. N.; Scheutjens, J.; Hatton, T. A., Molecular modeling of micelle formation and solubilization in block copolymer micelles 2. Lattice theory for monomers with internal degrees of freedom *Macromolecules* **1993,** *26* (19), 5030-5040; (d) Linse, P., Micellization of poly(ethylene oxide)-poly(propylene oxide) block copolymers in aqueous solution *Macromolecules* **1993,** *26* (17), 4437-4449.

49.   (a) Forbes, M. D. E.; Jarocha, L. E.; Sim, S.; Tarasov, V. F., Time-Resolved Electron Paramagnetic Resonance Spectroscopy: History, Technique, and Application to Supramolecular and Macromolecular Chemistry. In *Advances in Physical Organic Chemistry, Vol 47*, Williams, I. H.; Williams, N. H., Eds. 2013; Vol. 47, pp 1-83; (b) Imamura, T.; Onitsuka, O.; Obi, K., Memory of spin polarization in triplet-doublet systems. *The Journal of Physical Chemistry* **1986,** *90* (26), 6741-6744.

50.   (a) Blättler, C.; Jent, F.; Paul, H., A novel radical-triplet pair mechanism for chemically induced electron polarization (CIDEP) of free radicals in solution. *Chem. Phys. Lett.* **1990,** *166* (4), 375-380; (b) Kawai, A.; Okutsu, T.; Obi, K., Spin polarization generated in the triplet-doublet interaction: hyperfine-dependent chemically induced dynamic electron polarization. *The Journal of Physical Chemistry* **1991,** *95* (23), 9130-9134.

51.   (a) Porter, G.; Wright, M. R., Modes of energy transfer from excited and unstable ionized states. Intramolecular and intermolecular energy conversion involving change of multiplicity. *Discussions of the Faraday Society* **1959,** *27* (0), 18-27; (b) Hoytink, G. J., Intermolecular electron exchange *Accounts Chem. Res.* **1969,** *2* (4), 114-&.

52.   Corvaja, C.; Franco, L.; Toffoletti, A., Electron spin polarization of doublet state species due to interaction with excited triplet states in single crystals. *Appl. Magn. Reson.* **1994,** *7* (2-3), 257-269.

53.   (a) Corvaja, C.; Maggini, M.; Prato, M.; Scorrano, G.; Venzin, M., C60 Derivative Covalently Linked to a Nitroxide Radical: Time-Resolved EPR Evidence of Electron Spin Polarization by Intramolecular Radical-Triplet Pair Interaction. *J. Am. Chem. Soc.* **1995,** *117* (34), 8857-8858; (b) Jockusch, S.; Porel, M.; Ramamurthy, V.; Turro, N. J., CIDEP from a Polarized Ketone Triplet State Incarcerated within a Nanocapsule to a Nitroxide in the Bulk Aqueous Solution. *J. Phys. Chem. Lett.* **2011,** *2* (22), 2877-2880.

54.   (a) Sartori, E.; Toffoletti, A.; Corvaja, C.; Garlaschelli, L., Electron spin polarization transfer and radical-triplet pair polarization in nitroxide-C-60 derivative systems. *J. Phys. Chem. A* **2001,** *105* (48), 10776-10780; (b) Jockusch, S.; Zeika, O.; Jayaraj, N.; Ramamurthy, V.; Turro, N. J., Electron Spin Polarization Transfer from a Nitroxide Incarcerated within a Nanocapsule to a Nitroxide in the Bulk Aqueous Solution. *J. Phys. Chem. Lett.* **2010,** *1* (18), 2628-2632; (c) Sartori, E.; Garlaschelli, L.; Toffoletti, A.; Corvaja, C.; Maggini, M.; Scorrano, G., Time-resolved EPR characterisation of radical-triplet pairs formed by host-guest interaction of a photoexcited C60-crown ether with an ammonium aminoxyl in liquid solution. *Chem. Commun.* **2001,** (4), 311-312.

55.   Turro, N. J.; Kleinman, M. H.; Karatekin, E., Electron spin polarization and time-resolved electron paramagnetic resonance: Applications to the paradigms of molecular and supramolecular photochemistry. *Angew. Chem.-Int. Edit.* **2000,** *39* (24), 4436-4461.

56.   (a) Fujisawa, J. I.; Ishii, K.; Ohba, Y.; Iwaizumi, M.; Yamauchi, S., Electron spin polarization transfer from excited triplet porphyrins to a nitroxide radical via a spin exchange mechanism *J. Phys. Chem.* **1995,** *99* (47), 17082-17084; (b) Tarasov, V. F.; Shkrob, I. A.; Trifunac, A. D., Spin-polarized nitroxide radicals in organic glasses. *J. Phys. Chem. A* **2002,** *106* (19), 4838-4845.

57.   Fujisawa, J.-i.; Ohba, Y.; Yamauchi, S., Electron-Spin Polarizations Generated from Interactions between Excited Triplet Porphyrins and Stable Radicals Studied by Time-Resolved Electron Paramagnetic Resonance. *The Journal of Physical Chemistry A* **1997,** *101* (4), 434-439.

58.   (a) Kawai, A.; Obi, K., Viscosity dependence of chemically induced dynamic electron spin polarization generated by the radical-triplet pair mechanism. *The Journal of Physical Chemistry* **1992,** *96* (14), 5701-5704; (b) Gorelik, V. R.; Tarasov, V. F.; Shakirov, S. R.; Bagryanskaya, E. G., Effect of nitroxide radicals on chemically induced dynamic electron polarization of spin-correlated radical pairs in aqueous micellar solutions of sodium dodecyl sulfate. *Russ. Chem. Bull.* **2008,** *57* (7), 1416-1427; (c) Jenks, W. S.; Turro, N. J., Electron spin polarization transfer between radicals. *J. Am. Chem. Soc.* **1990,** *112* (24), 9009-9011.

59.   Sim, S.; Forbes, M. D. E., *in preparation for Macromolecules* **2014**.

60.   Yamauchi, S.; Tominaga, K.; Hirota, N., Existence of the triplet mechanism in the CIDEP spectrum of acetone *J. Phys. Chem.* **1986,** *90* (11), 2367-2369.

61.   Adrian, F. J., Dynamic level crossing model of the antiphase electron spin polarization in spin-correlated radical pairs *J. Chem. Phys.* **1995,** *102* (11), 4409-4418.

62.   Caregnato, P.; Jarocha, L. E.; Esinhart, H. S.; Lebedeva, N. V.; Tarasov, V. F.; Forbes, M. D. E., Electrostatic Control of Spin Exchange Between Mobile Spin-Correlated Radical Pairs Created in Micellar Solutions. *Langmuir* **2011,** *27* (9), 5304-5309.

63.   Landolt-Bornstein, *Organic C Centered Radicals*. Springer: Berlin, 1977.

64.   (a) Buxton, G. V.; Greenstock, C. L.; Helman, W. P.; Ross, A. B., Critical review of rate constants for reactions of hydrated electrons, hydrogen atoms and hydroxyl radicals ($\cdot$ OH/$\cdot$ O$-$ in aqueous solution. *J. Phys. Chem. Ref. Data* **1988,** *17* (2), 513-886; (b) Goldstein, S.; Aschengrau, D.; Diamant, Y.; Rabani, J., Photolysis of Aqueous H2O2: Quantum Yield and Applications for Polychromatic UV Actinometry in Photoreactors. *Environmental Science & Technology* **2007,** *41* (21), 7486-7490; (c) Sanz, J.; Lombraña, J. I.; Luís, A., Ultraviolet-H2O2 oxidation of surfactants. *Environ Chem Lett* **2003,** *1* (1), 32-37.

65.   Windle, J. J., Hyperfine coupling constants for nitroxide spin probes in water and carbon tetrachloride. *Journal of Magnetic Resonance (1969)* **1981,** *45* (3), 432-439.

66.   Wikander, G.; Eriksson, P. O.; Burnell, E. E.; Lindblom, G., ESR line shapes in lyotropic systems - the micellar and liquid crystalline phases of the dodecyltrimethylammonium chloride in waters system *J. Phys. Chem.* **1990,** *94* (15), 5964-5972.

67.   Vadnere, M.; Amidon, G.; Lindenbaum, S.; Haslam, J. L., Thermodynamic studies on the gel sol transition of some pluronic polyols *Int. J. Pharm.* **1984,** *22* (2-3), 207-218.

68.   Brown, W.; Schillen, K.; Almgren, M.; Hvidt, S.; Bahadur, P., Micelle and gel formation in a poly(ethylene oxide) poly(propylene oxide) poly(ethylene oxide) triblock copolymer in water solution - dynamic and light scattering and oscillatory shear measurements. *J. Phys. Chem.* **1991,** *95* (4), 1850-1858.

69.   Turro, N. J.; Chung, C. J., Photoluminescent probes for water soluble polymers - pressure and temperature effects on a polyol surfactant *Macromolecules* **1984,** *17* (10), 2123-2126.

70.   Tarasov, V. F.; Jarocha, L. E.; Avdievich, N. I.; Forbes, M. D. E., TREPR spectra of micelle-confined spin-correlated radical pairs: I. Molecular motion and simulations. *Photochem. Photobiol. Sci.* **2014,** *13* (2), 439-453.

71.   Kurzbach, D.; Junk, M. J. N.; Hinderberger, D., Nanoscale Inhomogeneities in Thermoresponsive Polymers. *Macromol. Rapid Commun.* **2013,** *34* (2), 119-134.

72.   Nivaggioli, T.; Alexandridis, P.; Hatton, T. A.; Yekta, A.; Winnik, M. A., Fluorescence probe studies of pluronic copolymer solutions as a function of temperature *Langmuir* **1995,** *11* (3), 730-737.